MODELING TECHNIQUE FOR GENERATING FLUVIAL RESERVOIR DESCRIPTIONS CONDITIONED TO STATIC AND DYNAMIC DATA

A DISSERTATION
SUBMITTED TO THE DEPARTMENT OF PETROLEUM ENGINEERING
AND THE COMMITTEE ON GRADUATE STUDIES
OF STANFORD UNIVERSITY
IN PARTIAL FULFILLMENT OF THE REQUIREMENTS
FOR THE DEGREE OF
DOCTOR OF PHILOSOPHY

Vinh Phan
June 2002

I certify that I have read this thesis and that in my opinion it is fully adequate, in scope and in quality, as a dissertation for the degree of Doctor of Philosophy.

Dr. Roland N. Horne
(Principal Advisor)

I certify that I have read this thesis and that in my opinion it is fully adequate, in scope and in quality, as a dissertation for the degree of Doctor of Philosophy.

Dr. Louis Durlofsky

I certify that I have read this thesis and that in my opinion it is fully adequate, in scope and in quality, as a dissertation for the degree of Doctor of Philosophy.

Dr. Jef Caers

Approved for the University Committee on Graduate Studies:

Abstract

One of the characteristic features of fluvial reservoirs is the presence of sinuous sand-filled channels embedded in the background of floodplain shale. In fluvial reservoirs, hydrocarbon reserves are mostly contained in a number of distributed sand bodies isolated by faults or partially connected to one another via good permeability/porosity material but small pathways. This poses special challenges for reservoir modeling because the existence of such connected pathways and barriers between isolated fluvial bodies has great influence on fluid transport and thus production profiles. Detailed knowledge of sand channel geometry, spatial distribution, and connectedness are essential to develop a model that describes fluid flow accurately, predicts the future performance reliably, and helps in decision making.

One aspect of this work was to develop a mathematical foundation to describe multiple channels dynamically and realistically. Another aspect was to incorporate the mathematical formulations into an automated history matching process to enable the calculation of reservoir heterogeneity and sensitivity coefficients as functions of channel parameters.

This work proposed a subcell technique to approach these challenges. We found that this technique provides an efficient method for computing the sensitivity coefficients accurately and serves as a key for fast and effective inversion. The method is capable of supporting a closed-inversion loop matching various sources of *static* and *dynamic* data simultaneously. The procedure also enables the assessment of uncertainty associated with the estimated channel geometry, spatial distribution, and permeability/porosity fields.

The application of the proposed technique was demonstrated through several examples in a two-phase, water-oil case. In these examples, the data that was matched included *static* (geology, geophysics, and petrophysics) and *dynamic* data such as permanent down-hole pressure and water-oil ratio histories, combined with the information available from 4-D seismic surveys. The resulting reservoir descriptions included multiple channels with different orientation, thickness, width/thickness ratio, length, sinuosity and permeability/porosity contrast.

Acknowledgements

I am grateful to my thesis advisor, Professor Roland N. Horne, for his guidance and constant support during the course of this study. His expertise in well testing and optimization provided numerous fruitful advices and has a valuable impact on the success of this research. I thank my other committee members, Professors Louis Durlofsky and Jef Caers, for their helpful suggestions and comments during my study.

I thank Dr. R. Raghavan and Dr. Thomas N. Dixon, Phillips Petroleum Company, for providing me the opportunity to experience practical aspects of fluvial reservoirs. I benefited a great deal from working with them. I also thank Professor Marc Levoy, Departments of Computer Science and Electrical Engineering, whose expertise in computer graphics have initiated my early approaches to subproblems in this research.

Sincere thanks are due to my friend, Andres E. Mantilla, Stanford Rock Physics Laboratory, for his useful discussions on seismic-related materials.

I would like to thank my mom and my brother, An Phan, and sister, Nhung Phan, and their families. Needless to say, I owe them a great deal for their patient support and confidence in me through the years. I wished that I could share the delight of this accomplishment soon.

Especially, I would like to give my special thanks to my fiance, Tram, a lovely lady whose patient love, care, and encouragement enabled me to complete this work.

Financial support provided by SUPRI-D, Consortium on Innovation in Well Testing, Stanford University, and its affiliate members is gratefully acknowledged.

Finally, I am also grateful to all my old friends for still keeping in touch and making jokes with me and anyone I talked to, learned from, and hung out with during my years at Stanford. For those who are still to come - there is so much to explore and to learn...

Contents

List of Tables

List of Figures

Chapter 1

Introduction

1.1 Statement of the Problem

A fluvial reservoir is characterized by the presence of sinuous sand-filled channels embedded in the background of floodplain shale. This work deals with the problem of estimating the channel geometry, the spatial distribution of channels, and also the property distribution of the rock constituting the channels and background such as permeability and porosity.

Problems in many areas of mathematics, economics, medicine, statistics, and engineering can be stated in terms of mathematical models associated with parameter estimation. In particular, mathematical equations are often developed in order to describe complex phenomena while parameter estimation is used to determine the form and characteristics of the model that corresponds most closely to reality. The constructed model is then used to analyze and understand the phenomena being studied. In many engineering problems, constructing such models is not a serious concern since the parameters that define the system can be obtained by direct measurements. On the other hand, defining the channel parameters for the problem of this work is extremely difficult. The reservoir is located several thousands of feet underground and is physically inaccessible. The channels are invisible and can only be described through indirect measurements.

Estimating channel parameters from indirect measurements is difficult for the following reasons:

1. Channels have irregular geometric shapes.
2. The spatial distributions of channels can only be known at very few locations (wells).
3. Permeability and porosity are spatially dependent.
4. Information is scarce.
5. Measurement techniques possess limited accuracy.
6. Data are obtained with errors.
7. The construction of mathematical models is usually not exact and complete.
8. The response of a reservoir is complex and must be computed making use of a numerical simulator.

The response of a fluvial reservoir depends on spatial distribution of rock property (permeability/porosity) which, in turn, can be determined by the set of parameters describing channels. The procedure of computing such set of parameters from measurement data usually begins with an inverse technique because the data are nonlinearly related to the reservoir rock properties, and thus channel parameters, through a system of mass balance equations. Due to the complexity of the problem, the reservoir response must be computed numerically making use of a numerical simulator.

Data of different nature are collected during the life of a reservoir and can be grouped into two classes as *static* and *dynamic* data. Static data is time-independent and has no association with fluid transport. Geological, geophysical, petrophysical, seismic and geostatistical information are classified as static data. Dynamic data comprise those related to the transport of fluid and are time-dependent. This type of data could be derived from pressure transient test, shut-in surveys, downhole permanent gauges, production history, water-cut, gas-oil ratio (GOR), and 4-D seismic surveys.

Inverting both *static* and *dynamic* data simultaneously for reservoir characterization is a difficult problem A common procedure in practice is to upscale a fine-scale geological/geostatistical model generated conditioning to *static* data. The upscaled model is then adjusted in such a way to quantify *dynamic* data observed in the field. Current techniques for this adjustment are disconnected from the procedure of generating the original fine-scale model. Consequently, the final reservoir model constructed may honor the *dynamic* data but may not honor *static* data and in many cases, is unacceptable from a geological point of view. Future performance of a reservoir predicted from such models is less reliable than from the models that honor both *static* and *dynamic* data. This work also addresses this problem.

1.2 Literature Review

The recognition of the importance of sand/shale heterogeneity in the fluvial reservoirs dates back to at least 1978 (see Allen, 1978). One characteristic feature of fluvial reservoirs is the existence of sand-filled channel complexes embedded in the background of low permeability/porosity shale. Several researchers have addressed the problem of characterization of fluvial reservoirs using geological intuition to simple interpretation of well log data and more recently to integration of data from various sources (geological, geophysical, petrophysical, and even production history). The traditional methods for describing complex reservoir geology such as contouring parameters and hand-made maps are not able to represent the heterogeneities adequately and, therefore, to capture most of the aspects that impact on fluid displacement. The hand-made models proposed by Johnson and Krol (1984) rely on the geological interpretation of well-log data. The well data provided locations where the channels certainly passed through, but the channels are positioned arbitrarily in the interwell areas as sandstone are insufficiently extensive laterally to be correlated between wells. Alternative methods are random-object distribution of the sand bodies (see Haldorsen and Lake 1984, Augedal, Stanley, and More 1986, and Clementsen 1989) or sedimentological process related models (see Bridge and Leeder, 1997 and Alexander, 1986). These methods made use of stochastic simulations to describe the complex geological architecture honoring the well data and conditioned to the probability distributions obtained from outcrops or other studies of analog depositional environments. This stochastic technique was first credited to Haldorsen and Lake (1984). Henriquez et al. (1990) applied the method to first build a stochastic model conditioned to sand-body thickness and position in wellbores and then the geological model was transferred to a reservoir simulation grid by use of transmissibility multipliers and an NGR(net/gross ratio) value for each block. The authors reported that the transfer of data smoothes out much of the detailed geological information and the calculated recovery factors are insensitive to the continuity measured in the geological model and therefore they proposed an improvement to the interface between geological and reservoir simulation model. Smith and Morgan (1986) developed conceptual and stochastic models for both faulted reservoir sands and fluvial sands. These models enabled the calculations of the permeability reduction across fault sections and the recovery factors in fluvial reservoirs that can be used in a conventional numerical simulator.

Stochastic simulation is an excellent tool to integrate static data from various sources (well log, seismic, etc.). Stochastic simulation can be used to describe or generate the complex geological architecture and the spatial distributions of facies, sand-bodies, and the rock properties within each compartmented unit. Although these simulated scenarios are conditioned to hard data at the well locations and subject to secondary constraints, the simulated models still incur large uncertainty in the interwell areas and predictions of reservoir performance.

There are a number of recently developed techniques for characterizing interwell heterogeneities that were reported to be efficient and useful to study the sensitivity of production performance to the uncertainty in geological modeling. Begg, Gustason, and Deacon (1992) and Begg, Kay, Gustason, and Angert (1996) developed a new, quantitative, object-based model of the distribution of lithotypes within each major facies and converted these models to spatial distributions of porosity/permeability and then upscaled these for use in flow simulation. The authors reported that the quantitative lithotype models contain a number of variable parameters that enable sensitivities to uncertainties in the geological description to be studied. However, other researchers have proposed a systematic technique that allows the description of the geological features in fluvial system even more efficiently and realisticaly. Among these are Deutsch and Wang (1996). The technique is based on a hierarchical set of coordinate transformations involving relative stratigraphic coordinates, translations, rotations, and straightening functions. Most recent work in this area was credited to Strebelle (2002). The method was based on geological structures drawn from training images to generate fluvial reservoir models constrained to seismic and well-log data. The author reported that the algorithm developed can efficiently be applied to real three-dimensional reservoirs with up to 10^7 cells.

All of the methods mentioned so far made use of *static* information (time-independent data). For reservoirs characterized by simple configurations, the models obtained by these methods provide a good reservoir descriptions and are sufficiently reliable for use in predicting future reservoir performance. However, other cases, particularly in many fluvial systems, often require a more reliable model - the model that honors the most available information. The introduction of *dynamic* data (time-dependent data) in the problem of characterization of fluvial reservoirs is useful in terms of obtaining detailed model configurations and significantly reducing the uncertainty in modeling and in reservoir predictions.

Branagan, Lee, Cipolla, and Wilmer (1988) performed three-well interference testing of a naturally fractured, tight fluvial reservoir located near Rifle, Colorado incorporating geologic and geophysical data in a series of simulations using a naturally-fractured reservoir model. The model parameters were then altered systematically in order to provide the best history match of the well test data. The work showed that the reservoir simulation history matching of well test and interference data from the three wells produced a very detailed model of the Fluvial El reservoir. The model provided significant insight into the complex production characteristics of this tight, anisotropic, naturally-fractured reservoir. Lord, Collins, and Kocberber (1992) have demonstrated that the history matching of well performance with a simple multicompartment material balance model provides excellent estimates for directly drained pore volumes and intercompartment transmissibilities in fluvial reservoirs. They also reported that a successful history match for the interchannel model was achieved using only rate history and a single pressure observation at the end of production. However, the limitations of the compartment model showed in the case of a dual permeability reservoir where the real pressure is not distributed uniformly as in a tank, and therefore, is not described accurately by compartmental models. Stewart and Whaballa (1989) have shown that a material-balance simulator can be used with pressure histories from well tests in compartmented oil reservoirs to identify geological configurations. Hower and Collins (1989) divided a fluvial gas reservoir into two compartments coupled by a low permeability barrier and also introduced a two-compartment material-balance model. A further study by Lord and Collins (1991) extended this approach to any number of permeable compartments with communication between compartment pairs through low-permeability barriers. This numerical method provided two ways of history matching either by matching pressure history specifying rate data or by matching rate history by specifying pressure data. In 1996, Zheng and Corbett (1996) studied the impact of variable formation thickness on pressure transient behavior and well test permeability in fluvial meander loop reservoirs using a commercial simulator. The modeling of the meander loop reservoir was based on a simple linear-channel model with parabolic cross-sectional profile.

The numerical and analytical representations of channel complexes in fluvial reservoirs have been studied for several decades but the use of numerical simulators to incorporate fluvial channels dynamically into the interpretation of seismic and production data has not yet become common in a complete or systematic process. Recent works (Landa, 1997 and Landa and Horne, 1997) have addressed this problem by defining channels using mathematical formulas and then using these fomulas to relate the discrete permeability at every cell of the simulation mesh grid to the channel parameters. Landa and Horne, however, only considered relatively simple fluvial reservoirs consisting of single two-dimensional channel.

Early papers (see Dixon, Seinfeld, Starzman, and Chen, 1973) were concerned more with numerical than geological considerations. The missing scale between geological and simulation models results in a loss of information which could increase the difficulty in integrating well test and/or production data. Sometimes in practice, the same problem could also arise due to another missing scale between a simulation model used for long term forecast and an inversion model used in the history matching process. Massonnat and Bandiziol (1991) review the interdependence between geology and well test interpretation. The authors investigated the effects of the geological model on the well test response and how the well tests are used to confirm a geological model through several field examples. Recent papers (Oliver, Reynolds, Bi, and Abacioglu, 2001) have reviewed the progress towards the incorporation of production data into reservoir models and also pointed out remaining challenges that must be solved before the incorporation of production data in reservoir characterization can be termed routine.

1.3 Overview of Recent Approaches

Recently developed numerical techniques for describing geological features in a fluvial reservoir from measurement data can be divided into three main groups:

1. Pixel-based. Geological objects are constituted from mesh grids. The value of each pixel/cell of the mesh is independent from the others. Numerical models built using this technique easily honor well data and reproduce given variograms. However, this technique gives poor representations of the actual geometric shapes and results in high uncertainty.

2. Multiple-point statistics. This technique has been discussed by Strebelle (2002) based on the concept of data template consisting of a number of data locations (greater than two). Multiple-point statistics describe the statistical relation between multiple spatial locations considered jointly. Therefore, the technique is capable of describing important curvilinear geological structure from training images beyond the modelling capabilities of the traditional variogram which can only capture two-point statistics.

3. Object-based. This technique produces two types of objects: Dynamic objects are defined by a set of geometric parameters and capable of such transformations as rotation, translation, and scaling. Static objects, on the other hand, comprise those constituted from a set of cells and therefore, are not capable

of performing any transformations. In contrast to pixel-based methods, the object-based technique allows reproduction of more realistic geometries with higher certainty, but the conditioning on well data is difficult and often requires time-consuming iterative processes.

The algorithms implementing these techniques can be divided into three groups:

1. Deterministic algorithm.

   This group of algorithms generally produces a single model consisting of a limited number of objects by the integration of *dynamic* data. Deterministic algorithms have been widely used in two areas:

   - Numerical modeling.

     The response of the reservoir is computed making use of a numerical simulator. The data being integrated could be long-term pressure history, water cut, 4-D seismic, composition, and gas-oil ratio, etc. Normally, the procedure uses automated history matching with a numerical simulator.

   - Analytical modeling.

     The response of the reservoir is computed making use of a set of analytical or semianalytical model equations. Nonlinear regression algorithms are frequently used to match the analytical response of the reservoir to the pressure transient data. The data used in this area are well test or pressure transients of short duration. Such data could be from shut-in surveys, interference tests, pulse tests, etc.

2. Stochastic algorithm.

   Stochastic algorithms integrate *static* data and usually can be divided into two major steps: (a) generating multiple equiprobable realizations of facies distributions conditioned to *static* data such as global proportion, vertical and areal proportion curves, and well data of facies indicator. (b) populating petrophysical properties for each facies honoring such *static* data as hard data, secondary seismic amplitude map, variogram models, etc.

3. Hybrid algorithm.

   This is a combination of both deterministic and probabilistic algorithms in an attempt to integrate *static* and *dynamic* data simultaneously. This type of algorithm has not yet been developed completely and currently is a major research area in several institutes. Previously developed approaches have been applicable only to a very limited number of objects and dependent heavily on simple predefined geometric shapes. Generalizing these solutions to complex geological models remains difficult. The current work also addresses this problem.

1.4 Research Objectives

This research aims at following objectives:

1. To describe multiple channels dynamically and realistically.
2. To develop a hybrid algorithm integrating various sources of *static* and *dynamic* data simultaneously.
3. To incorporate information from geological scale to simulation scale in a self-consistent way, that is to develop a procedure to construct models that honor both static and dynamic data.
4. To develop a method to evaluate the uncertainty associated with channel parameters. The procedure presented here matches numerical stochastic/flow simulation results with various sources of data and represents an advanced history matching process. The algorithm is advanced in terms of regressing on a complex set of the parameters comprising not only the petrophysical variables such as permeability and porosity that appear explicitly in the discrete flow equations but also the variables that are not found in the model equations such as geometric and geostatistical parameters.

The principle components of the investigation were as follows:

1. A numerical stochastic simulator was used for the generation of stochastic channels from a set of geometric random variables that describe the position, shape, and size.
2. A numerical sequential Gaussian simulator was used for the population of petrophysical properties, namely permeability and porosity, of the rock constituting the channels and background.
3. A numerical flow simulator was used to compute the response of a geologically complex fluvial reservoir.
4. An algorithm was developed to convert continuous channels to discrete permeability and porosity fields.
5. A method was developed to calculate sensitivity coefficients of the model response efficiently, a key for fast and feasible inversion.
6. A method was developed to describe channels and calculate petrophysical properties at geological scale and their derivatives as a function of channel parameters.
7. A *constrained* optimization algorithm was used.
8. The assessment of uncertainty in estimating channel parameters was also investigated.

Chapter 2

Fundamental Modeling

2.1 Major Steps in Approaching the Problem

Since the data are related nonlinearly to the reservoir rock properties, and thus channel parameters, through a system of complex mass balance equations, the procedure of computing the channel parameters from measurement data usually begins with an inverse technique and is posed as a parameter estimation problem. Seeking parameter values to satisfy the model equations is usually implemented by an inverse approach consisting of three major steps:

1. Constructing mathematical relationships among the problem variables.
2. Defining an *objective function* that is a suitable measure of the discrepancy between the data and the model.
3. Minimizing the defined objective function.

Having constructed the forward mathematical models and defined an objective function, a common algorithm for minimizing the defined objective function in the inverse problem is as follows:

1. Compute or reasonably assign values to the set of unknown parameters. This is referred to as the first guess.

2. Compute the model response.
3. Compute the objective function. If the value of the objective function is less than a predefined tolerance then the algorithm is terminated.
4. Compute a change in the set of parameters. If the change of parameters is less than a certain predefined tolerance and the parameters are not updated significantly then the algorithm is terminated.
5. Go back to step 2.

2.2 Object Modeling

One critical issue to be addressed in finding the inverse results by integrating data of various sources in fluvial systems is the development of mathematical foundations to describe multiple channels consistent with geological information and efficient in the automated history matching process. Mathematical formulations describing channels play an important role not only in achieving reliable solution but also calculating the sensitivity coefficients of the model response (data) with respect to the parameters for the inversion. The relationship between the formulations describing channels and the associated sensitivity coefficients is complex. In many cases, virtually all the effort of model development is aimed toward constructing geological objects that reflect the real world as closely as possible. Only after the formulation describing the objects is complete, one then focuses on finding a method for calculating sensitivity coefficients.

On the other hand, we do not advocate oversimplification or distortion in formulations simply to be able to calculate the sensitivity coefficients more easily. There has been a tendency to simply model a channel by a set of simple rectangular shapes in order to ease the sensitivity calculations and this is obviously contrary to outcrop and subsurface observations. Among outcrop observations are the channel sinuosity and the discontinuity of rock material across the channel boundary.

Finally, mathematical formulations describing channels should be developed by striking a reasonable balance between the aims of reality (which implies complexity in the formulations) and that of efficiency in calculating sensitivity coefficients.

This work considers two types of modeling. These are deterministic and stochastic modeling, as discussed in detail in the next two sections.

2.2.1 Deterministic Modeling

The objects we are modeling are located many thousands of feet underground, and have no preexisting physical representation visible to us. In reality, the shapes are irregular and can not be described exactly by mathematical formulations. Of course, the object could be modeled by an infinite set of points but this is not feasible for a computer with finite storage and impossible for the inversion process regressing on infinite number of parameters. More often, in computer graphics, the objects are approximated with pieces of planes, spheres, or other shapes that are easy to describe mathematically. Another difficulty that arises in our problem is that the objects need to be described dynamically. This requires the formulations to be invariant under rotation, translation, and scaling. One convenient way to meet these requirements is to make use of a parametric representation technique of the form

$$\begin{cases} x &= x(t) \\ y &= y(t) \end{cases} \tag{2.1}$$

where coordinates are functions of parameter t. To deal with finite segments of the curve, without loss of generality, we restrict the parameter t to the $[0, 1]$ interval. $(x(0), y(0))$ is starting point and $(x(1), y(1))$ is end point. Figure 2.1 shows three examples of an arbitrary curve in two-dimensional space. The curve in the left is single-segmented with point A being the starting point correspondent to $t = 0$ and point B being the end point correspondent to $t = 1$. The curve in the middle is a closed curve where the starting and end point are coincident and represented by

$$\begin{cases} x(0) &= x(1) \\ y(0) &= y(1) \end{cases} \tag{2.2}$$

The curve at the right of Figure 2.1 is constructed from two joined parametric segments. The end point of the first segment is coincident with the starting point of

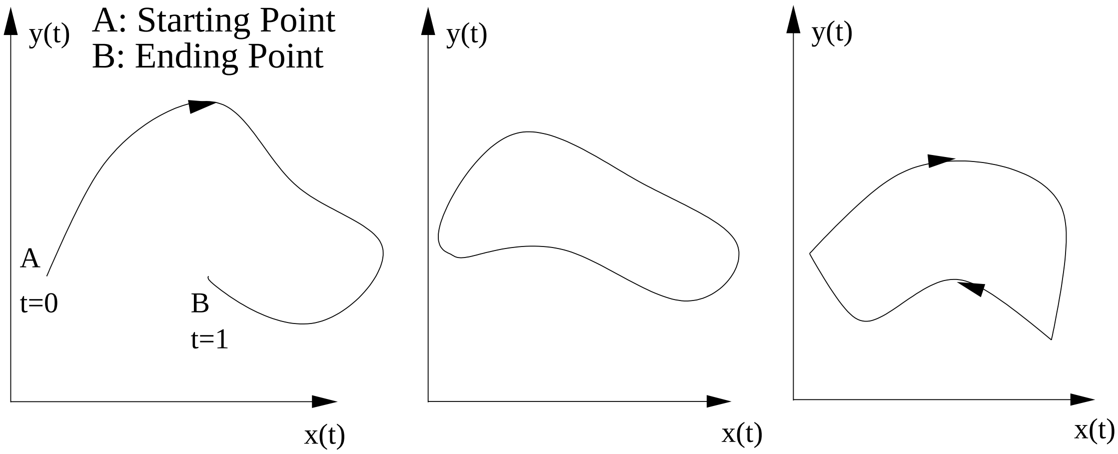

Figure 2.1: Examples of parametric curves.

the second segment and the end point of the second is coincident with the starting point of the first segment.

A curve having irregular shape can be approximated by a number of *piecewise* polynomial parametric segments, where each coordinate is a polynomial in parameter t. Cubic polynomials are most often used because low-degree polynomials give too little flexibility in controlling the shape of the curve while high-degree polynomials can introduced unwanted and unrealistic wiggles. The cubic polynomials that define a curve segment $Q(t) = [x(t), y(t)]$ are of the forms

$$\begin{aligned} x(t) &= a_x t^3 + b_x t^2 + c_x t + d_x, \\ y(t) &= a_y t^3 + b_y t^2 + c_y t + d_y, \qquad 0 \leq t \leq 1 \end{aligned} \tag{2.3}$$

With $T = [t^3, t^2, t, 1]$, and defining the matrix of coefficients of the three polynomials as

$$\mathbf{C} = \begin{bmatrix} a_x & a_y \\ b_x & b_y \\ c_x & c_y \\ d_x & d_y \end{bmatrix} \tag{2.4}$$

we can write Equation 2.3 in matrix form as

$$Q(t) = [x(t), y(t)] = T\mathbf{C} \tag{2.5}$$

Differentiating $Q(t)$ gives the parametric tangent vectors of the curve segments:

$$\frac{dQ(t)}{dt} = \frac{dT}{dt}\mathbf{C} = [3t^2, 2t, 1, 0]C = [3a_x t^2 + 2b_x t + c_x, 3a_y t^2 + 2b_y t + c_y] \tag{2.6}$$

Each cubic polynomial has four coefficients, so four geometric constraints will be needed in order to formulate four equations in the four unknown coefficients. Therefore, the parameters defining the shape of the curve segment are the geometric constraints and need to be estimated in the inversion process. These geometric constraints used in this work were the two endpoints, $(x(0), y(0))$ and $(x(1), y(1))$, and the two tangent vectors at the endpoints, $(x'(0), y'(0))$ and $(x'(1), y'(1))$. It should be noted here that the selection of geometric constraints are arbitrary and does not affect the solution to the inversion problem. We chose such particular geometric constraints because they provide a more intuitive control of the curves. To see how the coefficients depend on the four constraints, let us rewrite the coefficient matrix $\mathbf{C}$ as $\mathbf{C} = \mathbf{MG}$, where $\mathbf{M}$ is a 4×4 constant matrix and $\mathbf{G}$ is a 4×2 matrix of geometric constraints and given as

$$\mathbf{G} = \begin{bmatrix} x(0) & y(0) \\ x(1) & y(1) \\ x'(0) & y'(0) \\ x'(1) & y'(1) \end{bmatrix} \tag{2.7}$$

It remains to find the constant matrix M given G. Equation 2.5 becomes

$$Q(t) = [x(t), y(t)] = T\mathbf{MG} = [t^3, t^2, t, 1]\mathbf{MG} \tag{2.8}$$

The constraints on $x(0)$ and $x(1)$ are found by direct substitution into Equation 2.8 as

$$x(0) = [0, 0, 0, 1]\mathbf{MG_x} \tag{2.9}$$

$$x(1) = [1, 1, 1, 1]\mathbf{MG_x} \tag{2.10}$$

where $\mathbf{G_x}$ is the first column of the geometric constraint matrix.

$$\mathbf{G_x} = \begin{bmatrix} x(0) \\ x(1) \\ x'(0) \\ x'(1) \end{bmatrix} \tag{2.11}$$

Differentiating $Q(t)$ in Equation 2.8 gives

$$Q'(t) = [x'(t), y'(t)] = [3t^2, 2t, 1, 0]\mathbf{MG} \tag{2.12}$$

Making use the Equation 2.12, the tangent vector constraint equations can be writen as

$$x'(0) = [0, 0, 1, 0]\mathbf{MG_x} \tag{2.13}$$

$$x'(1) = [3, 2, 1, 0]\mathbf{MG_x} \tag{2.14}$$

The four equations 2.9, 2.10, 2.13, and 2.14 can be writen in matrix form as

$$\mathbf{G_x} = \begin{bmatrix} x(0) \\ x(1) \\ x'(0) \\ x'(1) \end{bmatrix} = \begin{bmatrix} 0 & 0 & 0 & 1 \\ 1 & 1 & 1 & 1 \\ 0 & 0 & 1 & 0 \\ 3 & 2 & 1 & 0 \end{bmatrix} \mathbf{MG_x} \tag{2.15}$$

Similarly for the y coordinates, we obtained

$$\mathbf{G_y} = \begin{bmatrix} y(0) \\ y(1) \\ y'(0) \\ y'(1) \end{bmatrix} = \begin{bmatrix} 0 & 0 & 0 & 1 \\ 1 & 1 & 1 & 1 \\ 0 & 0 & 1 & 0 \\ 3 & 2 & 1 & 0 \end{bmatrix} \mathbf{MG_y} \tag{2.16}$$

For Equations 2.15 and 2.16 to be satisfied, the matrix $\mathbf{M}$ must be the inverse of the 4x4 matrix as follows

$$\mathbf{M} = \begin{bmatrix} 0 & 0 & 0 & 1 \\ 1 & 1 & 1 & 1 \\ 0 & 0 & 1 & 0 \\ 3 & 2 & 1 & 0 \end{bmatrix}^{-1} = \begin{bmatrix} 2 & -2 & 1 & 1 \\ -3 & 3 & -2 & -1 \\ 0 & 0 & 1 & 0 \\ 1 & 0 & 0 & 0 \end{bmatrix} \tag{2.17}$$

Now this matrix can be used to relate the coefficients to the geometric constraints through $\mathbf{C} = \mathbf{MG}$.

Since in fluvial reservoirs, geological objects with sinuous shapes are dominant, such special objects are called *channels*. In this work, the modeling of channels was discussed in a manner similar to that of Deutsch and Wang (1996).

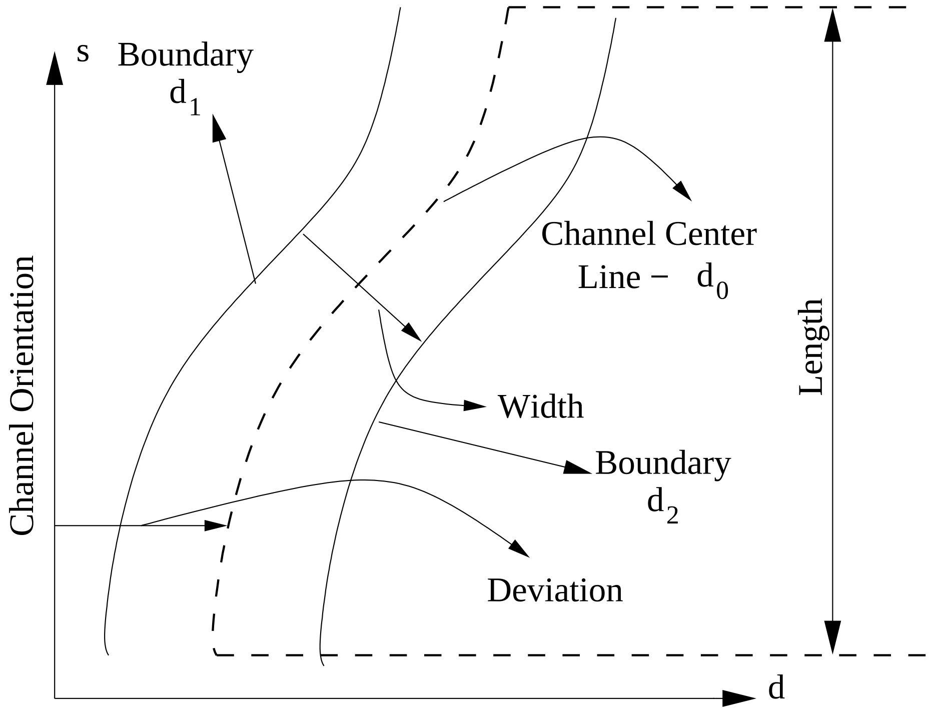

Figure 2.2: Channel geometry.

The geometry of a channel is defined by the following set of geometric parameters in a rectangular coordinate system (see Figure 2.2):

- Channel orientation:

  The orientation of a channel is described by six parameters, three of which are channel coordinates and the remaining three are azimuth, dip, and plunge. Rectangular coordinates are used for channel translations and the three angles are used to perform rotations on the axes such that they are oriented along principal structural directions (two areal directions of maximum and minimum continuity and one direction orthogonal to the areal).

- Deviation of channel center line from direction of maximum continuity:

  The center line of a channel deviates from the channel orientation and is described by a sinuous function with three parameters (amplitude, frequency, and phase) of the form

  $$d_0 = A\sin(2\pi f s + \theta) \tag{2.18}$$

  where each parameter represents the following physical concept:

  d_0 is deviation of the channel center line,

  A is the amplitude,

  f is the frequency or *sinuosity* of the channel,

  s is direction of maximum continuity,

  θ is the displacement of the channel along direction of maximum continuity.

  This function describes a single *harmonic* which is only applicable for an ideal sinuous shape. However, in fluvial reservoirs, the shape of a channel is not perfect but close to sinuous and can be approximated reasonably by a finite number of harmonics. For example, a two-harmonic shape can take the form

  $$d_0 = A_1\sin(2\pi f_1 s + \theta_1) + A_2\sin(2\pi f_2 s + \theta_2) \tag{2.19}$$

  The first harmonic represents the dominant sinuosity of the channel while the second represents a fluctuation superimposed on the first one. Higher frequency can be modeled by using more harmonics.

- Thickness of channel, by one parameter.

- Width of channel, by one parameter.

- Length of channel, by one parameter.

Thus, a deterministic channel is completely defined by a set of 12 parameters in three-dimensional space or eight in two-dimensional space. The physical meanings of the set of parameters decribing a channel includes translation, rotation, departure, sinuosity, displacement, thickness, width, and length. The channel boundaries can be computed from the channel center line (see Figure 2.2). In this figure, d_0 is the center line of the channel and is expressed by Equation 2.18. d_1 and d_2 are the two boundaries of the channel which are obtained by shifting the center line in the direction orthogonal to the direction of maximum continuity. This causes, as shown in Figure 2.3, the effective width (measured perpendicular to the tangent of the center line) of the channel to be too narrow especially when the tangent becomes perpendicular to the channel orientation. This problem may be fixed by increasing the apparent width $w(s)$ (measured perpendicular to the channel orientation) such that the effective width is approximately constant. The apparent width after correction is then given by

$$w(s) = \frac{w}{\cos(\beta(s))} \tag{2.20}$$

where w is the specified width and $\beta(s)$ is the angle between the local tangent to the center line and the channel orientation and is expressed as

$$\beta(s) = \arctan\left(\frac{d(d_0(s))}{ds}\right) = \arctan\left(2\pi f A \cos(2\pi f s + \theta)\right) \tag{2.21}$$

The mathematical formulas for the channel boundaries, d_1 and d_2, can then be computed as

$$\begin{cases} d_1 &= d_0 - \frac{w(s)}{2} \\ d_2 &= d_0 + \frac{w(s)}{2} \end{cases} \tag{2.22}$$

So far we have been discussing the modeling of a single object where the coordinate system describing the object stays unaltered and the object is transformed with respect to the coordinate system. Another way of thinking about a transformation is as a change of coordinate systems leaving the objects unaltered. This view is useful when dealing with multiple objects, each defined in its own local coordinate system and a global coordinate system is used to describe all these objects together. In this approach, the transformations of objects can be done by the transformations of local coordinate systems with respect to global coordinate system. Figure 2.4 illustrates the relationship between the local (s, d) and global (x, y) coordinate systems. The areal transformations (translation and rotation) has the form

$$\begin{bmatrix} x \\ y \end{bmatrix} = \begin{bmatrix} x_0 \\ y_0 \end{bmatrix} + \begin{bmatrix} \cos(\theta) & \sin(\theta) \\ -\sin(\theta) & \cos(\theta) \end{bmatrix} \begin{bmatrix} s \\ d \end{bmatrix} \tag{2.23}$$

where x_0 and y_0 are the two parameters defining the translation and θ is the parameter defining the rotation of the channel. In three dimensions, a transformation between a global (x, y, z) and a local coordinate system (s, d, t) can be done by four steps

1. A translation (x_0, y_0, z_0) from the origin.

$$\begin{bmatrix} x \\ y \\ z \end{bmatrix} = \begin{bmatrix} x_0 \\ y_0 \\ z_0 \end{bmatrix} + \begin{bmatrix} s \\ d \\ t \end{bmatrix} \tag{2.24}$$

2. A rotation about the z axis measured by the angle of *azimuth* α_1.

$$\mathbf{R}_z = \begin{bmatrix} \cos(\alpha_1) & \sin(\alpha_1) & 0 \\ -\sin(\alpha_1) & \cos(\alpha_1) & 0 \\ 0 & 0 & 1 \end{bmatrix} \tag{2.25}$$

3. A rotation about the x axis measured by the angle of *dipping* α_2.

$$\mathbf{R}_x = \begin{bmatrix} 1 & 0 & 0 \\ 0 & \cos(\alpha_2) & -\sin(\alpha_2) \\ 0 & \sin(\alpha_2) & \cos(\alpha_2) \end{bmatrix} \tag{2.26}$$

4. A rotation about the y axis measured by the angle of *plunging* α_3.

$$\mathbf{R}_y = \begin{bmatrix} \cos(\alpha_3) & 0 & \sin(\alpha_3) \\ 0 & 1 & 0 \\ -\sin(\alpha_3) & 0 & \cos(\alpha_3) \end{bmatrix} \tag{2.27}$$

A transformation in three-dimensional space can then be given as

$$\begin{bmatrix} x \\ y \\ z \end{bmatrix} = \begin{bmatrix} x_0 \\ y_0 \\ z_0 \end{bmatrix} + \mathbf{R}_z \mathbf{R}_x \mathbf{R}_y \begin{bmatrix} s \\ d \\ t \end{bmatrix} \tag{2.28}$$

where the rotation matrices about z axis ($\mathbf{R}_z$), about x axis ($\mathbf{R}_x$), and about y axis ($\mathbf{R}_y$) are given by Equations 2.25, 2.26, and 2.27.

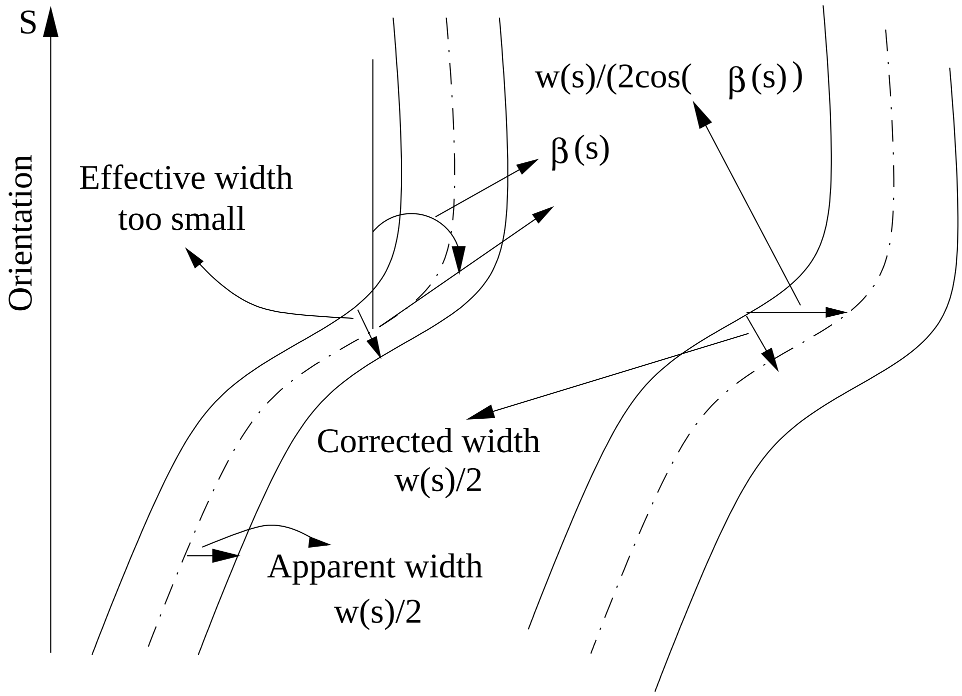

Figure 2.3: Correction of channel width.

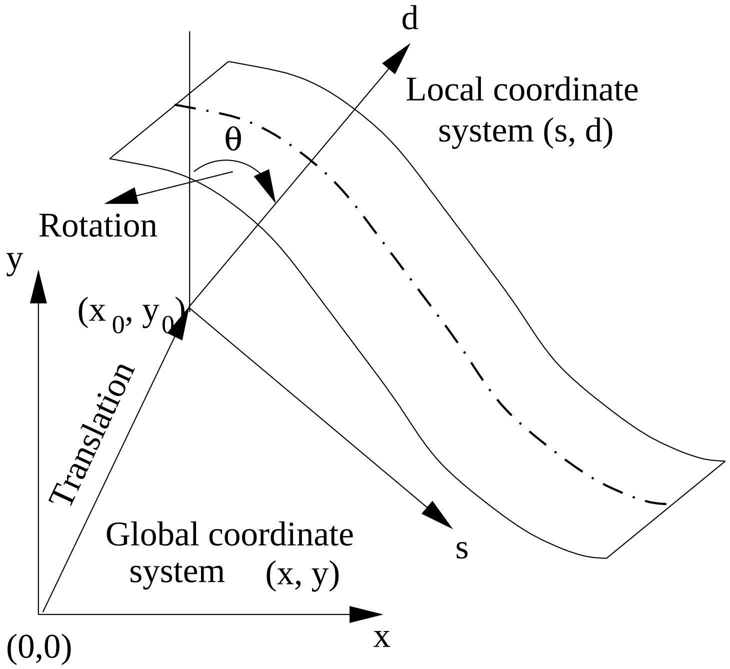

Figure 2.4: Areal transformation (translation and rotation).

2.2.2 Stochastic Modeling

The stochastic approach is more attractive than the deterministic approach for several reasons:

- Deterministic channels require the development of mathematical formulas for descriptions of channel geometry.
- The channel geometry is complex and can not be described exactly in algebraic form.
- Measured data have limited accuracy.
- The dynamic behavior of the system is not modeled completely.
- The data are insufficient to resolve channel parameters uniquely.
- We would like to have the capability of generating multiple equiprobable realizations for uncertainty assessments.

- The stochastic approach is simpler in integrating large scale geological/geostatistical information.

One novel approach to stochastical modeling of the channel geometry was presented by Deutsch and Wang (1996) making use of a simulated annealing algorithm for the conditioning to *static* data such as global, vertical, and areal facies proportions and well data. However, the problem of this technique is that it relies on the simulated annealing algorithm which is very inefficient for the integration of *dynamic* data. This problem is also addressed in this work. In the approach presented by Deutsch and Wang, a stochastic channel is defined by a set of geometric random variables that describe the location, size, and shape. These random variables are:

- Orientation
- Thickness
- Width/thickness ratio

The variables are characterized by triangular distributions, while the channel center line, the spatial width, and the spatial thickness are defined by one-dimensional Gaussian simulation. These three random variables plus the one-dimensional simulating function describe the channel completely.

2.3 Modeling of Petrophysical Properties

As was mentioned earlier, the spatial distribution of reservoir properties (permeability and porosity) can be computed as a function of geometric parameters describing the channels and the property of the rock in the channels (channel facies) and outside the channels (background facies). The following scenarios for the rock property fields in each of the facies (channel and background facies) were investigated:

1. Uniform distribution.

   The petrophysical property is distributed uniformly within each channel but may differ among channels. These rock properties are parameters of inversion.

2. Nonuniform distribution with fixed pattern.

   Petrophysical property fields of each facies are assumed to be heterogeneous and differ from the original fields only by a multiplier and a translation and described mathematically as

   $$Z = MZ_0 + T \tag{2.29}$$

   where Z represents the petrophysical property (permeability and porosity) fields of each of the facies.

   Z_0 represents the original fields of various sources of information including petrophysical and seismic-related properties such as P and S wave impedance, velocity, Poisson's ratio etc. M is the multiplication factor. T is the translation relative to the original field. M and T are two regression parameters defined on a facies basis. The rock property of each facies defined by Equation 2.29 preserves the original geological/geostatistical features.

3. Stochastic distribution.

   Petrophysical properties in each facies are populated stochastically using a pixel-based geostatistical algorithm. The populated property is constrained to variogram models in each facies. The parameters of inversion in this case are those defining the variogram models. A variogram model consists of an isotropic constant nugget effect and a number of nested standard structures, each defined by *correlation range* and *sill*. A set of parameters of inversion for stochastically generating petrophysical property in each facies are:

   - Random seed, one parameter,
   - Isotropic constant nugget, one parameter,
   - Sill, one parameter for each nested structure,
   - Correlation ranges in maximum, minimum, and vertical direction of continuity, three parameters for each nested structure,

- The three angles (azimuth, dip, and plunge) defining the geometric anisotropy, three parameters for each nested structure,

So far, we have discussed two fundamental steps in generating the heterogeneity in a fluvial reservoir constrained to static data. The first step is constructing geological objects using an object-based approach. The second step is populating petrophysical property within each facies using the pixel-based approach. These two steps are the task of current reservoir modeling approaches making use of very complex workflows to ensure the consistency with all static data and the geological information. The challenge arises when attempting to incorporate dynamic data into the reservoir modeling process in order to achieve more reliable models. This task is made difficult because of the high uncertainty associated with the static model constructed. There are an infinite number of such models quantifying a given static data set and each of them has different impact on reservoir performance. However, the data have limited accuracy and the dynamic relationships between these data and the underlying rock and fluid property distributions are not understood and modeled completely. Adjusting the upscaled models constrained to dynamic data usually results in a model that does not honor static data. Making use of such nongradient-based optimization methods as simulated anealing or Markov Chain Monte Carlo simulations has already shown to be very inefficient from the computational point of view. Accounting for dynamic data in geostatistical reservoir modeling is a difficult and challenging inverse problem and has become a research subject in many places. Recent work in this area includes Landa and Horne (1997), Landa (1997), and Bi, Oliver, and Reynolds (1999) and has already shown some promise. However, there remains targets for this work that can be stated as follows:

- The channel geometry is restricted to some predefined regular shapes.
- The number of objects is very limited and assumed to be known.
- Property distribution within objects is uniform.
- Computing the heterogeneity and the sensitivity coefficients is inaccurate because of the piecewise linearization of the channel boundaries.

- Geological events regarding how channels were formed are missing.
- Convergence is slow.

The goal is to integrate dynamic data into stochastic geological/geostatistical models constrained to static data. There are an infinite number of such static models, a subset of which can be constrained to the dynamic data. The application of the technique proposed in this work ensures that the fine-scale static models generated by existing geostatistical algorithms are also constrained to dynamic data. What distinguishes the method proposed in this work from the others described in literature is the choice of parameters for inversion, the use of geological events, the computational efficiency of the proposed algorithms, and the capability of solving more general problems.

The key concept for our parameter selection is that the quantities associated with uncertainty in model construction are subject to change in the process of history matching. Traditionally, such quantities could be considered as hard data, preassigned known values and interpreted from another process. A set of parameters chosen based on this concept can be described as follows:

- A random seed used in object-based stochastic algorithms for the generation of channel geometry.
- Geometric parameters used to define triangular distributions for the channel position, shape, and size such as orientation, thickness, and width/thickness ratio.
- A random seed used in pixel-based stochastic algorithms for the generation of petrophysical property within channels and background.
- Parameters of the variogram models.

Figure 2.5 summarizes the entire workflow process used to construct a fluvial reservoir model. This entire workflow process may be implemented in a single closed-inversion loop including such separate algorithms as object-based stochastic/deterministic simulation, pixel-based stochastic/deterministic simulation, upscaling, flow simulation, subcell technique, and constrained optimization. A set of inversion parameters is also listed including what are traditionally considered as certain and hard data.

2.4 Mathematical Model for Flow Response

As was mentioned at the beginning of this chapter, seeking parameter values in the inversion problem usually begins with the construction of mathematical relationships among relevant quantities by applying fundamental physical laws describing the situation under study. The purpose of this step is to relate the measurement data to the parameters being estimated. In this work, the physical system under study is a fluvial reservoir and the fundamental laws relevant to the dynamic behavior of the reservoir are material conservation and Darcy's law. The forward mathematical model equations used in this work were derived from these laws as described in this section. In petroleum engineering, the mass conservation for any component is normally converted to the volume conservation evaluated at standard conditions or surface conditions. Consider an arbitrary, fixed volume V embedded within a permeable medium through which is flowing an arbitrary number of components. The conceptual volume conservation equation for a component c in volume V is:

$$\begin{pmatrix} \text{Rate of} \\ \textit{accumulation} \\ \text{of } c \text{ in } V \end{pmatrix} = \begin{pmatrix} \text{Rate of} \\ \textit{production} \\ \text{of } c \text{ in } V \end{pmatrix} - \begin{pmatrix} \text{Net rate of } c \\ \textit{transported} \\ \text{from } V \end{pmatrix} \tag{2.30}$$

All terms in Equation 2.30 are volumetric flow rates evaluated at standard conditions. Assuming the material in the porous medium is transported only by convection:

$$\begin{pmatrix} \text{Net rate of } c \\ \textit{transported} \\ \text{from } V \end{pmatrix} = \sum_{p=1}^{np} \oint_S R_{cp} \frac{\tilde{U}_p.\tilde{n}}{B_p}\, dS \tag{2.31}$$

The surface integral in Equation 2.31 can be converted to a volume integral through the divergence theorem:

$$\sum_{p=1}^{np} \oint_S R_{cp} \frac{\tilde{U}_p.\tilde{n}}{B_p}\, dS = \sum_{p=1}^{np} \int_V \nabla. \left(R_{cp} \frac{\tilde{U}_p.\tilde{n}}{B_p} \right) dV \tag{2.32}$$

$$\begin{pmatrix} \text{Rate of} \\ \textit{accumulation} \\ \text{of } c \text{ in } V \end{pmatrix} = \frac{d}{dt} \sum_{p=1}^{np} \int_V R_{cp} \frac{S_p \phi}{B_p}\, dV = \sum_{p=1}^{np} \int_V \frac{\partial}{\partial t} \left(R_{cp} \frac{S_p \phi}{B_p} \right) dV \tag{2.33}$$

$$\begin{pmatrix} \text{Rate of} \\ \textit{production} \\ \text{of } c \text{ in } V \end{pmatrix} = \int_V q_c\, dV \tag{2.34}$$

where:

q_c is volume metric production rate of component c per unit bulk volume evaluated at standard conditions,

$\tilde{U}_p$ is the Darcy velocity of phase p,

R_{cp} is solubility of component c in phase p,

B_p is formation volume factor of phase p,

ϕ is the porosity of the porous medium,

np is the number of phases.

Combining Equations 2.31 through 2.34 into Equation 2.30 gives the following scalar equation for the component c:

$$\sum_{p=1}^{np} \int_V \frac{\partial}{\partial t} \left(R_{cp} \frac{S_p \phi}{B_p} \right) dV = \int_V q_c\, dV - \sum_{p=1}^{np} \int_V \nabla. \left(R_{cp} \frac{\tilde{U}_p.\tilde{n}}{B_p} \right) dV \tag{2.35}$$

Let the arbitrary volume V approach zero:

$$\sum_{p=1}^{np} \frac{\partial}{\partial t} \left(R_{cp} \frac{S_p \phi}{B_p} \right) = q_c - \sum_{p=1}^{np} \nabla. \left(R_{cp} \frac{\tilde{U}_p.\tilde{n}}{B_p} \right) \tag{2.36}$$

Equation 2.36 is the differential form for the component c. The forward flow model equations were constructed in this work with the following features:

- Three-dimensional flow in Cartesian coordinates,
- Slightly-compressible fluids (water and oil),

- Heterogeneous and anisotropic medium,
- No capillary pressure.

Applying these features to the general Equation 2.36 gives the following equations that were used in this work for the forward mathematical model:

$$\nabla.\left(\frac{\tilde{U}_w}{B_w}\right) + \frac{\partial}{\partial t}\left(\frac{\phi_0(\mathbf{u})f(p)S_w}{B_w}\right) + q_w = 0 \tag{2.37}$$

$$\nabla.\left(\frac{\tilde{U}_o}{B_o}\right) + \frac{\partial}{\partial t}\left(\frac{\phi_0(\mathbf{u})f(p)S_o}{B_o}\right) + q_o = 0 \tag{2.38}$$

$$\tilde{U}_w = -\frac{k_{rw}(S_w)\mathbf{k}(\mathbf{u})}{\mu_w}\nabla(\Phi_w) \tag{2.39}$$

$$\tilde{U}_o = -\frac{k_{ro}(S_o)\mathbf{k}(\mathbf{u})}{\mu_o}\nabla(\Phi_o) \tag{2.40}$$

$$\Phi_w = p - \gamma_w z \tag{2.41}$$

$$\Phi_o = p - \gamma_o z \tag{2.42}$$

$$\gamma_w = \frac{1}{144}\rho_w g \tag{2.43}$$

$$\gamma_o = \frac{1}{144}\rho_o g \tag{2.44}$$

$$B_w = B_w(p) \tag{2.45}$$

$$B_o = B_o(p); \tag{2.46}$$

where $\mathbf{k}(\mathbf{u})$ is the diagonal tensor permeability at location $\mathbf{u}$ and given by:

$$\mathbf{k}(\mathbf{u}) = \begin{bmatrix} k_x(\mathbf{u}) & & \\ & k_y(\mathbf{u}) & \\ & & k_z(\mathbf{u}) \end{bmatrix} \tag{2.47}$$

and $\phi_0(\mathbf{u})$ is porosity at location $\mathbf{u}$.

In this chapter, we have taken our first look at the fundamental modeling of geometry and petrophysical property of geological objects. These are the principal components in relating the heterogeneity of a typical fluvial reservoir to the set of parameters of inversion. We also constructed the forward mathematical model by combining various fundamental laws and resulted in a system of differential equations describing the dynamic relation between the data and the reservoir heterogeneity. The dynamic relation is well known and not our interest in this work. However, we have covered only the basics here with regard to the static relation between the reservoir heterogeneity and the matching geometric parameters. Many elaborations and further details must be considered for robust implementations. Chapter 4 will discuss these topics.

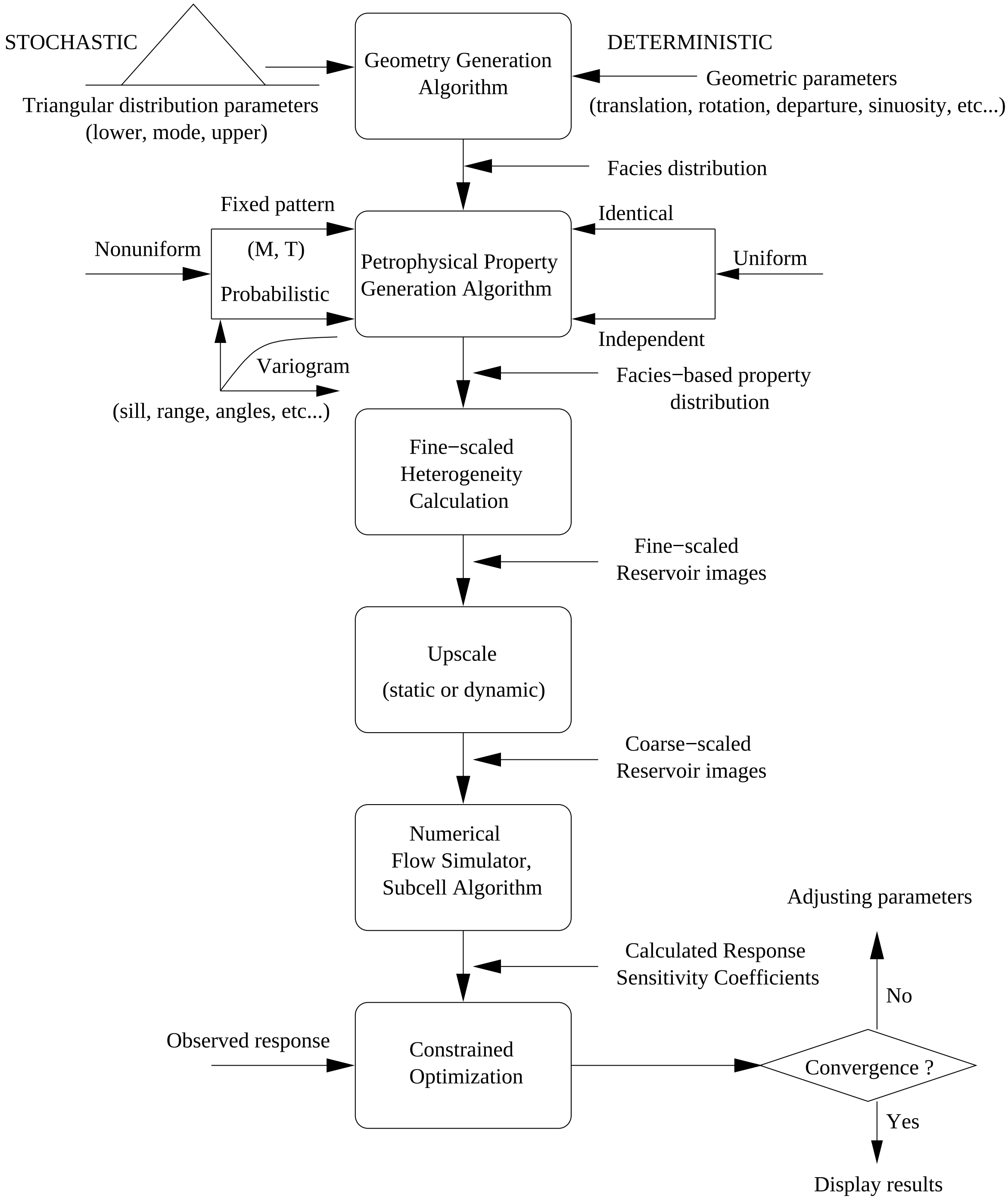

Figure 2.5: Work flow process.

Chapter 3

Parameter Estimation

3.1 Objective Function

After constructing the foward mathematical equations relating the measurement data to the underlying rock and fluid property distributions, the next step is establishing an objective function. The objective function defines the matching criterion and measures the mismatch between the model response calculated by a numerical simulator and the observed data.

The implemented objective function supports different terms to be included according to the optimization problem such as unweighted and weighted measurements, penalty or barrier functions, and inequality constraints. The formulation is based on the Bayesian theory.

3.1.1 Review of Bayesian Theory

Bayesian estimation theory is applied to an inversion problem to modify an initial geological model by constraining it to dynamic data. The goal is to reduce uncertainties of model construction by integrating dynamic data into the geological model probabilistically generated in the Gaussian field. Such an *a priori* model is considered in a probabilistic form. The uncertainty of the model is characterized by a probability density function $f_{\vec{\Theta}}(\vec{\alpha})$, where $\vec{\Theta}$ is the model parameters and $\vec{\alpha}$ is a realization of

$\vec{\Theta}$. Under the assumption of a Gaussian uncertainty model, the *a priori* probability density function takes the form

$$f_{\vec{\Theta}}(\vec{\alpha}) = C_1 exp\left\{-\frac{1}{2}(\mu_\alpha - \vec{\alpha})^T C_\alpha^{-1}(\mu_\alpha - \vec{\alpha})\right\} \tag{3.1}$$

where μ_α is the mean values, C_α is the covariance matrix, and C_1 is a constant factor. The *a priori* uncertainty model is constrained by integrating dynamic data denoted by $\vec{d}_{obs}$. The calculated response of the reservoir, $\vec{d}_{cal}$, is considered as a realization generated from a stochastic function vector $\vec{D}$. By applying the Bayesian formula, the conditional probability of obtaining the geological model, denoted by the parameters $\vec{\alpha}$, knowing the measurement $\vec{d}_{obs}$ can be expressed as:

$$f_{\vec{\Theta}|\vec{D}}\left(\vec{\alpha}|\vec{D} = \vec{d}_{obs}\right) = \frac{f_{\vec{D}|\vec{\Theta}}\left(\vec{D} = \vec{d}_{obs}|\vec{\alpha}\right) f_{\vec{\Theta}}\left(\vec{\alpha}\right)}{f\left(\vec{D} = \vec{d}_{obs}\right)} \tag{3.2}$$

where:

$f_{\vec{\Theta}}\left(\vec{\alpha}\right)$ is the *a priori* uncertainty model given by Equation 3.1,

$f\left(\vec{D} = \vec{d}_{obs}\right)$ is the normalization term of the *a posteriori* probability density function,

$f_{\vec{D}|\vec{\Theta}}\left(\vec{D} = \vec{d}_{obs}|\vec{\alpha}\right)$ is the likelihood function characterizing the numerical simulation results.

The errors between the measurements, $\vec{d}_{obs}$, and the calculated response, $\vec{d}_{cal}$, are assumed to be of Gaussian distribution with zero mean and covariance $\mathbf{C_d}$. The likelihood function becomes:

$$f_{\vec{D}|\vec{\Theta}}\left(\vec{D} = \vec{d}_{obs}|\vec{\alpha}\right) = C_2 exp\left\{-\frac{1}{2}\left(\vec{d}_{obs} - \vec{d}_{cal}\right)^T \mathbf{C_d^{-1}}\left(\vec{d}_{obs} - \vec{d}_{cal}\right)\right\} \tag{3.3}$$

Equation 3.3 expresses the mismatches between the calculated and the observed response in a probabilistic form. By combining Equations 3.1 to 3.3, the *a posteriori* probability density function can be expressed as:

$$\begin{gathered} f_{\vec{\Theta}|\vec{D}}\left(\vec{\alpha}|\vec{D} = \vec{d}_{obs}\right) = \\ C exp\left\{-\tfrac{1}{2}\left(\vec{d}_{obs} - \vec{d}_{cal}\right)^T \mathbf{C_d^{-1}}\left(\vec{d}_{obs} - \vec{d}_{cal}\right) - \tfrac{1}{2}(\mu_\alpha - \vec{\alpha})^T C_\alpha^{-1}(\mu_\alpha - \vec{\alpha})\right\} \end{gathered} \tag{3.4}$$

3.1.2 Objective Function Formulation

The objective function corresponds to a search for a maximum *a posteriori* probability given by Equation 3.4. Thus, the formulation to be minimized is written as follows:

$$E = \frac{1}{2}\left(\vec{d}_{obs} - \vec{d}_{cal}\right)^T \mathbf{C_d^{-1}} \left(\vec{d}_{obs} - \vec{d}_{cal}\right) + \frac{1}{2}(\mu_\alpha - \vec{\alpha})^T \mathbf{C}_\alpha^{\mathbf{-1}} (\mu_\alpha - \vec{\alpha}) \tag{3.5}$$

The first term measures the discrepancy between the calculated and the observed flow responses. Minimizing this term corresponds to the best match of the dynamic data whose uncertainty is characterized by the covariance matrix $\mathbf{C_d}$. Since the errors in measurements are typically assumed to be independent, this matrix is reduced to a diagonal. Otherwise, as will be shown later, there always exists a linear transformation of the data so that the new covariance matrix is diagonal. Elements along the diagonal represent variances (σ_d^2) of the data.

The second term represents the *a priori* knowledge of parameters included in the mean values, μ_α and the covariance matrix of parameters $\mathbf{C}_\alpha^{\mathbf{-1}}$. Both μ_α and $\mathbf{C}_\alpha^{\mathbf{-1}}$ can be obtained from geostatistical information.

3.1.3 Link to Weighted Least Square

A very well known formulation used to measure the difference between simulation results and data is in the form of weighted least square as follows:

$$E = \frac{1}{2}\left(\vec{d}_{obs} - \vec{d}_{cal}\right)^T \mathbf{W_d} \left(\vec{d}_{obs} - \vec{d}_{cal}\right) \tag{3.6}$$

where $\mathbf{W_d}$ is a diagonal weighting matrix to be included in the objective function to account for different numerical scales in measurement data. Equation 3.11 defines the first term in Equation 3.5 by stating that:

$$\mathbf{W_d} = \mathbf{C_d^{-1}} \tag{3.7}$$

Equation 3.7 implies that each data point should be weighted by the inverse of its variance. For data point i:

$$w_d^i = \frac{1}{{\sigma_d^i}^2} \tag{3.8}$$

Similarly, if the parameters are independent, the covariance matrix of parameters $\mathbf{C}_\alpha^{\mathbf{-1}}$ is diagonal and the second term in Equation 3.5 has a weighted least square form where:

$$\mathbf{W}_\alpha = \mathbf{C}_\alpha^{\mathbf{-1}} \tag{3.9}$$

or:

$$w_\alpha^i = \frac{1}{{\sigma_\alpha^i}^2} \tag{3.10}$$

implying that each parameter should be weighted by the inverse of its *a priori* variance.

3.1.4 Link to Unweighted Least Square

Another form of the objective function that is also very widely used is the unweighted least square where all weights are identical. This is typically the case when data represent measurements of the same quantity. The objective function is then given by:

$$E = \frac{1}{2}\left(\vec{d}_{obs} - \vec{d}_{cal}\right)^T \left(\vec{d}_{obs} - \vec{d}_{cal}\right) \tag{3.11}$$

3.2 Optimization Methods

Matching numerical flow simulation results with dynamic data is achieved by modifying the geometry and the properties of the geological objects and background. Such modification is implemented in such a way as to preserve all geological/geostatistical information. This can be achieved by perturbing the parameters used for the generation of the static model. The identification of such parameters is based on the solution of a constrained optimization problem minimizing the defined objective function. The objective is to construct an optimal set of parameters $\vec{\alpha}^*$ such that

$$\vec{\alpha}^* = arg \min_{\vec{\alpha} \in D} E(\vec{\alpha}) \tag{3.12}$$

where D is the feasible domain determined by a set of constraints on parameters. In reservoir parameter estimation problems, the objective function to be minimized is nonlinear and is related to the parameters in complex ways. Therefore, finding an optimal solution in parameter space is an iterative search process in which the successions of changes of parameters in each iteration are computed to satisfy these conditions:

1. Reduction of the objective function, and
2. Confinement of parameters inside the feasible domain.

In general, an iterative search process to find a point of interest includes three major steps:

1. Guess a starting point of interest.
2. Approximate the function in the neighborhood of the point of interest by a proxy whose point of interest is easy to find.
3. Go to Step 2 with the new point of interest.

Since we are dealing with parameters that are not found in the model equations, the evaluation of the objective function corresponding to a given set of parameters is expensive in terms of requiring both stochastic simulation at fine scale and flow simulation at coarse scale. The number of function evaluations should be as small as possible in order to obtain fast and feasible convergence. As shown in the literature, there are a large number of methods for minimizing a multivariate function. In devising or choosing an optimization method one attempts to minimize the total computation time required for convergence to the minimum. This time is composed primarily of the following two factors:

1. Function and derivative evaluations.
2. Algebraic manipulations such as matrix inversions or eigenvalue determinations.

It is usually possible to trade off these factors against each other. A method employing more laborious algebraic procedures may require fewer iterations, and hence fewer function evaluations. This is likely to pay off, particularly, in our case when the objective function is a complicated one and its computation is time consuming. We do not hesitate therefore to recommend methods which are sophisticated algebraically, as long as they are efficient in terms of the number of required function evaluations. Gradient-based methods have often been found to be most effective. Such methods require the calculation of the gradients of the objective function, E, with respect to all parameters.

$$\nabla E = \left(\frac{\partial E}{\partial \vec{\alpha}}\right)^T \tag{3.13}$$

Multiple gradient-based techniques were employed in this work according to the case difficulty, among them are:

- Steepest-Descent,
- Gauss-Newton,
- Levenberg-Marquardt,
- Powell ‘Dog-Leg’,
- BFGS.

Various algorithmic features regarding stabilization, quadratic proxy, constraints, etc. were also used with these techniques and are as follows:

- Line search,
- Penalty/barrier functions,

- Step-length controller,
- Scaling, modified Marquardt, and Cholesky solution techniques.

Detailed mathematical background of these methods can be found in Bard (1970) and Gill et al. (1981). Both books also deal with practical aspects of nonlinear parameter estimation problems. More concrete discussion and derivations of the first three techniques (excluding Powell 'Dog-Leg' and BFGS) in petroleum engineering applications can be found in Section 3 of Phan (1998). Here we only summarize important features of the first three methods and give a full discussion of the last two. To do this, let us define the following terms:

- $\vec{\alpha}$: Vector of parameters
- $\mathbf{G}$: Sensitivity coefficient matrix

$$\mathbf{G} = \frac{\partial \vec{d}_{cal}}{\partial \vec{\alpha}} \tag{3.14}$$

- $\mathbf{H}$: *Hessian* matrix

$$\mathbf{H} = \frac{\partial^2 E}{\partial \vec{\alpha}^2} \tag{3.15}$$

3.2.1 Steepest Descent

This algorithm searches for an optimal step along the direction of the gradient of the objective function. Therefore, it 'steps along' the line of 'steepest slope' on the surface expressed by the objective function.

Formulations

$$\nabla E = \mathbf{G}^T \mathbf{C}_{\mathbf{d}}^{\mathbf{-1}} \left(\vec{d}_{cal} - \vec{d}_{obs} \right) + \mathbf{C}_{\alpha}^{\mathbf{-1}} \left(\vec{\alpha} - \mu_{\alpha} \right) \tag{3.16}$$

Algorithm

- Compute the numerical response $\vec{d}_{cal}(\vec{\alpha})$ and its sensitivity coefficient matrix $\mathbf{G}$.

- Compute the gradient of the objective function ∇E.
- Compute steepest-descent direction $\delta\vec{\alpha} = -\nabla E$.
- Compute the optimal step ρ^* by univariate linearization proxy of E.
- Update parameters $\vec{\alpha}' = \vec{\alpha} + \rho^*\delta\vec{\alpha}$.

Remarks

The steepest-descent method is well known for its numerical stability. The convergence is ensured with sufficiently small steps. The convergence rate is high far from the solution but decreases significantly near the solution. This method is well suited for highly nonlinear problems but often converges too slowly.

3.2.2 Gauss-Newton

In this technique, a more sophisticated direction of descent is computed in order to overcome the performance degradation during the inversion process that is observed in the steepest descent method. The Gauss-Newton method is obtained by a first-order Taylor series expansion of the objective function gradient ∇E.

Formulations

$$\nabla E = \mathbf{G}^T \mathbf{C}_{\mathbf{d}}^{\mathbf{-1}} \left(\vec{d}_{cal} - \vec{d}_{obs}\right) + \mathbf{C}_{\alpha}^{\mathbf{-1}} \left(\vec{\alpha} - \mu_{\alpha}\right) \tag{3.17}$$

$$\mathbf{H} = \mathbf{G}^T \mathbf{C}_{\mathbf{d}}^{\mathbf{-1}} \mathbf{G} + \mathbf{C}_{\alpha}^{\mathbf{-1}} + \left[\frac{\partial \mathbf{G}}{\partial \alpha}\right]^T \mathbf{C}_{\mathbf{d}}^{\mathbf{-1}} \left(\vec{d}_{cal} - \vec{d}_{obs}\right) \tag{3.18}$$

In the Gauss-Newton method, we neglect the last term involving second-order derivatives in Equation 3.18 and the Hessian matrix $\mathbf{H}$ is replaced by the Gauss-Newton Hessian matrix:

$$\mathbf{H}_{\mathbf{gn}} = \mathbf{G}^T \mathbf{C}_{\mathbf{d}}^{\mathbf{-1}} \mathbf{G} + \mathbf{C}_{\alpha}^{\mathbf{-1}} \tag{3.19}$$

Algorithm

- Compute the numerical response $\vec{d}_{cal}(\vec{\alpha})$ and its sensitivity coefficient matrix $\mathbf{G}$.
- Compute the gradient of the objective function ∇E.
- Compute the *Hessian* matrix $\mathbf{H_{gn}}$.
- Compute descent direction $\delta\vec{\alpha} = -\mathbf{H_{gn}^{-1}}\nabla E$.
- Compute the optimal step ρ^* by univariate quadratic proxy of E.
- Update parameters $\vec{\alpha}' = \vec{\alpha} + \rho^*\delta\vec{\alpha}$.

Remarks

In general, the Gauss-Newton method has a better performance than the steepest-descent method in most cases and theoretically allows a quadratic convergence rate. The drawbacks are that the method may become numerically unstable near the solution when treating a highly nonlinear problem and when the initial parameters are too far off the optimal solution. The problem of instability is avoided in this work by using scaling, Marquardt, and Cholesky factorization techniques (see Section 3 of Phan, 1998).

3.2.3 Levenberg-Marquardt

In this approach, a sufficiently large number is introduced on the diagonal elements of the Hessian matrix in order to achieve a better numerical stability in the Gauss-Newton method.

Formulations

$$\nabla E = \mathbf{G}^T\mathbf{C_d^{-1}}\left(\vec{d}_{cal} - \vec{d}_{obs}\right) + \mathbf{C}_\alpha^{\mathbf{-1}}\left(\vec{\alpha} - \mu_\alpha\right) \tag{3.20}$$

$$\mathbf{H_{gn}} = \mathbf{G}^T\mathbf{C_d^{-1}}\mathbf{G} + \mathbf{C}_\alpha^{\mathbf{-1}} \tag{3.21}$$

$$\mathbf{H_{lm}} = \mathbf{H_{gn}} + \mu\mathbf{I} \tag{3.22}$$

$\mathbf{H_{lm}}$ is Levenberg-Marquardt Hessian matrix. μ is a positive number and sufficiently large to avoid ill-conditioning but small enough to retain the closeness between the modified matrix and the original.

Algorithm

- Compute the numerical response $\vec{d}_{cal}(\vec{\alpha})$ and its sensitivity coefficient matrix $\mathbf{G}$.
- Compute the gradient of the objective function ∇E.
- Compute the Gauss-Newton Hessian matrix $\mathbf{H_{gn}}$.
- Compute the *Levenberg-Marquardt* Hessian matrix $\mathbf{H_{lm}}$ by adding scalar μ to the diagonal of $\mathbf{H_{gn}}$.
- Compute descent direction $\delta\vec{\alpha} = -\mathbf{H_{lm}^{-1}}\nabla E$.
- Compute the optimal step ρ^* by univariate quadratic proxy of E.
- Update parameters $\vec{\alpha}' = \vec{\alpha} + \rho^* \delta\vec{\alpha}$.
- Reduce μ in iterations in which E is decreased, or increase μ in iterations in which E fails to decrease.

Remarks

The *Levenberg-Marquardt* method has proven to be very reliable for practical problems, and has a better numerical behavior with difficult starting points. However, the disadvantage lies in updating the Marquardt parameter which is often based on more or less empirical criteria.

3.2.4 Powell 'Dog-Leg'

The Powell 'Dog-Leg' method is a combination of steepest-descent and Gauss-Newton methods, based on an interpolation beween the two directions of descent. A trust region technique is also introduced to control the algorithm. The trust region is centered at $\vec{\alpha}$ and has a radius of norm ρ. The Gauss-Newton descent direction $\delta\vec{\alpha}_g$

and the steepest-descent direction $\delta\vec{\alpha}_s$ are calculated and compared with the trust region radius ρ to propose an optimal descent direction $\delta\vec{\alpha}_p$ for the Powell method.

Formulations

At each iteration, $\delta\vec{\alpha}_p$ is obtained according to following schemes:

- The Gauss-Newton solution is inside the trust region ($\|\delta\vec{\alpha}_g\| \leq \rho$) (see Figure 3.1). The steepest-descent solution is either inside ($\|\delta\vec{\alpha}_s\| \leq \rho$) or outside ($\|\delta\vec{\alpha}_s\| > \rho$) the trust region. The Gauss-Newton solution is retained.

$$\delta\vec{\alpha}_p = \delta\vec{\alpha}_g \tag{3.23}$$

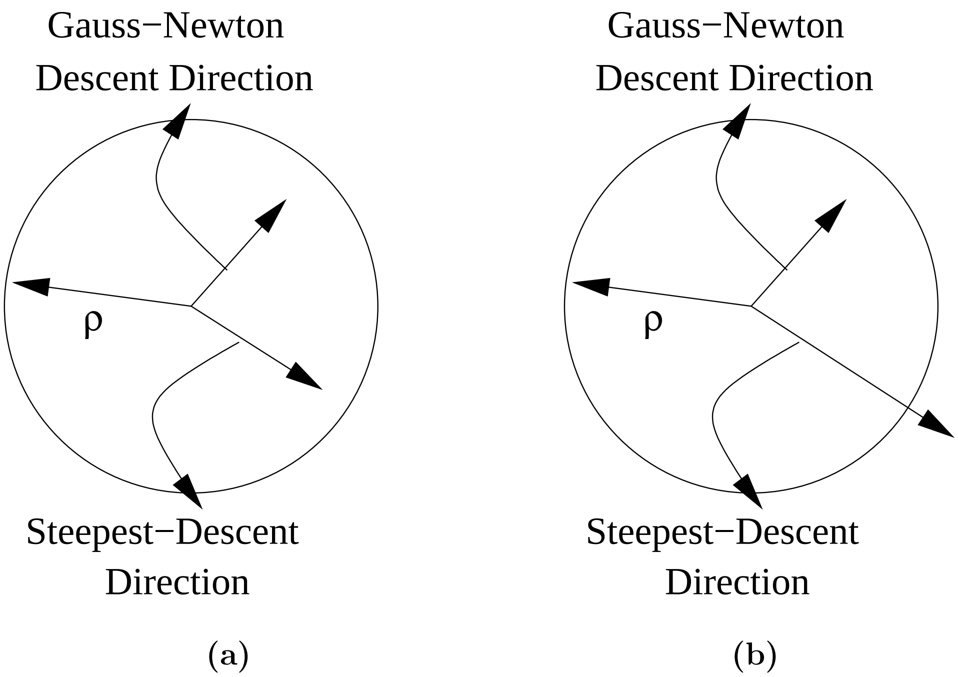

Figure 3.1: Gauss-Newton solution is inside the trust region.

- Two solutions are outside the trust region (($\|\delta\vec{\alpha}_g\| > \rho$ and $\|\delta\vec{\alpha}_s\| > \rho$). The steepest-descent method is retained. The steepest-descent solution is then rescaled to reach the boundary of the trust region (see Figure 3.2).

$$\delta\vec{\alpha}_p = \frac{\rho\delta\vec{\alpha}_s}{\|\delta\vec{\alpha}_s\|} \tag{3.24}$$

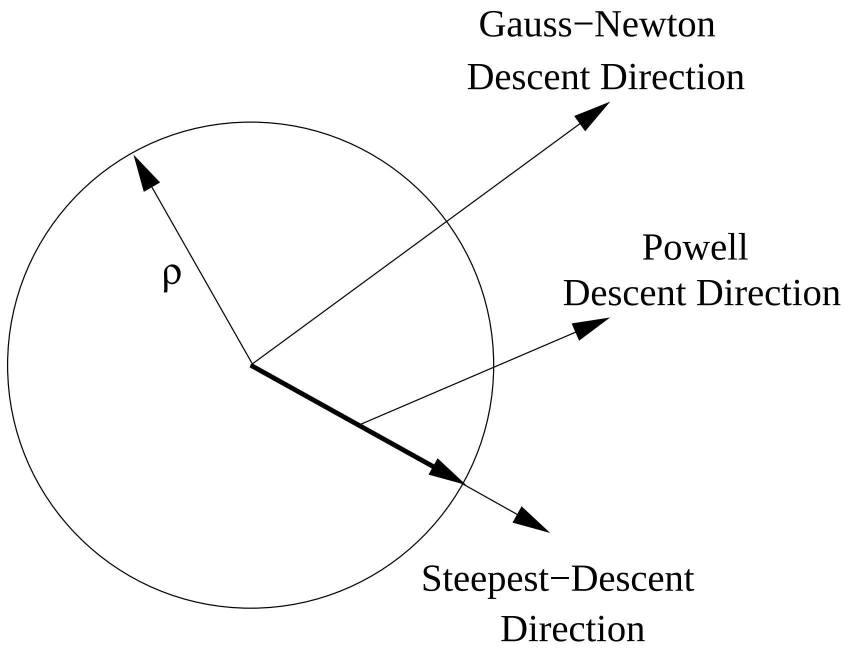

Figure 3.2: Gauss-Newton and steepest-descent solutions are outside the trust region

- The steepest-descent solution is inside and the Gauss-Newton solution is outside of the trust region (($\|\delta\vec{\alpha}_g\| > \rho$ and $\|\delta\vec{\alpha}_s\| \leq \rho$). The combined Powell solution is obtained by interpolating beween the two and rescaling to reach the boundary of the trust region (see Figure 3.3).

$$\delta\vec{\alpha}_p = \omega\delta\vec{\alpha}_s + (1-\omega)\delta\vec{\alpha}_g \tag{3.25}$$

In order for the combined solution to lie on the boundary of the trust region, ω must satisfy the relationship:

$$\|\delta\vec{\alpha}_p\| = \rho \tag{3.26}$$

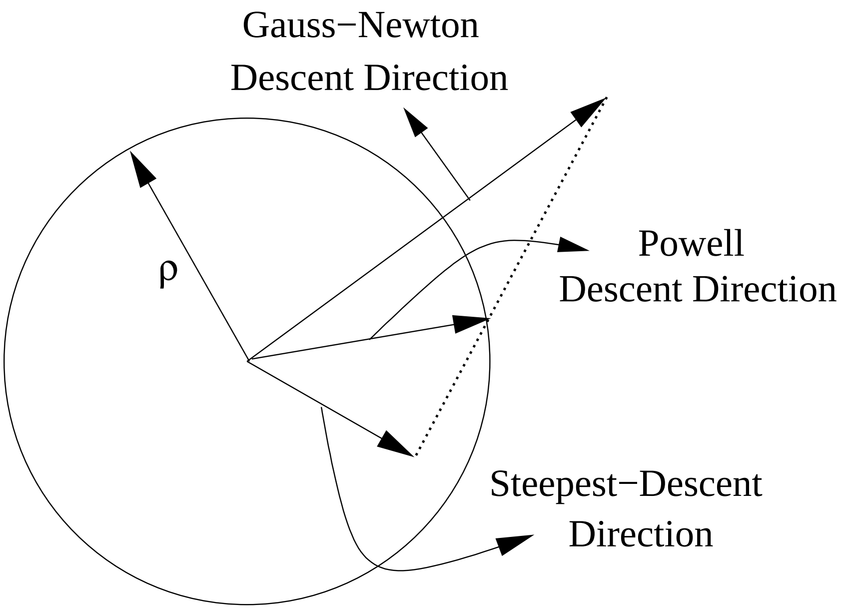

Figure 3.3: steepest-descent solution is inside and Gauss-Newton solution is outside of the trust region.

Algorithm

- Compute the numerical response $\vec{d}_{cal}(\vec{\alpha})$ and its sensitivity coefficient matrix $\mathbf{G}$.
- Compute the gradient of the objective function ∇E.
- Compute the Gauss-Newton Hessian matrix $\mathbf{H_{gn}}$.
- Compute the Gauss-Newton solution $\delta\vec{\alpha}_g$.
- Compute the steepest-descent solution $\delta\vec{\alpha}_s$.
- Test the norms of $\delta\vec{\alpha}_g$ and $\delta\vec{\alpha}_s$ with respect to ρ.
- Compute the Powell 'Dog-Leg' solution $\delta\vec{\alpha}_p$.
- Update parameters $\vec{\alpha}' = \vec{\alpha} + \delta\vec{\alpha}_p$.

Remarks

The purpose of the Powell 'Dog-Leg' method is to combine the advantages of the Gauss-Newton method which offers rapid convergence near the solution and the steepest-descent method which is robust and numerically stable far from the solution. It is guaranteed to converge to a minimum and avoid iteration failures by adjusting the trust region radius.

3.2.5 BFGS

The BFGS algorithm was proposed independently by Broyden (1970), Fletcher (1970a), Goldfarb (1970) and Shanno (1970). This technique approximates the inverse of a Hessian matrix and uses sequential updating technique to improve the approximation during the iterative search process.

Formulations

Let $\mathbf{U}$ denote a numerical approximation of the inverse of a Hessian matrix,

$$\mathbf{U} \approx \mathbf{H}^{-1} \tag{3.27}$$

then the sequential updating BFGS formula is given by:

$$\mathbf{U}^{k+1} = \mathbf{U}^k - \frac{\delta\vec{\alpha}\nabla E \mathbf{U}^k + \mathbf{U}^k(\nabla E)^T(\delta\vec{\alpha})^T}{\nabla E \delta\vec{\alpha}} + \left[1 + \frac{\nabla E \mathbf{U}^k (\nabla E)^T}{\nabla E \delta\vec{\alpha}}\right] \frac{\delta\vec{\alpha}(\delta\vec{\alpha})^T}{\nabla E \delta\vec{\alpha}} \tag{3.28}$$

where $\delta\vec{\alpha}$ is determined from previous step, i.e., $\delta\vec{\alpha} = \vec{\alpha}^k - \vec{\alpha}^{k-1}$.

Algorithm

- Initialize the approximated inverse of $\mathbf{H}$ by identity matrix $\mathbf{U} = \mathbf{I}$.
- Compute the numerical response $\vec{d}_{cal}(\vec{\alpha})$ and its sensitivity coefficient matrix $\mathbf{G}$.
- Compute the objective function and its gradient ∇E.
- Compute the BFGS solution $\delta\vec{\alpha} = -\mathbf{U}^k(\nabla E)^T$.
- Compute the optimal step ρ^* by univariate quadratic proxy of E.

- Update parameters $\vec{\alpha}^{k+1} = \vec{\alpha}^{k} + \rho^{*}\delta\vec{\alpha}$.
- Update the approximation matrix using BFGS formula given by Equation 3.28.

Remarks

This method is well suited for the inversion of a large number of parameters. It does not require the calculation of the Hessian matrix and avoids solving a system of linear equations.

In this chapter, we have formulated the objective function in a number of widely used forms and summarized multiple gradient-based techniques that were employed in this work. Various algorithmic features regarding stabilization, quadratic proxy, and constraints were also presented. The minimization algorithms using gradient-based techniques require the calculation of sensitivity coefficients of the flow simulated response. According to the chain rule, the gradients of the spatial distribution of petrophysical properties (permeability and porosity) must be computed with respect to matching geometric parameters. One way to accomplish this is to first develop mathematical functions describing permeability and porosity fields in terms of such geometric parameters. A detailed discussion of the development is given in the next chapter.

Chapter 4

Development of Mathematical Foundations

As was mentioned ealier, the reservoir heterogeneity depends completely on the geometry and the property of the rocks constituting the objects and the background. In reality, the rock material is discontinuous across the object boundary. Therefore, the mathematical functions defining spatial petrophysical properties of the reservoir are also discontinuous along the object boundary. This section will discuss a way to construct such functions and how to avoid the problem of discontinuity in the optimization algorithm.

4.1 Construction of Geometric Functions

Let us begin this section by first defining the term geometric function. A function is termed a geometric function defining a certain geological object if:

- It vanishes on the object boundary,
- It takes positive values at interior points,
- It takes negative values at exterior points.

One critical step in describing petrophysical fields analytically in terms of geometric parameters is the construction of the geometric functions defining the objects. In this section, we discuss in detail a technique for constructing various geometric functions.

We begin by considering a simple case, where the reservoir under study is assumed to be a two-dimensional rectangular box and consists of exactly one object with circular shape (see Figure 4.1, (a)). The circle is centered at (x_0, y_0) and delimited by radius r. For further simplicity, the rock permeability is homogeneous and has a value of 0 outside and 1 inside the circle. Thus, the permeability at location M is given by:

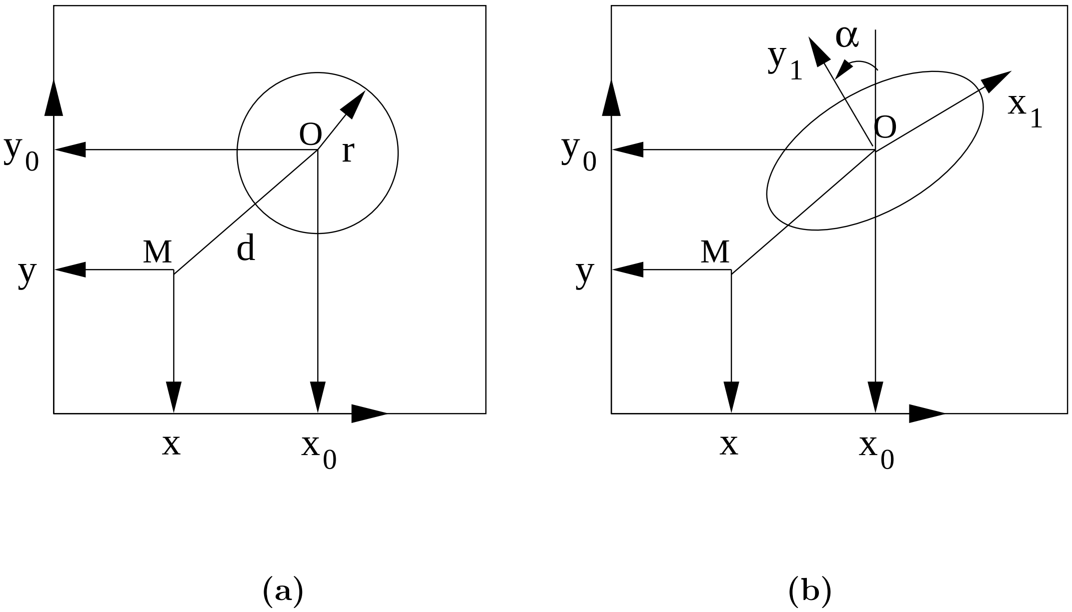

Figure 4.1: Circular and ellipse objects.

$$k(M) = \begin{cases} 1; & \text{M} \in \text{circle} \\ 0; & \text{otherwise} \end{cases} \tag{4.1}$$

or in a more mathematical format:

$$k(x,y) = \begin{cases} 1; & (x-x_0)^2 + (y-y_0)^2 \leq r^2 \\ 0; & \text{otherwise} \end{cases} \tag{4.2}$$

Recall the circle equation,

$$r^2 - (x-x_0)^2 - (y-y_0)^2 = 0 \tag{4.3}$$

Let $g(x,y)$ be the left side of Equation 4.3 representing the circle:

$$g(x,y) = r^2 - (x-x_0)^2 - (y-y_0)^2 \tag{4.4}$$

then it is easy to verify that $g(x,y)$ is a geometric function defining the circle. The spatial permeability of the reservoir can then be expressed in a compact form:

$$k(x,y) = \mathbf{1}(g(x,y)) \tag{4.5}$$

where $\mathbf{1}(.)$ is the step function. Similarly, the geometric function for ellipse is defined as (see Figure 4.1, (b)):

$$g(x,y) = 1 - \frac{x_1^2}{a^2} - \frac{y_1^2}{b^2} \tag{4.6}$$

where a and b are the semimajor and semiminor axes respectively. (x_1, y_1) is the local coordinate system in which the ellipse is defined. Using linear transformation to relate local to global coordinate system (x,y) gives

$$\begin{aligned} g(x,y) \quad = \quad & 1 - \left(\frac{(x-x_0)\cos(\alpha) + (y-y_0)\sin(\alpha)}{a}\right)^2 - \\ & \left(\frac{(x-x_0)\sin(\alpha) - (y-y_0)\cos(\alpha)}{b}\right)^2 \end{aligned} \tag{4.7}$$

and the spatial permeability of the ellipse reservoir can be expressed in an analytical form using step function as follows:

$$k(x,y) = \mathbf{1}(g(x,y)) \tag{4.8}$$

Let us consider a more realistic case, where objects possess sinuous shape as in a typical fluvial reservoir. Figure 4.2 depicts a simple channel delimited in the y axis by two sinuous boundaries and in the x axis by two vertical lines located at a and b. It is not difficult to verify that the geometric function defining a channel infinite in the x axis ($x \in (-\infty, +\infty)$) and delimited in the y axis by two sinuous boundaries y_1 and y_2 is given by:

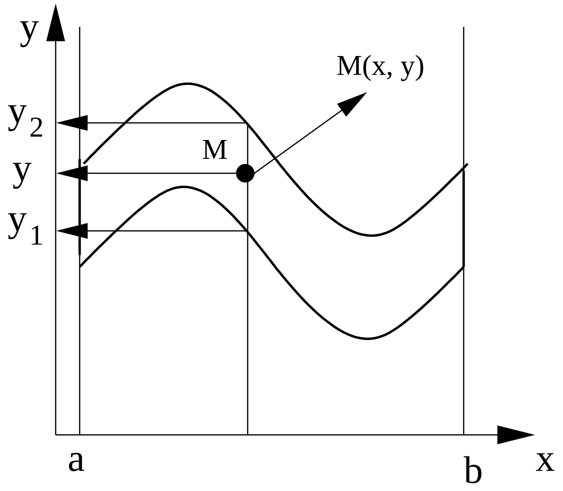

Figure 4.2: Sinuous object.

$$g_1(x, y) = (y_2(x) - y)(y - y_1(x)) \tag{4.9}$$

and the geometric function defining the vertical strip limited by the two vertical lines located at a and b along the x axis is given by:

$$g_2(x, y) = (b - x)(x - a) \tag{4.10}$$

However, finding the geometric function defining the delimited channel, formed by intersection between the vertical strip and the infinite channel, is complex and laborious. One such function could be:

$$g(x, y) = g_1 g_2 + A g_1 1(-g_1) + B g_2 1(-g_2) \tag{4.11}$$

The two constants A and B are chosen sufficiently large to guarantee $g(x, y)$ being negative when both g_1 and g_2 are negative. The spatial permeability of the channel reservoir can be given as:

$$k(x, y) = \mathbf{1}(g(x, y)) \tag{4.12}$$

So far, we have encountered no difficulties in constructing geometric functions for such simple geometries as circle, ellipse, and sinuosity. Let us consider a general case, where the objects are delimited by closed curves with irregular shape as depicted in Figure 4.3. Such a curve, as already discussed in Chapter 2, is normally represented by a set of parametric polynomial curve segments of the form:

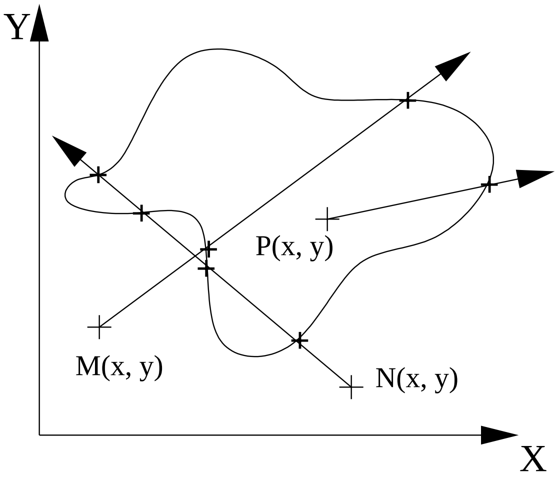

Figure 4.3: Irregular object and parity rules.

$$\text{for segment 1:} \quad \begin{cases} x &= x_1(t) \\ y &= y_1(t) \end{cases} \tag{4.13}$$

$$\text{for segment 2:} \quad \begin{cases} x &= x_2(t) \\ y &= y_2(t) \end{cases} \tag{4.14}$$

.

.

.

$$\text{for segment } n^{th}\text{:} \begin{cases} x &= x_n(t) \\ y &= y_n(t) \end{cases} \tag{4.15}$$

In this case, constructing geometric functions describing the object in terms of geometric parameters is extremely complex. One of the novel approaches proposed in this work is regarding the construction of such functions. The key idea is to use the parity rule that has been used widely in computer graphics (Foley *et al.*, 1997) for filling standard geometric primitives such as rectangles, circle, ellipse, polygons, polyhedra, and free-form surfaces in three dimensions. The rule consists of checking whether an arbitrary point is inside an object by drawing a line (test line) from the point to some other arbitrary point. If this test line crosses the object an odd number of times, the point is inside the object, if not, it is outside. It is important that the test lines pass through no vertices of the polygons and the jointed points between segments, else the intersections count can be ambiguous. Figure 4.3 illustrates this concept. Both lines from points M and N cross the object an even number of times (twice for point M and four times for point N). According to the parity rule, these two points are outside the object. On the other hand, point P is inside the object because the line from this point crosses the object an odd number of times (one). The *parity* rule is conceptually simple, although its implementation is complex in terms of calculating the intersections between the line and the object boundary. To illustrate the complexity of the issue, consider the following intersection equation between a line, defined by $ax+by+c=0$, and a parametric curve, defined by, $x=x(t), y=y(t)$:

$$ax(t)+by(t)+c=0 \tag{4.16}$$

Since, in general, $x(t)$ and $y(t)$ are nonlinear functions with respect to t, solving this equation for unknown t normally requires an iterative method such as Newton-Raphson. Finding roots of a nonlinear equation can be done easily using iterative methods. However, the problem arises, as in our case, where the number of roots but not the roots themselves is what we need to find in order to compute the number of intersection points. Numerical error and convergence criteria may introduce artificial roots and result in the wrong number of intersections, causing an exterior point to be wrongly considered as interior and vice versa.

Fortunately, as was discussed in Chapter 2, cubic polynomials are sufficient to describe each segment of a relatively complex closed curve. In this case, the left side of Equation 4.16 is a cubic polynomial in terms of t whose roots can be computed easily by analytical formulas resulting in an accurate number of intersections.

However, there remains one difficulty in implementing the parity rule. That is how to construct the valid test line that does not pass through the joint points between segments. Figure 4.4 shows how an invalid test line could cause problem of ambiguity resulting in a wrong count of the intersections. Two segments are jointed at points M and N. The invalid test lines, drawn from points P_2 and P_3 passing through the jointed point N, intersect the closed curve once and twice respectively. Thus, according to the parity rule, the point P_2 is interior and the point P_3 is exterior. However, the line drawn from point P_1 intersects the closed curve once and is considered to be interior and this is obviously a wrong decision (point P_1 is actually exterior).

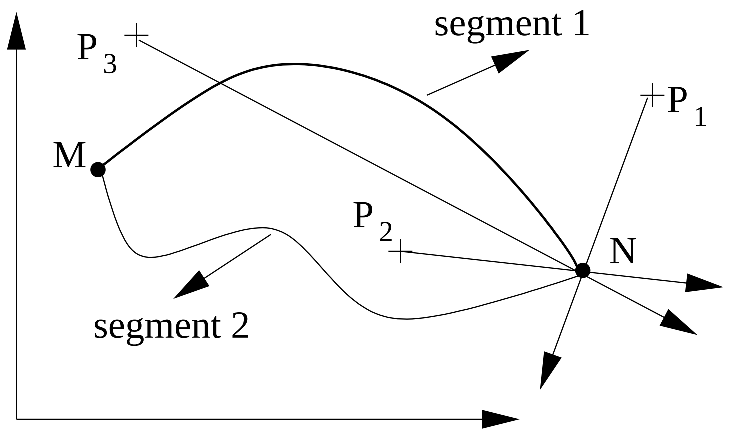

Figure 4.4: Invalid test lines in parity rules.

One way to construct a test line is to draw a line from a point (testing point) to another arbitrary point, say point O. Suppose point O is chosen to be fixed for all testing points. As will be known later, we need to evaluate the indicator function at every location in the reservoir including those points on the lines connecting the fixed point (O) and the joined points. Such lines are invalid test lines and result in a problem of ambiguity. Thus, to avoid this ambiguity problem, point O can not be fixed but it rather changes in some fashion. One efficient way is to chose point O randomly for each testing point. In this work, we made use of this random approach. The probability of encountering the problem of ambiguity is the probability that the random point O lies on the lines connecting the testing point to the jointed points and such probability is very small. In the worst case, if this occurs, another random point O can always be chosen.

Therefore, cubic parametric representations for curves together with the parity rule offers an analytical and efficient technique for constructing geometric functions defining objects with complex shapes.

It is important to introduce another type of function, the so-called indicator function, which will become useful in dealing with multiple objects. This function maps a location $\mathbf{u}$ to $0, 1$. The function returns a value of 1 at location $\mathbf{u}$ inside the object and 0 at location $\mathbf{u}$ outside the object.

$$I(\mathbf{u}) = \begin{cases} 1; & \mathbf{u} \in \text{object} \\ 0; & \text{else} \end{cases} \tag{4.17}$$

It is easy to see the following relation between the indicator function $I(.)$ and the geometric funtion $g(.)$ at location $\mathbf{u}$:

$$I(\mathbf{u}) = \mathbf{1}(g(\mathbf{u})) \tag{4.18}$$

4.2 Boolean Algebra Operations

Applying Boolean algebra on the set of indicator functions enables the construction of more complex bodies from simple objects. Such complex bodies are called composite because they are composed of two or more simple objects. The process of creating composite objects from geometric primitives using Boolean operations is known as

Constructive Solid Geometry (*CSG*). The *CSG* method makes possible the construction of complex geometric functions and calculations of intersection volumes.

The three standard Boolean operations are:

- union,
- difference, and
- intersection.

Following are examples of each operation with a brief description of how it works. We also made use of these following terms:

- $\mathbf{u}$ denotes a location,
- n is the number of objects,
- $I_k(.)$ is the indicator function associated with object k^{th},
- $I(.)$ is the indicator function associated with the composite body.

Boolean Union Operation: The indicator function of the composite body created by an union of multiple objects is simply the summation of all individual indicators.

$$I(\mathbf{u}) = \sum_{k=1}^{n} I_k(\mathbf{u}) \tag{4.19}$$

Figure 4.5(a) depicts two separate channel objects while the figure on the right, (b), presents a single body created as a result of the Boolean union operation.

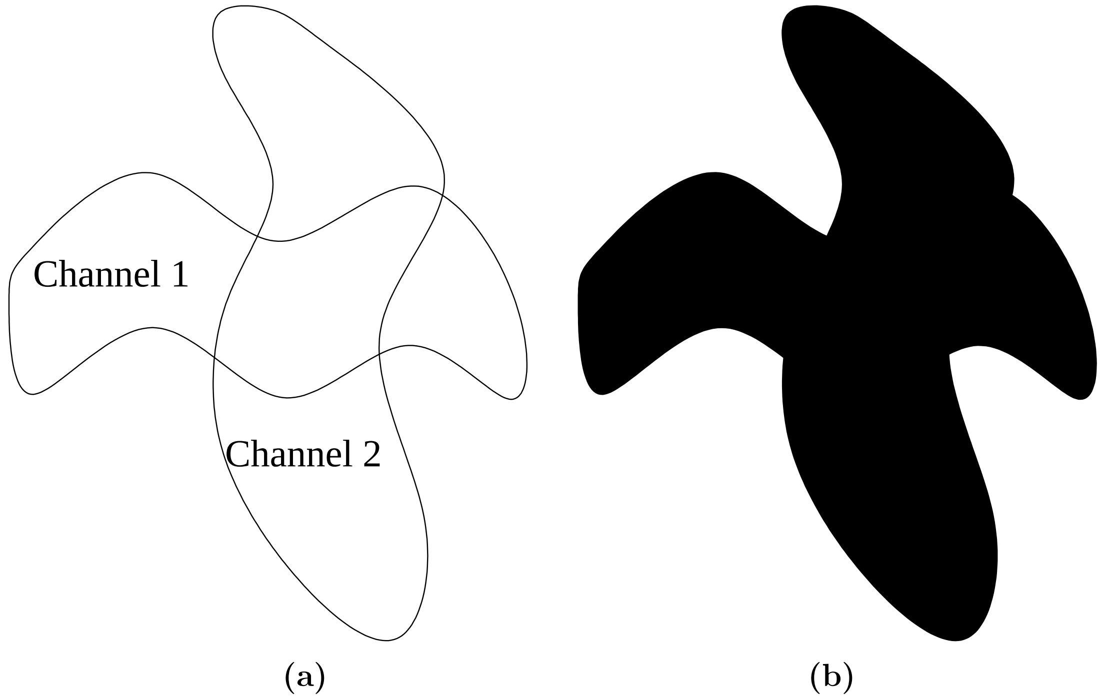

Figure 4.5: Composite body created as a result of Boolean union operation.

Boolean Difference Operation: The indicator function of the composite body created by the subtraction of a set of objects from another object is simply the Boolean difference between the individual indicator of the latter and those of the former.

$$I(\mathbf{u}) = I_0(\mathbf{u}) - \sum_{k=1}^{n} I_k(\mathbf{u}) \tag{4.20}$$

Figure 4.6(a) depicts two separate channel objects while the figure on the right, (b), presents two isolated bodies (black color) created as a result of the Boolean difference operation.

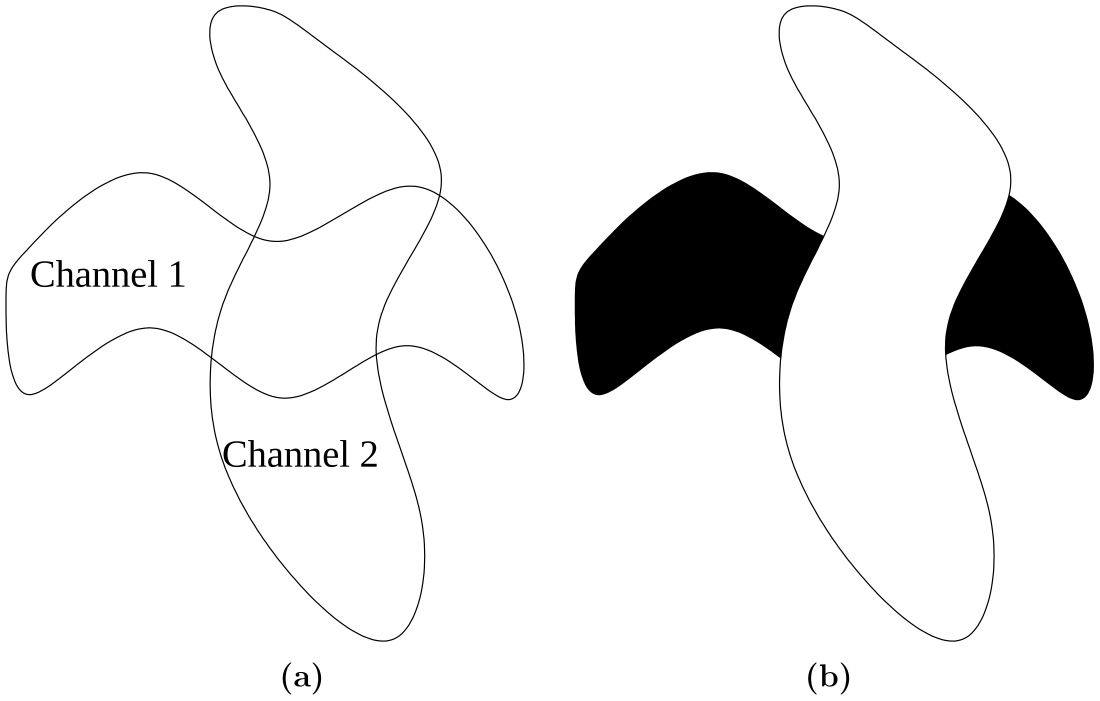

Figure 4.6: Composite body created as a result of Boolean difference operation.

Boolean Intersection Operation: The indicator function of the composite body created by the intersection of a set of objects is simply the Boolean intersection between the individual indicators.

$$I(\mathbf{u}) = \prod_{k=1}^{n} I_k(\mathbf{u}) \tag{4.21}$$

Figure 4.7(a) depicts two separate channel objects while the figure on the right, (b), presents a single body created as a result of the Boolean intersection operation.

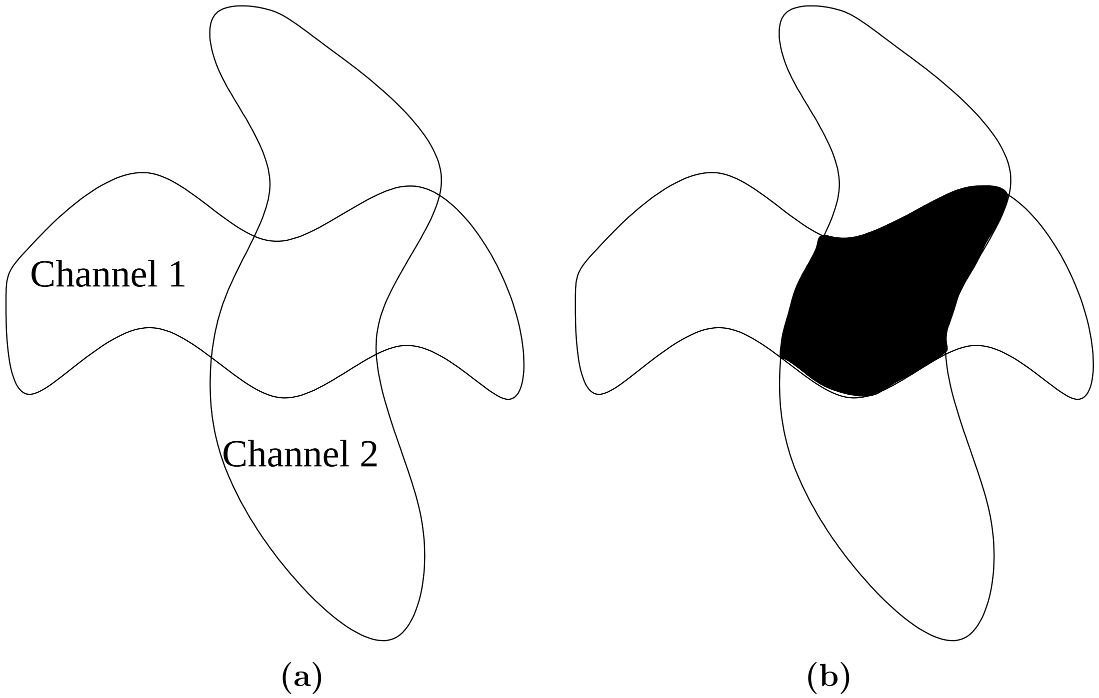

Figure 4.7: Composite body created as a result of Boolean intersection operation.

In this section, we have discussed a novel technique using the parity rules in computer graphics to construct geometric functions defining objects with complex geometry. We also introduced the concept of the indicator function which is a useful tool in dealing with multiple objects. Finally, the application of Boolean algebra on the set of indicator functions makes possible the volumetric calculations of complex composite bodies created as a result of such operations as union, difference, and intersection among a variety of complex objects.

4.3 Continuous Description of Permeability Field

So far, we have been concerned with the analytical construction of geometric and indicator functions. In this section, we will show how to use these functions to establish analytical expressions of the permeability field in terms of geometric parameters of the channels. Suppose we now consider the problem of finding the permeability field for a simple reservoir consisting of only one single channel with homogeneous rock properties. The permeability of the rock inside the channel is k_1 and that of the background is k_b. Then the permeability field is given as:

$$k(\mathbf{u}) = I_1(\mathbf{u})k_1 + \bar{I}_1(\mathbf{u})k_b \tag{4.22}$$

where I_1 is the indicator function defining the channel and $\bar{I}_1 = 1 - I_1$ is its *negation*. Similarly, for the reservoir consisting of two channels with permeabilities of k_1 and k_2 and with the permeability of the intersection is k_{12}:

$$k(\mathbf{u}) = I_1(\mathbf{u})\bar{I}_2(\mathbf{u})k_1 + \bar{I}_1(\mathbf{u})I_2(\mathbf{u})k_2 + \bar{I}_1(\mathbf{u})\bar{I}_2(\mathbf{u})k_b + I_1(\mathbf{u})I_2(\mathbf{u})k_{12} \tag{4.23}$$

By induction, an analytical expression of the permeability field for the reservoir consisting of n channels, $1, 2, 3, ...n$, with permeabilities of k_1, k_2,...k_n can be established as:

$$k(\mathbf{u}) = \sum_{l=0}^{n} \sum_{1 \le j_1 < j_2 < ... j_l \le n} \Big(I_1(\mathbf{u})I_2(\mathbf{u})...\bar{I}_{j_1}(\mathbf{u})...\bar{I}_{j_2}(\mathbf{u})...\bar{I}_{j_l}(\mathbf{u})...I_n(\mathbf{u}) \Big) \, k_{t_l} \tag{4.24}$$

where k_{t_l} denotes the permeability at the intersection between channels in the set $\{1, 2, ...n\}$ but not in the set $\{j_1, j_2, ...j_l\}$. By the assumption of identical properties across all channels, $k_1 = k_2 = ...k_n = k_c$, Equation 4.24 is simplified to be:

$$k(\mathbf{u}) = I_c(\mathbf{u})k_c + \bar{I}_c(\mathbf{u})k_b \tag{4.25}$$

where I_c is the indicator function of the composite body created as a result of the Boolean union operation and given as:

$$I_c(\mathbf{u}) = \sum_{k=1}^{n} I_k(\mathbf{u}) \tag{4.26}$$

In general, the formula given in Equation 4.24 is complex and composed of 2^n terms. However, since it has exactly only one term nonzero for each location $\mathbf{u}$, the complexity is still linear in n. It is important to note that, according to Equation 4.24, the stand-alone descriptions of all objects do not suffice to resolve the permeability field, it requires a knowledge regarding the geological interactions between objects when they were formed. In this work, we made use of the *a priori* knowledge of such geological events to resolve the intersections between objects. According to different depositional environments, the material in the areas intersected by two or more channels in a braided fluvial reservoir can be determined by either of the two following assumptions:

1. Immature channels replace the mature ones (used in this work).
2. Channels coexist at the intersections.

4.4 Discrete Description of Permeability Field

It can be verified from Equation 4.24 that the permeability field is discontinuous along the object boundary and this is consistent with outcrop and subsurface observations. Unfortunately, methods for solving optimization problems depend on the *continuity* of the objective function with respect to geometric parameters. Recall that the objective function is evaluated based on numerical simulation results which are, in turn, functions of geometric parameters through discrete reservoir description. Therefore, in approximating the exact flow partial differential equations (PDEs) to the finite-difference equations, techniques for discretizing the permeability field should be chosen with care. The continuity of the objective function would be violated if the point-support technique were used. This is because as the object boundary displaces across any discrete point, the permeability at that point jumps between the two values inside and outside the object. Figure 4.8 depicts a homogeneous reservoir model consisting of one channel. The value inside the channel is assumed to be 1 and outside to be 0. Figure 4.9 shows a discretized permeability field of the reservoir depicted in Figure 4.8 by using point-support technique. Thus, to ensure the continuity of the objective function, in this work, the discrete permeability field is not determined by just simply taking the values from the continuous field at the discrete points. Instead, it is calculated as the effective values over every cell in the simulation mesh grid. In principle, there are two techniques to calculate the effective values at each grid cell.

Unweighted area sampling: This technique sets the cell values proportional to the fraction of the cell occupied by the object. Equal areas contribute equally to the cell values. This technique is well-suited for large scale descriptions.

Weighted area sampling: This technique sets the cell values weighted more to the values of the closer overlap areas. Equal areas contribute unequally to the cell values. Areas closer to the cell center contribute more than those farther away. This technique is well-suited for small scale descriptions. Figure 4.10 shows one of such weighting functions. The area under the curve is 1.

More sophisticated sampling techniques can be obtained by changing the shapes of the weighting functions. Some of the techniques would be to assign different weights in different directions resulting in a discrete anisotropic permeability field. Both unweighted and weighted area sampling techniques were used in this work to describe the reservoir at different scales. The same reservoir, as shown in Figure 4.8, was discretized using the former technique. The resulting permeability field is depicted in Figure 4.11. Notice from this figure that all cells along the channel boundary are assigned values between those inside and outside the channel. The net effect is to decrease the constrast and to provide a smoother transition across the channel boundary. Let k^* be the discretized permeability at a cell along the boundary, then the expression for k^* using unweighted area sampling technique is

$$k^* = f_c k_c + (1 - f_c) k_b \tag{4.27}$$

or equivalently in integral form

$$k^* = \frac{1}{A} \int_A k(\mathbf{u}) d\mathbf{u} \tag{4.28}$$

The expression for k^* using weighted area sampling technique is given in integral form

$$k^* = \int_S k(\mathbf{u})\omega(\mathbf{u})d\mathbf{u} \tag{4.29}$$

where $\omega(.)$ is the weighting function such that the total volume under the weighting surface is unity.

$$\int_S \omega(\mathbf{u})d\mathbf{u} = 1 \tag{4.30}$$

where f_c is the fraction of the cell occupied by the channel as shown in Figure 4.12. k_c and k_b are the channel and background permeabilities respectively. A is the area of the simulation grid cell and S is the projected area under the weighting surface.

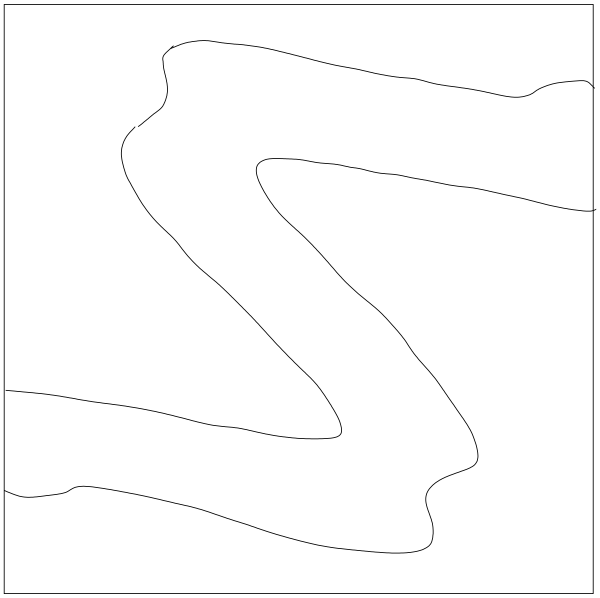

Figure 4.8: Continuous channel.

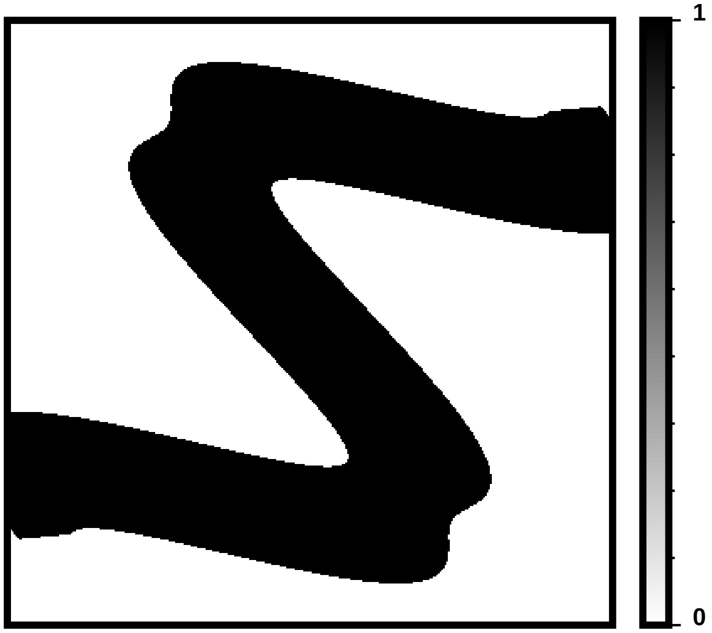

Figure 4.9: Discrete channel - point-support.

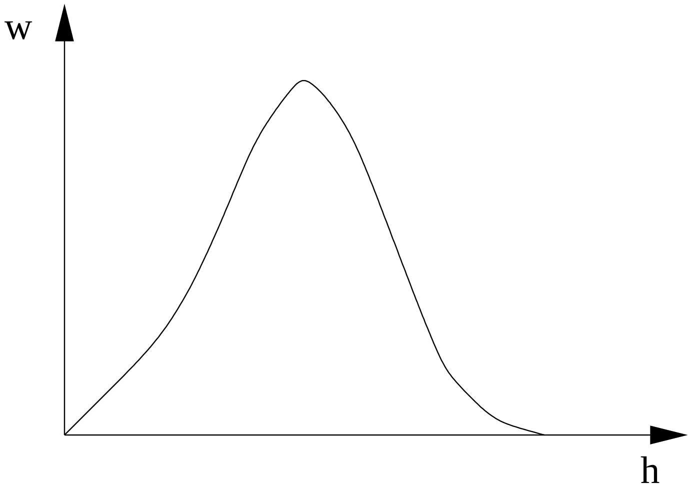

Figure 4.10: Weighting function - distance (h).

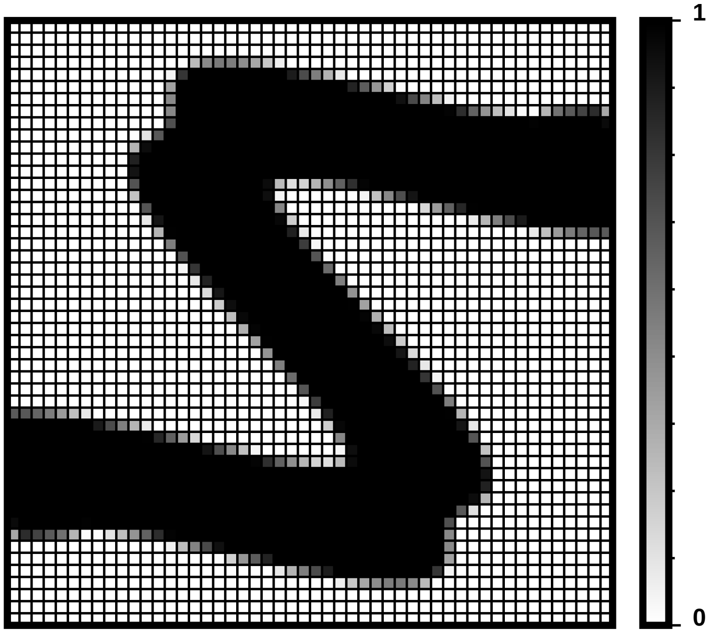

Figure 4.11: Discrete channel - area-support.

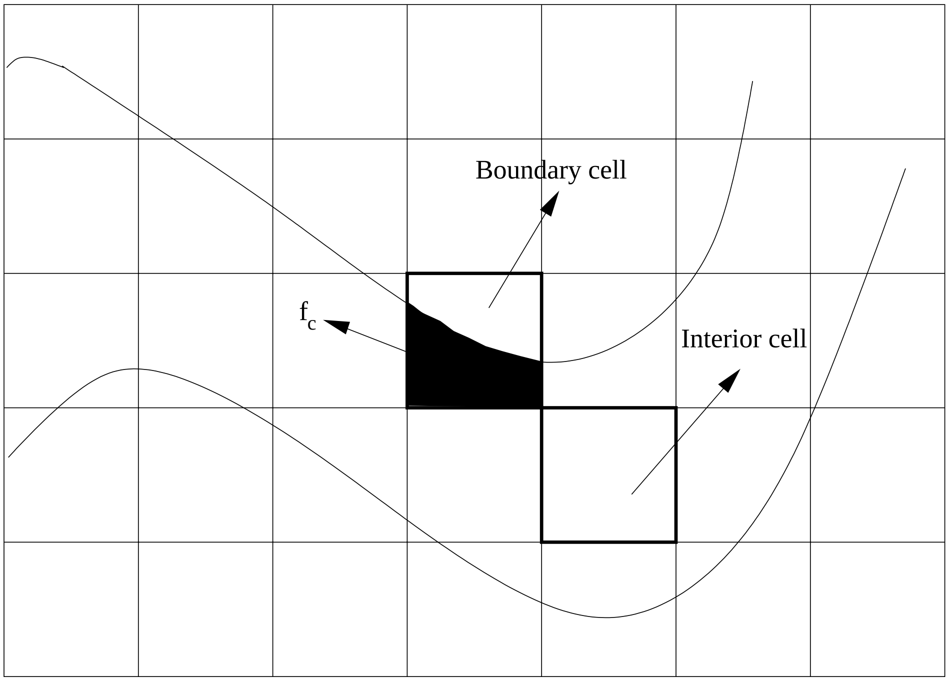

Figure 4.12: Intersected area - area-support.

4.5 Subcell Method

In the previous section, we have been concerned with issues regarding spatial discretization techniques in the methods for solving optimization problem. We have selected one technique to guarantee the continuity of the objective function with respect to the matching geometric parameters. The selected discretization technique requires the calculation of the intersection areas between the cells and objects and this represents an important step in developing an efficient and accurate method of calculating sensitivity coefficients. Calculation of intersection areas as functions of channel parameters for the single channel case is relatively simple and the method has been described by a number of researchers, among whom are Landa (1997) and Landa and Horne (1997). One limitation of this method is that it requires the computation of the intersections between object boundaries and the simulation mesh grid, which is feasible only when the channel is described by simple geometric functions. Another limitation of this method is that despite large efforts in computing such intersection points, the area in each cell occupied by a channel is still far from being accurate as the channel boundaries are approximated by piecewise linear functions. Finally, generalizing the proposed method to deal with complex or multiple objects remains difficult. In this section, we shall describe a method, called subcell, which is conceptually simple but key for efficient and accurate calculations in the following important applications:

- Numerical representation of objects at various scales from fine scale geological/geostatistical (if interested in small scale reservoir description) to coarse scale simulation mesh grid (if interested in large scale reservoir description),
- Processing complex geological models regardless of the number of objects,
- Calculation of sensitivity coefficients, and
- Integration of geological events.

For multiple channels, the calculation of grid cell properties becomes extremely complex as the intersection areas between channels need to be resolved. To illustrate the complexity of the issue, consider Figure 4.13 where the boundary cell is intersected by two channels and subdivided into four areas with different colors as follows:

A: the background area,

B: overlap area between cell and channel II,

C: overlap area between cell and channel I, and

D: overlap area between two channels.

These areas are either computed by integral formulas or approximated by polygons (as was done by Landa, 1997 and Landa and Horne, 1997), either way requires us to find at least five intersections including those between the two channel boundaries (P_5) and between each channel boundary and the mesh grid (P_1, P_2, P_3, P_4). These intersection equations are nonlinear for even such relatively simple geometry as ellipse or sinuousity and can only be solved by an iterative process which is time consuming. Another difficulty comes from the fact that the derivations of these integrals are complex and are derived differently across different areas. Identifying and finding the set of vertices of a particular area or polygon is laborious and the number of areas in each cell increases exponentially with the number of channels (2^n). This implies that this approach can only be feasible for very limited number of channels (two or three). One novel aspect of the subcell method proposed in this work is its application in calculating these intersected areas making use of Boolean algebra operations discussed in Section 4.2 on page 54 regardless of the number of objects with complex geometric shapes. For instance, the four areas in Figure 4.13 can easily be expressed in terms of the channel indicator functions using Boolean algebra as follows (indicator function of the cell is unit since we are interested in the cell interior).

$$
\begin{aligned}
A &= \bar{I}_1 \bar{I}_2 && (4.31)\\
B &= I_2 - I_1 && (4.32)\\
C &= I_1 - I_2 && (4.33)\\
D &= I_1 I_2 && (4.34)
\end{aligned}
$$

where I_1 and I_2 are indicator functions defining channel I and channel II respectively. This procedure also encounters no difficulty in expressing the intersected areas in the general case of n channels. Let I_1, I_2, ... I_n denote indicator functions of the n channels then the area A intersected by channels j_1, j_2, $..j_k$ is given by

$$A = I_{j_1} I_{j_2} ... I_{j_k} \tag{4.35}$$

The intersected areas can be computed first, then make use of an equation similar to Equation 4.27 to compute the effective permeability. In general, some weighting functions, such as the one used in weighted area sampling technique, may be distributed unequally over the cell or the objects may possess nonuniform permeability. Thus, in terms of implementation, the effective permeability is computed from the subcell permeabilities. The idea behind the subcell method is that (see Figure 4.14) each simulation grid cell is subdivided into a number of subcells where each subcell is associated with a binary value returned from an indicator function indicating the channels the subcell center belongs to and thus the subcell property is determined by that of the channels. Finally, the cell effective property is simply computed from the subcell properties making use of appropriate discretization techniques such as unweighted or weighted area samplings. To demonstrate the application of subcell method to complex geological models, consider Figure 4.15 where the true reservoir consists of six objects with various geometric shapes from simplest to complex, including square, circle, ellipse, fault, channel, and irregular. The discrete reservoir heterogeneity of this model is computed using the subcell technique and depicted in Figure 4.16. It should be noted here that the intersected permeability is resolved by the assumption of geological events which states that the immature channels replace the mature ones. This figure illustrates how the permeability is assigned to a simulation grid cell intersected by multiple objects. Since the boundaries of the objects are represented by distributions of permeability contributed from all intersected objects weighted by intersection areas, any minute displacement of one object causes a minute change in the discrete boundaries. This validates the calculation of the gradients of the discrete permeability field with respect to geometric parameters, as will be discussed in the next section.

4.6 Numerical Gradients of Discrete Permeability Field

Another useful application of the subcell method is found in calculating numerical gradients of discrete permeability field with respect to matching geometric and property (object porosity and permeability) parameters. Having established the relation of grid cell properties to channel parameters as discussed in the previous section, in this work the derivatives of grid cell properties are computed numerically with respect to geometric parameters and analytically with respect to the channel properties (porosity and permeability). The procedure is as follows:

1. Generate a set of objects in their own local coordinate systems.
2. Calculate linear transformation matrices for each of the local systems.
3. Multiply linear transformation matrices to the subcell coordinates.
4. Calculate indicator functions for all objects.
5. Apply Boolean algebra operations on the set of calculated indicator functions.
6. Calculate subcell permeability field.
7. Calculate effective grid cell permeability field using unweighted or weighted volume sampling techniques.
8. Analytically calculate the gradients with respect to the channel properties (porosity and permeability).
9. Numerically calculate the gradients with respect to geometric parameters.
10. Perturb geometric parameters.
11. Go back to Step 1.

Figures 4.17 through 4.24 depict the gradients of the discrete permeability field with respect to the channel geometric parameters calculated using the procedure described above. Such geometric parameters include translations in x-direction and y-direction, rotation, departure, sinuosity, displacement, width, and length. One common observation drawn from these figures is that the gradients are only nonzero along the channel boundary. This can be explained by observing that as the channel geometry changes the permeability at the cells intersecting the channel boundary vary but the permeability at the cells located completely either inside or outside the channel stay unaltered. However, these figures indicate several distinguishable features. The gradient with respect to the translation in the x-direction shown in Figure 4.17 has negative values at the left boundary and positive values at the right boundary. This is because as the channel is shifted to the right (positive x-direction) it moves out the cells on the left boundary causing a decrease in effective permeability and moves in the cells on the right boundary causing an increase in effective permeability. A similar explanation is also valid for Figure 4.18 where positive values are observed on the upper and negative values are observed on the lower bounday. Figure 4.23 shows the gradient with respect to the channel width and indicates positive values on both boundaries because as the width of the channel increases the channel is extended toward both sides. The gradient with respect to the channel length as depicted in Figure 4.24 is zero at all locations because the channel length is longer than the reservoir size. Changing the channel length should not influence the reservoir permeability. A reservoir consisting of a shorter channel is depicted in Figure 4.25. The gradient of this reservoir permeability field with respect to the channel length is shown in Figure 4.26 where nonzero values (and also positive) are only observed at the two ends of the channels. The reason is that as the channel length increases the channel is extended causing an increase in permeability at the two ends and leaving the permeability elsewhere unaltered.

Let us extend to a more general model where the shape of the object is completely irregular. Figure 4.27 depicts an example of such an object. The object is delimited by four cubic polynomial curve segments with different colors: blue, red, green, and black. The tangent vectors at the starting and end point for each segment are also presented in the same colors. The four geometric constraints defining the closed curve, $(x(0), x(1), x'(0), x'(1), y(0), y(1), y'(0), y'(1))$, are given in Table 4.1

Table 4.1: Geometric constraint data (ft)

seg no	$x(0)$	$x(1)$	$x'(0)$	$x'(1)$	$y(0)$	$y(1)$	$y'(0)$	$y'(1)$
1	100	1000	1000	100	100	500	6000	100
2	1000	600	100	100	500	800	-1000	100
3	600	500	-400	-300	800	100	2000	-300
4	500	100	-200	-200	100	100	1000	-1000

The matrix given in Equation 2.17 was used to calculate the corresponding polynomial coefficients from the geometric constraint data. The results are shown in Table 4.2.

Table 4.2: Cubic polynomial coefficients

seg no	a_x	b_x	c_x	d_x	a_y	b_y	c_y	d_y
1	-700	600	1000	100	5300	-10900	6000	100
2	1000	-1500	100	1000	-1500	2800	-1000	500
3	-500	800	-400	600	3100	-5800	2000	800
4	400	-600	-200	500	0	-1000	1000	100

Figure 4.28 depicts the actual object with irregular shape together with the four tangent vectors to represent the slopes at the joint points. The discrete permeability distribution is calculated using the subcell technique and is shown in Figure 4.29. The blurred boundary indicates a smooth transition between the object and the background and this validates the gradient calculations. The gradients of the discrete permeability field with respect to the object geometric parameters, particularly the four pairs of geometric constraints $(x(0), x(1), x'(0), x'(1), y(0), y(1), y'(0), y'(1))$, were calculated using the subcell technique. The results are shown from Figure 4.30 through Figure 4.41 The same observations as in the single channel case are also drawn from these figures. The gradients are only nonzero along the object boundary. By examining the signs of the gradients along the object boundary from these figures, we can verify the correctness of the gradient calculations. For instance, Figure 4.30 depicts the gradient with respect to the $x-$translation (positive x-direction

is to the right). Negative values should be observed along the left boundary and positive values should be observed along the right boundary. This is because as the object is translated toward the positive x-direction, it moves out the cells along the left boundary causing a decrease in effective permeability and moves in the cells along the right boundary causing an increase in effective permeability. Figure 4.33 depicts the gradient with respect to the parameter $x(0)$ of the first segment. The two segments 1^{st} and segment 4^{nd} are joined at point $(x(0), y(0))$. Any minute change of either $x(0)$ or $y(0)$ should reflect a change in these two segments. This is consistent with the observations from Figure 4.33 where the gradient is only nonzero along these two segments. However, changing the slope of a certain segment at either starting or end point causes only a change in that segment. This effect is illustrated clearly in Figure 4.41.

So far, we have shown results for a single object case where the only concern is the calculation of intersection areas between the object and the cells along the object boundary. This calculation is key for obtaining accurate gradients. Let us consider a much more complex test reservoir model as depicted in Figure 4.15 and the discrete permeability field is depicted in Figure 4.16. This test model consists of six objects with various geometric shapes including (in order of decreasing historical ages) channel, circle, ellipse, fault, irregular geometry and square. The *subcell* method was used to compute the gradients of the discrete permeability field with respect to geometric parameters of all objects. The results are shown from Figure 4.42 to Figure 4.48 and also yields similar observations as in the single object reservoir. The gradient field is zero everywhere except at the boundary. The difference is that the gradient is nonzero only for the part of the object boundary that is not overlapped by other more immature objects.

In this chapter, we have introduced several concepts and tools as the building blocks for approaching the problem. We have also proposed a novel method, the so-called subcell method, which makes possible the construction of geometricaly complex composite objects and provides keys for efficient and accurate calculations in many important applications in the parameter estimation problem. These areas include the calculations of intersection volumes, discrete reservoir heterogeneity, and the gradients of the heterogeneity field with respect to geometric parameters. The success in obtaining the gradient fields plays an critical role in the sensitivity calculations that will be discussed in the next chapter.

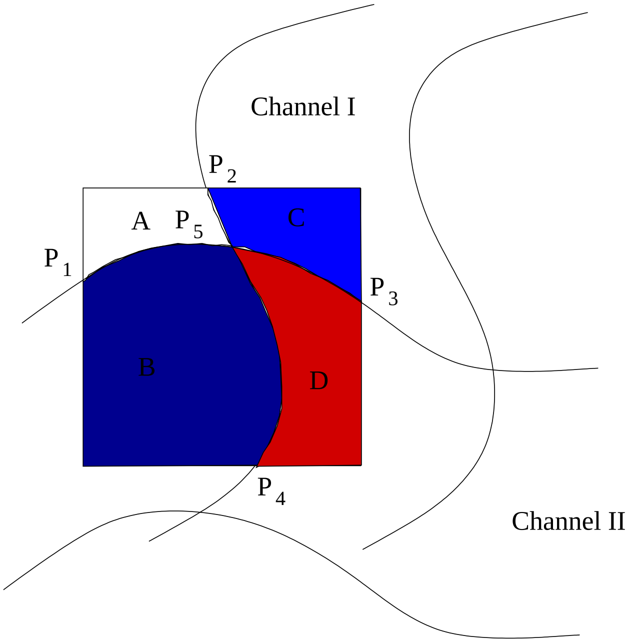

Figure 4.13: Four different intersection areas.

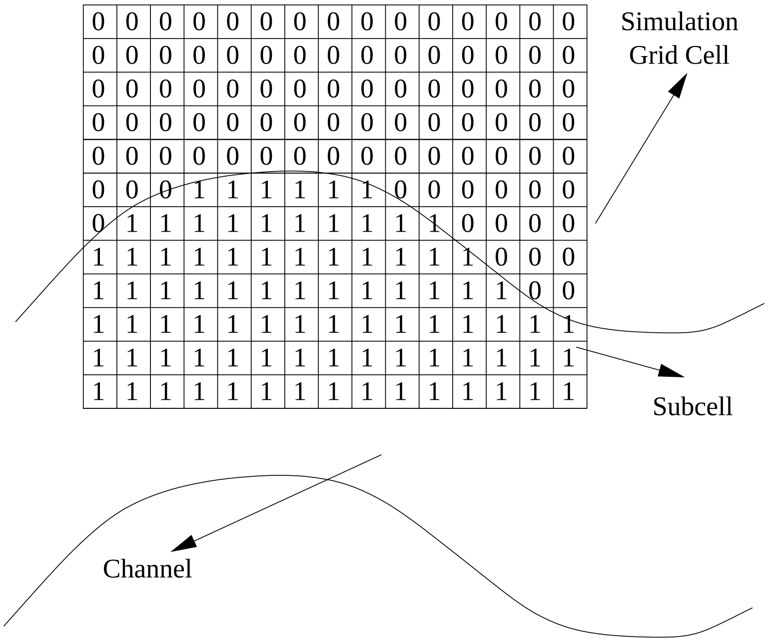

0	0	0	0	0	0	0	0	0	0	0	0	0	0	0
0	0	0	0	0	0	0	0	0	0	0	0	0	0	0
0	0	0	0	0	0	0	0	0	0	0	0	0	0	0
0	0	0	0	0	0	0	0	0	0	0	0	0	0	0
0	0	0	0	0	0	0	0	0	0	0	0	0	0	0
0	0	0	1	1	1	1	1	1	0	0	0	0	0	0
0	1	1	1	1	1	1	1	1	1	1	0	0	0	0
1	1	1	1	1	1	1	1	1	1	1	1	0	0	0
1	1	1	1	1	1	1	1	1	1	1	1	1	0	0
1	1	1	1	1	1	1	1	1	1	1	1	1	1	1
1	1	1	1	1	1	1	1	1	1	1	1	1	1	1
1	1	1	1	1	1	1	1	1	1	1	1	1	1	1

Figure 4.14: Subcell method.

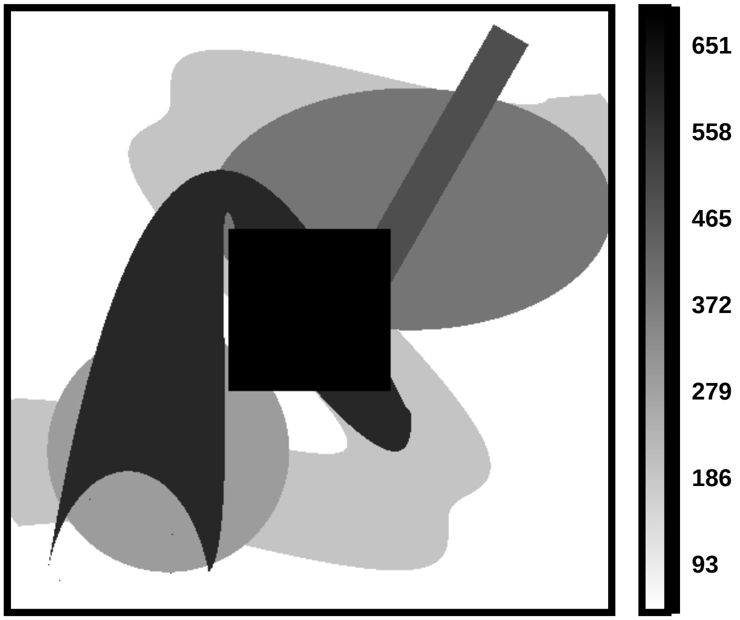

Figure 4.15: True complex geological model.

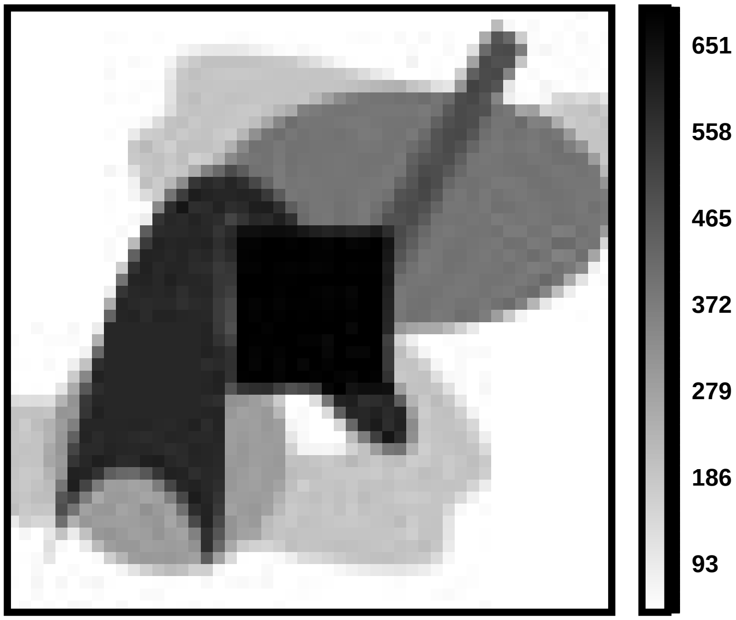

Figure 4.16: subcell representation of complex geological model - unweighted area sampling technique.

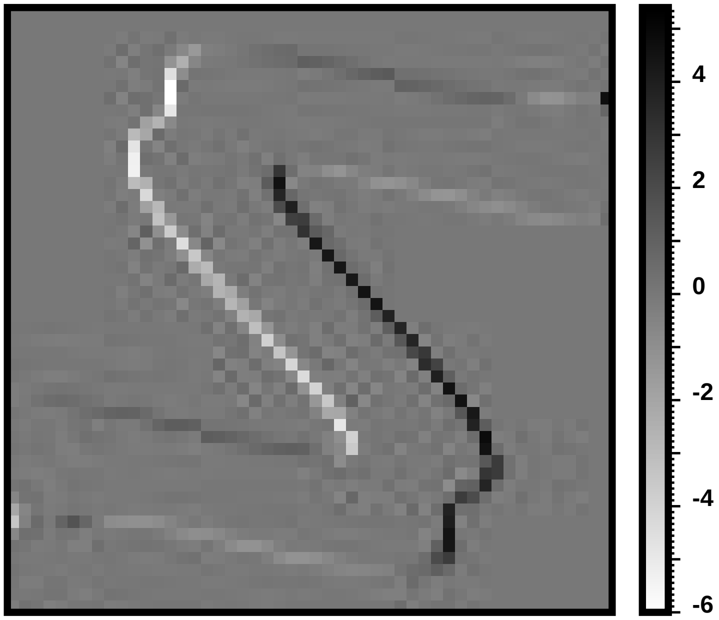

Figure 4.17: Gradient of permeability field with respect to the channel translation in x-direction.

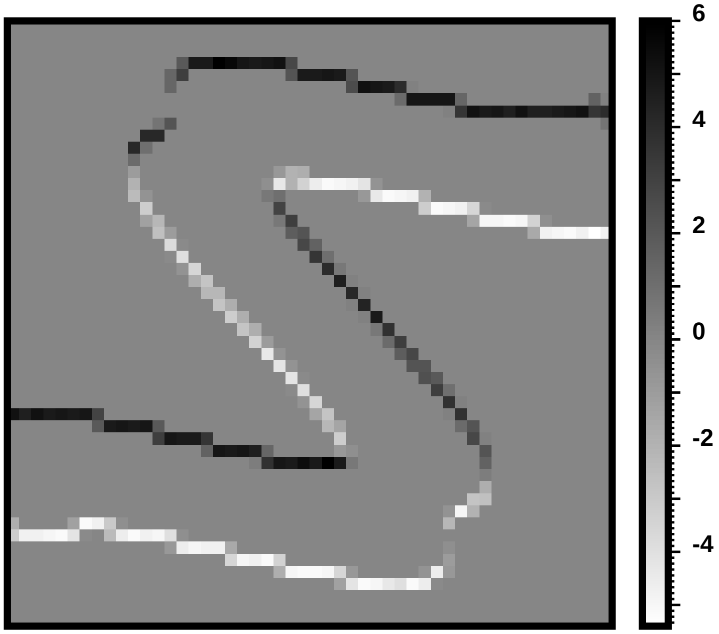

Figure 4.18: Gradient of permeability field with respect to the channel translation in y-direction.

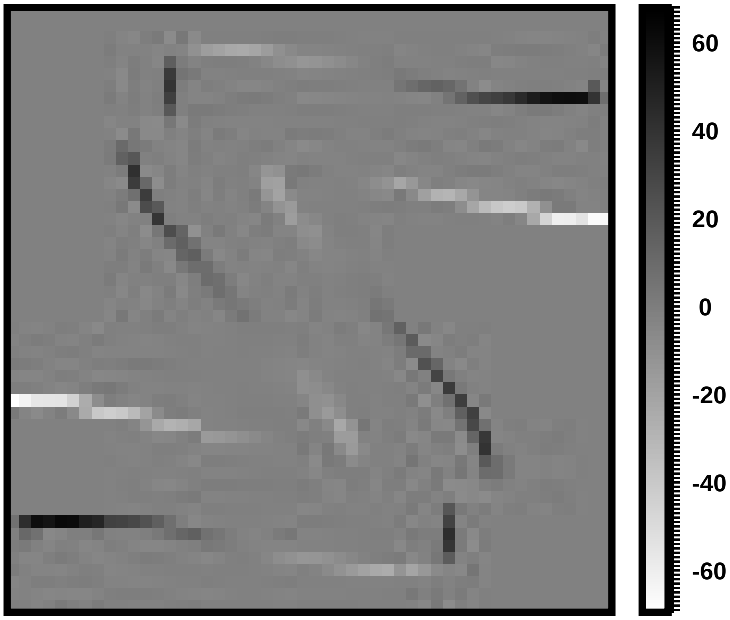

Figure 4.19: Gradient of permeability field with respect to the channel rotation.

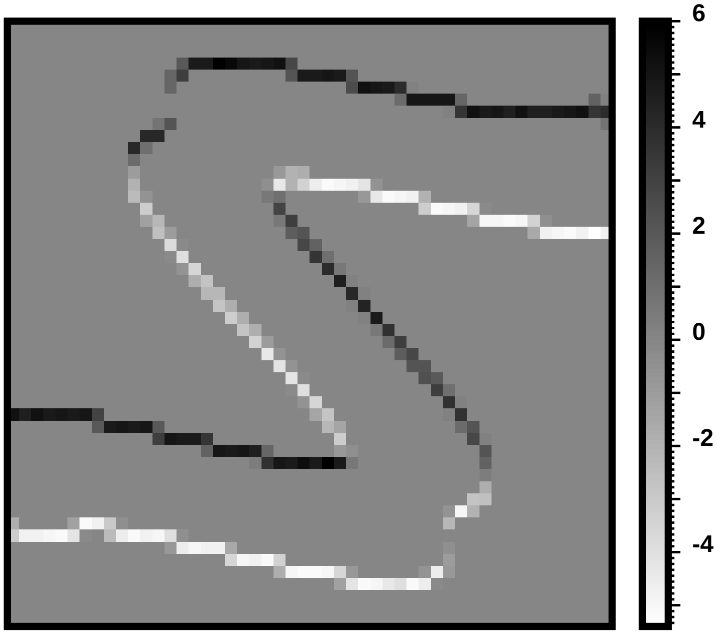

Figure 4.20: Gradient of permeability field with respect to the channel departure.

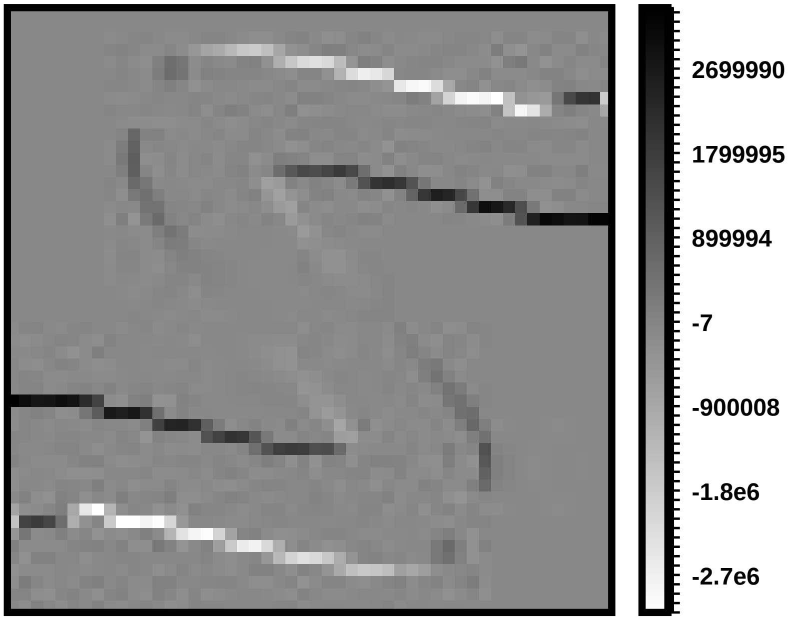

Figure 4.21: Gradient of permeability field with respect to channel sinuosity.

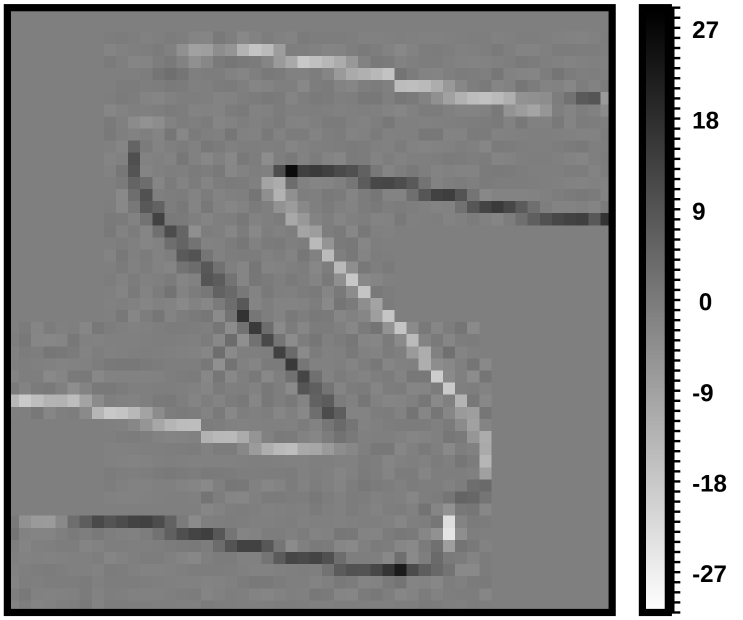

Figure 4.22: Gradient of permeability field with respect to channel displacements.

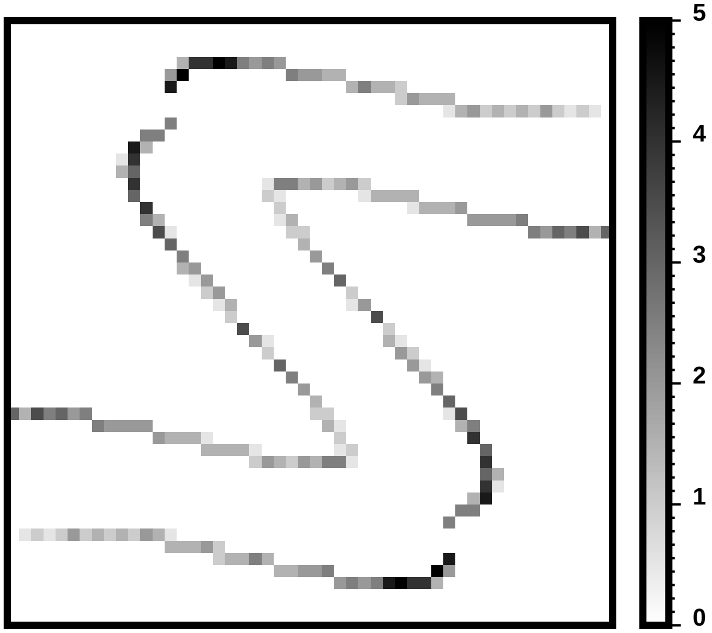

Figure 4.23: Gradient of permeability field with respect to channel width.

Figure 4.24: Gradient of permeability field with respect to channel length - zero gradient field for channel length greater than the reservoir size.

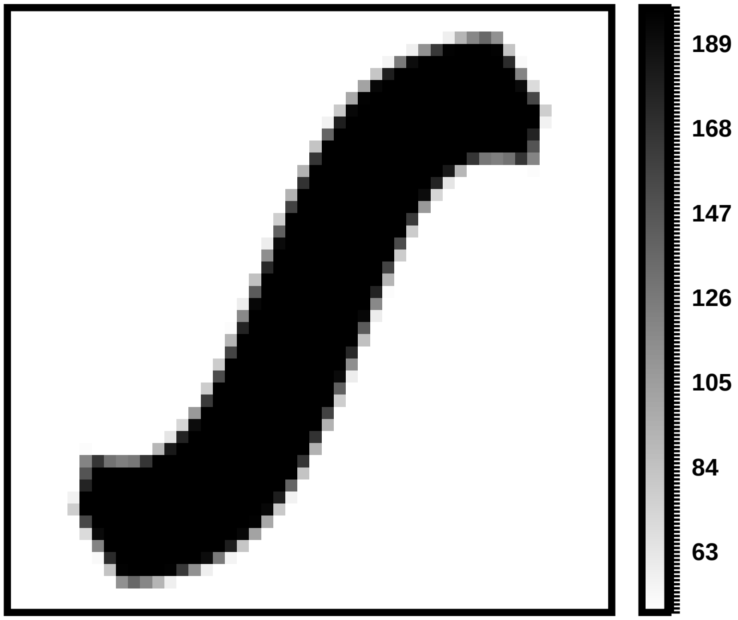

Figure 4.25: Discrete permeability field.

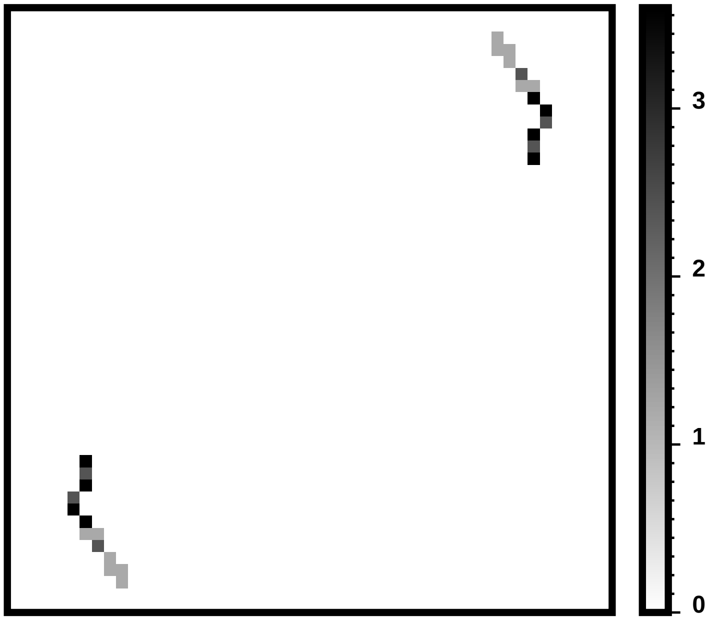

Figure 4.26: Gradient of permeability field with respect to channel length.

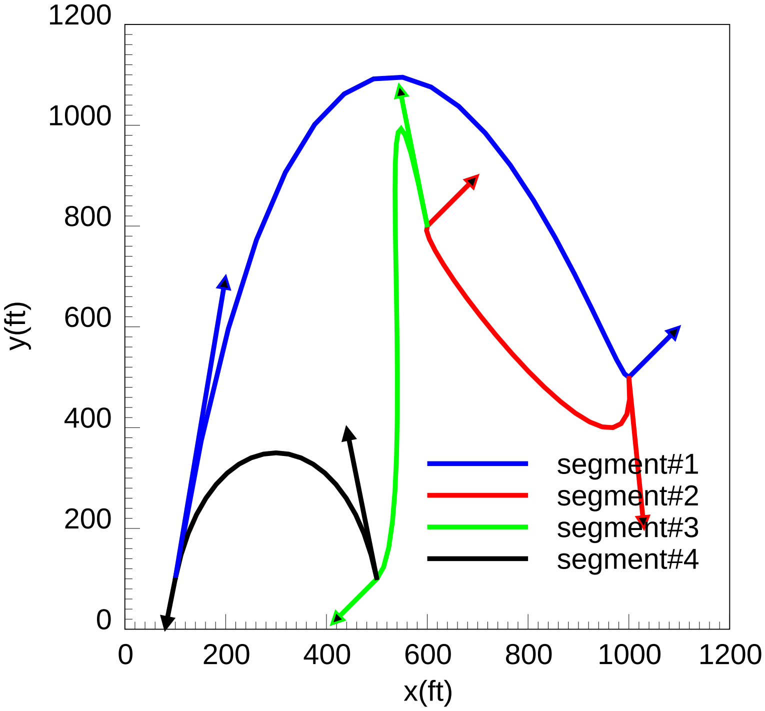

Figure 4.27: Parametric representation of irregular object.

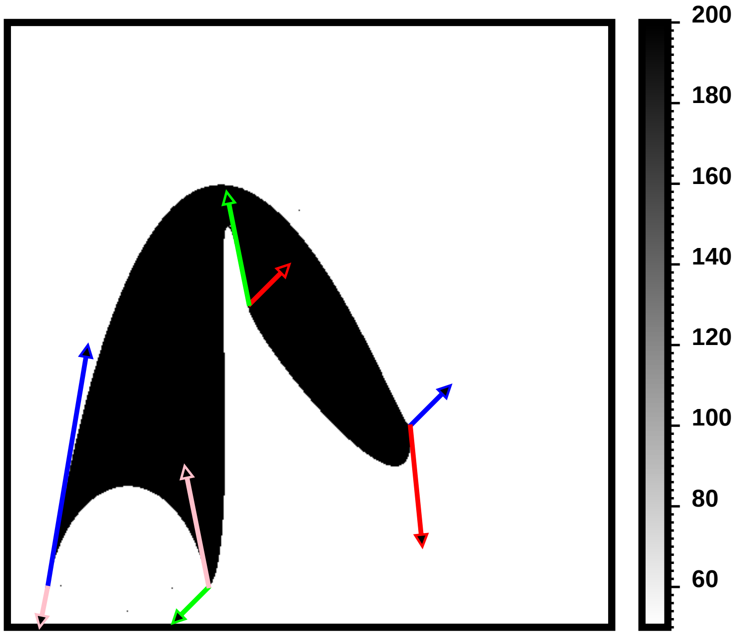

Figure 4.28: The continuous permeability distribution of irregular object.

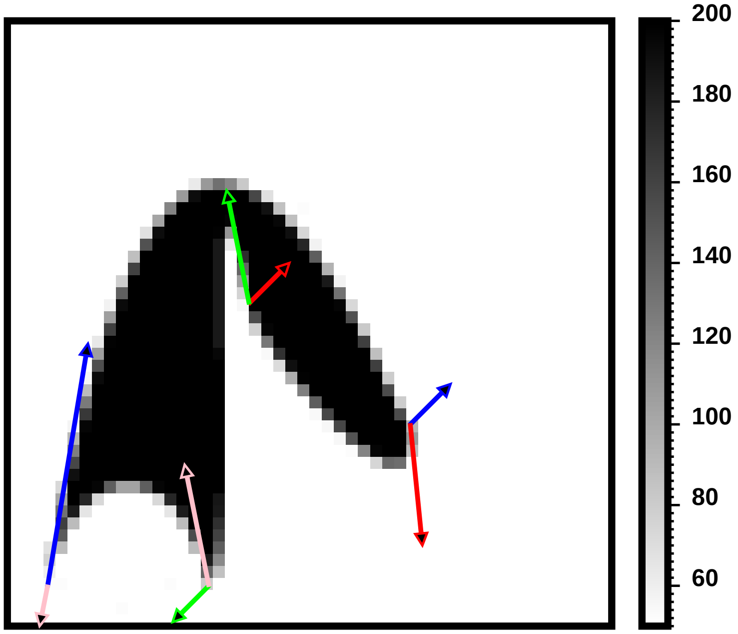

Figure 4.29: The discrete permeability distribution of irregular object.

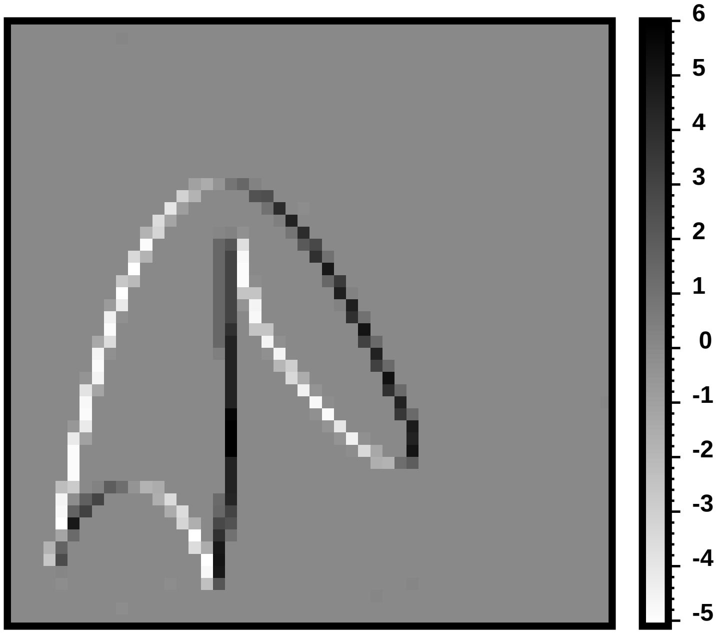

Figure 4.30: Gradient of permeability field with respect to translation in x-direction: irregular object.

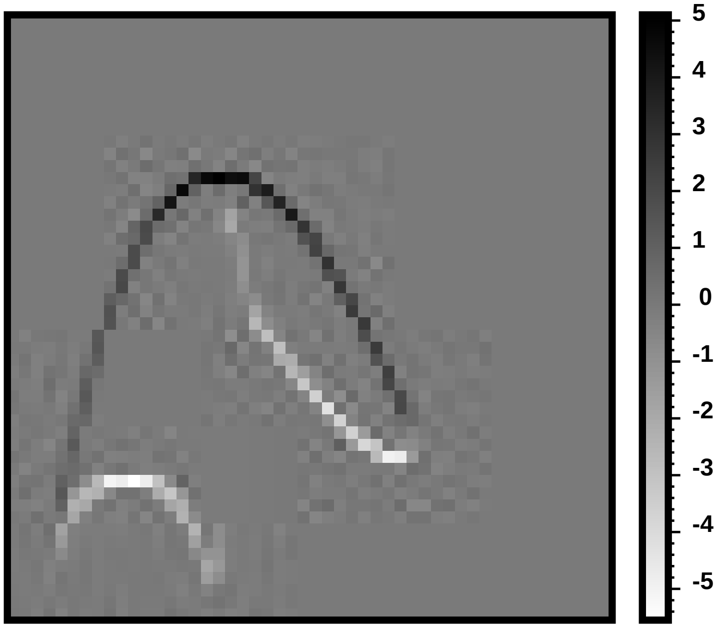

Figure 4.31: Gradient of permeability field with respect to translation in y-direction: irregular object.

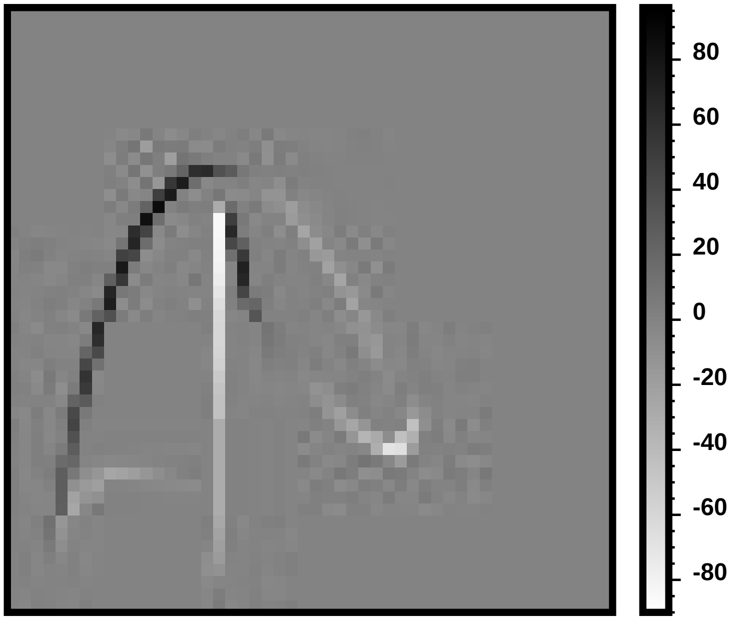

Figure 4.32: Gradient of permeability field with respect to rotation: irregular object.

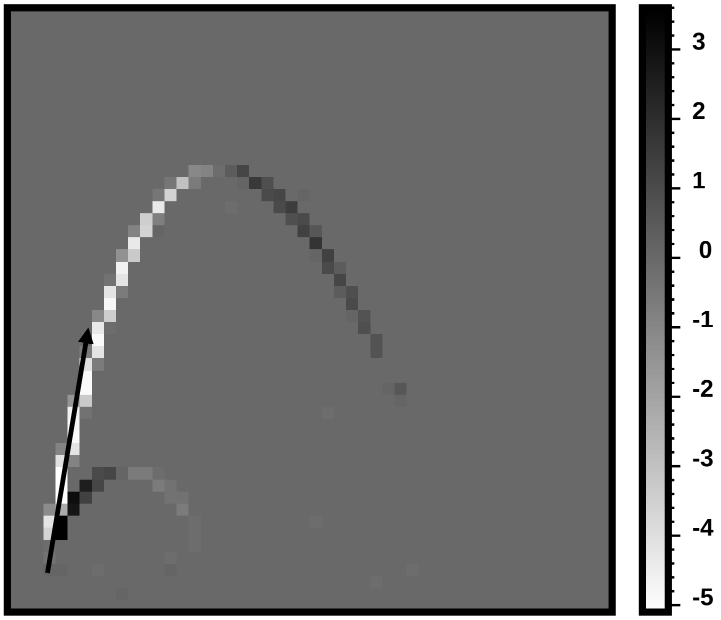

Figure 4.33: Gradient of permeability field with respect to $x(0)$ of the first segment: irregular object.

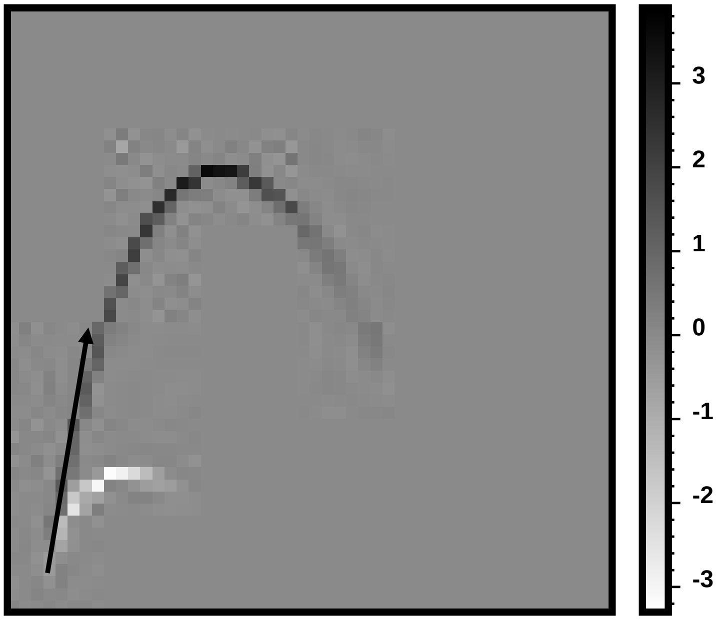

Figure 4.34: Gradient of permeability field with respect to $y(0)$ of the first segment: irregular object.

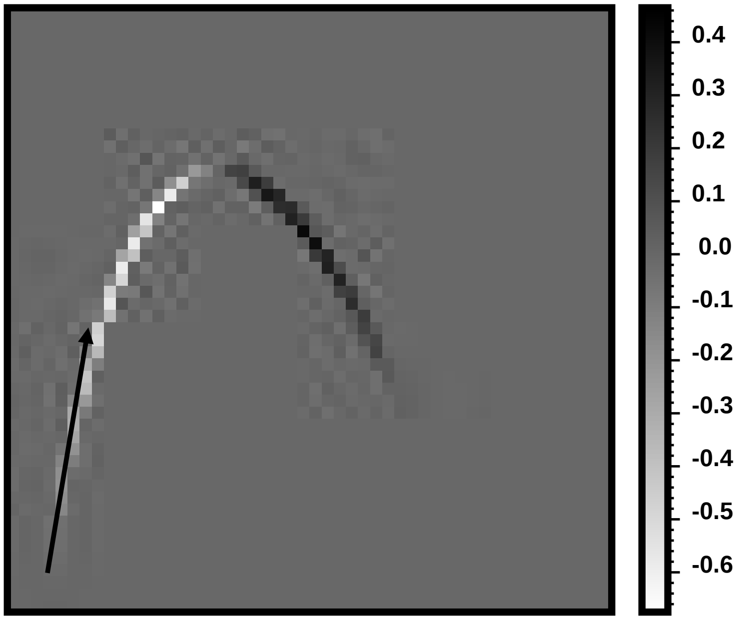

Figure 4.35: Gradient of permeability field with respect to $x'(0)$ of the first segment: irregular object.

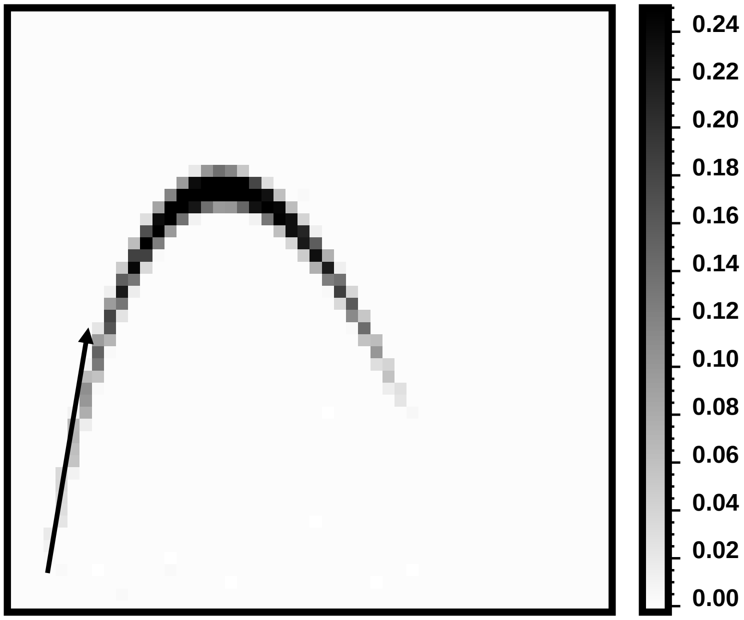

Figure 4.36: Gradient of permeability field with respect to $y'(0)$ of the first segment: irregular object.

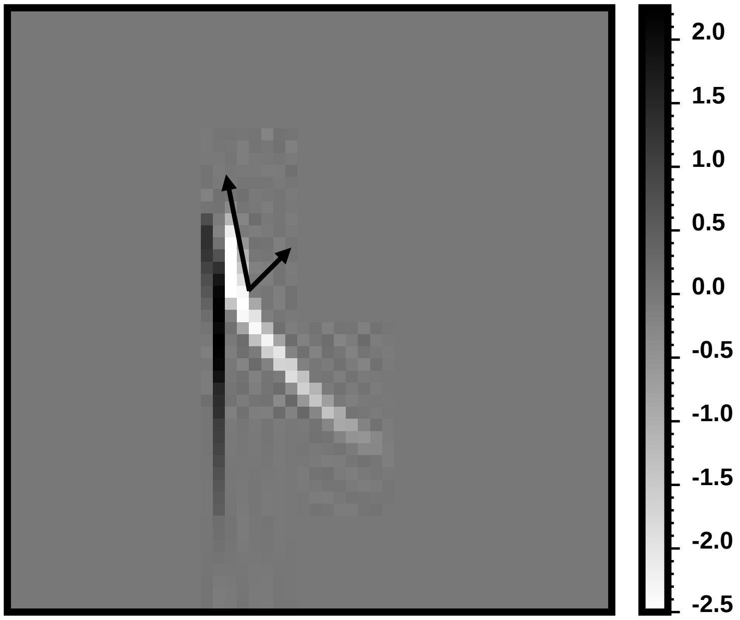

Figure 4.37: Gradient of permeability field with respect to $x(0)$ of the third segment: irregular object.

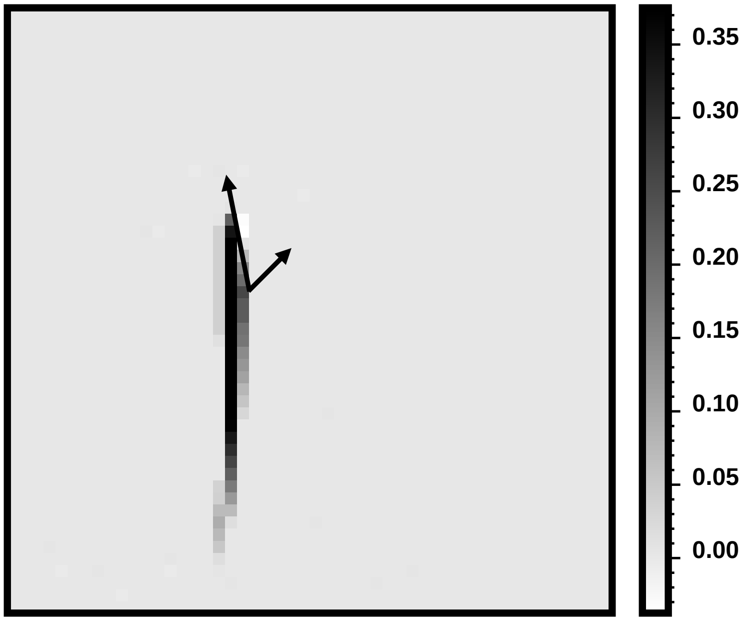

Figure 4.38: Gradient of permeability field with respect to $x'(0)$ of the third segment: irregular object.

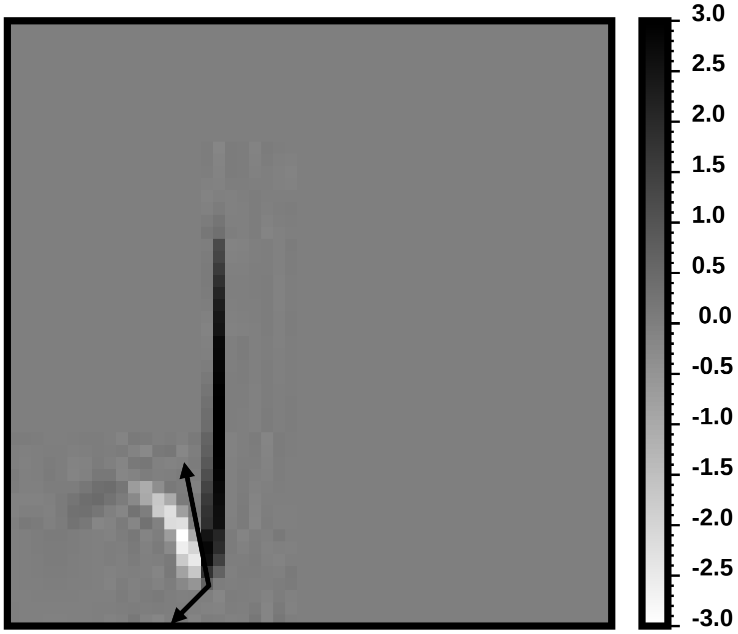

Figure 4.39: Gradient of permeability field with respect to $x(0)$ of the fourth segment: irregular object.

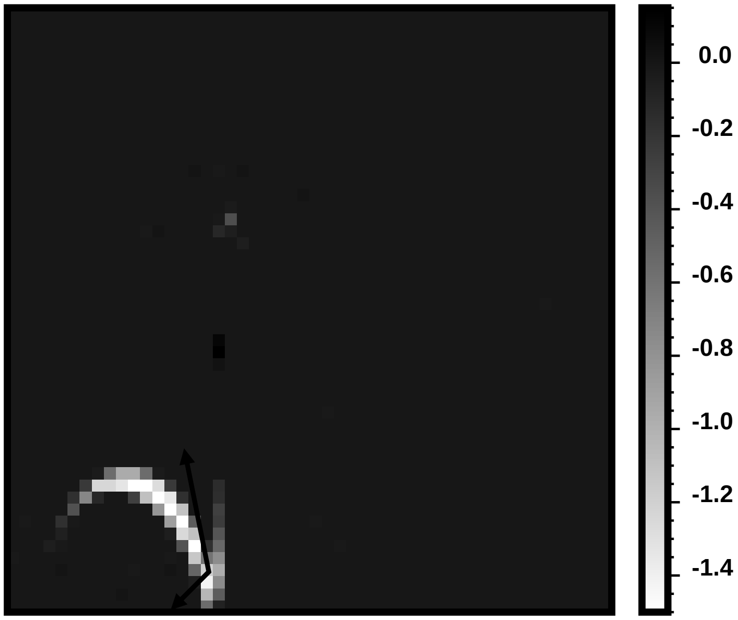

Figure 4.40: Gradient of permeability field with respect to $y(0)$ of the fourth segment: irregular object.

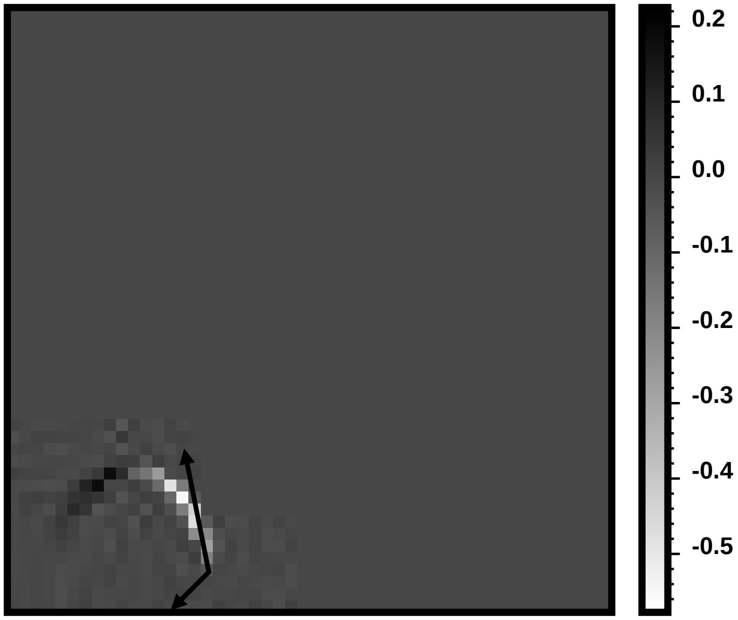

Figure 4.41: Gradient of permeability field with respect to $x'(0)$ of the fourth segment: irregular object.

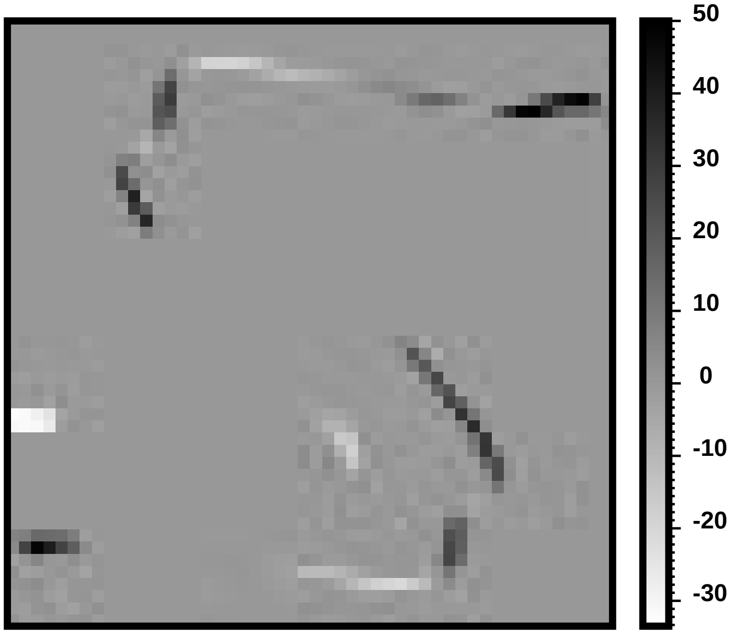

Figure 4.42: Gradient of permeability field with respect to the channel rotation: multiple objects.

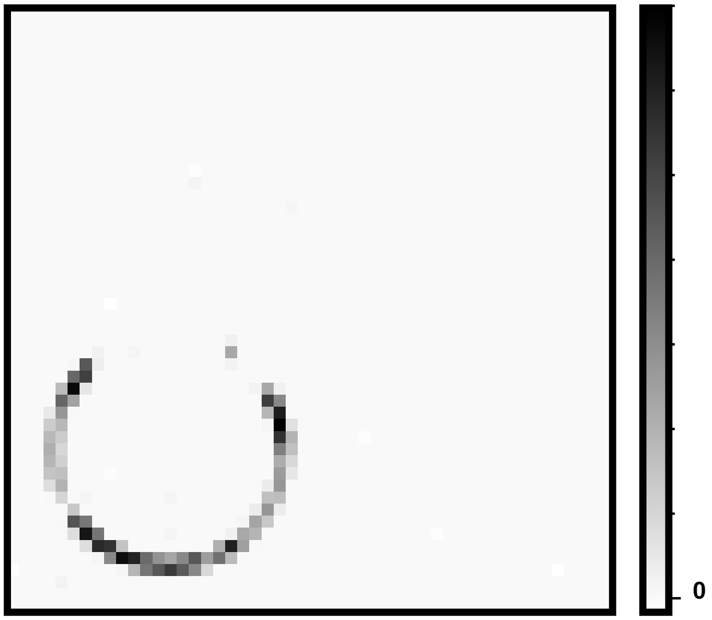

Figure 4.43: Gradient of permeability field with respect to the circle radius: multiple objects.

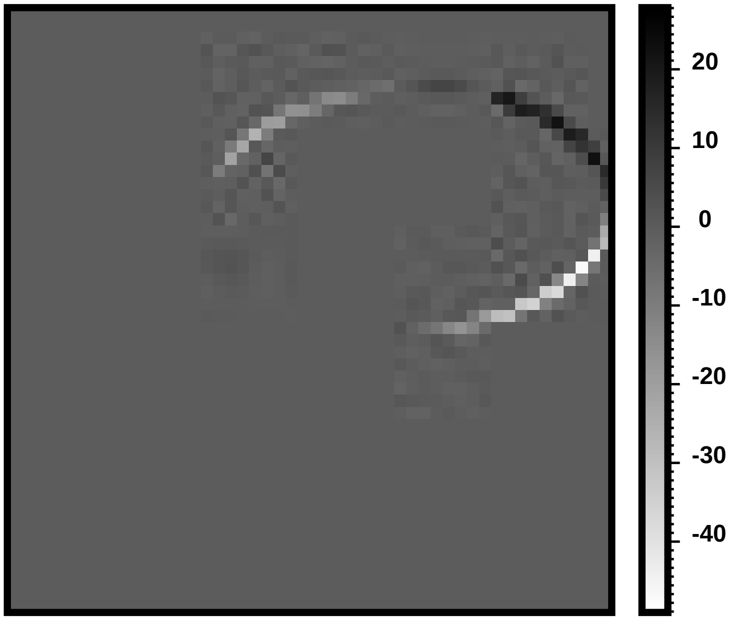

Figure 4.44: Gradient of permeability field with respect to the ellipse rotation: multiple objects.

Figure 4.45: Gradient of permeability field with respect to the ellipse semimajor axis: multiple objects.

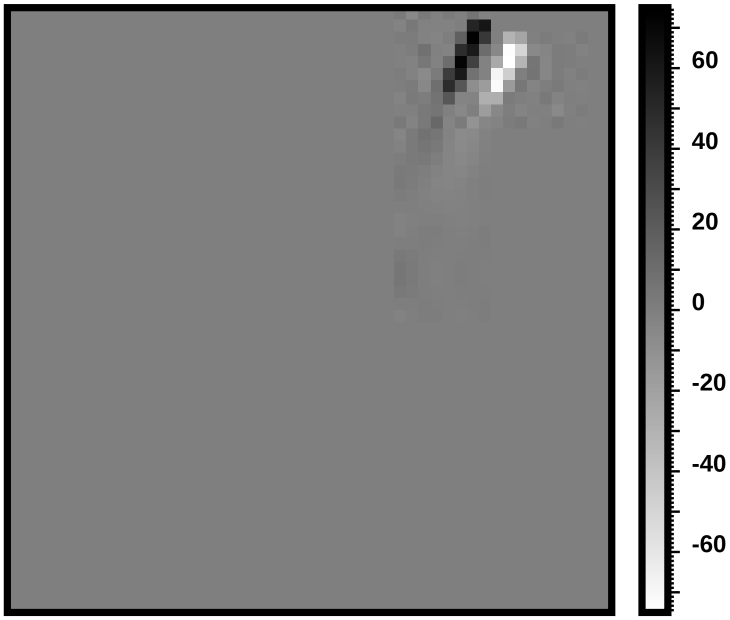

Figure 4.46: Gradient of permeability field with respect to the fault rotation: multiple objects.

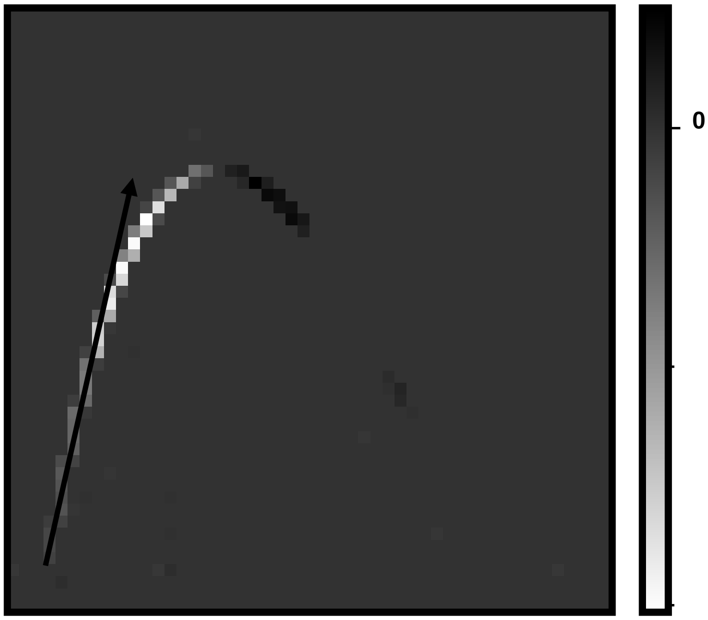

Figure 4.47: Gradient of permeability field with respect to the slope of the irregular object: multiple objects.

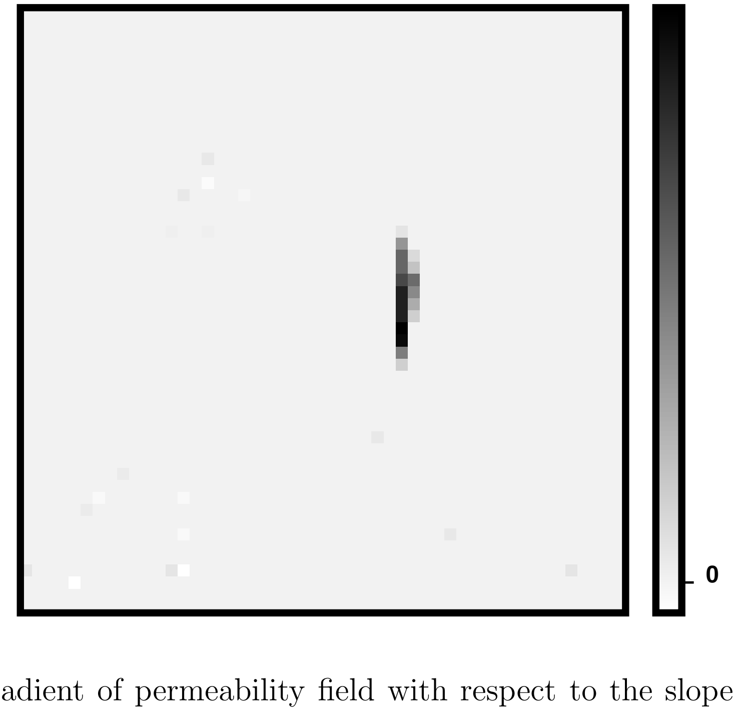

Figure 4.48: Gradient of permeability field with respect to the slope of the square: multiple objects.

Chapter 5

Sensitivity Coefficients

The set of parameters for inversion, as was discussed in Chapter 2, consists of two subsets of parameters. A subset of geometric parameters describes the position, size, and shape of geological bodies present in the reservoir and a subset of petrophysical parameters defines permeability and porosity distribution within each object. These two subsets could either be random or deterministic variables. To be efficient, a gradient-based technique was employed for the minimization algorithm and this requires the derivative calculations of numerical simulation results with respect to the matching parameters. The gradients with respect to grid cell permeabilities and porosities which appear explicitly in the discrete equations of state may be calculated by substitution method or by using the so-called adjoint-state recursive equations (see Landa 1997, or Phan 1998). The substitution method is simple and easy to implement, however its obvious drawback is in requiring many function evaluations, which is expensive from the computational point of view. This drawback is emphasized in cases where the number of parameters is large or as in our case where the function evaluation involves both flow and stochastic simulations. The adjoint-state method, on the other hand, has been shown to be efficient since it requires only one function evaluation to calculate all sensitivity coefficients with respect to grid cell permeabilities and porosities. In the case of geometric parameters, the sensitivity calculations become much more complex as the matching parameters are not found in the model discrete equations and thus the sensitivity coefficients can not be determined directly from the flow equations. Recent works (Landa, 1997 and Landa and Horne, 1997) have handled this problem by defining geological objects using mathematical formulas and then using these fomulas to calculate the gradients of grid cell permeabilities with respect to the channel parameters. To maintain continuity of the *objective* function with respect to the matching geometric parameters, the authors assigned to each simulation grid cell a permeability value proportional to the fraction of the cell overlapped by the objects. Landa and Horne also proposed a modified version of the original adjoint-state equations that allows direct calculation of sensitivity coefficients with respect to channel parameters, avoiding the calculations of the sensitivities with respect to all grid cell permeabilities and porosities. All sensitivity coefficients with repect to channel parameters are calculated by solving a matrix problem of $npar$ right-hand sides at every time step in the forward solution procedure. Unlike Landa and Horne (1997), Bi, Oliver, and Reynolds (1999) generated sensitivity coefficients with respect to channel parameters by first calculating the sensitivities with respect to all grid cell permeabilities and porosities by using the procedure developed by He, Reynolds, and Oliver (1997) which requires $nw + 1$ runs of the reservoir simulator where nw is the number of wells. These results are then inserted into analytical formulas to compute the sensitivity of pressure to the channel parameters. The technique developed by He *et al.* is restricted to single-phase flow and cases in which the pressure gradient along the wellbore is negligible. Phan (1998) has shown that neglecting these gradients can sometimes cause a significant underestimation of the sensitivity coefficients and therefore, degrades the rate of convergence. Another limitation that makes the technique unattractive for practical problems is that it requires $nw + 1$ simulation runs which is very time consuming if the number of wells nw is large. Previous works have developed various formulas for sensitivity coefficients with respect to the geometric parameters that are not found in the discrete model equations. However, generalizing these solutions to complex geological models remains difficult.

In this chapter, we shall describe another useful application of the subcell technique to the calculation of sensitivity coefficients. In a sense, this work extends some key earlier applications of the adjoint-state equations developed by Landa and Horne (1997) to a more general problem of conditioning deterministic/stochastic channels to both static and dynamic data. The subcell technique allows the formulas for sensitivity coefficients to be unrestrictedly applied to any number of geological objects with arbitrary geometric shapes. Since the algorithm for sensitivity calculations is embedded in the forward solution procedure, it is important first to summarize the forward solution technique.

5.1 Forward Solution Technique

Let us first define the following terms:

- $\tilde{y}$ denotes the forward solution of a set of discrete flow equations. This solution vector is composed of pressures and saturations in all grid blocks and the reference pressures at all specified rate wells.

$$\tilde{y} = \begin{bmatrix} \tilde{p} \\ \tilde{s}_w \\ \tilde{p}_{ref} \end{bmatrix} = \begin{bmatrix} p_1 \\ s_{w_1} \\ p_2 \\ s_{w_2} \\ . \\ . \\ . \\ p_{nb} \\ s_{w_{nb}} \\ p_{ref_1} \\ p_{ref_2} \\ . \\ . \\ . \\ p_{ref_{nw}} \end{bmatrix} \tag{5.1}$$

where nx, ny, and nz are the number of blocks respectively in x, y, and z directions. $nb = nx\,ny\,nz$ is the total number of gridblocks nw is the number of specified rate wells. $\tilde{p}$ and $\tilde{s}_w$ are respectively the pressures and water saturations at all gridblocks. $\tilde{p}_{ref}$ are the well pressures at reference layers.

- $\tilde{d}$ denotes the dynamic response of the model correspondent to any dynamic data set such as production and interpreted 4-D seismic data.

$$\tilde{d} = \tilde{d}(\tilde{y}, \tilde{\mathbf{k}}(\tilde{\mathbf{u}}), \tilde{\phi}(\tilde{\mathbf{u}}), \tilde{s}) = \begin{bmatrix} \tilde{p}_{wf} \\ \tilde{w}_{ct} \\ \Delta\tilde{s}_w \end{bmatrix} \tag{5.2}$$

where $\tilde{p}_{wf}$ is downhole pressure at the tool depth. $\tilde{w}_{ct}$ is water cut and $\Delta\tilde{s}_w$ is the change in water saturations. The dynamic response $\tilde{d}$ is a function of the forward solution vector $\tilde{y}$, the discrete permeability field $\tilde{\mathbf{k}}(\tilde{\mathbf{u}})$, the discrete porosity field $\tilde{\phi}(\tilde{\mathbf{u}})$, and the set of well skin factors $\tilde{s}$.

Discretizing the forward partial differential equations as described in Equations 2.37 to 2.40 in space and time, we obtain a set of residual flow equations that are used to determine the solution of the forward flow problem:

$$\tilde{R}(\tilde{\mathbf{k}}(\tilde{\mathbf{u}}), \tilde{\phi}(\tilde{\mathbf{u}}), \tilde{s}, \tilde{y}^{(n)}, \tilde{y}^{(n+1)}, \tilde{\mathbf{u}}) = 0 \tag{5.3}$$

where $\tilde{R}$ is a set of residuals in all gridblocks, including well constraints. $\tilde{\mathbf{u}}$ is a set of discrete locations. $\tilde{y} = \tilde{y}(\tilde{\mathbf{k}}(\tilde{\mathbf{u}}), \tilde{\phi}(\tilde{\mathbf{u}}), \tilde{s}, \tilde{\mathbf{u}}, t)$ is a vector solution at discrete locations $\tilde{\mathbf{u}}$ and time t and depends on the discrete permeability field $\tilde{\mathbf{k}}(\tilde{\mathbf{u}})$, the discrete porosity field $\tilde{\phi}(\tilde{\mathbf{u}})$, and the set of well skin factors $\tilde{s}$. $\tilde{y}^{(n)}$ and $\tilde{y}^{(n+1)}$ are respectively vector solutions at time step n and $(n+1)$. Since Equation 5.3 is nonlinear with respect to $\tilde{y}^{(n)}$ and $\tilde{y}^{(n+1)}$, given the solution at time step n, the solution at time step $(n+1)$ can only be solved by iteration such as by the Newton-Raphson method.

$$\mathbf{J}^{n+1}\delta\tilde{y}^{(n+1)} = \frac{\partial\tilde{R}}{\partial\tilde{y}^{(n+1)}}\delta\tilde{y}^{(n+1)} = -\tilde{R}(\tilde{\mathbf{k}}(\tilde{\mathbf{u}}), \tilde{\phi}(\tilde{\mathbf{u}}), \tilde{s}, \tilde{y}^{(n)}, \tilde{y}^{(n+1)}, \tilde{\mathbf{u}}) \tag{5.4}$$

where $\mathbf{J}^{n+1} = \frac{\partial\tilde{R}}{\partial\tilde{y}^{(n+1)}}$ is the *Jacobian* matrix of $\tilde{R}$ determined at $\tilde{y}^{(n+1)}$. The Newton-Raphson algorithm can be summarized as:

1. Set $\tilde{y}^{(n+1)} = \tilde{y}^{(n)}$ as an initial guess for the new time step.
2. Compute the residual vector $\tilde{R}$ at $\tilde{y}^{(n+1)}$.
3. Compute the Jacobian matrix $\mathbf{J}$ at $\tilde{y}^{(n+1)}$.
4. Solve Equation 5.4 for $\delta\tilde{y}^{(n+1)}$
5. If converged, then replace $n+1$ by n and go to Step 1.
6. Update the new $\tilde{y}^{(n+1)}$ by:

   $$\tilde{y}^{(n+1)} = \tilde{y}^{(n+1)} + \delta\tilde{y}^{(n+1)}$$

7. Go to Step 2.

By iterating forward in time, the entire vector solution $\tilde{y}$ can be obtained and hence the response of the model $\tilde{d} = \tilde{d}(\tilde{y}, \tilde{\mathbf{k}}(\tilde{\mathbf{u}}), \tilde{\phi}(\tilde{\mathbf{u}}), \tilde{s})$ is also determined. If the permeability or porosity at certain gridblock, or the well skin factor at certain well is perturbed to a new value and Equation 5.3 is solved for the new forward solution. If this process is repeated until all unknown permeabilities, porosities, or well skin factors at all wells are perturbed, the sensitivity coefficients can be approximated by a finite difference method. This is the basic idea of the substitution method that will be discussed in detail next.

5.2 Substitution Method

In this work, since the discrete permeability and porosity at every gridblock are not independent variables but rather are functions of the matching parameters $\vec{\alpha}$

$$\begin{aligned} \tilde{\mathbf{k}}(\tilde{\mathbf{u}}) &= \tilde{\mathbf{k}}(\vec{\alpha}) \\ \tilde{\phi}(\tilde{\mathbf{u}}) &= \tilde{\phi}(\vec{\alpha}) \end{aligned} \tag{5.5}$$

and if the unknown well skin factors $\tilde{s}$ are also included in the matching parameter $\vec{\alpha}$, the dynamic response given in Equation 5.2 becomes a function of the forward flow solution $\tilde{y}$ and the matching parameters $\vec{\alpha}$

$$\tilde{d} = \tilde{d}(\tilde{y}, \vec{\alpha}) \tag{5.6}$$

The purpose is to compute the sensitivity matrix **G** defined as:

$$\mathbf{G} = \frac{\partial \tilde{d}}{\partial \vec{\alpha}} \tag{5.7}$$

The first-order approximation to $\tilde{d}$ in terms of $\vec{\alpha}$ by Taylor series is:

$$\tilde{d}(\tilde{y}, \vec{\alpha} + \delta\vec{\alpha}) \approx \tilde{d}(\tilde{y}, \vec{\alpha}) + \frac{\partial \tilde{d}}{\partial \vec{\alpha}}\delta\vec{\alpha} \tag{5.8}$$

Thus, the matrix **G** can be approximated as:

$$\mathbf{G} = \frac{\partial \tilde{d}}{\partial \vec{\alpha}} \approx \frac{\tilde{d}(\tilde{y}, \vec{\alpha} + \delta\vec{\alpha}) - \tilde{d}(\tilde{y}, \vec{\alpha})}{\delta\vec{\alpha}} = \frac{\Delta\tilde{d}}{\Delta\vec{\alpha}} \tag{5.9}$$

or for the element (i, j) of the sensitivity matrix

$$G_{i,j} = \frac{\Delta d_i}{\Delta \alpha_j} \tag{5.10}$$

The algorithm of the substitution method implemented in this work is as follows:

1. Set $\vec{\alpha} = \vec{\alpha}_0$ at which the sensitivity is computed.
2. Compute the gridblock permeabilities and porosities using Equation 5.5.
3. Solve Equation 5.3 for $\tilde{y}_0 = \tilde{y}(\vec{\alpha}_0, t)$,
4. Compute $\tilde{d}_0 = \tilde{d}(\tilde{y}_0, \vec{\alpha}_0)$.
5. For $j = 1 \rightarrow npar$:

   Perturb $\alpha_j = \alpha_j + \delta\alpha_j$. Where $\delta\alpha_j$ is a fraction of α_j; $\delta\alpha_j = \mathbf{F}\,\alpha_j$. **F** is a positive number prespecified based on types of data and parameters (typically 10^{-7}). The new $\vec{\alpha}$ becomes $\vec{\alpha}_j = (\alpha_1.\alpha_2, ...\alpha_{j-1}, \alpha_j + \delta\alpha_j, \alpha_{j+1}, ...\alpha_{npar})$.

   Compute the gridblock permeabilities and porosities at $\vec{\alpha}_j$ using Equation 5.5.

   Solve Equation 5.3 for $\tilde{y}_j = \tilde{y}(\vec{\alpha}_j, t)$,

   Compute $\tilde{d}_j = \tilde{d}(\tilde{y}_j, \vec{\alpha}_j)$.

   Compute column j^{th} of **G** as $G_j = \frac{\tilde{d}_j - \tilde{d}_0}{\delta\alpha_j}$.

6. End.

Although this method is straightforward and very easy to implement, it requires $npar + 1$ simulation runs which is very expensive in terms of computational work when the number of parameters $npar$ is large. A far more efficient method to compute sensitivity coefficients is by embedding the algorithm to compute the full sensitivity matrix inside the forward solution procedure as will be shown in the next section.

5.3 Analytical Method

The matrix of sensitivity coefficients **G** can be computed through another matrix, the so-called full sensitivity matrix denoted by **S** which can be calculated recursively as described in this section.

5.3.1 Full Sensitivity Matrix

The purpose is to compute the full sensitivity matrix **S** defined as the gradients of the forward solution vector $\tilde{y}$ with respect to all parameters

$$\mathbf{S} = \frac{\partial \tilde{y}}{\partial \vec{\alpha}} \tag{5.11}$$

In this work, this matrix was computed in a manner similar to that of Landa and Horne (1997). The size of the vector solution $\tilde{y}$ is the same as the number of unknown variables in the forward flow problem, that is the total of pressures and saturations in all gridblocks and the number of specified rate wells:

$$size = 2nb + nw \tag{5.12}$$

where nb and nw are the number of gridblocks and specified rate wells respectively. Therefore, the size of the full sensitivity matrix **S** is ($size$ x $npar$). Since the gridblock permeabilities and porosities are functions of parameters, Equation 5.3 becomes

$$\tilde{R}(\vec{\alpha}, \tilde{y}^{(n)}, \tilde{y}^{(n+1)}) = 0 \tag{5.13}$$

Approximating this residual flow equation by first-order Taylor series expansions with respect to $\vec{\alpha}$, $\tilde{y}^{(n)}$, and $\tilde{y}^{(n+1)}$ gives:

$$\begin{aligned}\tilde{R}(\vec{\alpha}+\delta\vec{\alpha},\tilde{y}^{(n)}+\delta\tilde{y}^{(n)},\tilde{y}^{(n+1)}+\delta\tilde{y}^{(n+1)}) = \tilde{R}(\vec{\alpha},\tilde{y}^{(n)},\tilde{y}^{(n+1)}) +& \\ \frac{\partial\tilde{R}}{\partial\vec{\alpha}}\delta\vec{\alpha}+\frac{\partial\tilde{R}}{\partial\tilde{y}^{(n)}}\delta\tilde{y}^{(n)}+\frac{\partial\tilde{R}}{\partial\tilde{y}^{(n+1)}}\delta\tilde{y}^{(n+1)}&\end{aligned} \tag{5.14}$$

However,

$$\tilde{R}(\vec{\alpha}+\delta\vec{\alpha},\tilde{y}^{(n)}+\delta\tilde{y}^{(n)},\tilde{y}^{(n+1)}+\delta\tilde{y}^{(n+1)}) = \tilde{R}(\vec{\alpha},\tilde{y}^{(n)},\tilde{y}^{(n+1)}) = \vec{0} \tag{5.15}$$

thus,

$$\frac{\partial\tilde{R}}{\partial\vec{\alpha}}\delta\vec{\alpha}+\frac{\partial\tilde{R}}{\partial\tilde{y}^{(n)}}\delta\tilde{y}^{(n)}+\frac{\partial\tilde{R}}{\partial\tilde{y}^{(n+1)}}\delta\tilde{y}^{(n+1)} = \vec{0} \tag{5.16}$$

Dividing both sides of Equation 5.16 by $\delta\vec{\alpha}$ gives:

$$\frac{\partial\tilde{R}}{\partial\vec{\alpha}}+\frac{\partial\tilde{R}}{\partial\tilde{y}^{(n)}}\frac{\delta\tilde{y}^{(n)}}{\delta\vec{\alpha}}+\frac{\partial\tilde{R}}{\partial\tilde{y}^{(n+1)}}\frac{\delta\tilde{y}^{(n+1)}}{\delta\vec{\alpha}} = \vec{0} \tag{5.17}$$

which becomes, by rearranging:

$$\frac{\partial\tilde{R}}{\partial\tilde{y}^{(n+1)}}\frac{\delta\tilde{y}^{(n+1)}}{\delta\vec{\alpha}} = -\frac{\partial\tilde{R}}{\partial\tilde{y}^{(n)}}\frac{\delta\tilde{y}^{(n)}}{\delta\vec{\alpha}}-\frac{\partial\tilde{R}}{\partial\vec{\alpha}} \tag{5.18}$$

Combining the Equation 5.18 to Equation 5.11 and denoting the Jacobian matrix as $\mathbf{J}$ give:

$$\mathbf{J}^{(n+1)}\mathbf{S}^{(n+1)} = -\mathbf{J}^{(n)}\mathbf{S}^{(n)}-\mathbf{J}_{\alpha} \tag{5.19}$$

where $\mathbf{S}^{(n)}$ and $\mathbf{S}^{(n+1)}$ are full sensitivity matrices at time step n and $(n+1)$ and are given by:

$$\mathbf{S}^{(n)} = \frac{\partial\tilde{y}^{(n)}}{\partial\vec{\alpha}} \tag{5.20}$$

$$\mathbf{S}^{(n+1)} = \frac{\partial\tilde{y}^{(n+1)}}{\partial\vec{\alpha}} \tag{5.21}$$

and $\mathbf{J}^{(n+1)}$ and $\mathbf{J}^{(n)}$ are the Jacobian matrices with respect to $\tilde{y}^{(n)}$ and $\tilde{y}^{(n+1)}$ respectively and given by:

$$\mathbf{J}^{(n)} = \frac{\partial\tilde{R}}{\partial\tilde{y}^{(n)}} \tag{5.22}$$

$$\mathbf{J}^{(n+1)} = \frac{\partial \tilde{R}}{\partial \tilde{y}^{(n+1)}} \tag{5.23}$$

$$\mathbf{J}_\alpha = \frac{\partial \tilde{R}}{\partial \vec{\alpha}} \tag{5.24}$$

The matrix equation 5.19 is called the *adjoint-state* recursive equations and used to compute the full sensitivity matrix $\mathbf{S}$ as function of time. From this equation, given $\mathbf{S}^{(n)}$, to compute $\mathbf{S}^{(n+1)}$ we need to compute the three matrices $\mathbf{J}^{(n+1)}$, $\mathbf{J}^{(n)}$, and $\mathbf{J}_\alpha$. $\mathbf{J}^{(n+1)}$ is the Jacobian matrix and is already computed in the forward solution procedure (Equation 5.4). $\mathbf{J}^{(n)}$ is computed by differentiating the residual flow equations with respect to the solution at old time step, $\tilde{y}^{(n)}$. $\mathbf{J}_\alpha$ is computed by differentiating the residual flow equations with respect to the parameters. Detailed calculations of the first two matrices, $\mathbf{J}^{(n+1)}$ and $\mathbf{J}^{(n)}$, can be found in Phan (1998). The calculation of $\mathbf{J}_\alpha$ where the parameters $\vec{\alpha}$ are gridblock permeabilities and porosities can also be found in Phan (1998) and the calculation of $\mathbf{J}_\alpha$ where the parameters $\vec{\alpha}$ are geometric parameters will be discussed later.

Overall, $\mathbf{S}^{(n+1)}$ is computed by columns. If $S_i; i = 1 \rightarrow npar$ denotes column i of matrix $\mathbf{S}$, Equation 5.18 is equivalent to $npar$ systems of linear equations:

$$\frac{\partial \tilde{R}}{\partial \tilde{y}^{(n+1)}} S_i^{(n+1)} = -\frac{\partial \tilde{R}}{\partial \tilde{y}^{(n)}} S_i^{(n)} - \frac{\partial \tilde{R}}{\partial \alpha_i}; \quad i = 1 \rightarrow npar \tag{5.25}$$

To compute the full sensitivity matrix $\mathbf{S}$, it is necessary to solve Equation 5.25 $npar$ times. As was mentioned at the beginning of this section, our final interest is to compute the sensitivity of the responses corresponding to the observed data with respect to the parameters of the inverse problem. These sensitivities can be computed from the full sensitivity matrix $\mathbf{S}$ as will be explained next.

5.3.2 Sensitivity Coefficients

By knowing the full sensitivity matrix $\mathbf{S}$, the matrix of sensitivity coefficients $\mathbf{G}$ can be computed by differentiating the model response $\tilde{d}_m = \tilde{d}(\tilde{y}, \vec{\alpha})$

$$\mathbf{G} = \frac{\partial \tilde{d}_m}{\partial \vec{\alpha}} = \frac{\partial \tilde{d}}{\partial \tilde{y}} \frac{\partial \tilde{y}}{\partial \vec{\alpha}} + \frac{\partial \tilde{d}}{\partial \vec{\alpha}} = \frac{\partial \tilde{d}}{\partial \tilde{y}} \mathbf{S} + \frac{\partial \tilde{d}}{\partial \vec{\alpha}} \tag{5.26}$$

where **S** is the full sensitivity matrix and is computed from the adjoint-state equation 5.19. The two matrices $\frac{\partial \tilde{d}}{\partial \tilde{y}}$ and $\frac{\partial \tilde{d}}{\partial \vec{\alpha}}$ depend on the particular set of dynamic data in the inverse problem. The set of data for the parameter estimation problem in this work consists of:

1. Bottom-hole pressure history measured at all wells (denoted by $\tilde{p}_{wf}$).
2. Water cut history from all wells (denoted by $\tilde{w}_{ct}$).
3. 4-D seismic data interpreted as the change in water saturation distribution over the reservoir between two given instants (denoted by $\Delta\tilde{s}_w$).

The model response correspondent to this dynamic data set is given as

$$\tilde{d}_m = \begin{bmatrix} \tilde{p}_{wf} \\ \tilde{w}_{ct} \\ \Delta\tilde{s}_w \end{bmatrix} \tag{5.27}$$

and the forward solution vector $\tilde{y}$ given in Equation 5.1 is rewritten here as

$$\tilde{y} = \begin{bmatrix} \tilde{p} \\ \tilde{s}_w \\ \tilde{p}_{ref} \end{bmatrix} \tag{5.28}$$

Therefore,

$$\mathbf{G} = \frac{\partial \tilde{d}_m}{\partial \vec{\alpha}} = \begin{bmatrix} \frac{\partial \tilde{p}_{wf}}{\partial \vec{\alpha}} \\ \frac{\partial \tilde{w}_{ct}}{\partial \vec{\alpha}} \\ \frac{\partial \Delta\tilde{s}_w}{\partial \vec{\alpha}} \end{bmatrix} \tag{5.29}$$

$$\mathbf{S} = \frac{\partial \tilde{y}}{\partial \vec{\alpha}} = \begin{bmatrix} \frac{\partial \tilde{p}}{\partial \vec{\alpha}} \\ \frac{\partial \tilde{s}_w}{\partial \vec{\alpha}} \\ \frac{\partial \tilde{p}_{ref}}{\partial \vec{\alpha}} \end{bmatrix} \tag{5.30}$$

From Equation 5.29, computing the sensitivity matrix **G** is equivalent to computing the three matrices $\frac{\partial \tilde{p}_{wf}}{\partial \vec{\alpha}}$, $\frac{\partial \tilde{w}_{ct}}{\partial \vec{\alpha}}$, and $\frac{\partial \Delta\tilde{s}_w}{\partial \vec{\alpha}}$. The last one is obtained directly from the full sensitivity matrix **S**:

$$\frac{\partial \Delta\tilde{s}_w}{\partial \vec{\alpha}} = \left.\frac{\partial \tilde{s}_w}{\partial \vec{\alpha}}\right|_{t2} - \left.\frac{\partial \tilde{s}_w}{\partial \vec{\alpha}}\right|_{t1} \tag{5.31}$$

where $t1$ and $t2$ are the two given instants in time at which 3-D seismic information is collected to infer the time-lapse (4-D) seismic signal. The first two matrices can not be obtained easily from the full sensitivity matrix and the computation of these matrices emphasizes the difference in the level of difficulty between two-dimensional and three-dimensional problems. In two-dimensional problems, each vertical well is completed within one single gridblock and the pressure along the wellbore of horizontal wells are constant. The derivatives of the wellbore pressure with respect to the parameters can be derived directly from the derivatives of the wellblock pressure and saturation by differentiating the well constraint equations. This is not true for three-dimensional problems. Particularly when wells are completed over several layers, the derivatives of wellbore pressure and water cut with respect to the parameters becomes extremely complicated. Bi, Oliver, and Reynolds (1999) and He, Reynolds, and Oliver (1997) simplified the derivative calculations by assuming a zero pressure gradient along the wellbore. This assumption can sometimes cause, as stated by the authors and shown by Phan (1998), a significant underestimation of the sensitivity coefficients and therefore degrades the rate of convergence. In the case of three-dimensional problems, the layer flow rate is parameter dependent. Moreover, the pressure gradient varies along the wellbore and is a function of pressure and saturation in all connecting wellblocks and thus the derivatives of the wellbore pressure with respect to the parameters can no longer be derived directly from the derivatives of the wellblock pressure in the well constraint equations. Similarly, the water cut is no longer just a simple function of mobility ratio as is the case in single-layer problems but is a complex function of mobility ratios, pressure, and saturation in all layers. Thus, the derivative of water cut with respect to the parameters requires the derivatives of mobility, pressure, and saturation in each layer penetrated by the wells. The derivations of a complete set of formulas for computing pressure gradient and its derivative along the wellbore and the derivatives of wellbore pressure and water cut with respect to parameters in a two-phase and three-dimensional problem are extremely lengthy and algebraically complex. Detailed derivations of these formulas can be found in Phan (1998).

5.4 Hybrid Method

In this section, we introduce a *hybrid* method in which the gradients of the gridblock permeabilties and porosities with respect to the geometric parameters are computed numerically and the sensitivity coefficients are then generated making use of the adjoint-state equation. The matrix $\mathbf{J}_\alpha$ in the adjoint-state equation 5.19 can be computed using the chain rules as follows:

$$\mathbf{J}_\alpha = \left.\frac{\partial \tilde{R}}{\partial \vec{\alpha}}\right|_{\tilde{y}^{(n)},\tilde{y}^{(n+1)}} = \frac{\partial \tilde{R}}{\partial \tilde{\mathbf{k}}}\frac{\partial \tilde{\mathbf{k}}}{\partial \vec{\alpha}} + \frac{\partial \tilde{R}}{\partial \tilde{\phi}}\frac{\partial \tilde{\phi}}{\partial \vec{\alpha}} + \frac{\partial \tilde{R}}{\partial \tilde{s}}\frac{\partial \tilde{s}}{\partial \vec{\alpha}} \tag{5.32}$$

where detailed calculations of the matrices $\frac{\partial \tilde{R}}{\partial \tilde{\mathbf{k}}}$, $\frac{\partial \tilde{R}}{\partial \tilde{\phi}}$, and $\frac{\partial \tilde{R}}{\partial \tilde{s}}$ can be found in Phan (1998). Since unknown well skin factors, $\tilde{s}$, are considered to be parameters, the elements of matrix $\frac{\partial \tilde{s}}{\partial \vec{\alpha}}$ are given by

$$\left.\frac{\partial \tilde{s}}{\partial \vec{\alpha}}\right|_{ij} = \frac{\partial s_i}{\partial \alpha_j} = \begin{cases} 1; & \alpha_j = s_i \\ 0: & \text{otherwise} \end{cases} \tag{5.33}$$

The two matrices $\frac{\partial \tilde{\mathbf{k}}}{\partial \vec{\alpha}}$ and $\frac{\partial \tilde{\phi}}{\partial \vec{\alpha}}$ are the gradients of the gridblock permeabilities and porosities with respect to the geometric parameters and can be computed numerically as was shown in Chapter 4.

5.5 Implementation

In this section we present some of the fundamental ideas and comments on how to implement the calculations of sensitivity coefficients using the formulas developed in the previous sections in a computationally efficient way. It is important to note that the static gradients of the gridblock permeabilities and porosities with respect to the geometric parameters depend on how to convert a continuous nature of the object boundary to a discrete distributions of permeability and porosity in the discrete domain of the simulation mesh grid. This conversion between the continuous and the discrete spatial domains depends on how the permeability and porosity are defined in gridblocks intersected by the object boundaries. As was shown in Chapter 2, most gradients of gridblock properties with respect to the geometric parameters are zeros and thus there is no need to compute these derivatives. Only the gradients in the gridblocks along the object boundaries are nonzero and need to be computed. This enhances computationally efficiency. Additional enhancement is also achieved by considering the element (i, j) of the matrix $\mathbf{J}_\alpha$ given in Equation 5.32.

$$(\mathbf{J}_\alpha)_{i,j} = \sum_{p=1}^{nb} \left(\frac{\partial R_i}{\partial \mathbf{k}_p} \frac{\partial \mathbf{k}_p}{\partial \alpha_j} + \frac{\partial R_i}{\partial \phi_p} \frac{\partial \phi_p}{\partial \alpha_j} + \frac{\partial R_i}{\partial s_p} \frac{\partial s_p}{\partial \alpha_j} \right) \tag{5.34}$$

This equation indicates that we need to compute $\frac{\partial R_i}{\partial \mathbf{k}_p}$ if and only if $\frac{\partial \mathbf{k}_p}{\partial \alpha_j} \neq 0$ and we need to compute $\frac{\partial R_i}{\partial \phi_p}$ if and only if $\frac{\partial \phi_p}{\partial \alpha_j} \neq 0$. However, since $\frac{\partial \mathbf{k}_p}{\partial \alpha_j}$ and $\frac{\partial \phi_p}{\partial \alpha_j}$ are nonzero only in the cells along the boundaries, we need to compute $\frac{\partial R_i}{\partial \mathbf{k}_p}$ and $\frac{\partial R_i}{\partial \phi_p}$ also only at the cells along the boundaries. By avoiding the unnecessary computations, the computational efficiency is further enhanced.

5.5.1 Linear Solver

Calculating the sensitivity coefficients using the adjoint-state recursive equation 5.19 requires, at the end of each time step of the forward problem, the solution of a matrix problem of the type:

$$\mathbf{J}\mathbf{X} = \mathbf{B} \tag{5.35}$$

where the solution matrix $\mathbf{X}$ and the right hand-side matrix $\mathbf{B}$ are of size $m \times npar$. $\mathbf{J}$ is the $m \times m$ jacobian matrix built at the end of the time step when the Newton-Raphson algorithm converges.

$$\mathbf{J}\vec{x} = \vec{b} \tag{5.36}$$

In general, methods for solving a system of linear equations depend on the size of the matrix and the machine memory. Iterative methods become preferable when the system is large or the memory is limited while direct methods have distinct advantages when the system is relatively small or has many right-hand sides. In cases where the computer memory is limited or the size of the forward problem is large, an iterative solver is used by the numerical simulator to solve the system represented by Equation 5.36. If an iterative solver is also used for each right-hand side of the Equation 5.35, then it is clear that this may not be an efficient approach because it does not take advantage of the fact that the matrix $\mathbf{J}$ on the left-hand side is fixed during the sequential solution process. A better approach would be to implement the iterative solver on a parallel processor computer.

The optimal strategy for solving the multiple right-hand side problem can be analyzed quantitatively by considering the computation time. Let us define the following terms:

t_{lu}: CPU time required to perform LU decomposition.

t_s: CPU time required to perform both back and forward substitutions for each right-hand side.

t_i: CPU time required to solve for each right-hand side using iterative solver.

k: The number of right-hand sides ($= npar$).

t_{lu}, t_s, and t_i depend on the size of the forward problem. The CPU time required to solve a matrix problem of k right-hand sides can be approximated as:

By direct LU solver:

$$t_{dir} = t_{lu} + kt_s \tag{5.37}$$

By iterative solver:

$$t_{iter} = kt_i \tag{5.38}$$

Since the computational efficiency is defined as the inverse of the CPU time, the comparison of the two methods is given by the ratio

$$\frac{\text{efficiency of iterative solver}}{\text{efficiency of direct solver}} = \frac{\frac{1}{t_{iter}}}{\frac{1}{t_{dir}}} = \frac{t_{dir}}{t_{iter}} = \frac{t_{lu} + kt_s}{kt_i} = \frac{\frac{t_{lu}}{k} + t_s}{t_i} \tag{5.39}$$

From this equation, as the number of right-hand sides k decreases, the ratio increases and iterative solver becomes more efficient. The smallest efficiency ratio between the iterative and direct solvers, t_s/t_i, is achieved as the number of parameters approaches infinity. If $t_s/t_i > 1$, the iterative solver always indicates an optimal choice regardless of the number of right-hand sides. However, for most algorithms $t_s/t_i \leq 1$, so the optimal choice of methods depends on the number of right-hand sides as depicted in Figure 5.1.

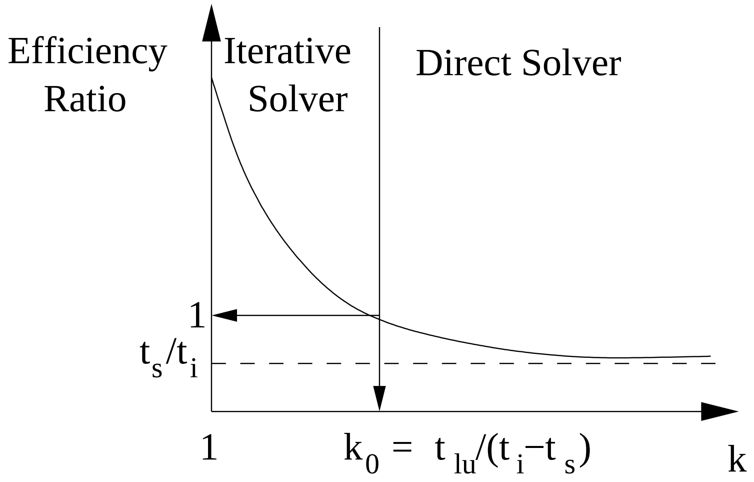

Figure 5.1: Optimal strategy.

The unit efficiency ratio is obtained at $k_0 = t_{lu}/(t_i - t_s)$. At this value, both iterative and direct solvers are computationally equivalent. For the particular problem in this work, a direct sparse matrix solver was used to solve the multiple right hand problem. Since the adjoint-state equation and the forward problem have the same left-hand side matrix, the same direct solver was also used by the numerical simulator for the forward solution technique. As the Newton-Raphson algorithm converges at the end of each time step, the appropriate factors LU produced by the sparse solver is used for the solution of the adjoint-state equation. Solving the multiple right-hand problem requires only back and forward substitutions which are very cheap in terms of computation. The back and forward substitutions require only up to nb^2 flops as compared to an order of nb^3 flops for the LU factorization. The direct sparse matrix solver used in this work was the *Yale Sparse Matrix Solver* in Fortran (see Eisenstat, Schultz, and Sherman, 1997).

5.6 Computational Results

In this work, the sensitivity coefficients with repect to geometric parameters were calculated using a hybrid method described previously in this chapter. In the hybrid method, the subcell technique was used to compute the last term $\mathbf{J}_\alpha$ in the adjoint-state equation 5.19. The correctness and efficiency of the method in calculating sensitivity coefficients was tested and ensured by comparing computational results to the results obtained from the numerical substitution method. To serve this purpose, a numerical experiment was prepared. A three-dimensional, water-oil reservoir was modeled with the object modeling approach where the object in this case was a three-dimensional channel with parameters given in Table 5.1.

Table 5.1: Channel parameters.

Parameters	Values
Channel translation in x-direction(ft)	1250
Channel translation in y-direction(ft)	1250
Channel translation in z-direction(ft)	500
Channel azimuth(deg)	0
Channel dip(deg)	0
Channel plunge(deg)	90
Channel departure(ft)	100
Channel sinuosity(ft^{-1})	0.001
Channel displacement(ft)	0
Channel width(ft)	1000
Channel length(ft)	2000
Channel thickness(ft)	400
Channel porosity(fraction)	0.3
Channel permeability in x-direction(md)	500
Channel permeability in y-direction(md)	500
Channel permeability in z-direction(md)	500
Background porosity(fraction)	0.1
Background permeability in x-direction(md)	100
Background permeability in y-direction(md)	100
Background permeability in z-direction(md)	100

The size of the reservoir was 2500 ft in both x and y areal dimensions and 1000 ft in the vertical z dimension. The top of the reservoir was located at a depth of 8000 ft. The gridded simulation model consisted of 50x50x5 regular grid-blocks each has the size of 50 ft. x 50 ft. 200 ft. Each cell of the simulation mesh was refined into 32 subcells with two subcells in the x dimension, two subcells in the y dimension, and eight subcells in the z dimension. Each subcell is a cube with the length of each side equal to 25 ft. This translates the coarse-scale reservoir model into a fine-scale mesh of 100x100x40 for defining the channel as depicted in Figure 5.2. The top figure presents a three-dimensional view of the channel. The bottom three figures present two-dimensional slices at $x = 50$, $y = 50$, and $z = 20$. There were one injection well (well #1) and two production wells (well #2 and #3) all fully penetrated through the reservoir thickness. Well #1 was positioned at gridblock (1,50) and injected water at a constant rate of 20,000 STB/day. Well #2 penetrated through the channel at gridblock (25,25) and produced at a constant total liquid rate of 15,000 STB/day. Well #3 was positioned at gridblock (50,1) and produced at a constant total liquid rate of 3,000 STB/day. The simulated numerical results covered a period of 1000 days. The volume of the reservoir and the rates of injection and production were set in such a way that allowed the water injection front to reach all the producing wells in a time period of 1000 days. The gradients of simulation gridblock permeabilities with repect to all matching parameters were calculated using the subcell method and the results are shown in Figures 5.3 to 5.14. The observations drawn from these figures are the same as in two-dimensional cases investigated previously in Chapter 4. The gradients vanish everywhere except at the channel boundaries. These computed gradients are required for the sensitivity calculations making use of the adjoint-state equation 5.19. The analysis of the sensitivity was restricted to the pressure and water cut at each of the three wells and to the average change in water saturation between 100 and 800 days. The long term pressure and water cut at the three wells (well #1, #2, and #3) are shown in Figure 5.15, Figure 5.16, and Figure 5.17 respectively. The water front reached well #2 as early as 40 days after well #1 had started water injection. This is because well #2 was located inside the channel and close to the injection well. Well #3 was located outside the channel and far from the injector and had water breakthrough at 640 days. The injection pressure at well #1 dropped rapidly at early time due to a rapid accumulation of water in the well blocks causing an abrupt increase in water mobility. However, since the net injection rate into the reservoir was positive the pressure at all wells increased at late time. The average change in water saturation between 100 and 800 days is depicted in Figure 5.18. Figures 5.19 through 5.98 show the comparison of the sensitivities of pressure and water cut at all three wells and the average change in water saturation between 100 and 800 days with respect to all matching parameters calculated using the hybrid method described previously in this chapter and the substitution method, which was used as a reference. Figure 5.99 shows a plot of the sensitivity of pressure at well #2 with respect to the channel width at three different times. Note that well #2 was positioned at the center of the channel as indicated by a vertical arrow. The x axis represents the channel half-width. The lowest curve represents the sensitivity coefficients at a very early time ($t = 0.01$ days). The middle curve represents the sensitivity coefficients at ($t = 0.5$ days). The uppermost curve represents the sensitivity coefficients at a later time ($t = 10$ days). As expected, as the channel width increases, the pressure is less sensitive to the channel boundary far from the well and at early time only the boundaries close to the well influence the well response. At later times, the well becomes sensitive to the channel boundaries at distance far from the well. The effect of the channel width on the seismic data was also studied by computing the sensitivity of the latter with respect to the former. The results were calculated at various values of the channel width from 100 ft to 2500 ft and shown in Figures 5.100 to 5.102. These maps depict the absolute values of the sensitivities coefficients in logarithmic scale. The color regions indicate where the 4-D seismic data is most sensitive and thus rich in information about the channel width. It is interesting to observe that the most sensitive regions may not always be those inside the channel or the cells along the NE-SW diagonal connecting the injector and producers. As the channel width does not exceed 1500 ft, the most sensitive regions lie close to the NE-SW diagonal connecting the three wells. However, this is not true for widths greater than 1500 ft when sensitive regions are far from the NE-SW diagonal. This could be explained by the observation that for sufficiently large channels the water saturation becomes stabilized rapidly. The observations and concluding remarks drawn from the computational results are summarized as follows:

1. The subcell method calculated the sensitivity coefficients accurately and efficiently.
2. The magnitude of sensitivity of water cut with respect to all parameters increases abruptly after the arrival of water front.
3. The sensitivity coefficients with respect to the channel sinuosity are largest. This is to be expected since a small variation in the frequency results in a large spatial displacement of the channel.

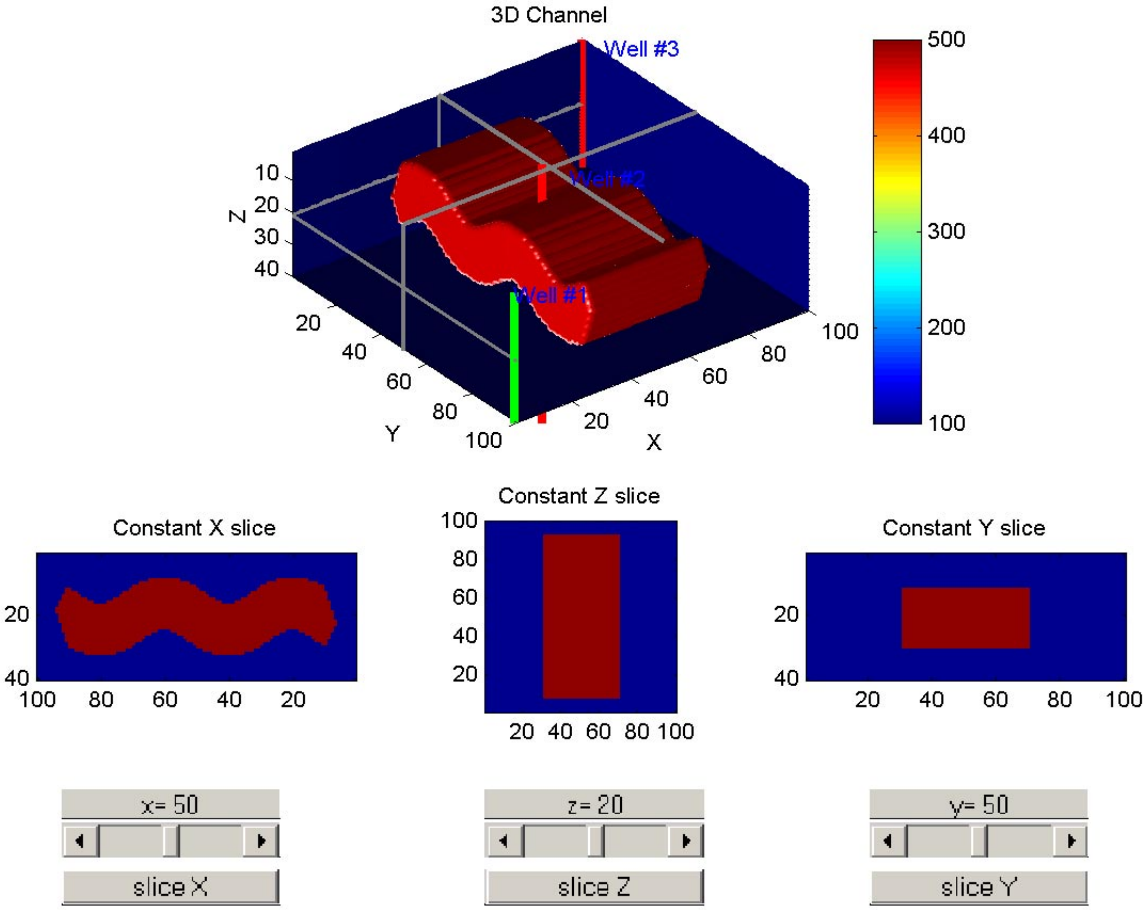

Figure 5.2: Three-dimensional Channel.

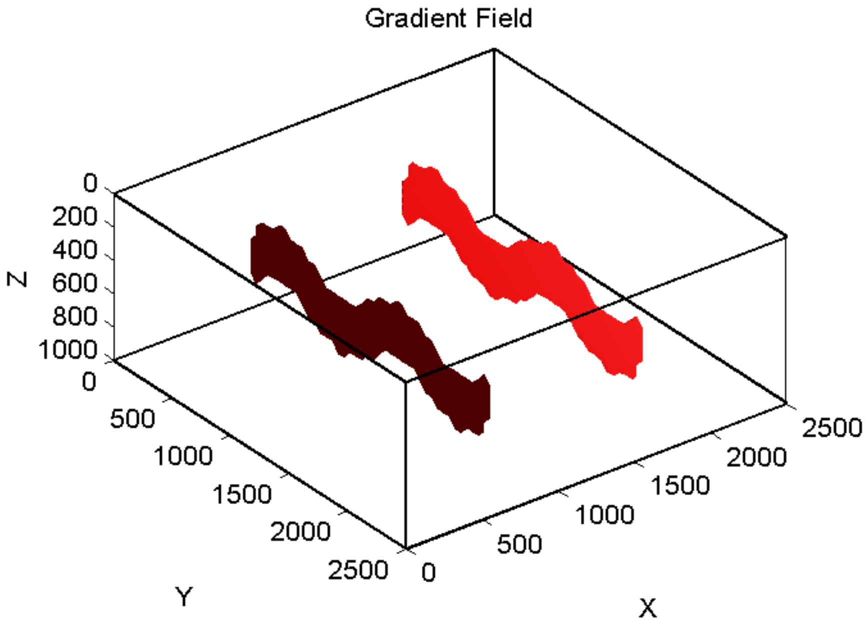

Figure 5.3: Gradient of permeability field with respect to translation in x-direction.

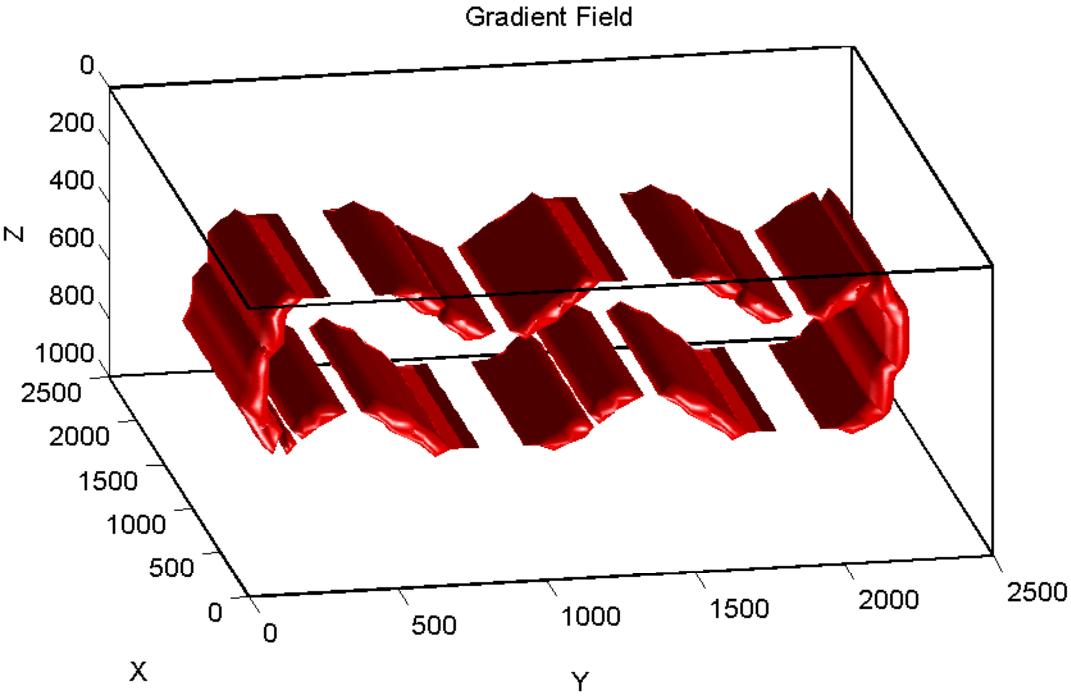

Figure 5.4: Gradient of permeability field with respect to translation in y-direction.

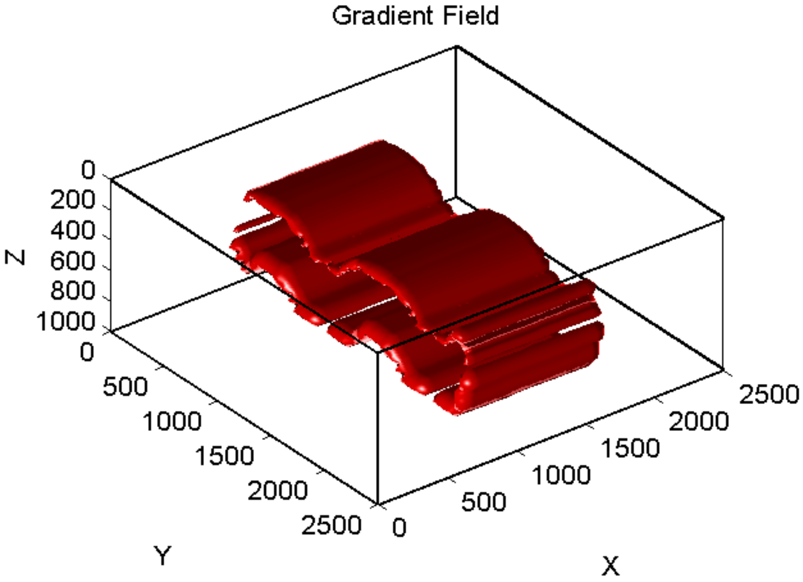

Figure 5.5: Gradient of permeability field with respect to translation in z-direction.

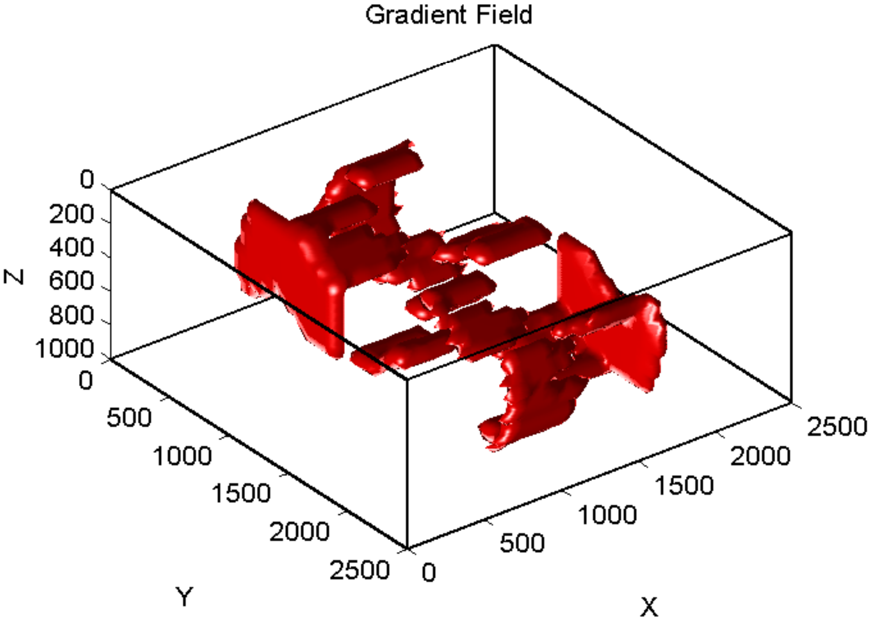

Figure 5.6: Gradient of permeability field with respect to the azimuth.

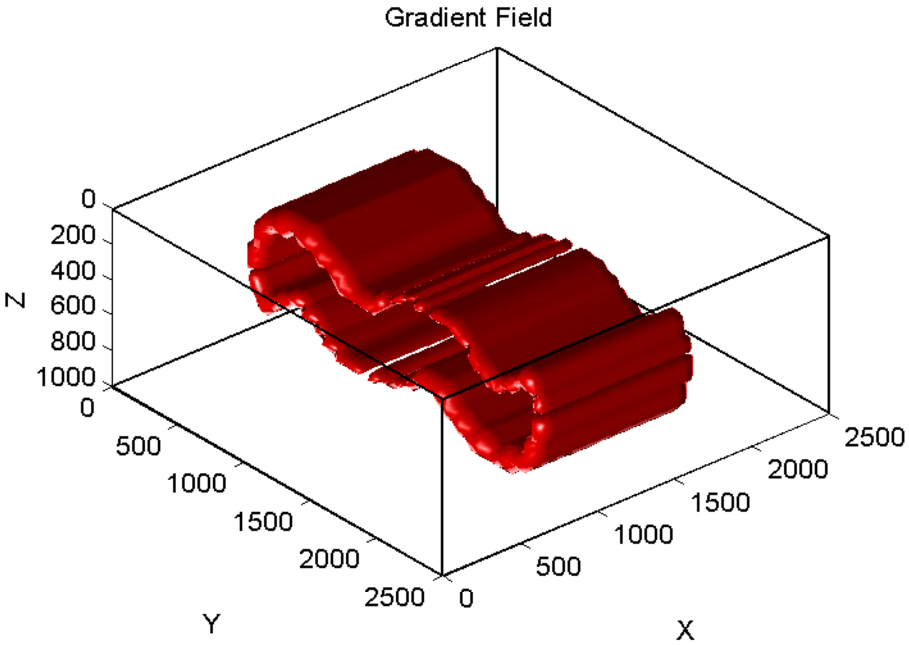

Figure 5.7: Gradient of permeability field with respect to the dip.

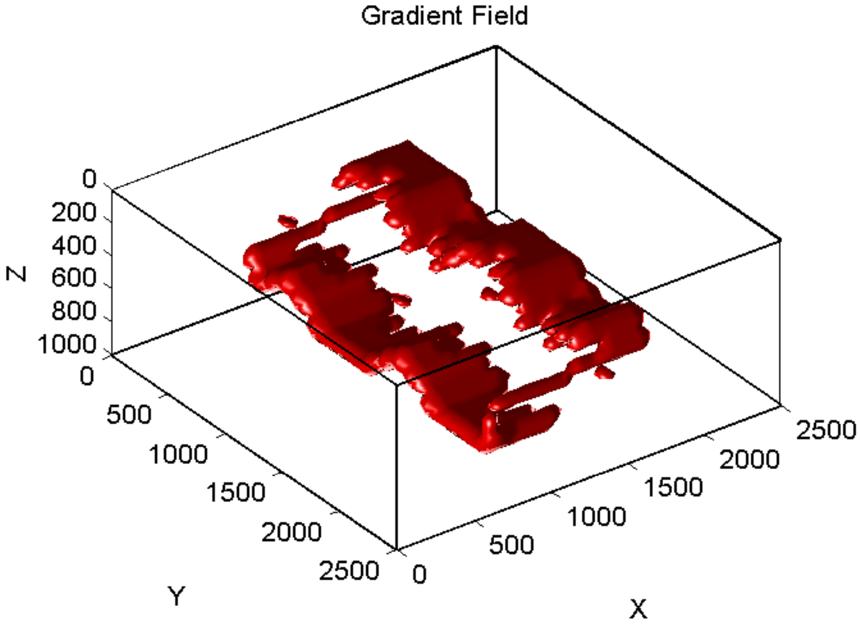

Figure 5.8: Gradient of permeability field with respect to the plunge.

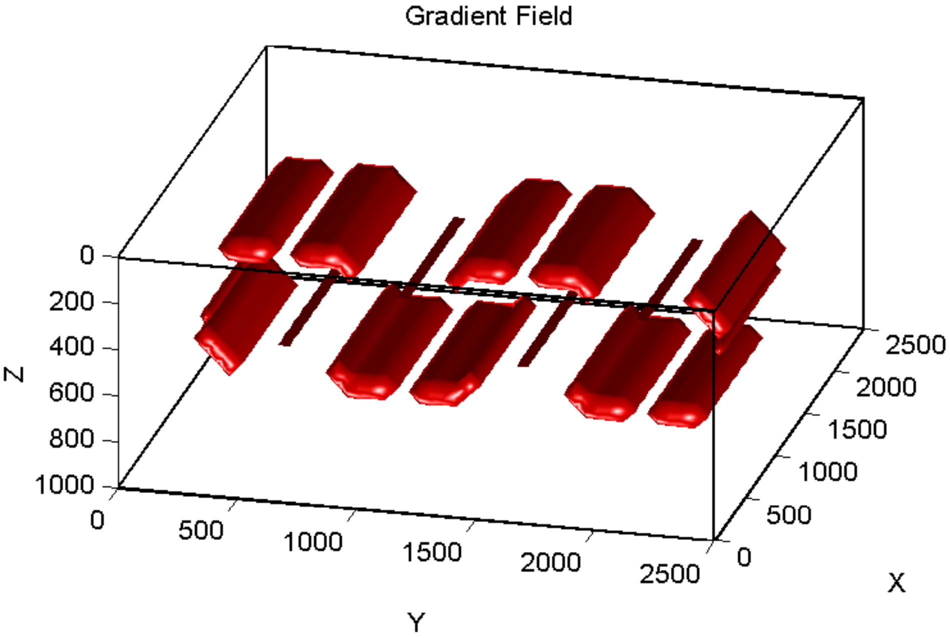

Figure 5.9: Gradient of permeability field with respect to the channel departure.

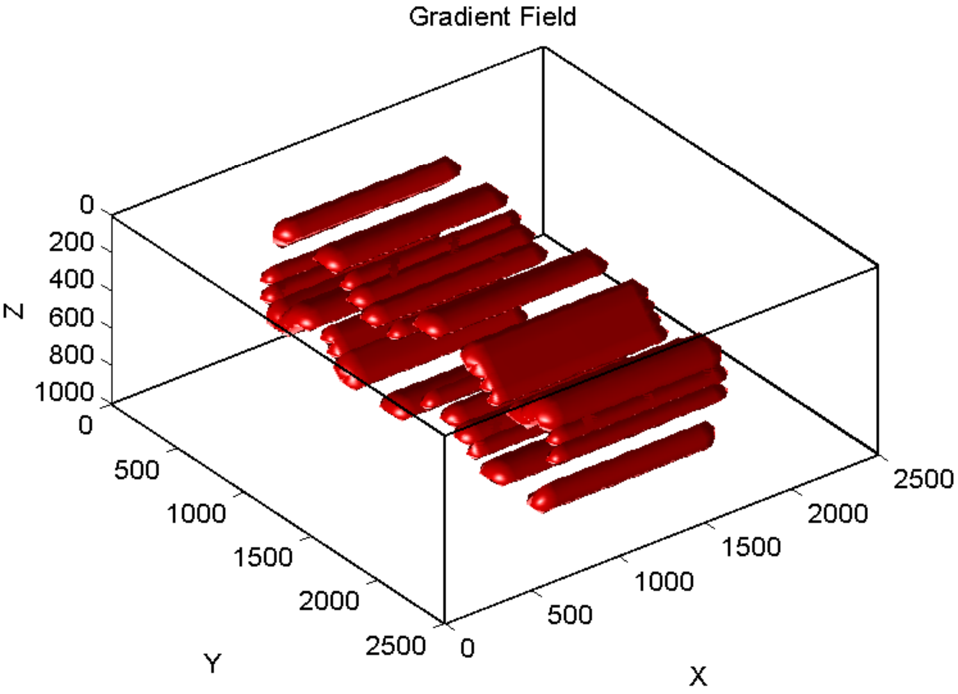

Figure 5.10: Gradient of permeability field with respect to the channel sinuosity.

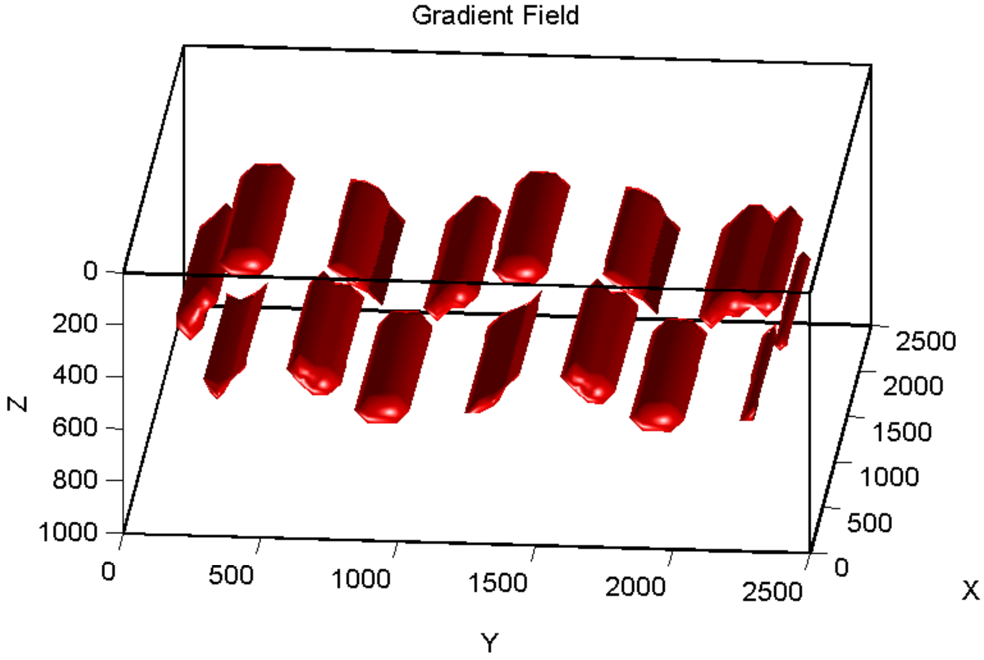

Figure 5.11: Gradient of permeability field with respect to the channel displacement.

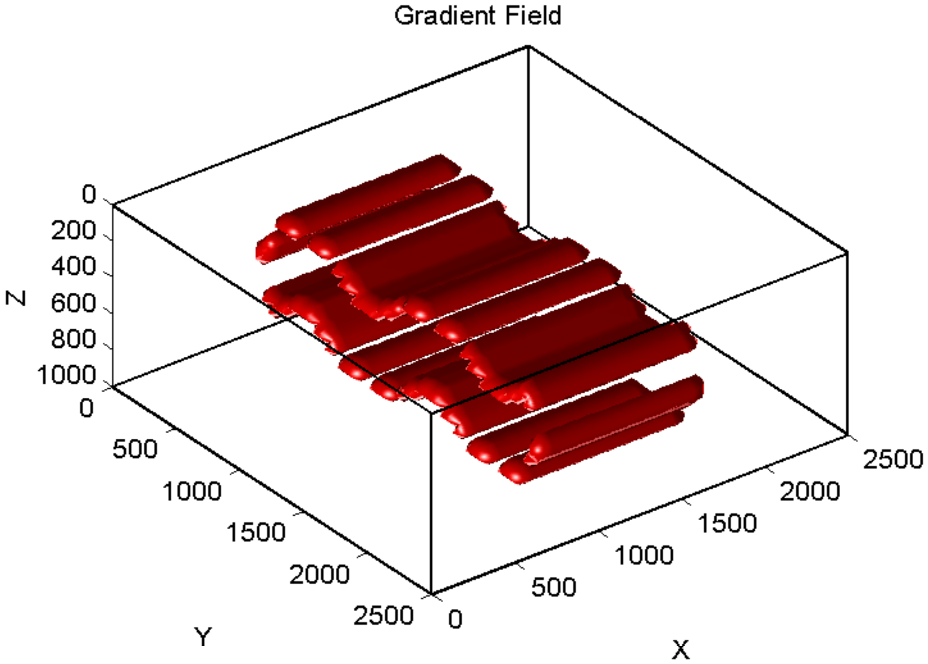

Figure 5.12: Gradient of permeability field with respect to the channel thickness.

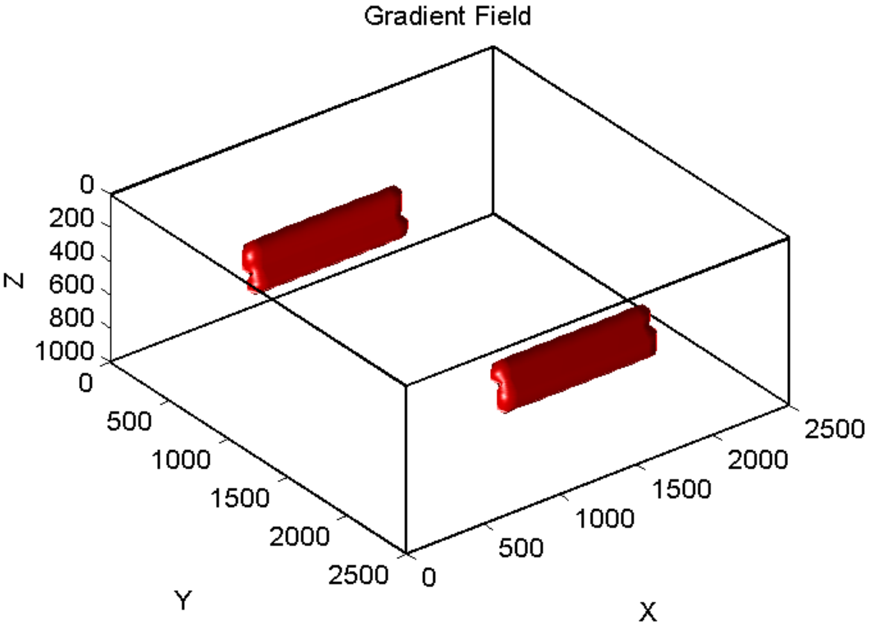

Figure 5.13: Gradient of permeability field with respect to the channel length.

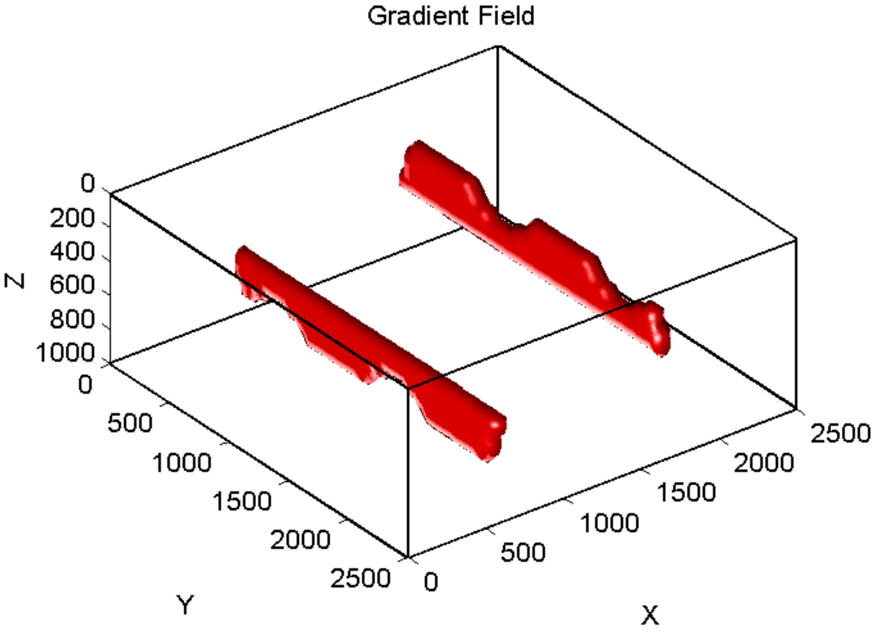

Figure 5.14: Gradient of permeability field with respect to the channel width.

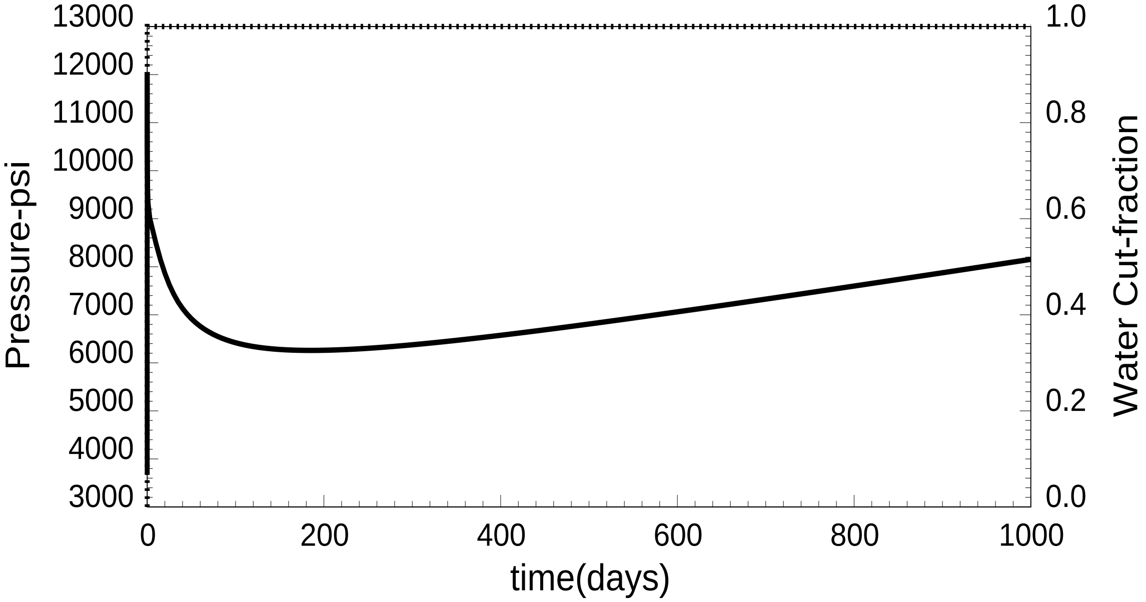

Figure 5.15: Long term pressure and water cut at Well #1 - Injector.

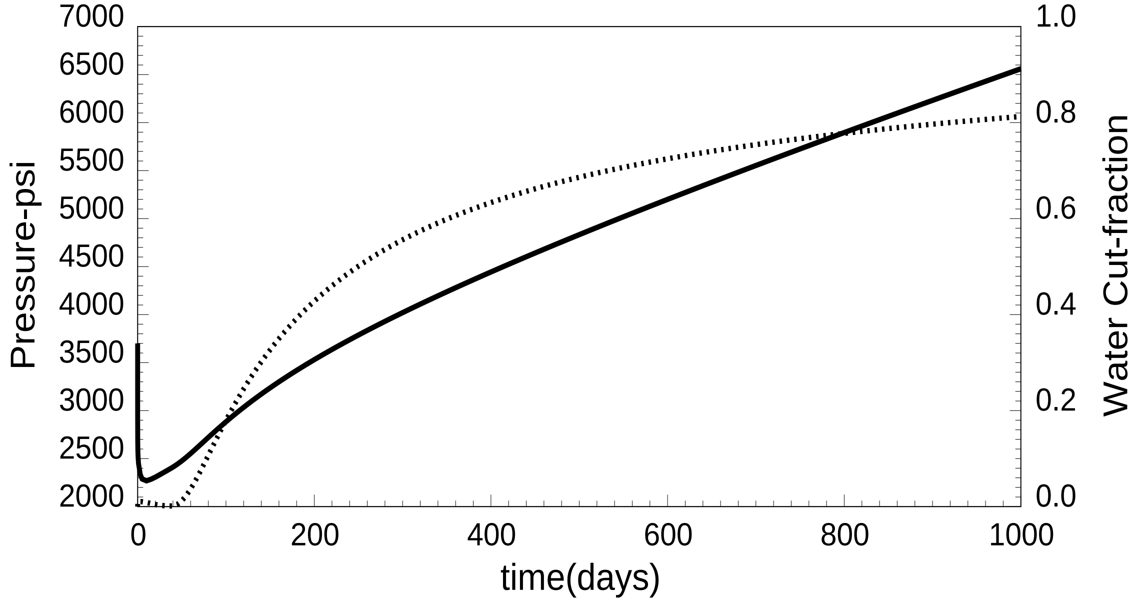

Figure 5.16: Long term pressure and water cut at Well #2 - Producer.

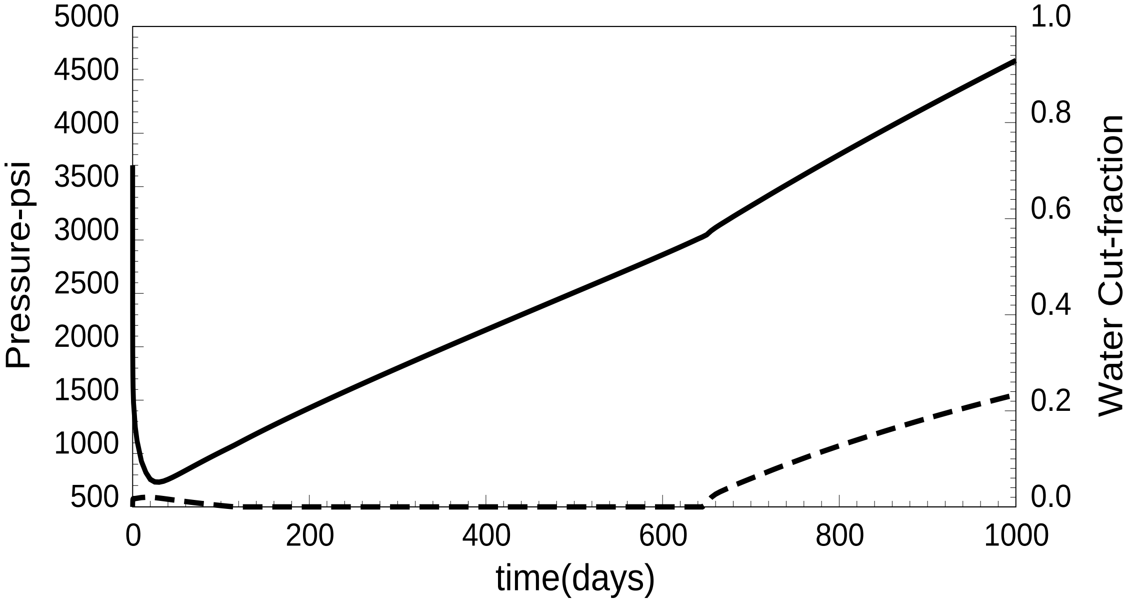

Figure 5.17: Long term pressure and water cut at Well #3 - Producer.

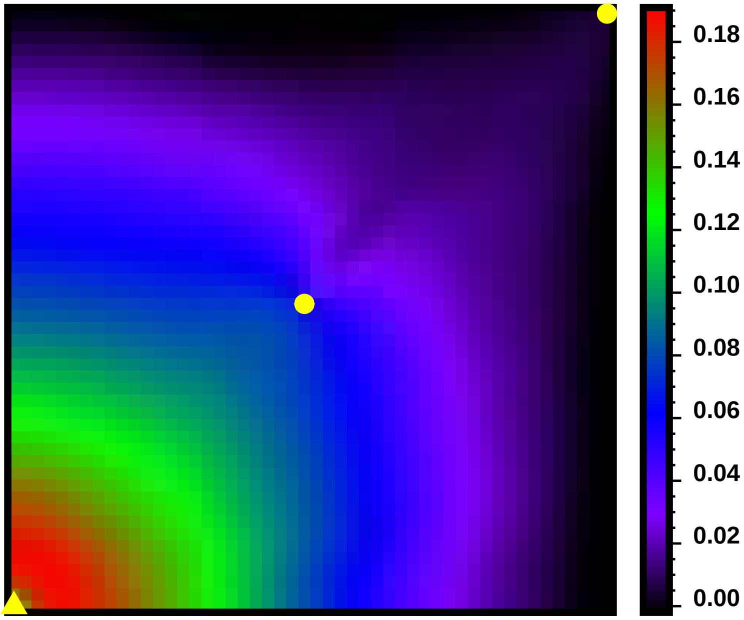

Figure 5.18: Change in water saturation between 100 and 800 days.

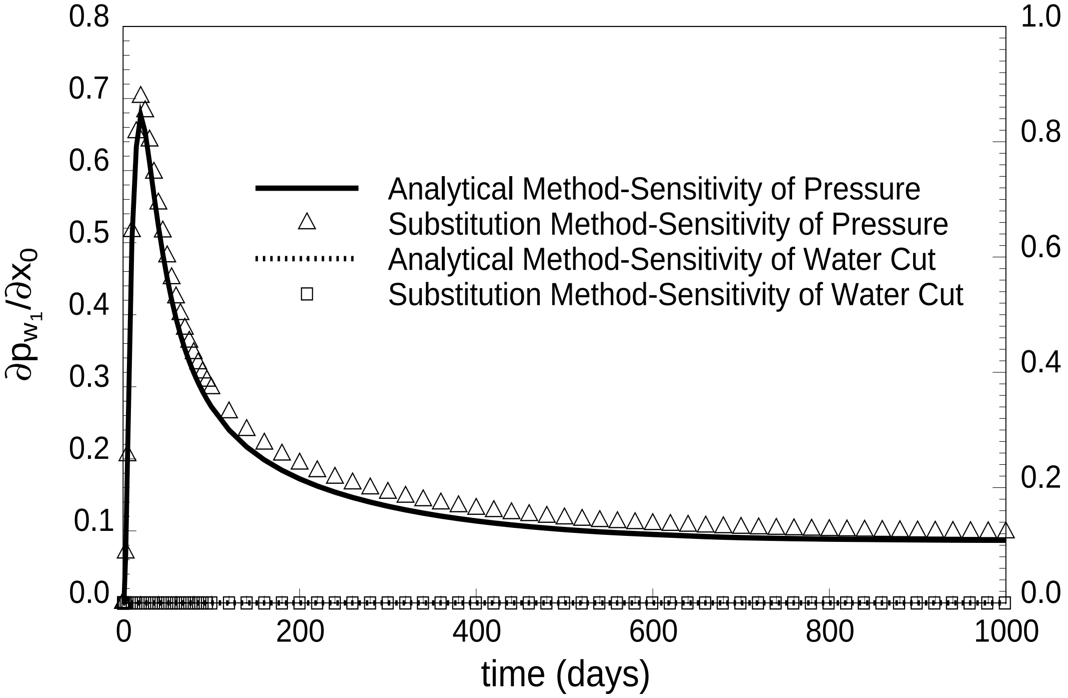

Figure 5.19: Sensitivity of pressure and water cut at well # 1 with respect to translation in x-direction.

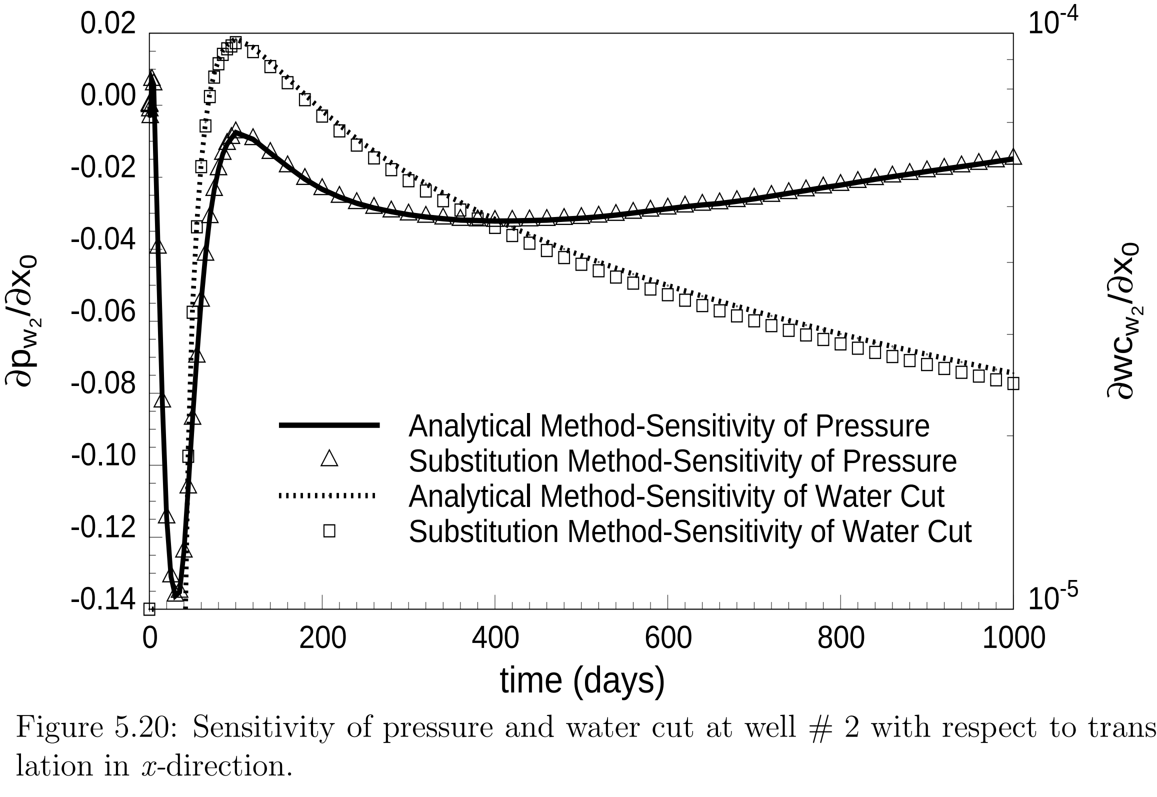

Figure 5.20: Sensitivity of pressure and water cut at well # 2 with respect to translation in x-direction.

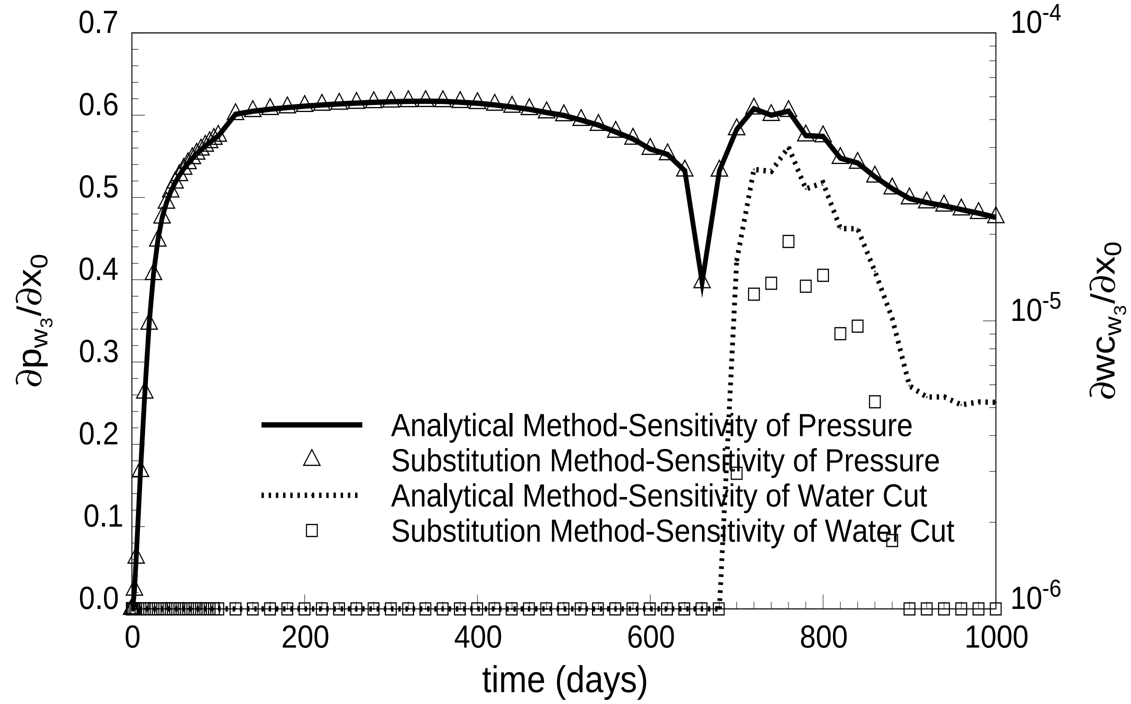

Figure 5.21: Sensitivity of pressure and water cut at well # 3 with respect to translation in x-direction.

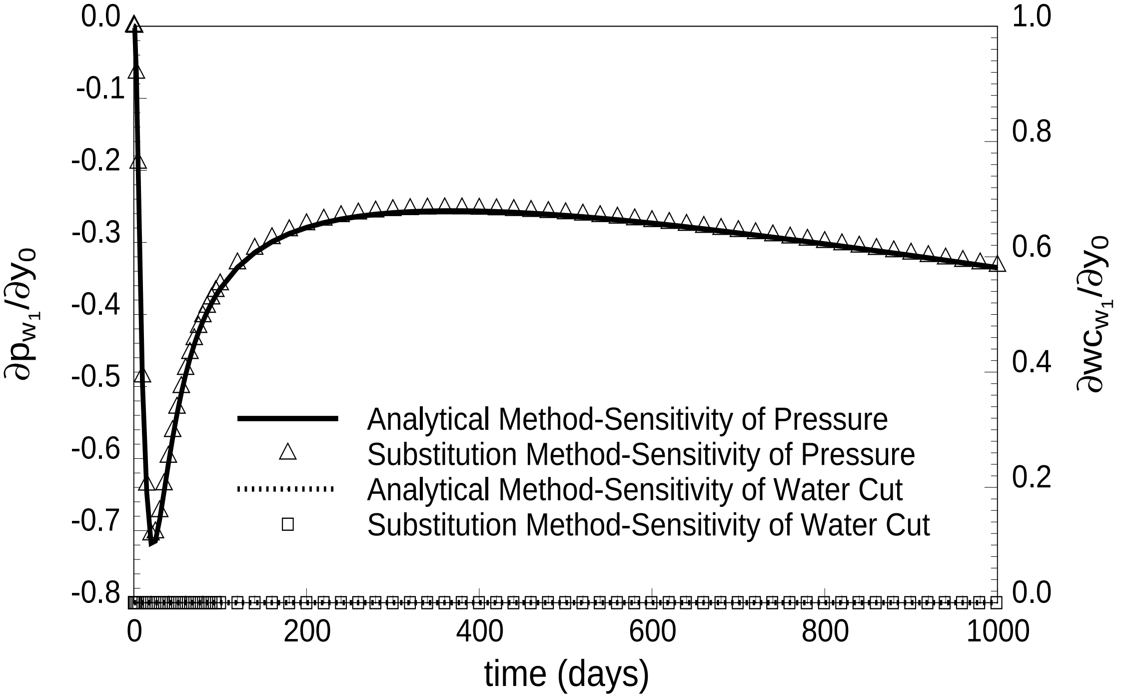

Figure 5.22: Sensitivity of pressure and water cut at well # 1 with respect to translation in y-direction.

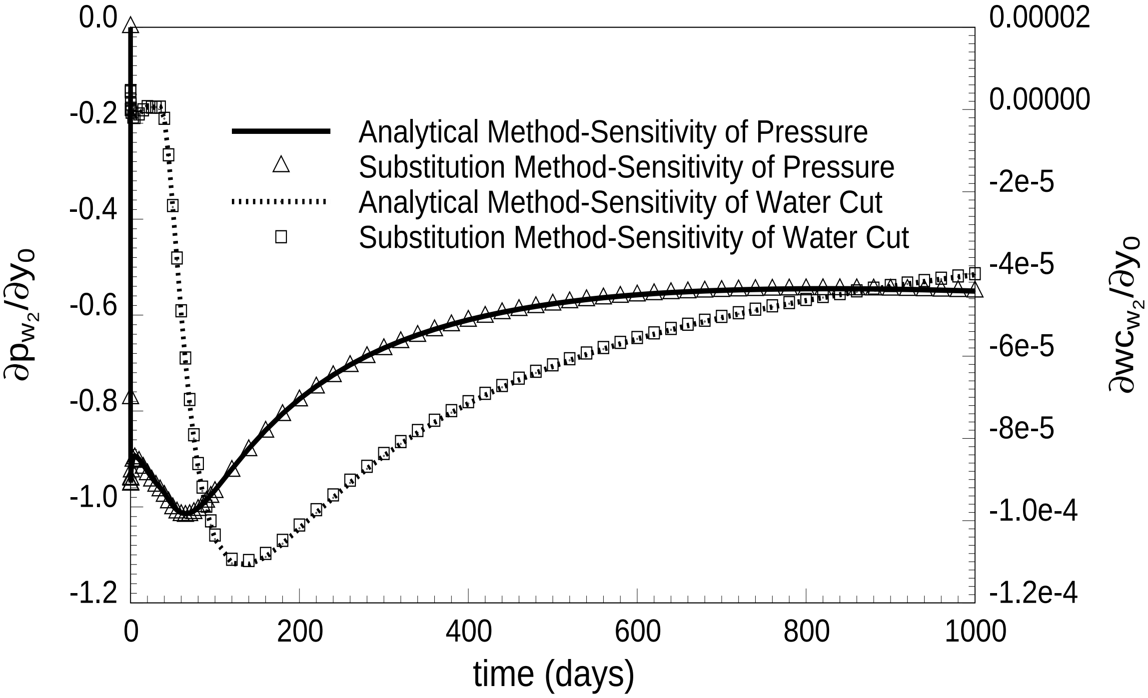

Figure 5.23: Sensitivity of pressure and water cut at well # 2 with respect to translation in y-direction.

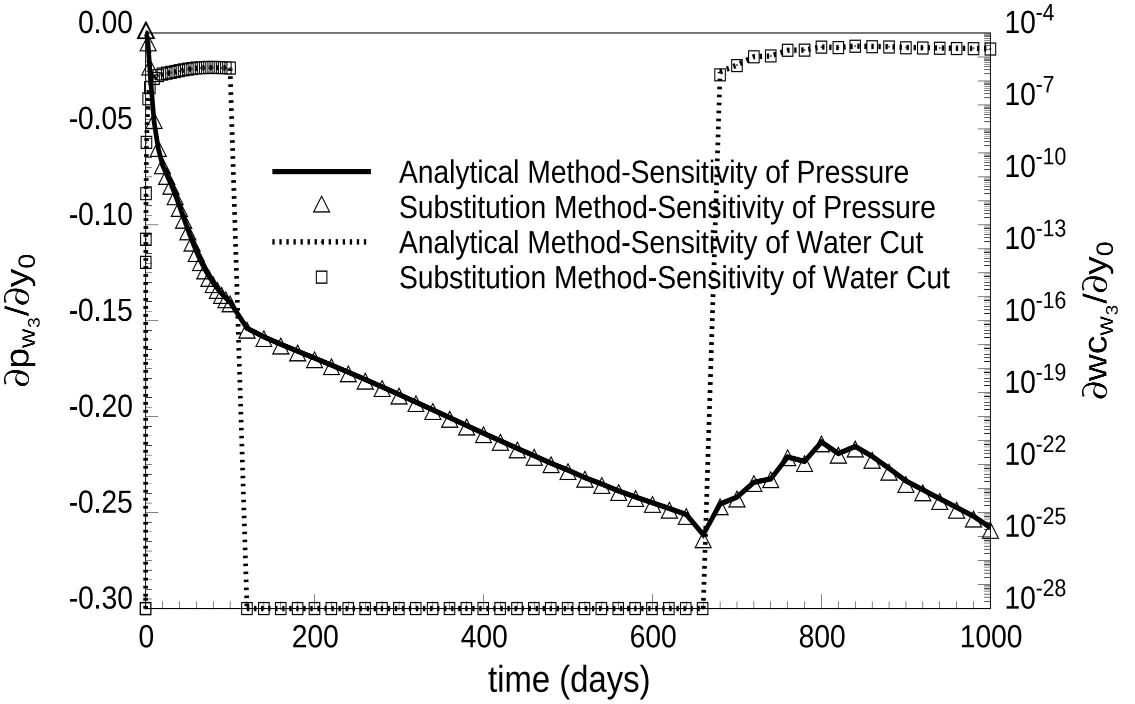

Figure 5.24: Sensitivity of pressure and water cut at well # 3 with respect to translation in y-direction.

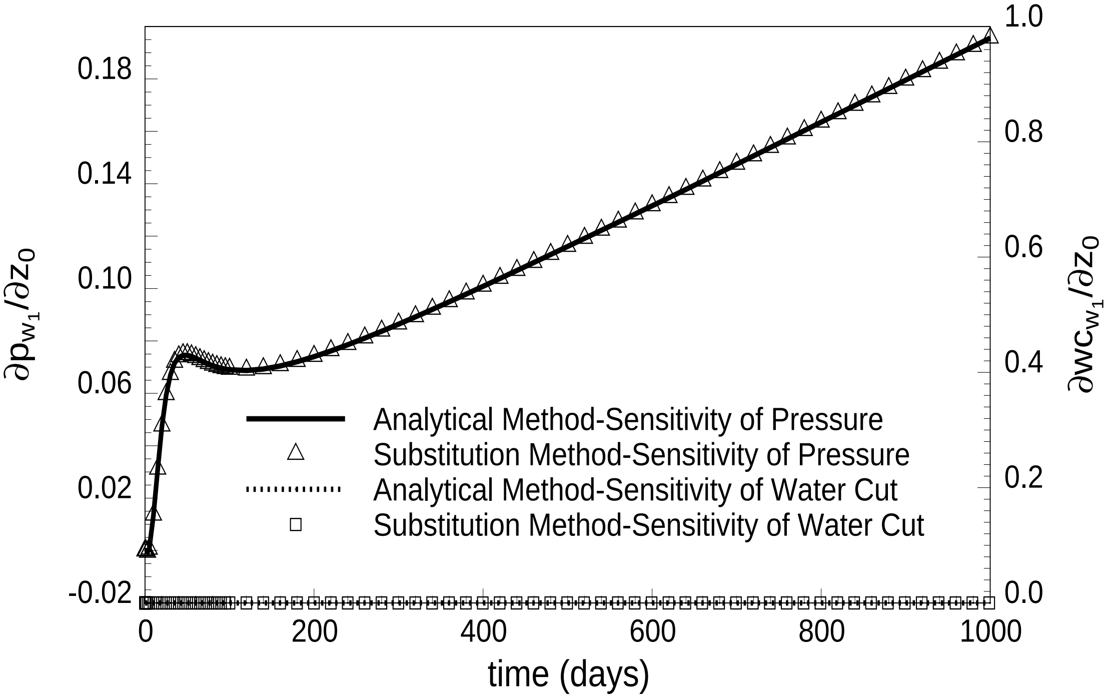

Figure 5.25: Sensitivity of pressure and water cut at well # 1 with respect to translation in z-direction.

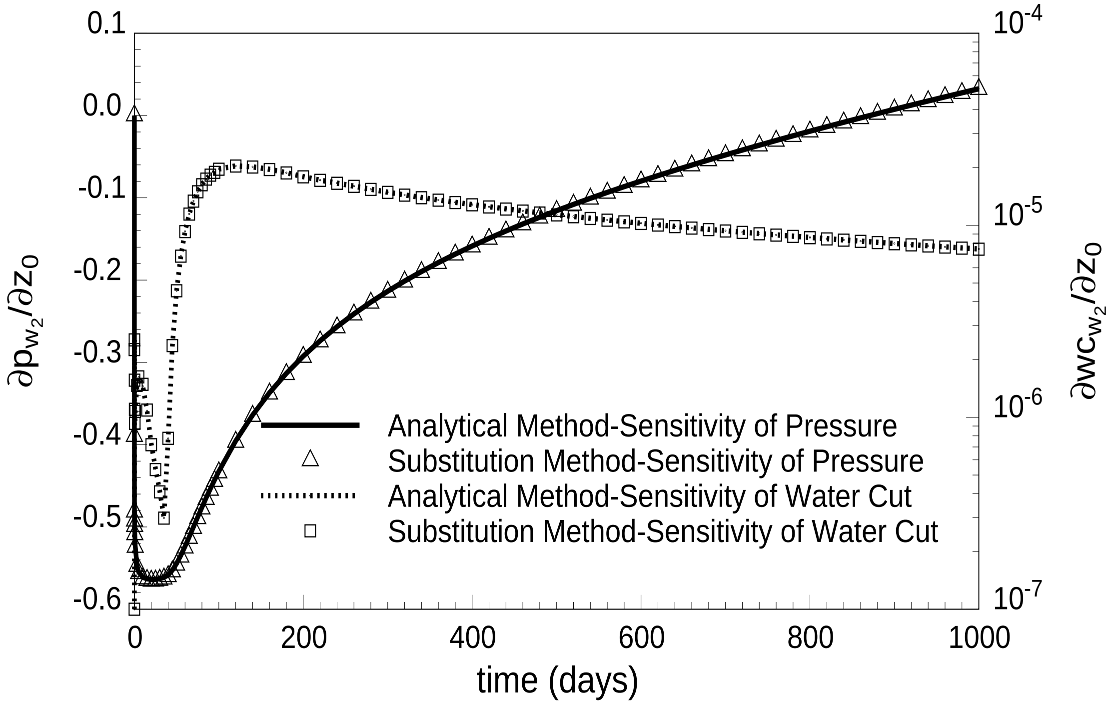

Figure 5.26: Sensitivity of pressure and water cut at well # 2 with respect to translation in z-direction.

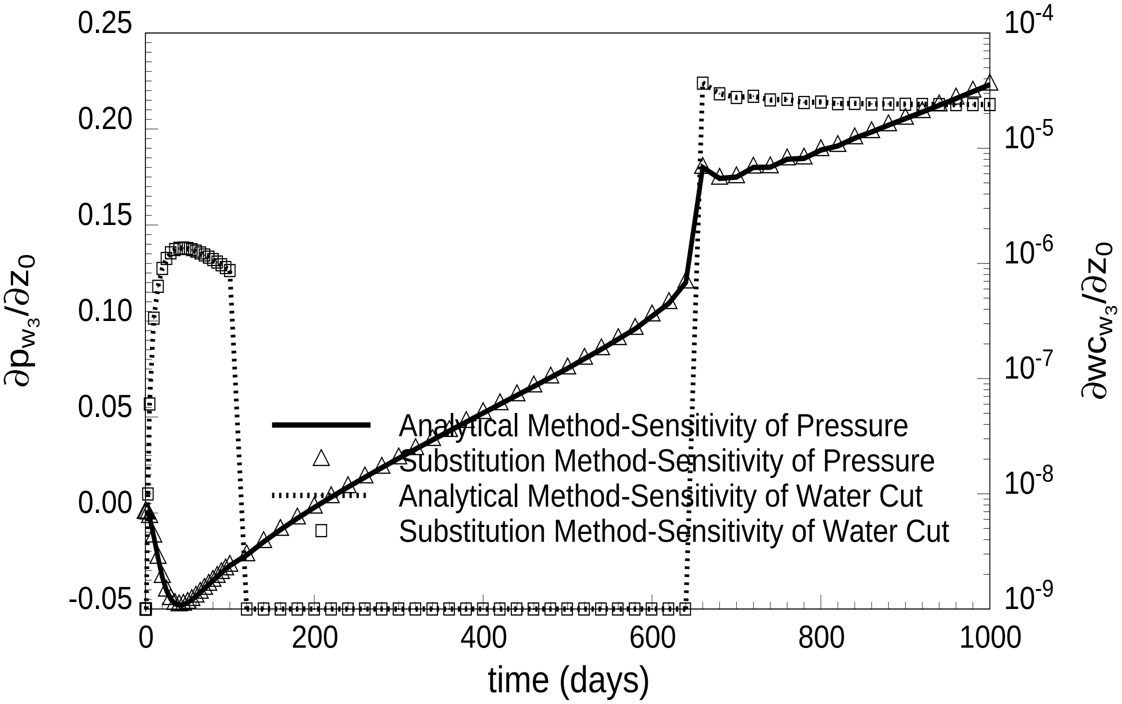

Figure 5.27: Sensitivity of pressure and water cut at well # 3 with respect to translation in z-direction.

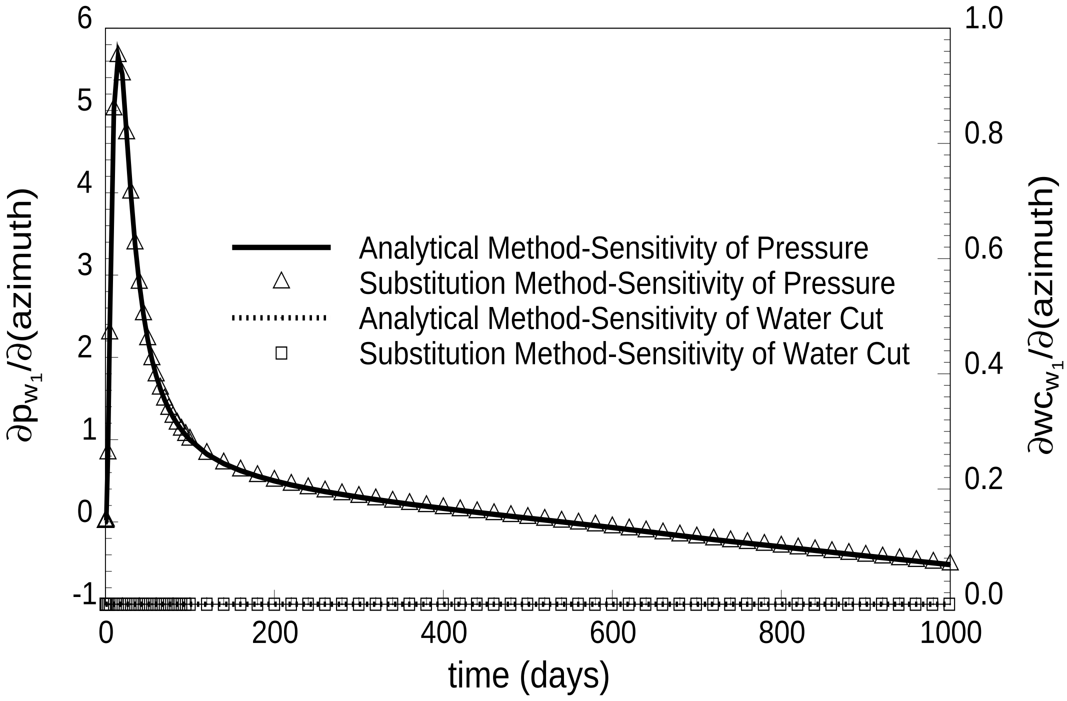

Figure 5.28: Sensitivity of pressure and water cut at well # 1 with respect to the channel azimuth.

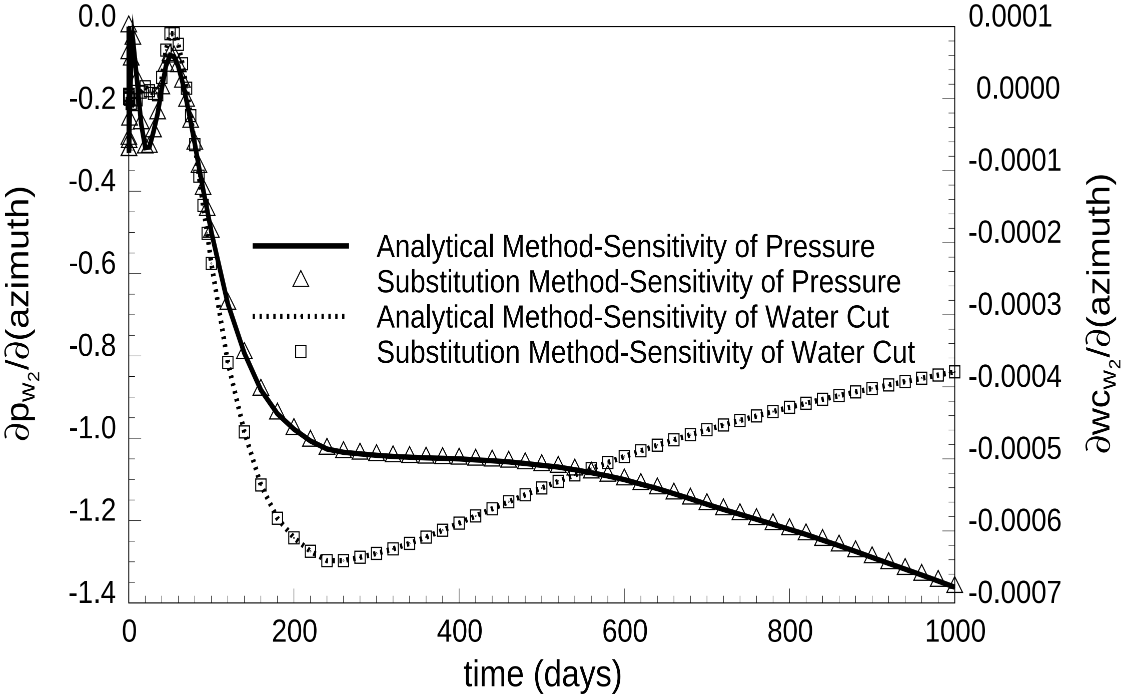

Figure 5.29: Sensitivity of pressure and water cut at well # 2 with respect to the channel azimuth.

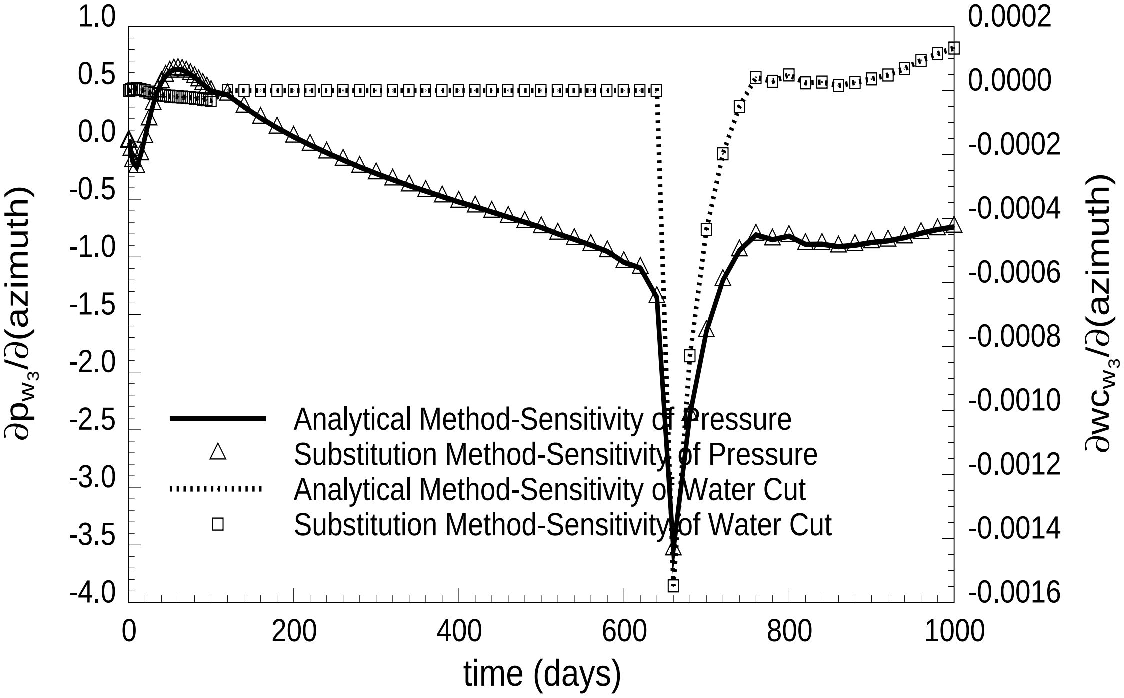

Figure 5.30: Sensitivity of pressure and water cut at well # 3 with respect to the channel azimuth.

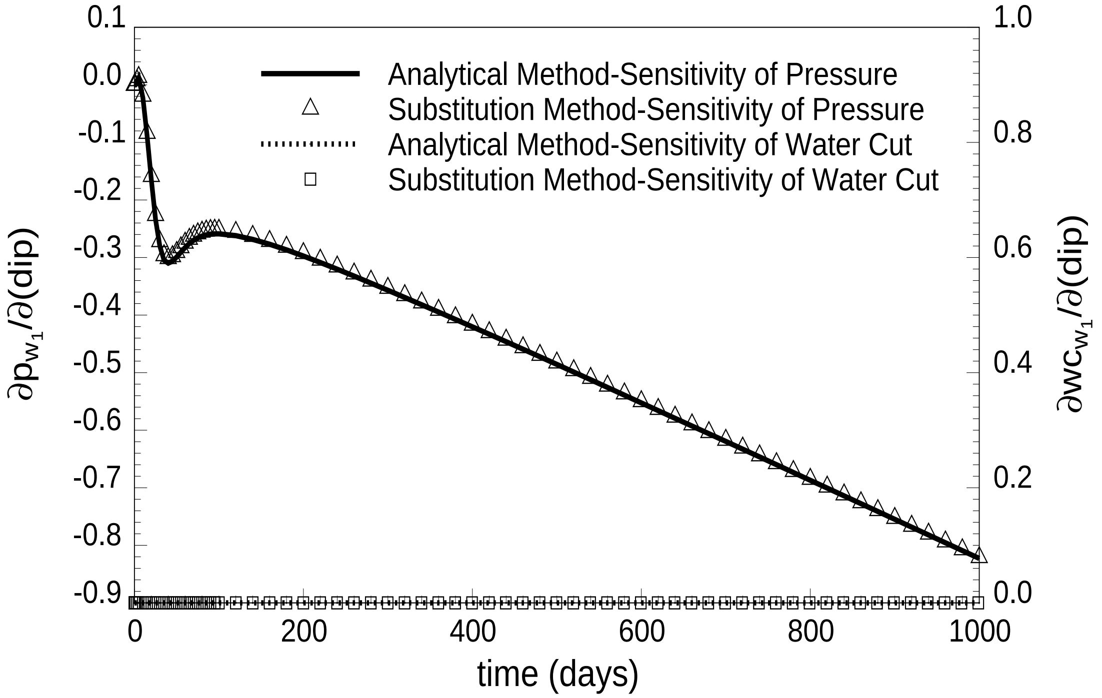

Figure 5.31: Sensitivity of pressure and water cut at well # 1 with respect to the channel dip.

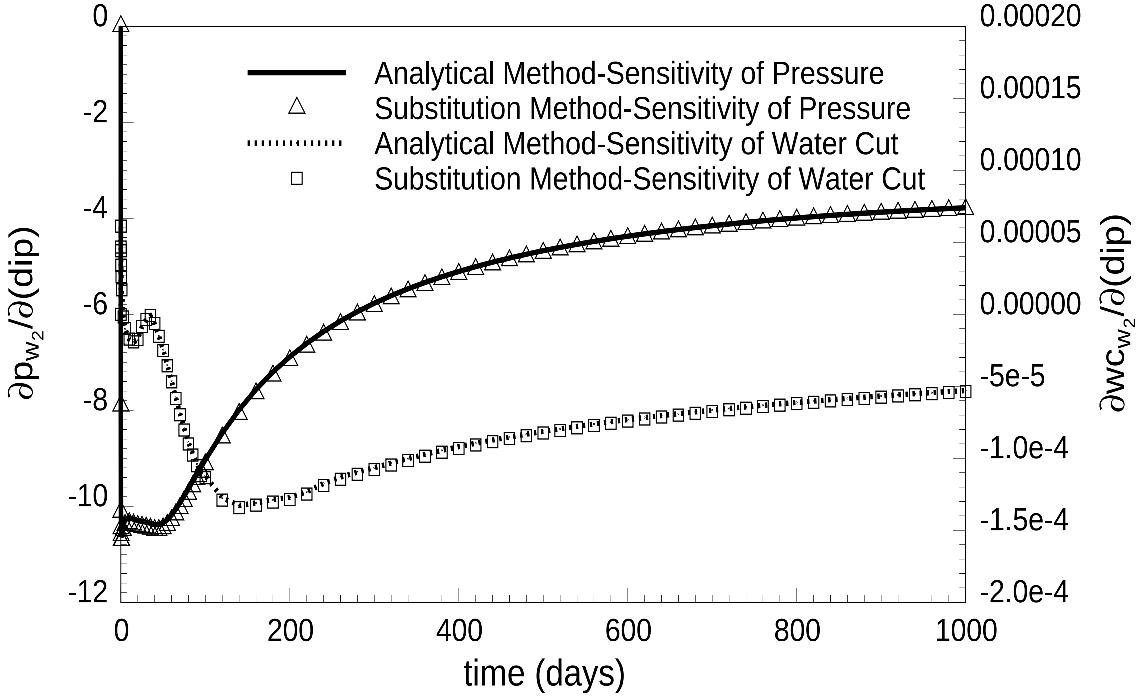

Figure 5.32: Sensitivity of pressure and water cut at well # 2 with respect to the channel dip.

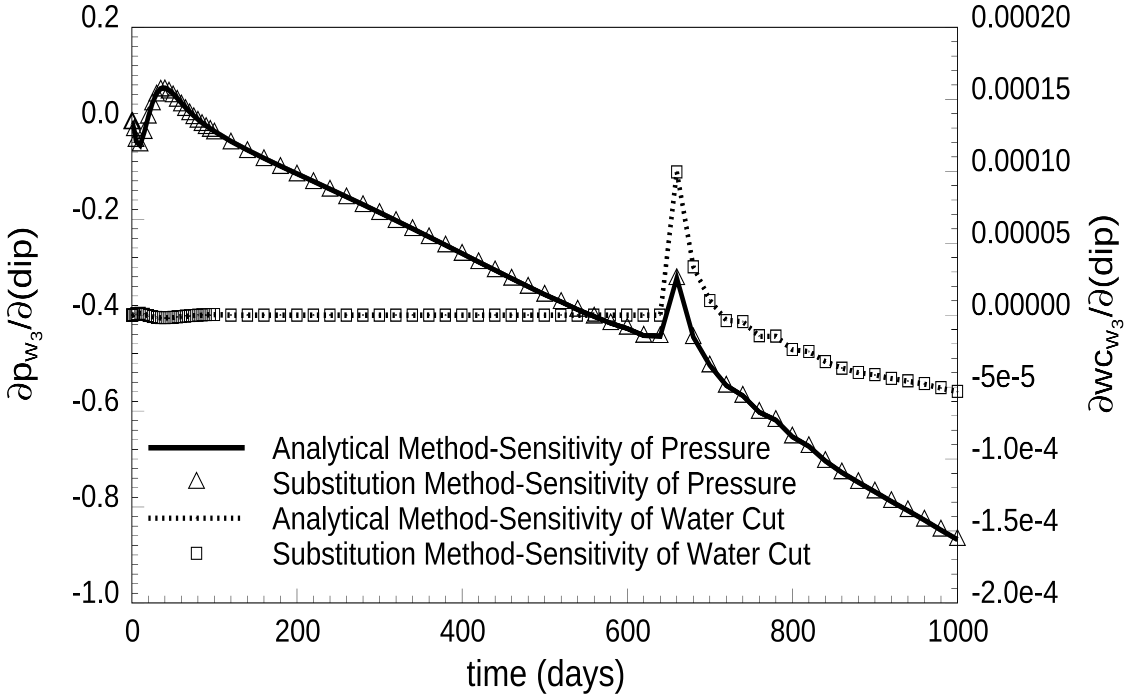

Figure 5.33: Sensitivity of pressure and water cut at well # 3 with respect to the channel dip.

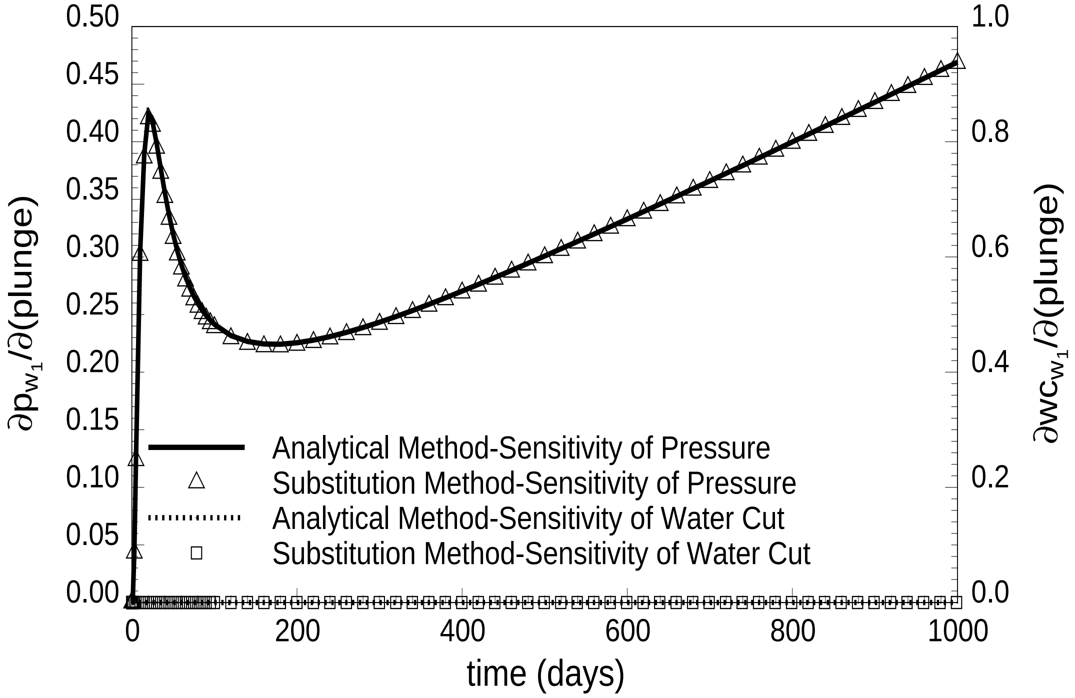

Figure 5.34: Sensitivity of pressure and water cut at well # 1 with respect to the channel plunge.

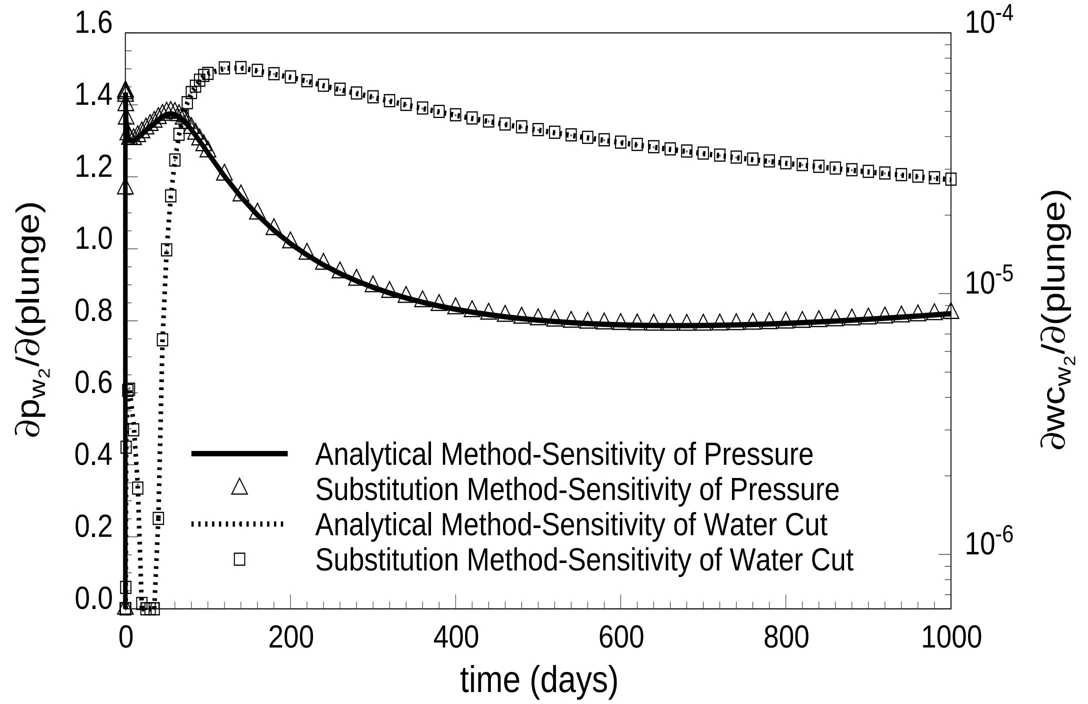

Figure 5.35: Sensitivity of pressure and water cut at well # 2 with respect to the channel plunge.

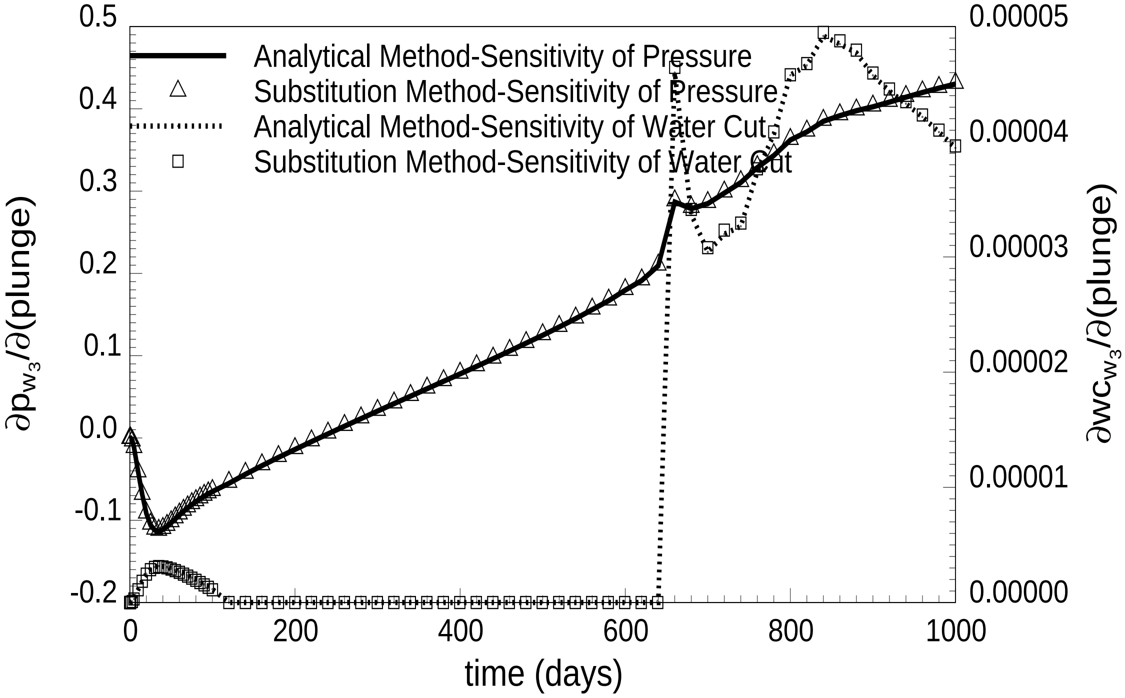

Figure 5.36: Sensitivity of pressure and water cut at well # 3 with respect to the channel plunge.

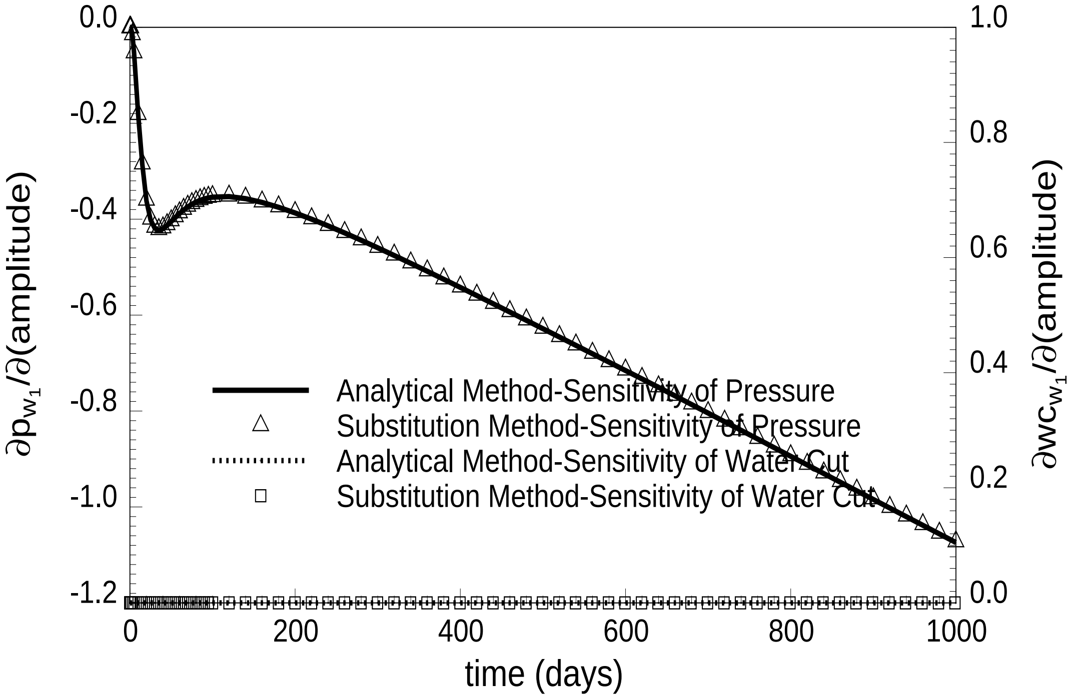

Figure 5.37: Sensitivity of pressure and water cut at well # 1 with respect to the channel departure.

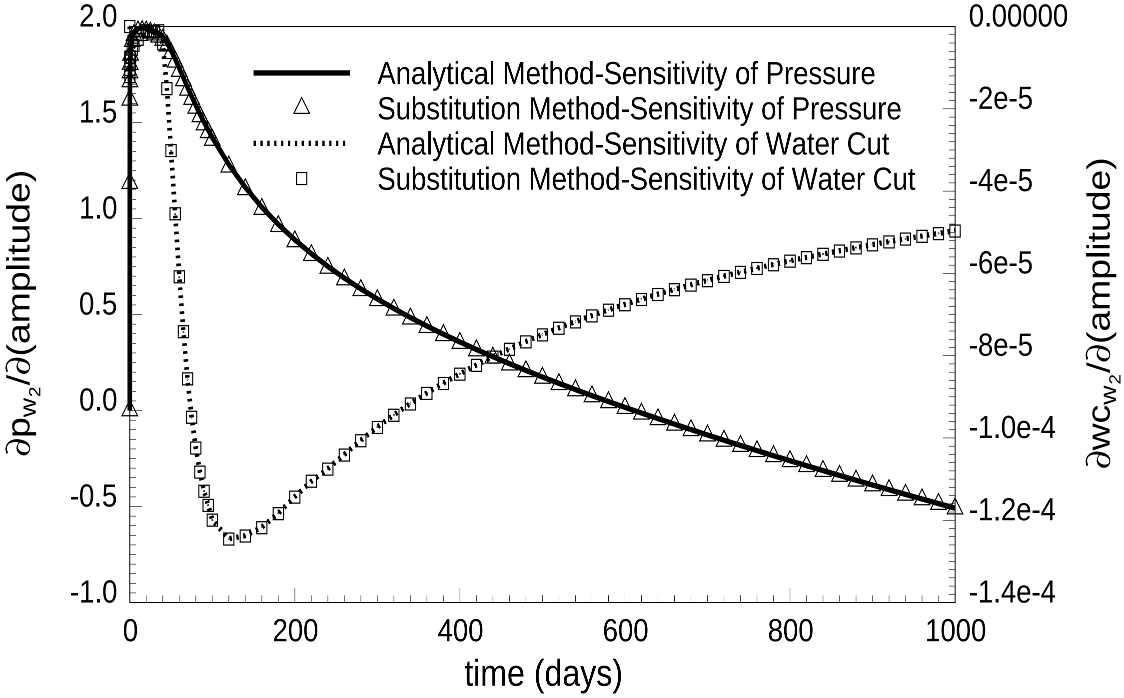

Figure 5.38: Sensitivity of pressure and water cut at well # 2 with respect to the channel departure.

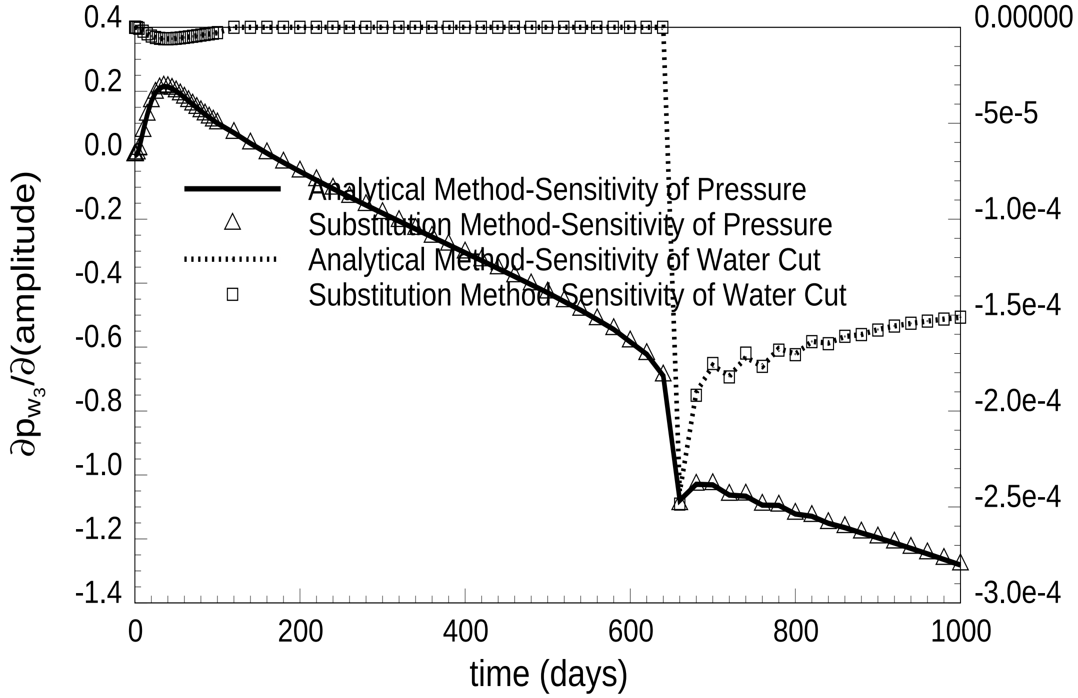

Figure 5.39: Sensitivity of pressure and water cut at well # 3 with respect to the channel departure.

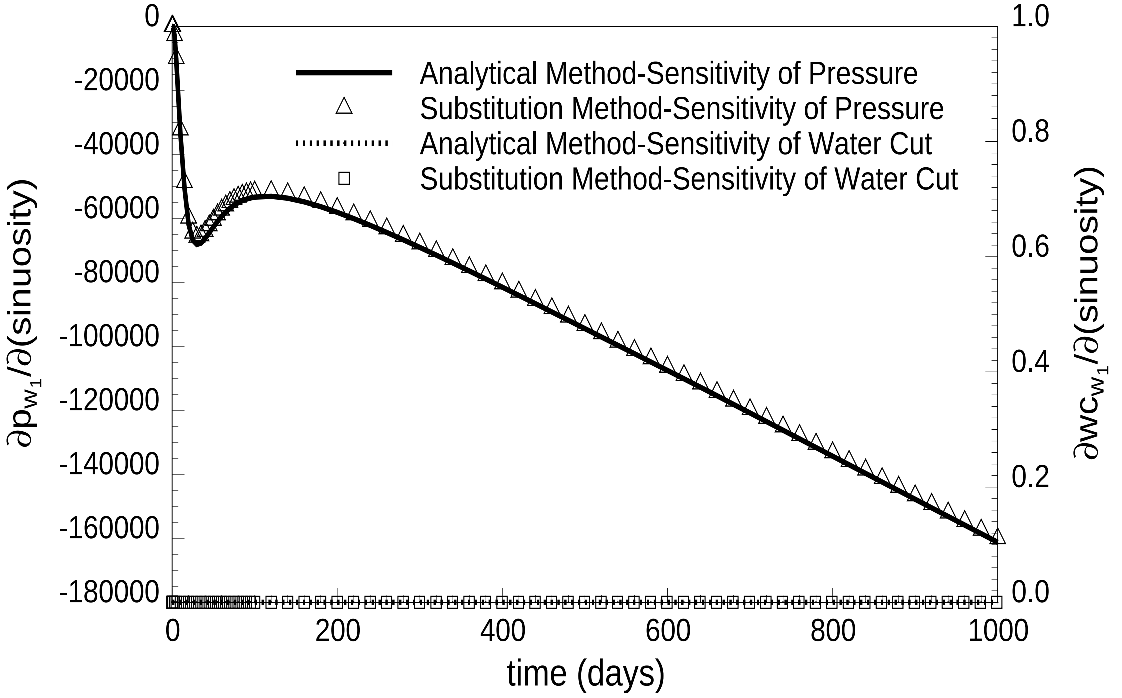

Figure 5.40: Sensitivity of pressure and water cut at well # 1 with respect to the channel sinuosity.

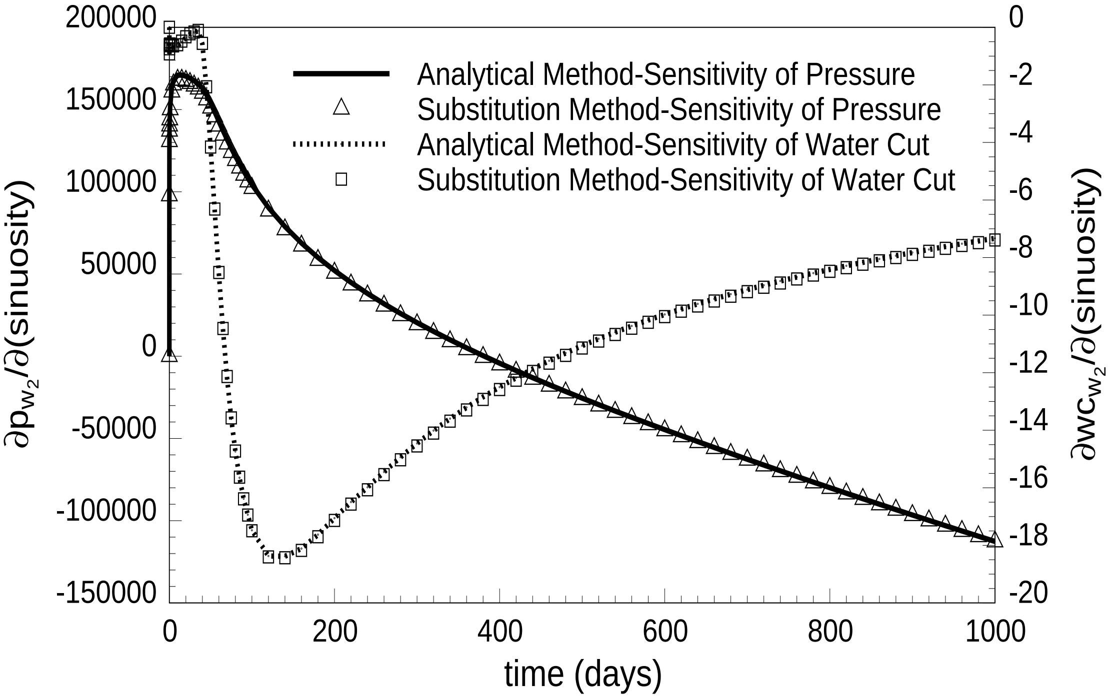

Figure 5.41: Sensitivity of pressure and water cut at well # 2 with respect to the channel sinuosity.

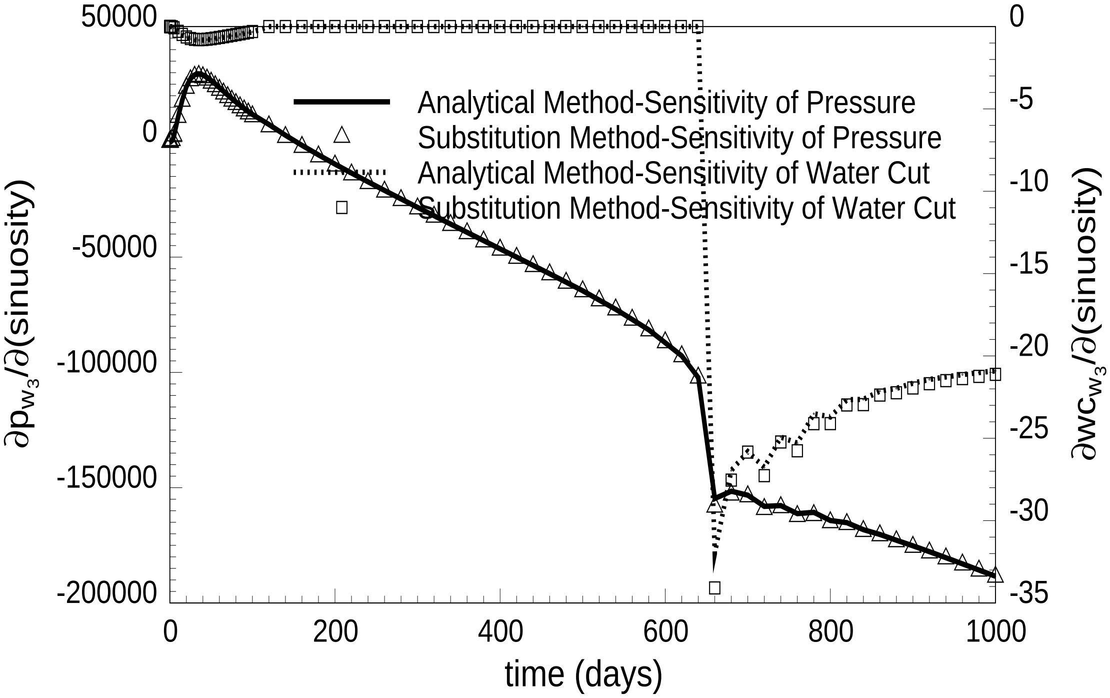

Figure 5.42: Sensitivity of pressure and water cut at well # 3 with respect to the channel sinuosity.

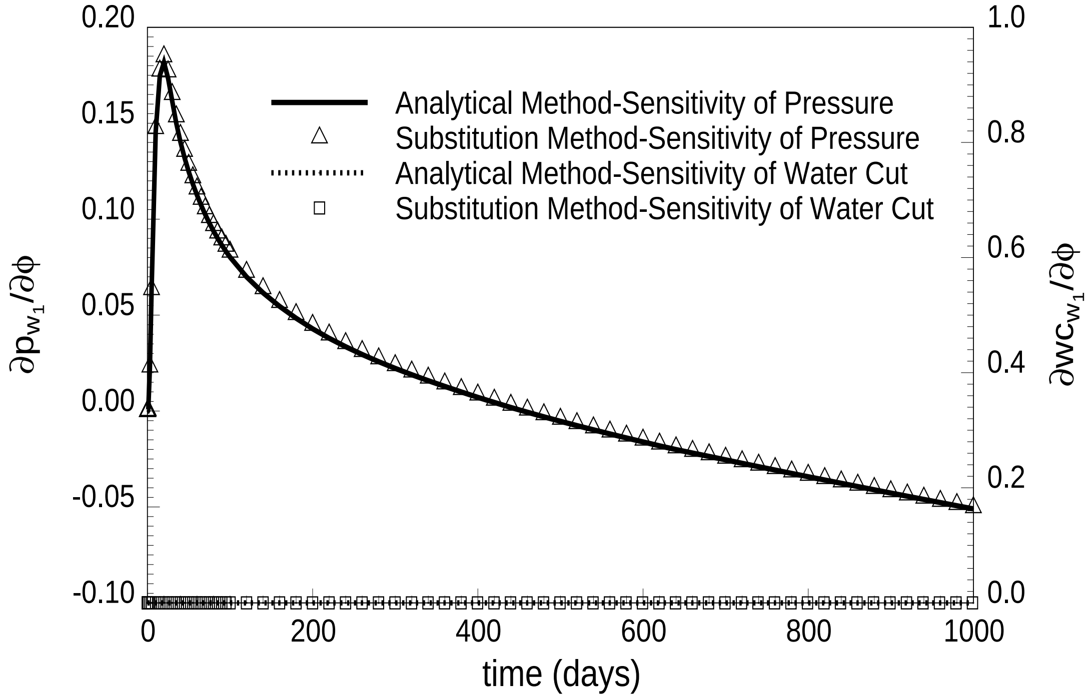

Figure 5.43: Sensitivity of pressure and water cut at well # 1 with respect to the channel displacement.

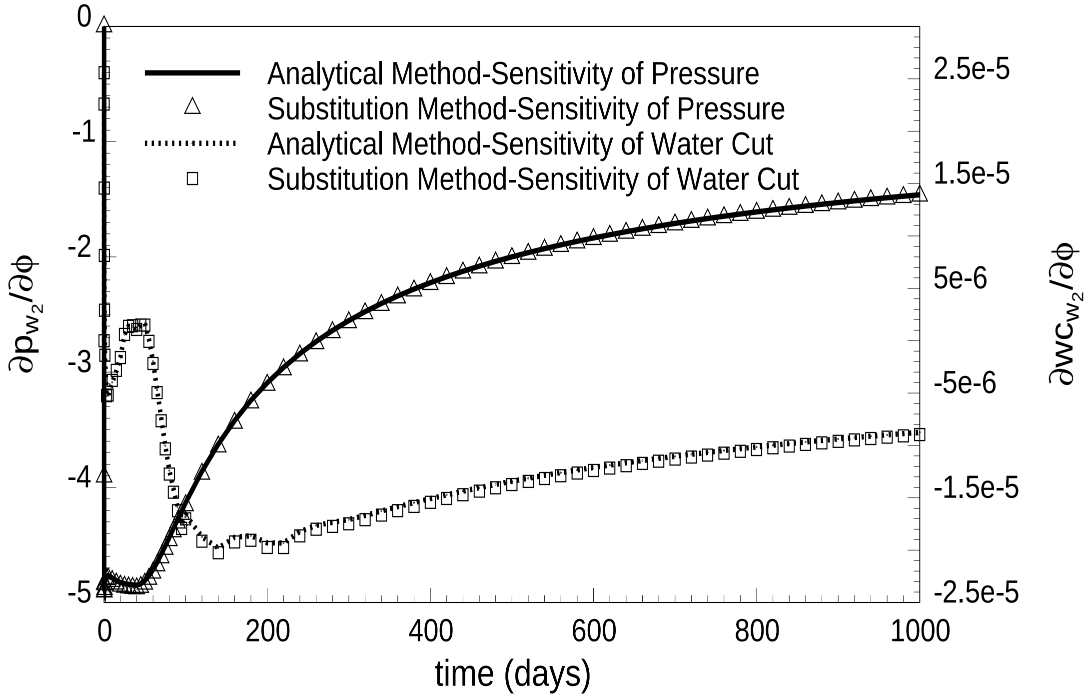

Figure 5.44: Sensitivity of pressure and water cut at well # 2 with respect to the channel displacement.

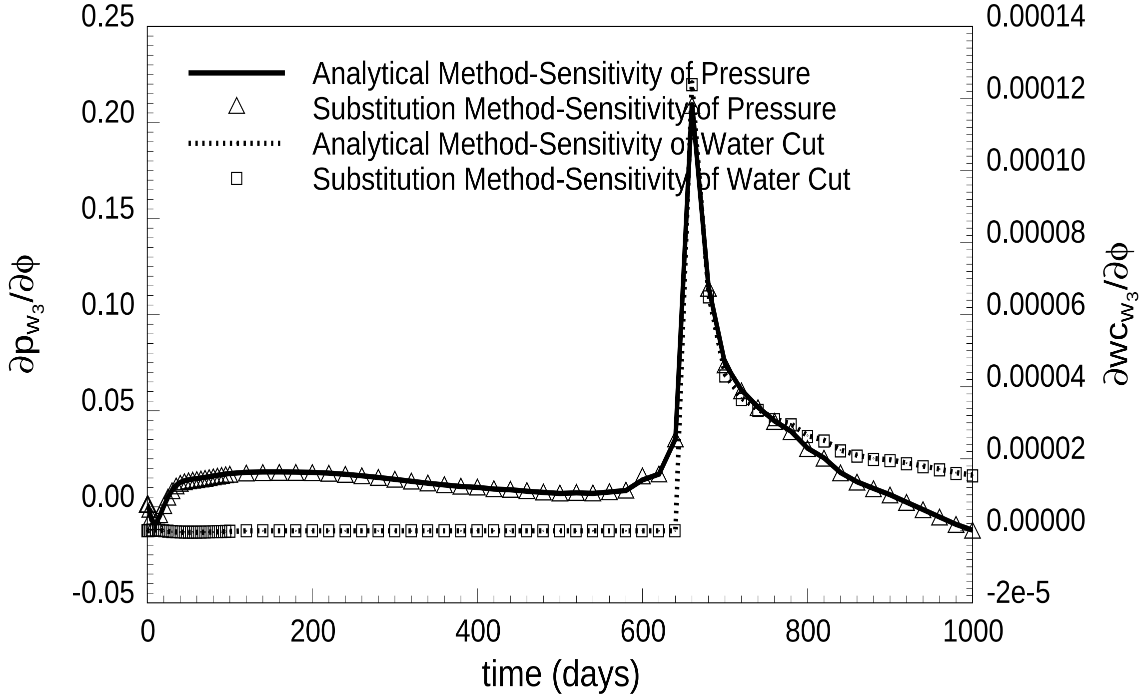

Figure 5.45: Sensitivity of pressure and water cut at well # 3 with respect to the channel displacement.

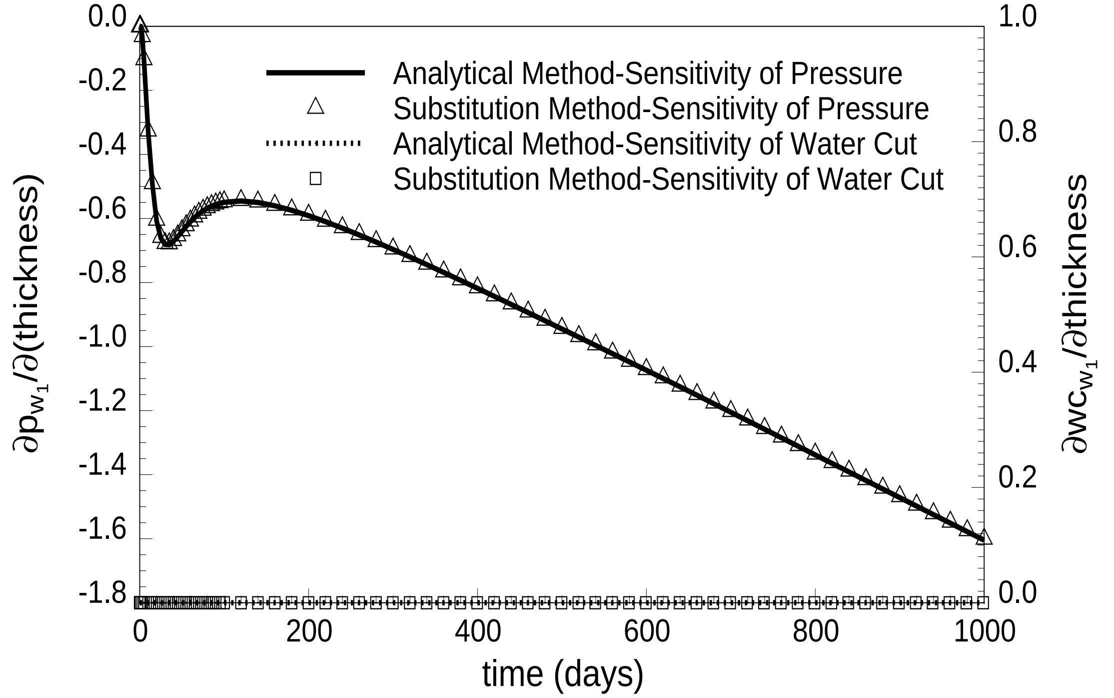

Figure 5.46: Sensitivity of pressure and water cut at well # 1 with respect to the channel thickness.

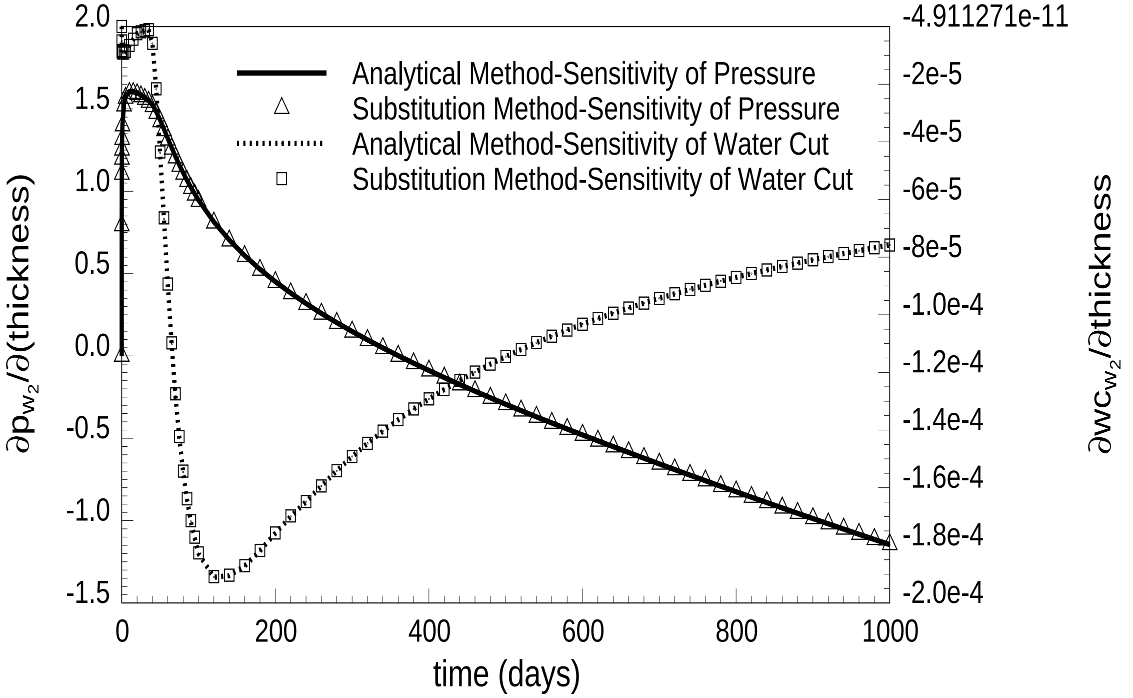

Figure 5.47: Sensitivity of pressure and water cut at well # 2 with respect to the channel thickness.

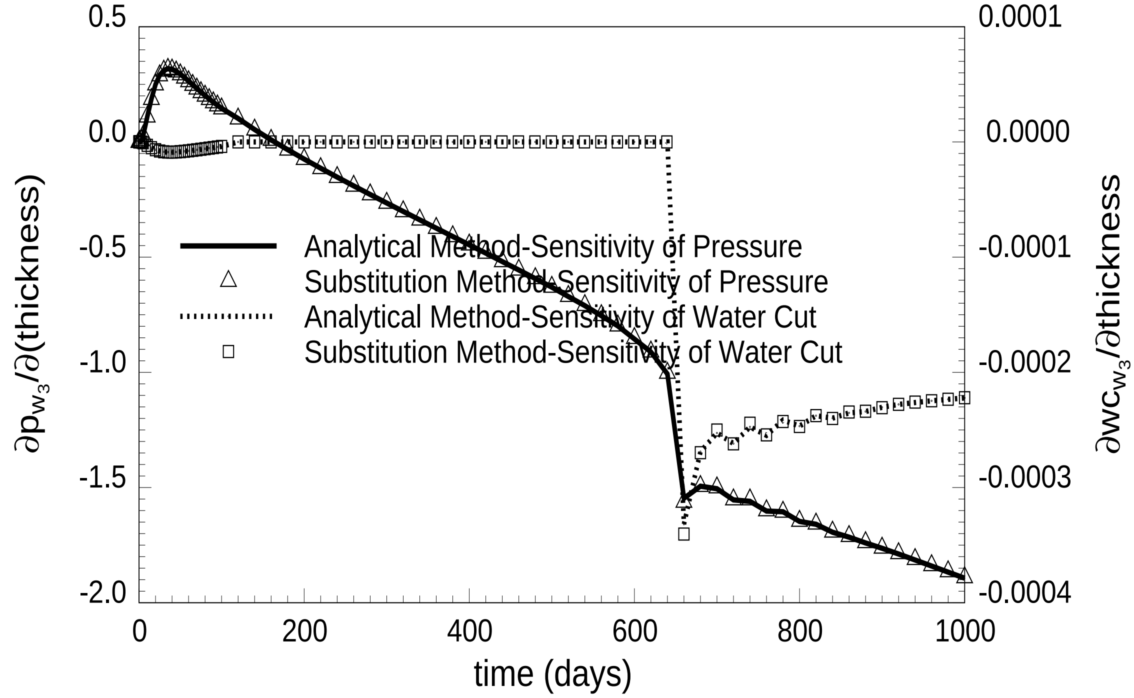

Figure 5.48: Sensitivity of pressure and water cut at well # 3 with respect to the channel thickness.

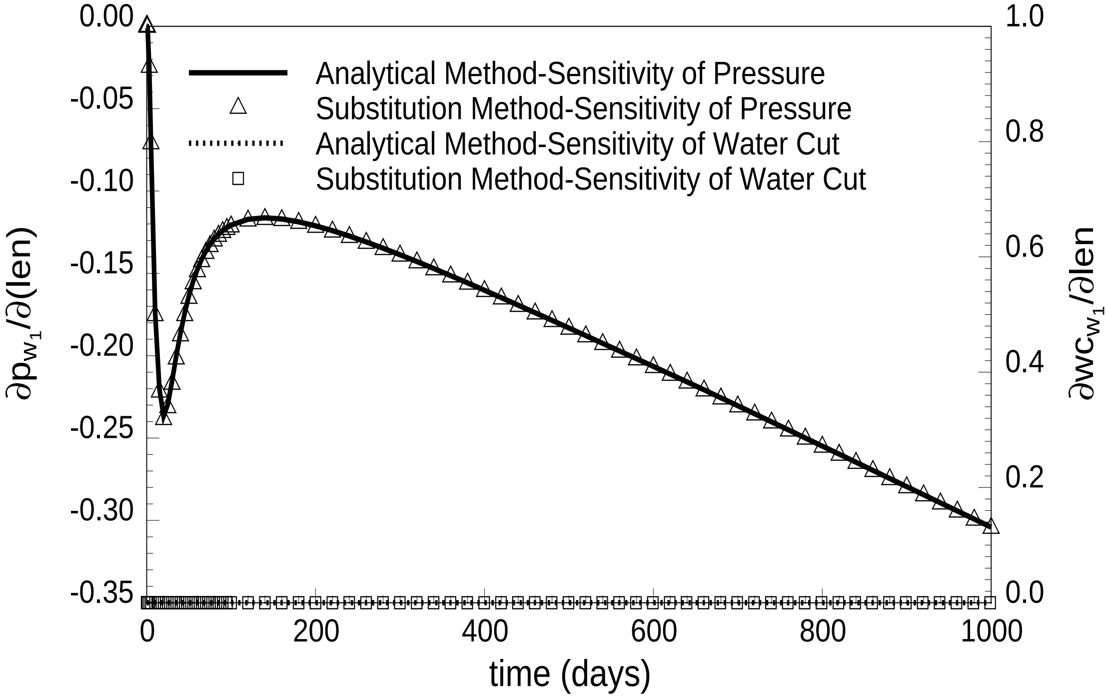

Figure 5.49: Sensitivity of pressure and water cut at well # 1 with respect to the channel length.

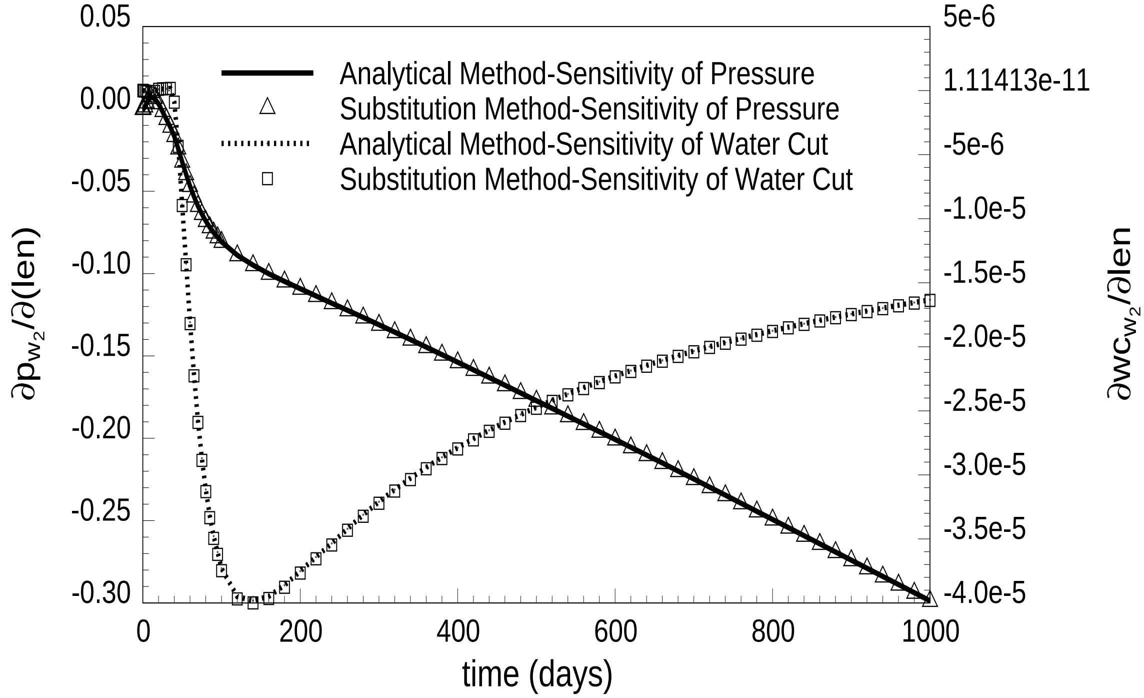

Figure 5.50: Sensitivity of pressure and water cut at well # 2 with respect to the channel length.

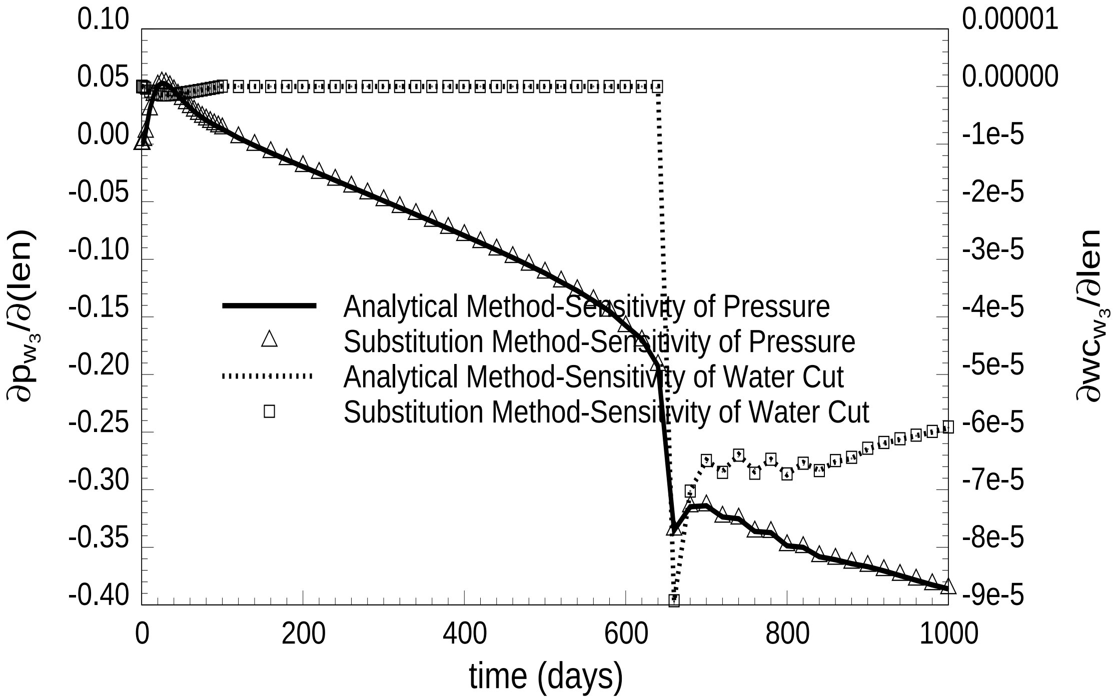

Figure 5.51: Sensitivity of pressure and water cut at well # 3 with respect to the channel length.

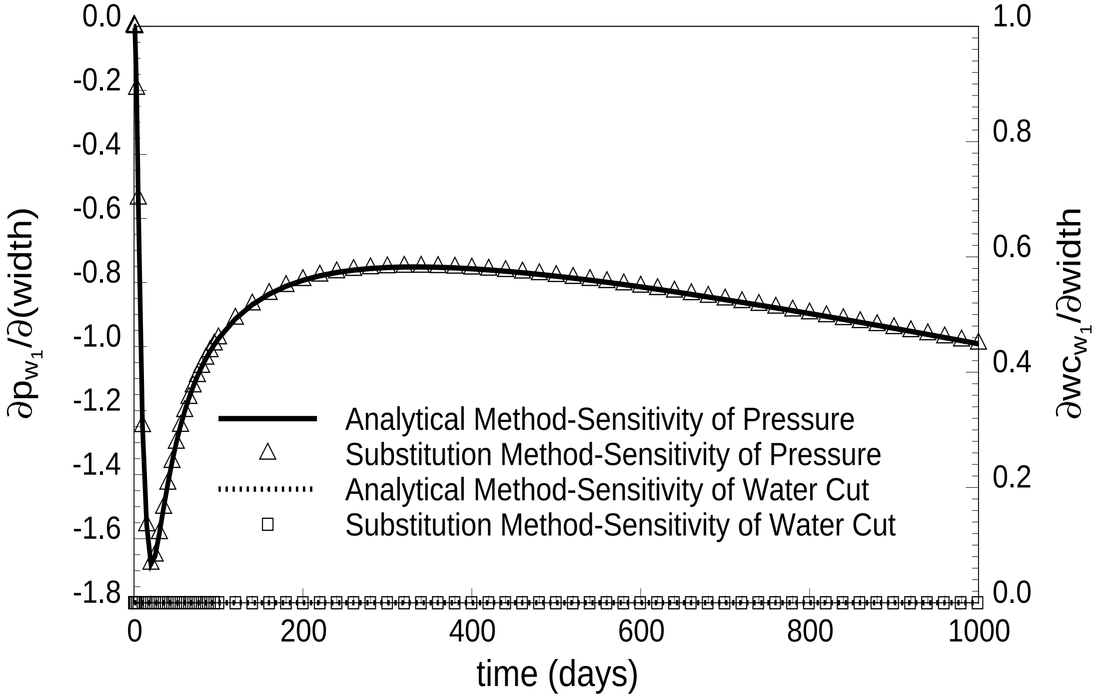

Figure 5.52: Sensitivity of pressure and water cut at well # 1 with respect to the channel width.

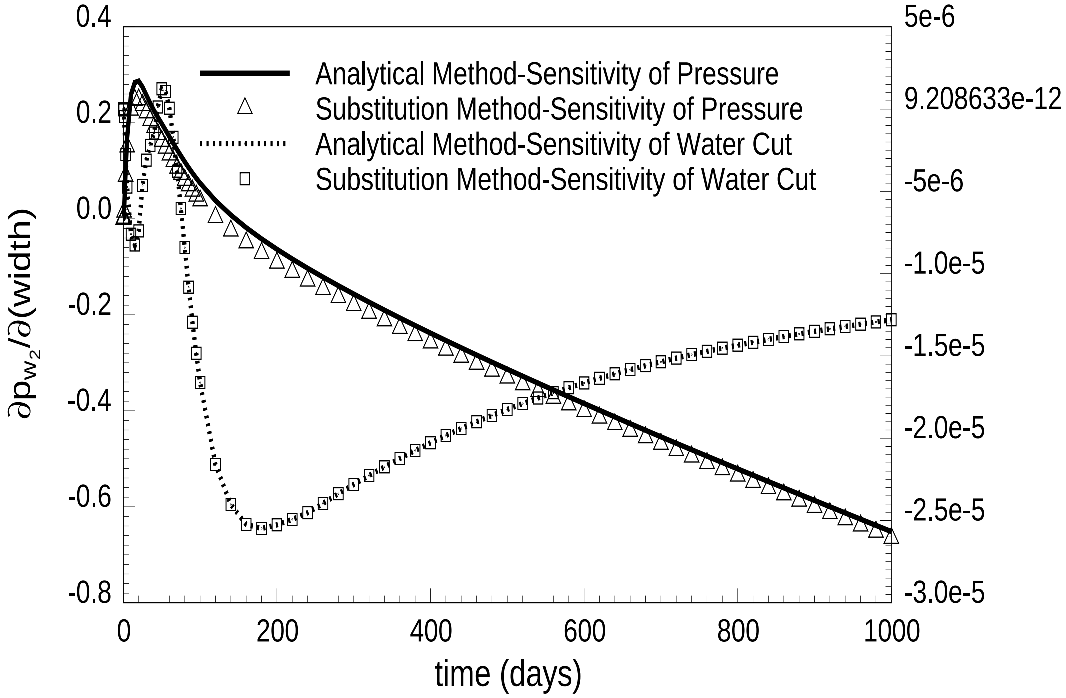

Figure 5.53: Sensitivity of pressure and water cut at well # 2 with respect to the channel width.

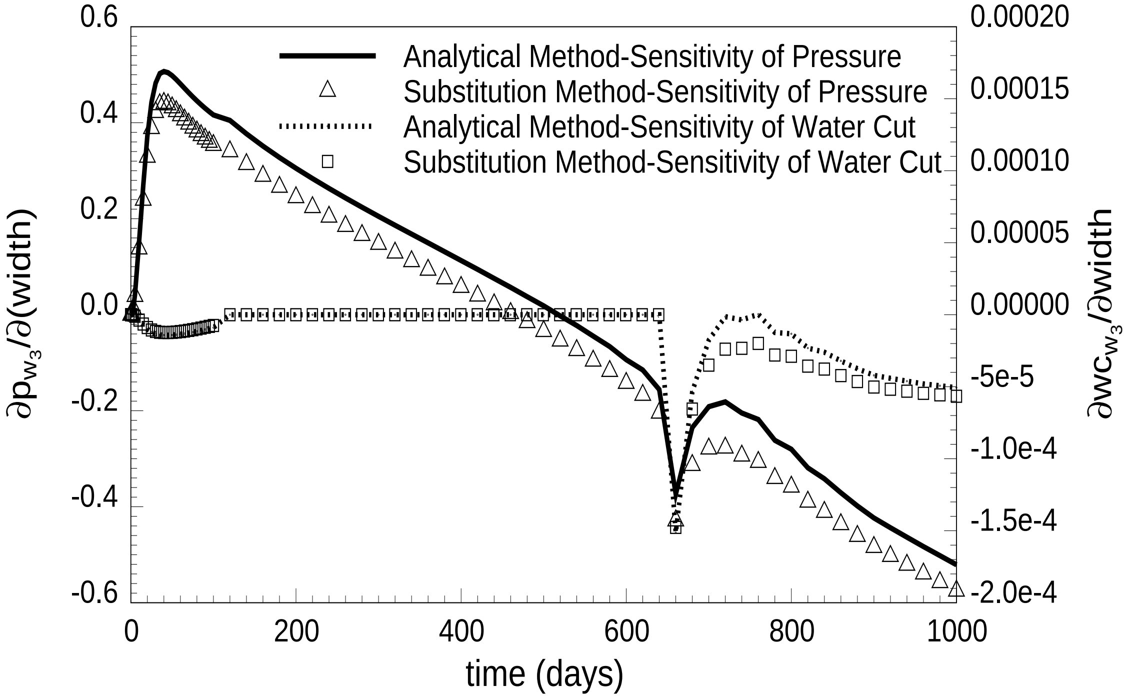

Figure 5.54: Sensitivity of pressure and water cut at well # 3 with respect to the channel width.

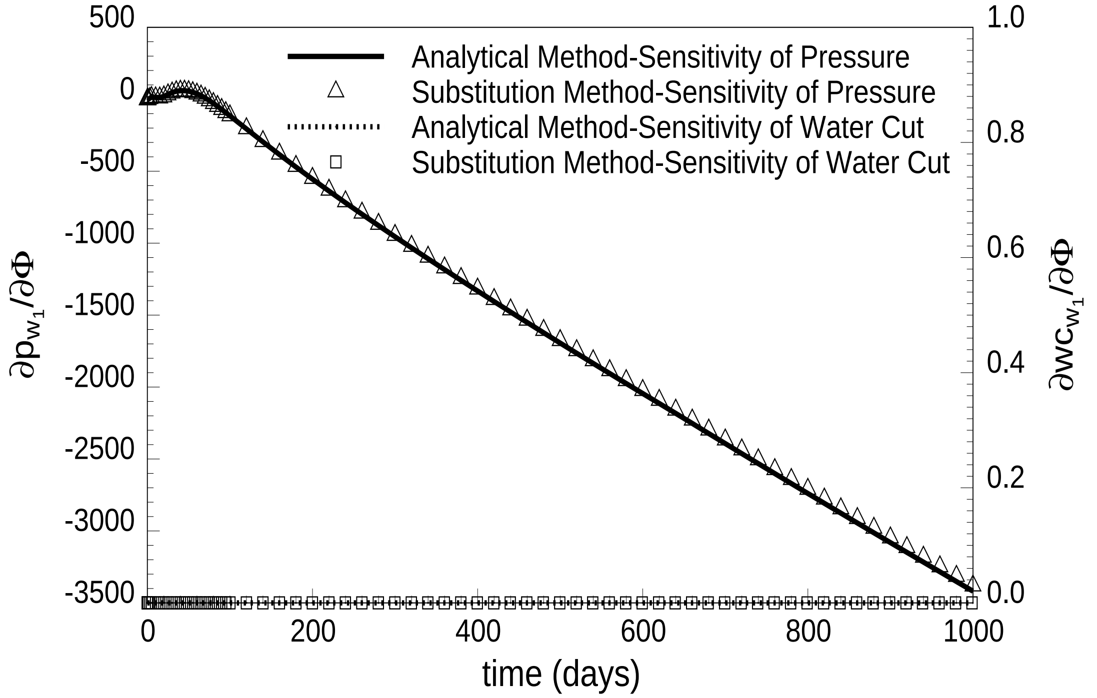

Figure 5.55: Sensitivity of pressure and water cut at well # 1 with respect to the channel porosity.

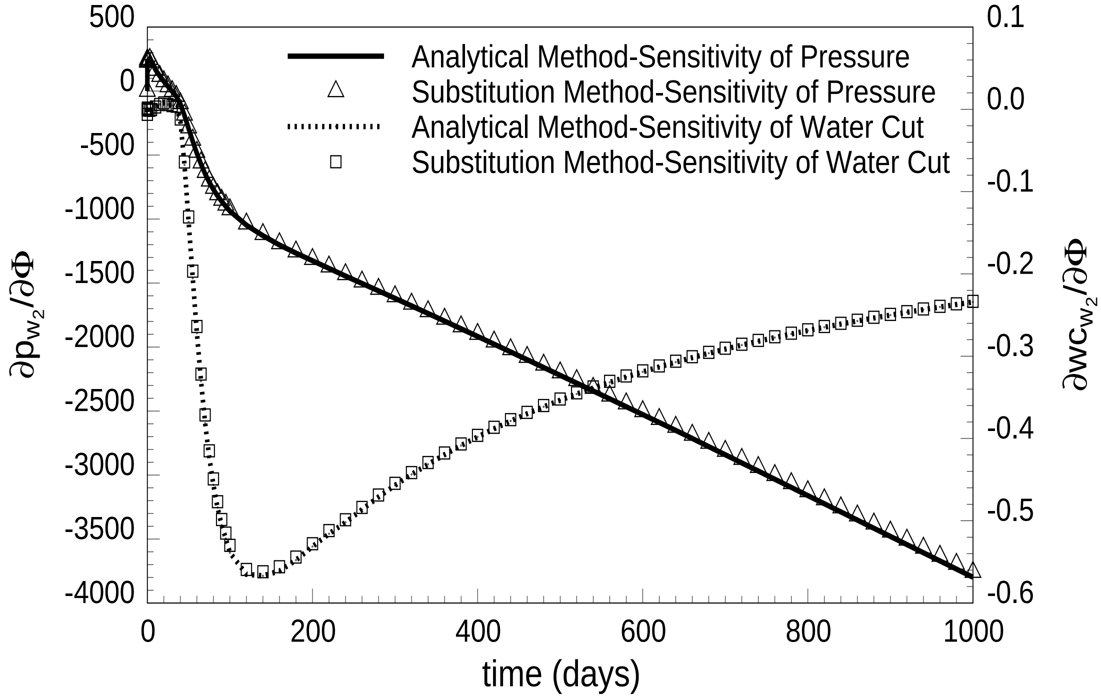

Figure 5.56: Sensitivity of pressure and water cut at well # 2 with respect to the channel porosity.

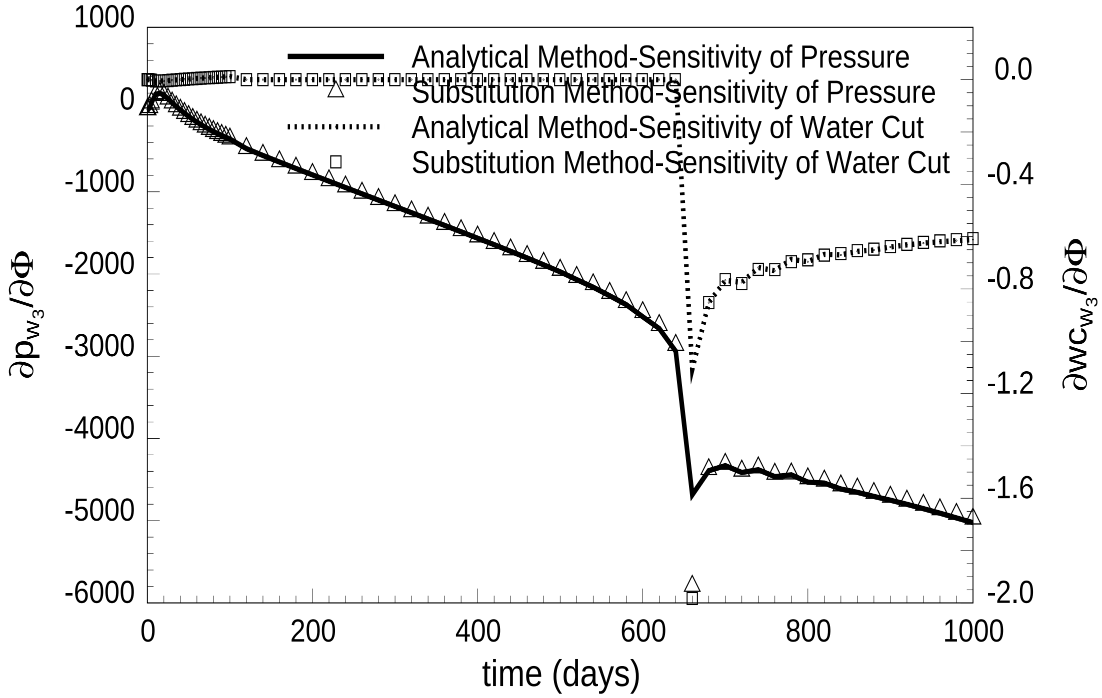

Figure 5.57: Sensitivity of pressure and water cut at well # 3 with respect to the channel porosity.

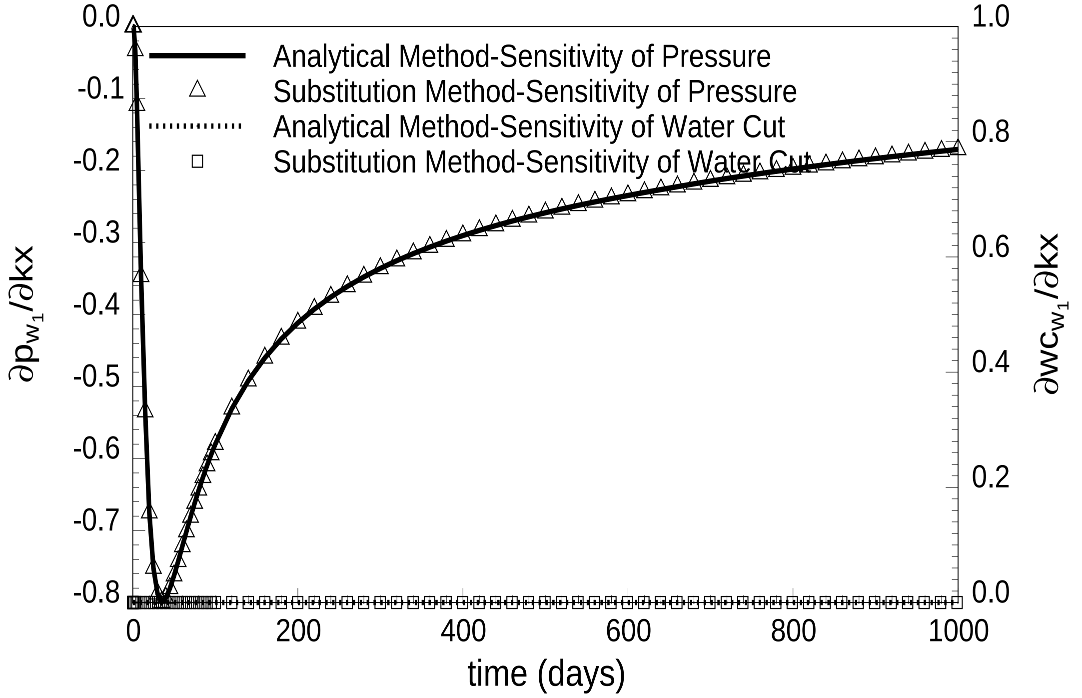

Figure 5.58: Sensitivity of pressure and water cut at well # 1 with respect to the channel permeability in x-direction.

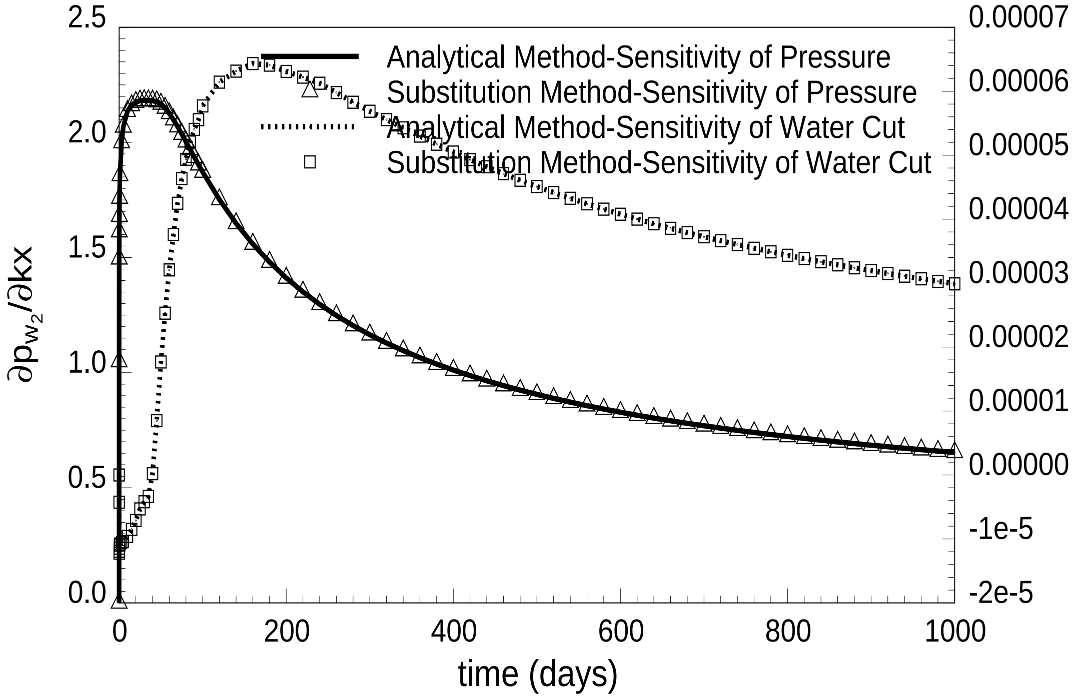

Figure 5.59: Sensitivity of pressure and water cut at well # 2 with respect to the channel permeability in x-direction.

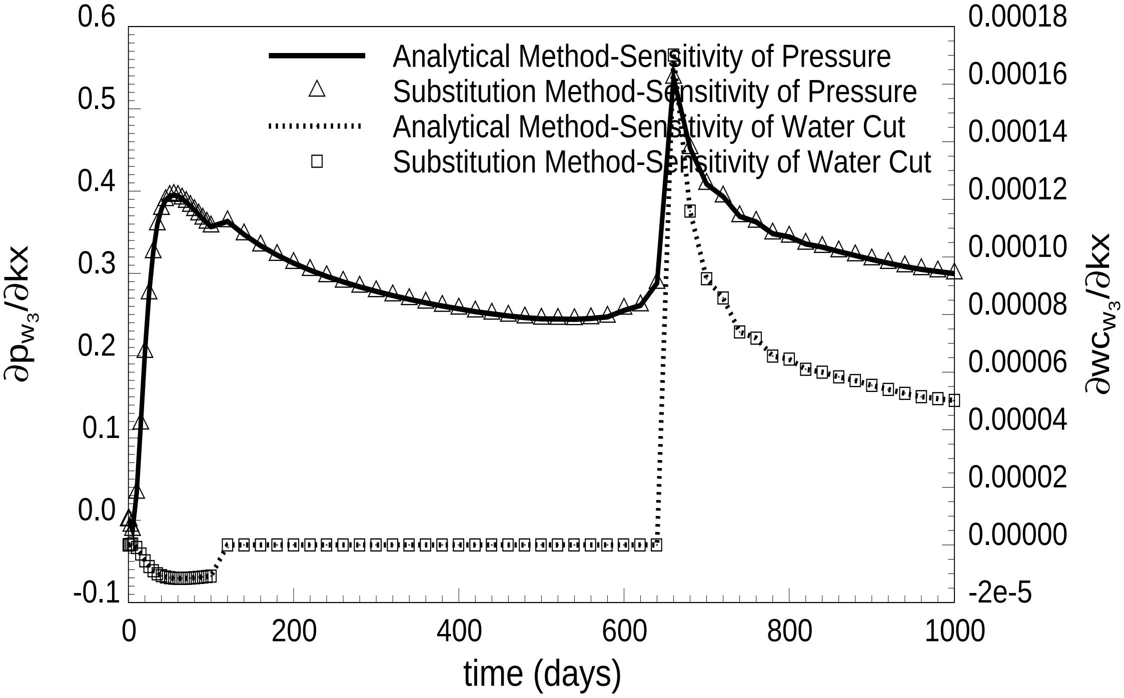

Figure 5.60: Sensitivity of pressure and water cut at well # 3 with respect to the channel permeability in x-direction.

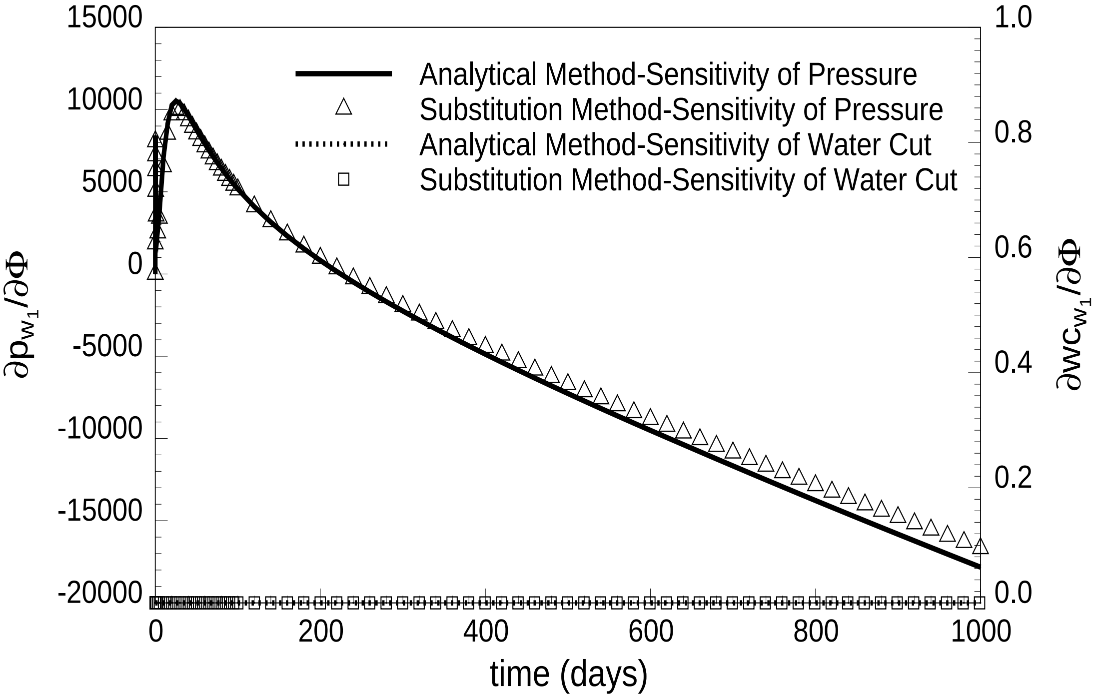

Figure 5.61: Sensitivity of pressure and water cut at well # 1 with respect to the background porosity.

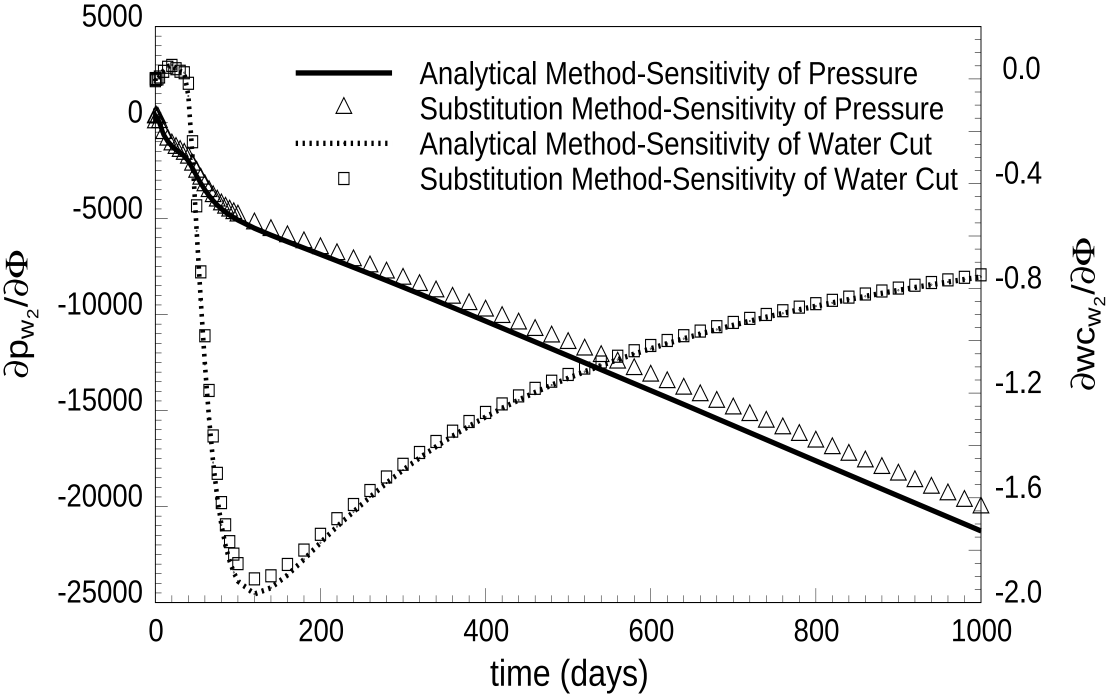

Figure 5.62: Sensitivity of pressure and water cut at well # 2 with respect to the background porosity.

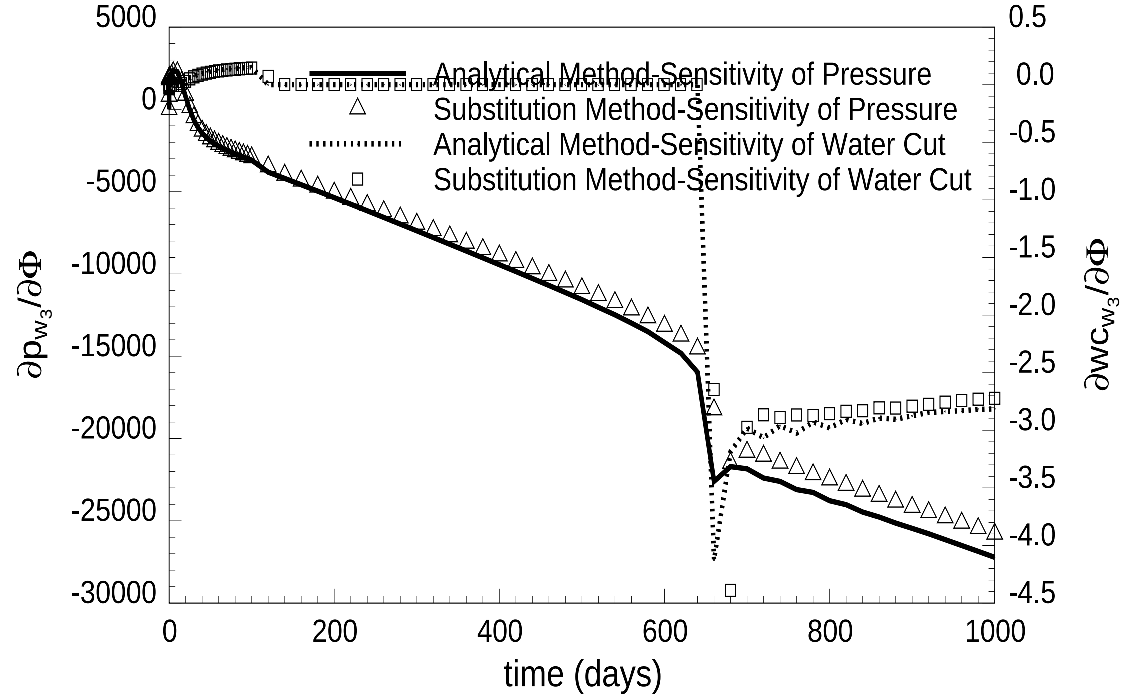

Figure 5.63: Sensitivity of pressure and water cut at well # 3 with respect to the background porosity.

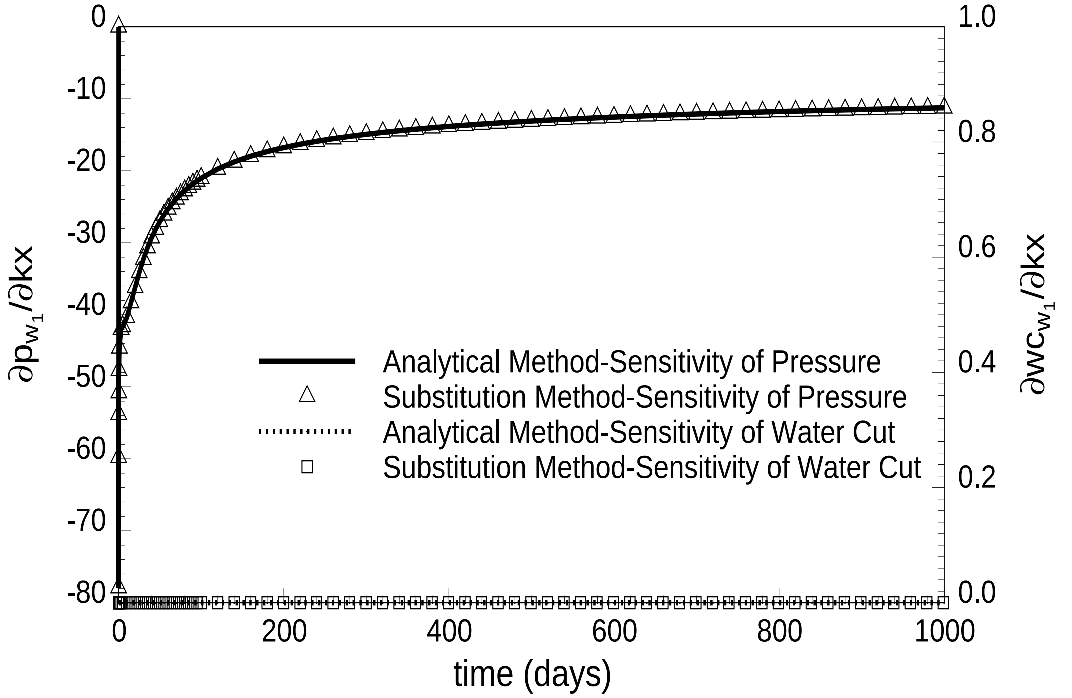

Figure 5.64: Sensitivity of pressure and water cut at well # 1 with respect to the background permeability in *x*-direction.

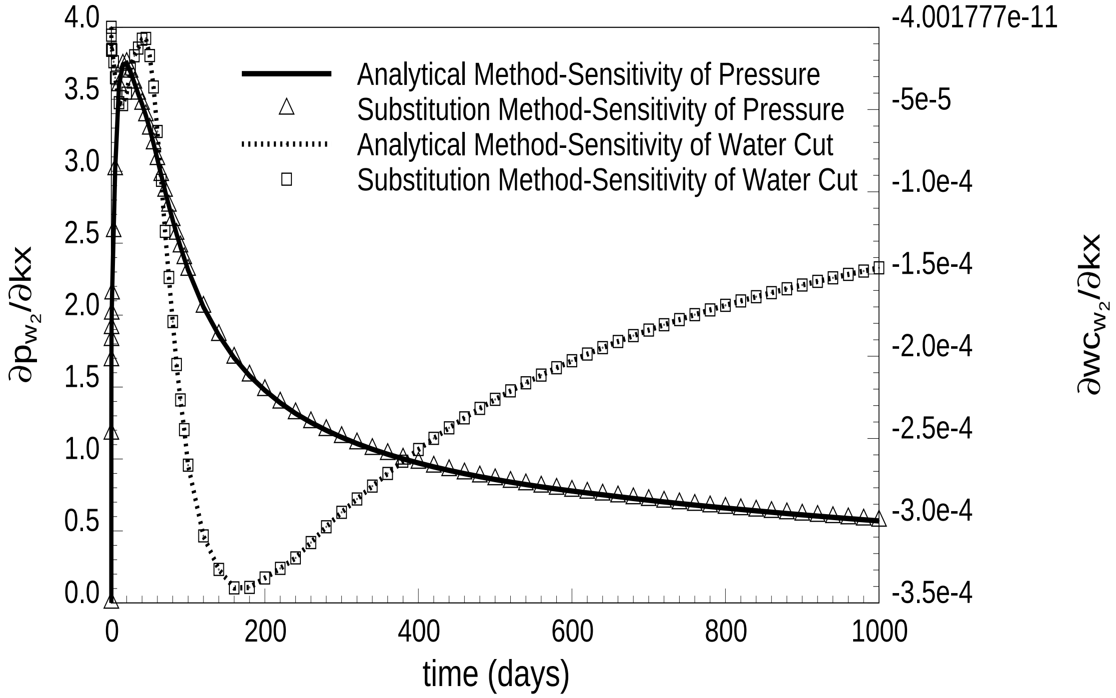

Figure 5.65: Sensitivity of pressure and water cut at well # 2 with respect to the background permeability in x-direction.

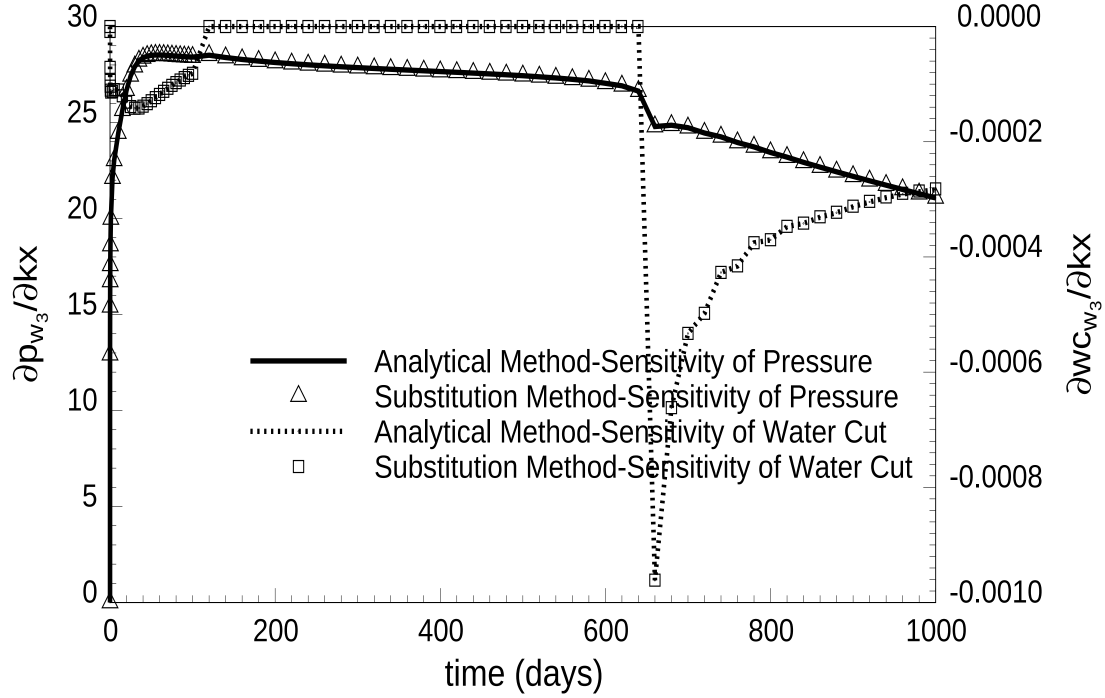

Figure 5.66: Sensitivity of pressure and water cut at well # 3 with respect to the background permeability in x-direction.

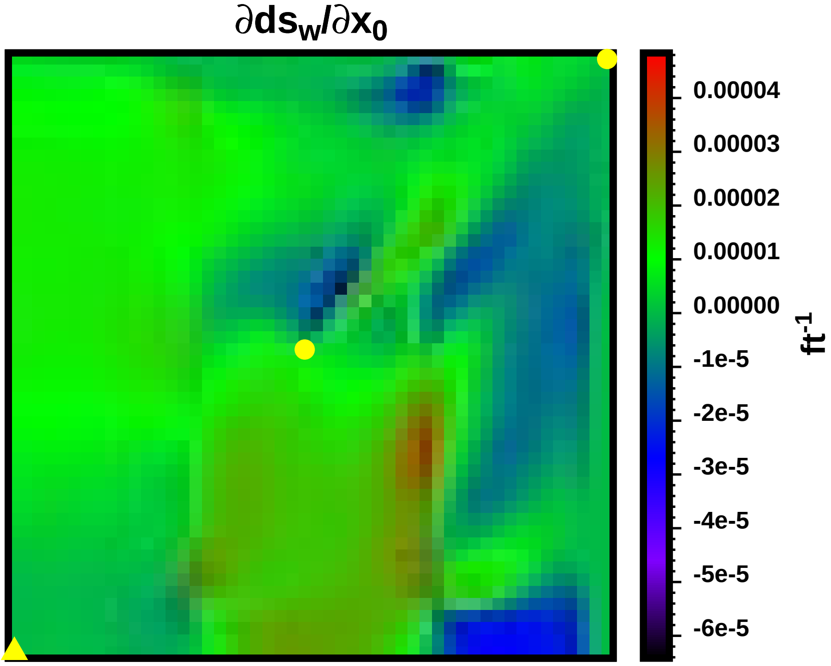

Figure 5.67: Sensitivity of the average change in water saturation between 100 and 800 days with respect to the channel translation in $x-$ direction, as calculated by analytical method.

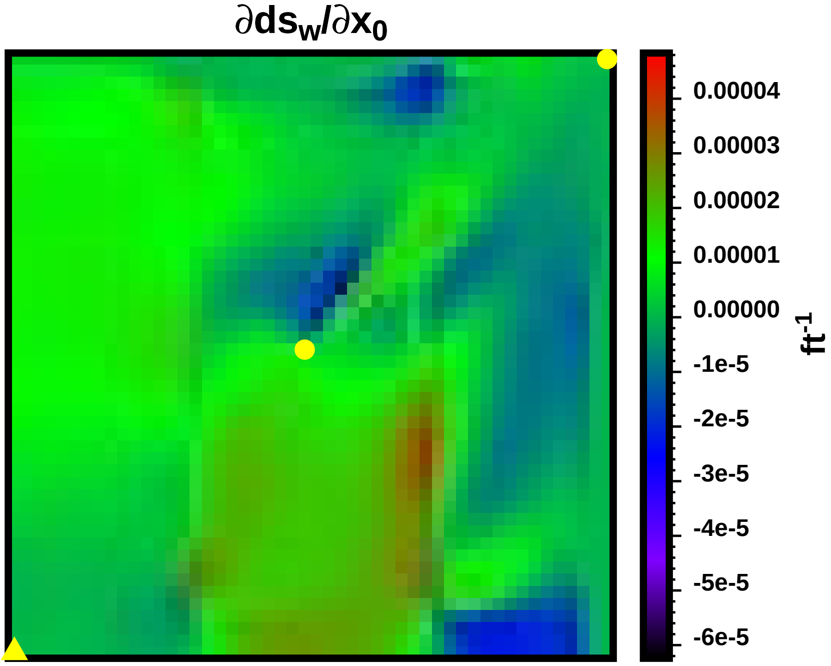

Figure 5.68: Sensitivity of the average change in water saturation between 100 and 800 days with respect to the channel translation in $x-$ directioni, as calculated by substitution method.

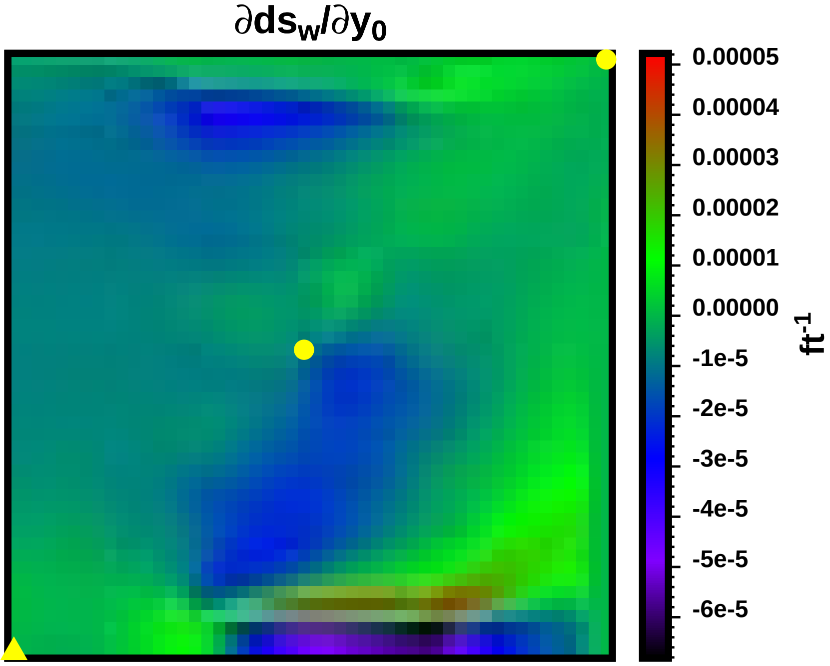

Figure 5.69: Sensitivity of the average change in water saturation between 100 and 800 days with respect to the channel translation in $y-$ direction, as calculated by analytical method.

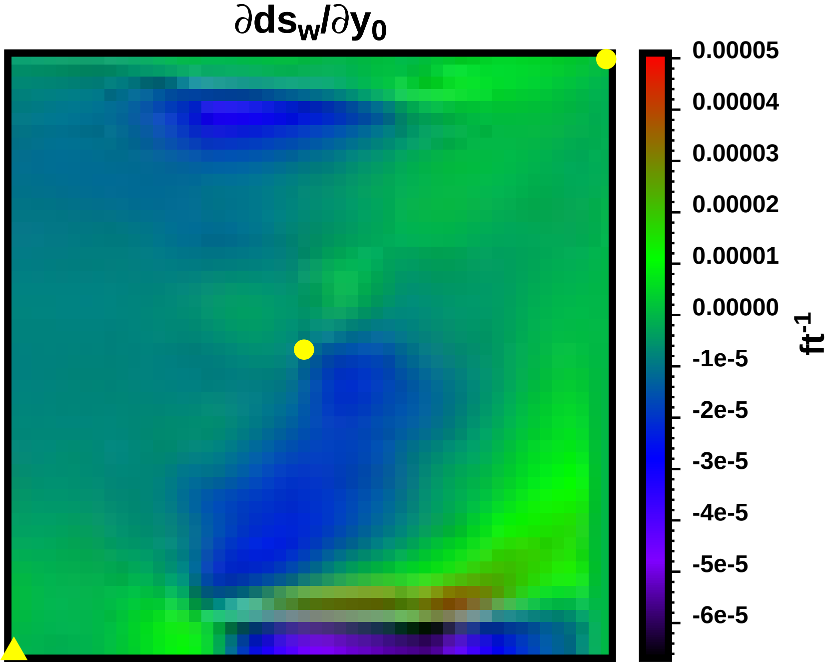

Figure 5.70: Sensitivity of the average change in water saturation between 100 and 800 days with respect to the channel translation in $y-$ directioni, as calculated by substitution method.

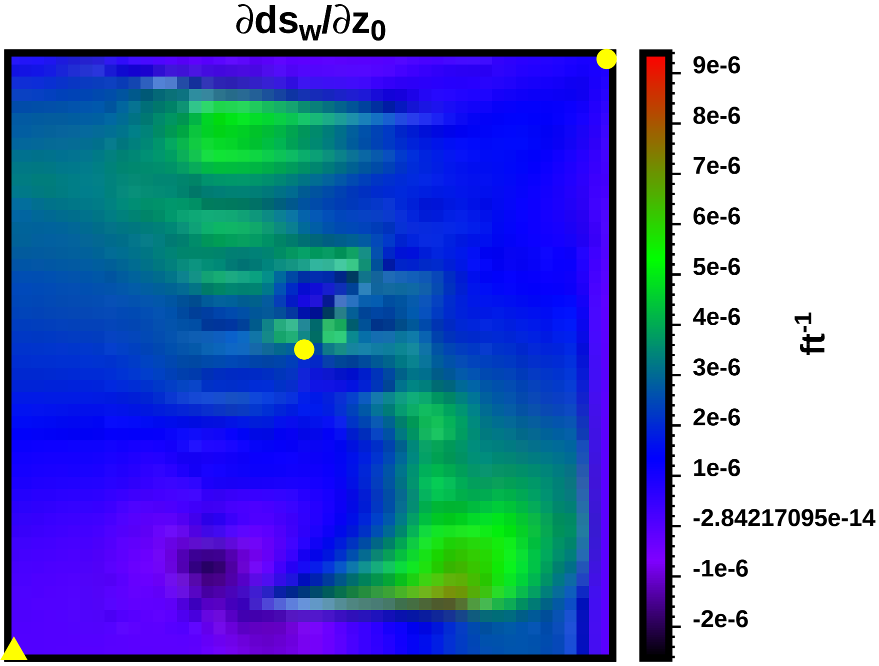

Figure 5.71: Sensitivity of the average change in water saturation between 100 and 800 days with respect to the channel translation in $z-$ direction, as calculated by analytical method.

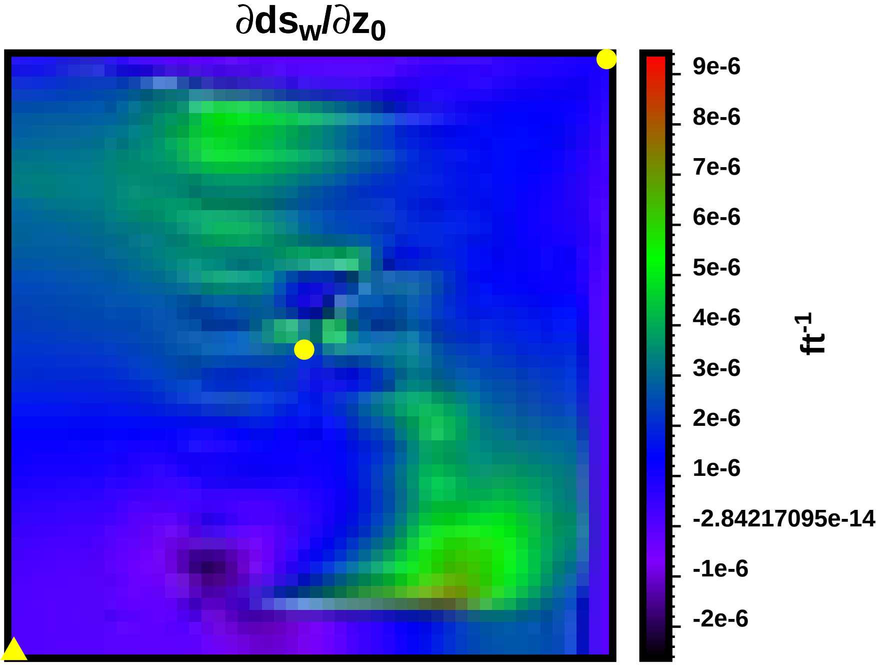

Figure 5.72: Sensitivity of the average change in water saturation between 100 and 800 days with respect to the channel translation in $z-$ directioni, as calculated by substitution method.

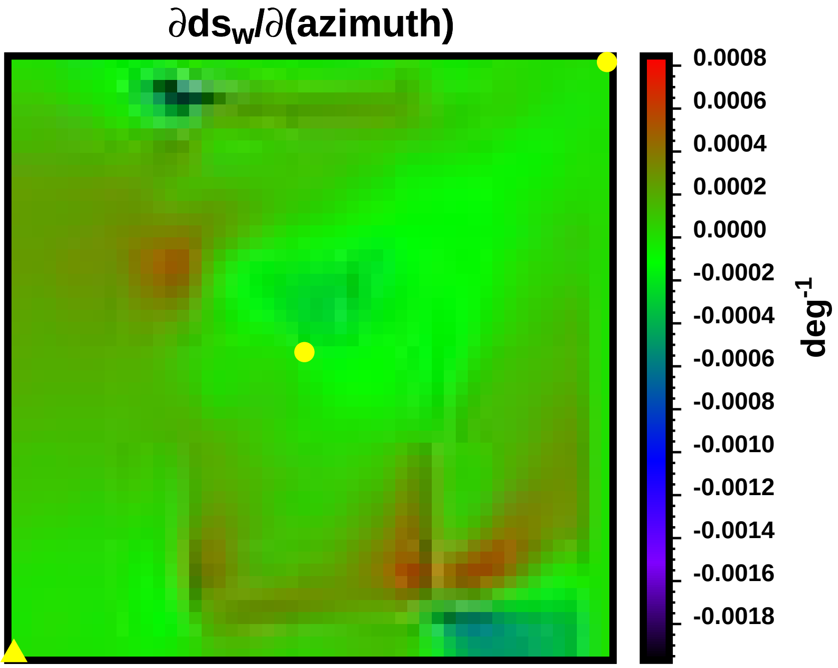

Figure 5.73: Sensitivity of the average change in water saturation between 100 and 800 days with respect to the channel azimuth, as calculated by analytical method.

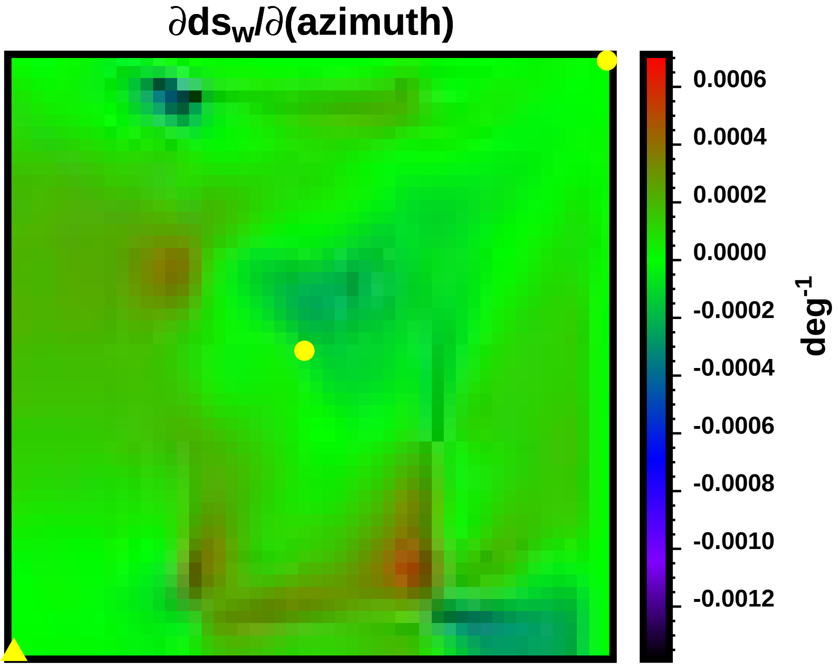

Figure 5.74: Sensitivity of the average change in water saturation between 100 and 800 days with respect to the channel azimuth, as calculated by substitution method.

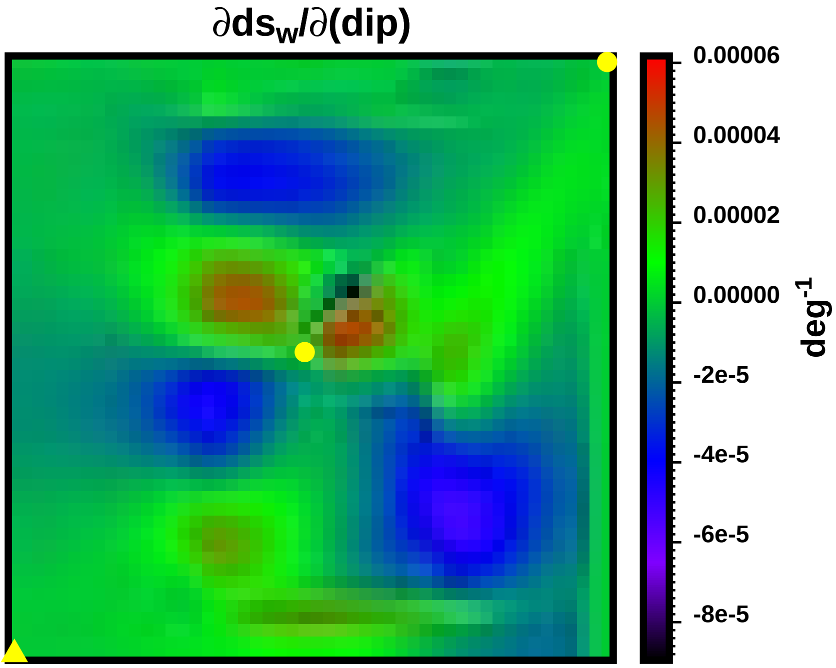

Figure 5.75: Sensitivity of the average change in water saturation between 100 and 800 days with respect to the channel dip, as calculated by analytical method.

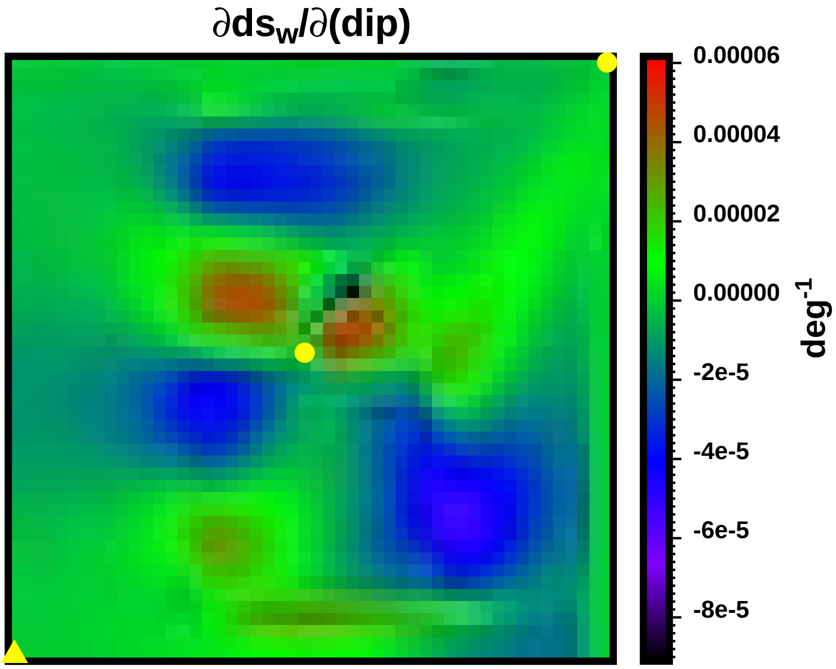

Figure 5.76: Sensitivity of the average change in water saturation between 100 and 800 days with respect to the channel dip, as calculated by substitution method.

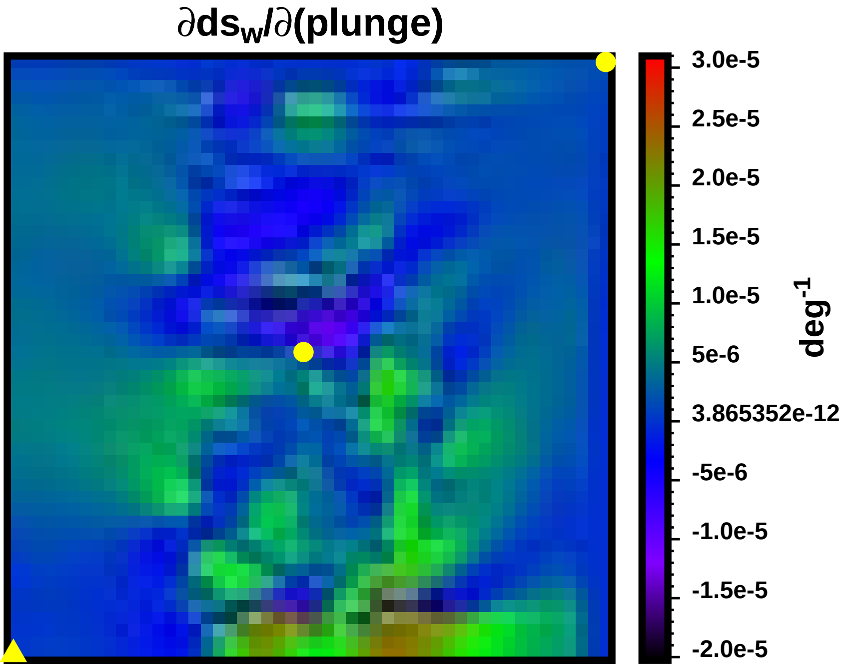

Figure 5.77: Sensitivity of the average change in water saturation between 100 and 800 days with respect to the channel plunge, as calculated by analytical method.

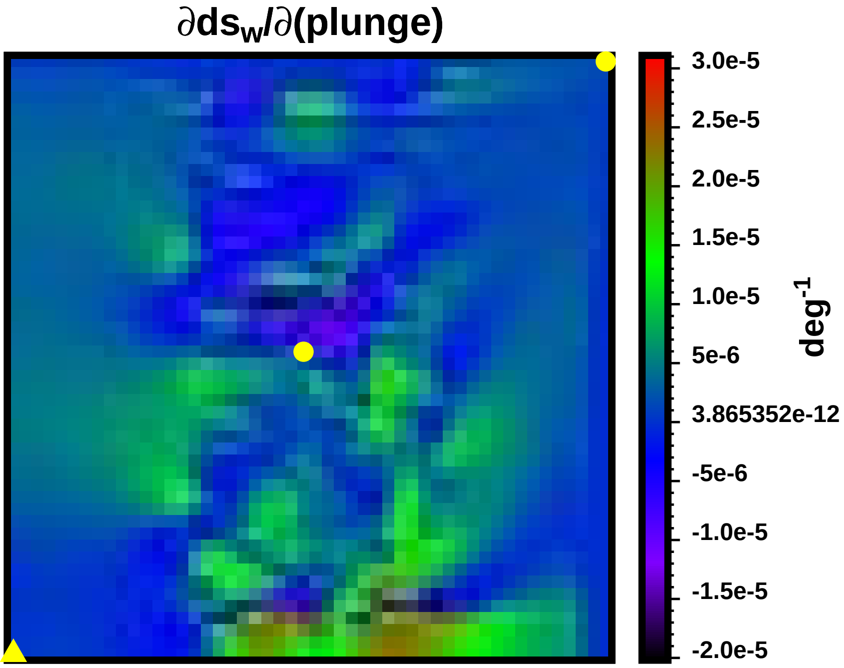

Figure 5.78: Sensitivity of the average change in water saturation between 100 and 800 days with respect to the channel plunge, as calculated by substitution method.

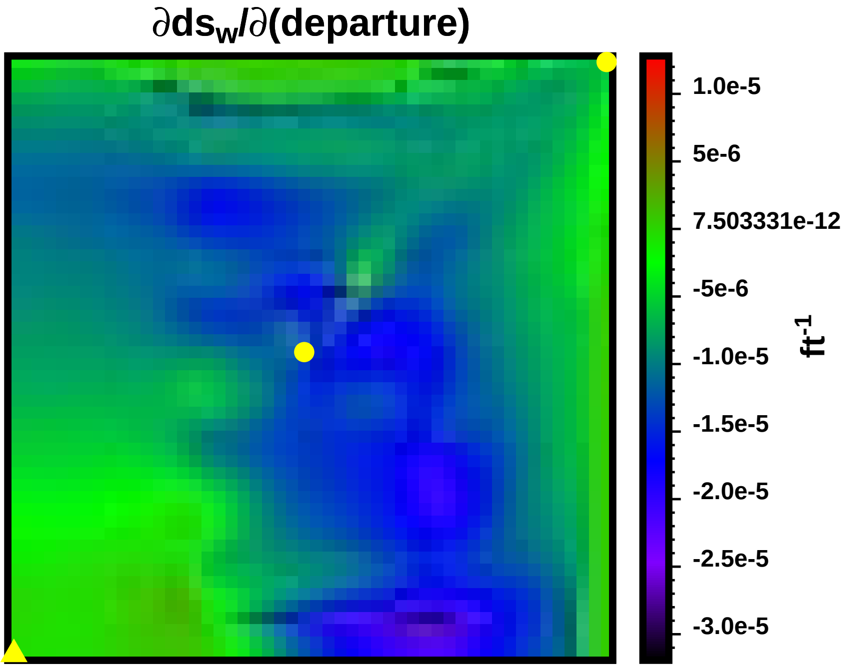

Figure 5.79: Sensitivity of the average change in water saturation between 100 and 800 days with respect to the channel departure, as calculated by analytical method.

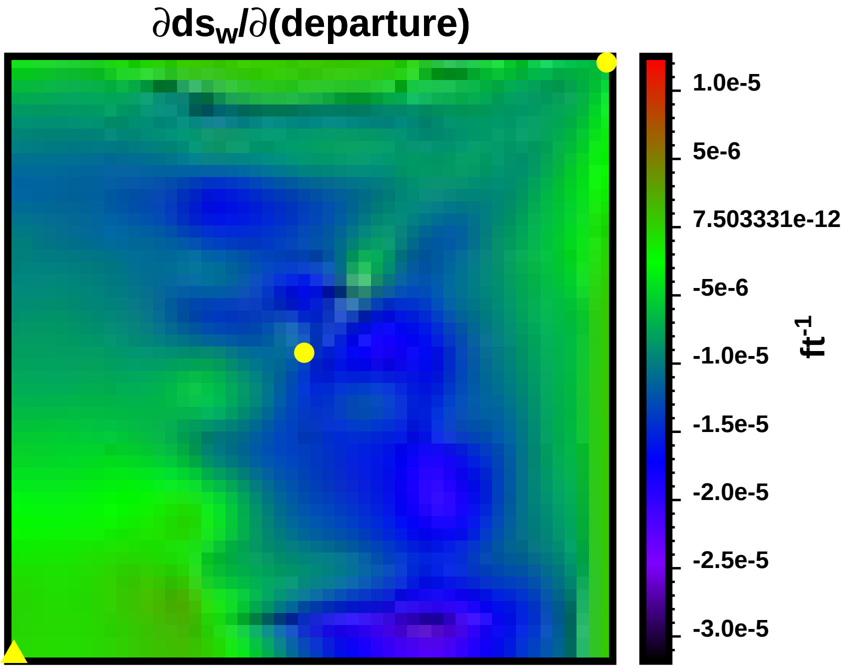

Figure 5.80: Sensitivity of the average change in water saturation between 100 and 800 days with respect to the channel departure, as calculated by substitution method.

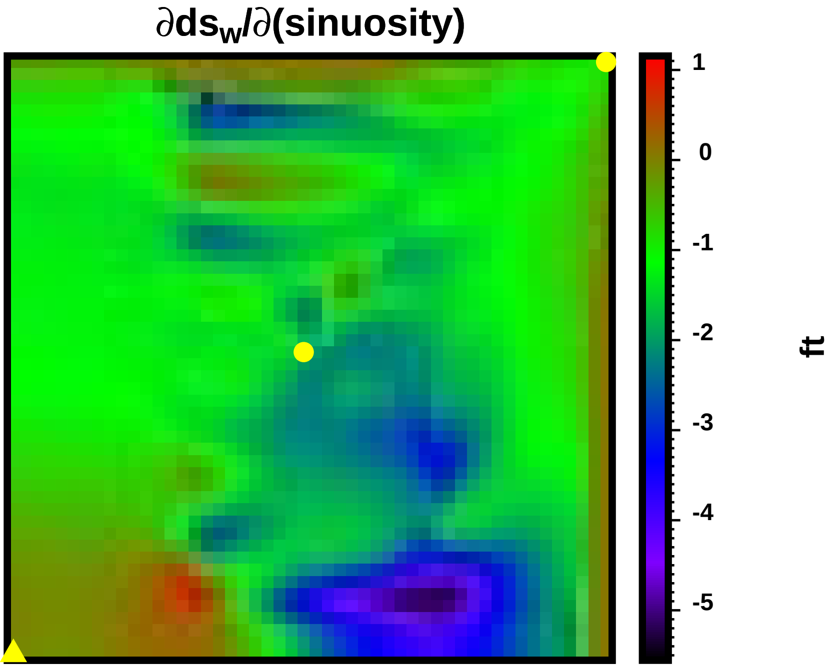

Figure 5.81: Sensitivity of the average change in water saturation between 100 and 800 days with respect to the channel sinuosity, as calculated by analytical method.

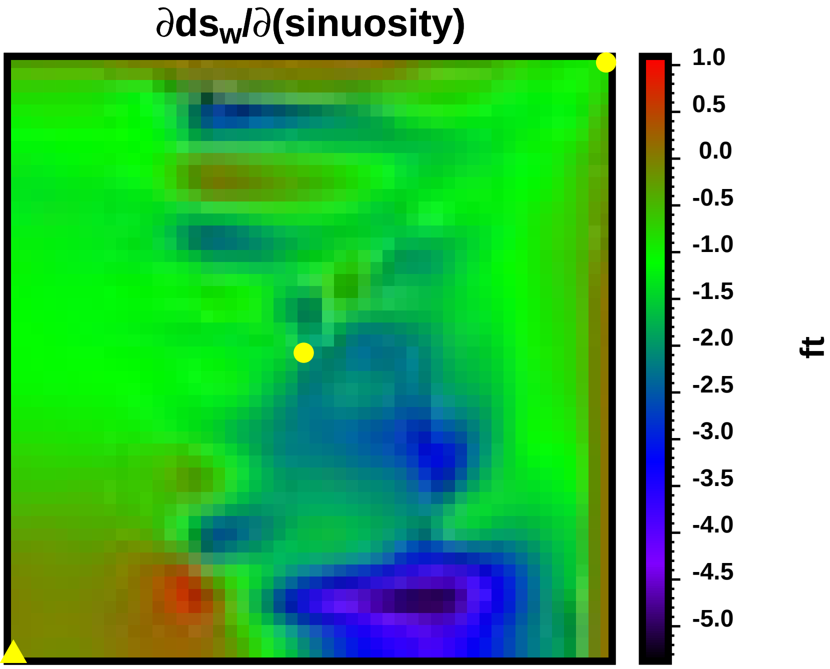

Figure 5.82: Sensitivity of the average change in water saturation between 100 and 800 days with respect to the channel sinuosity, as calculated by substitution method.

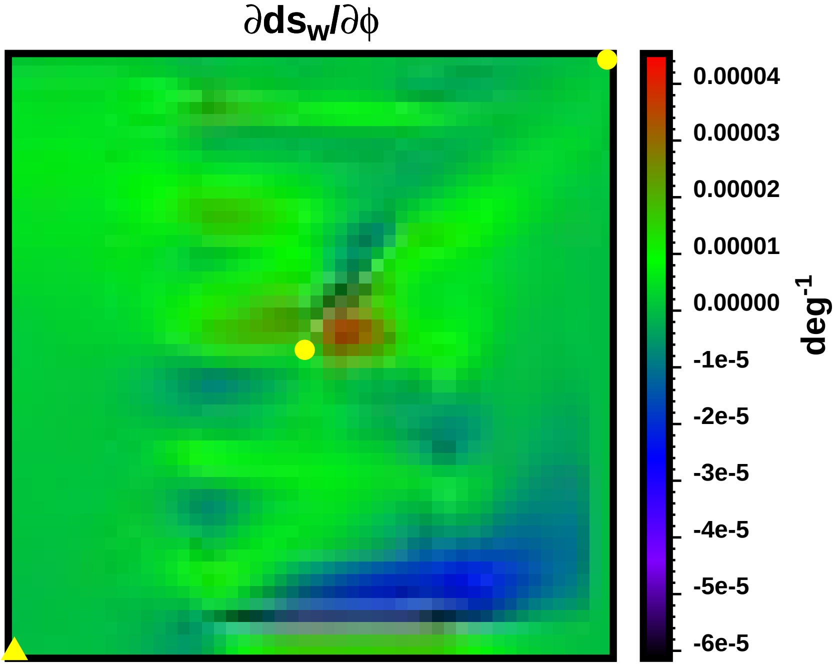

Figure 5.83: Sensitivity of the average change in water saturation between 100 and 800 days with respect to the channel displacement, as calculated by analytical method.

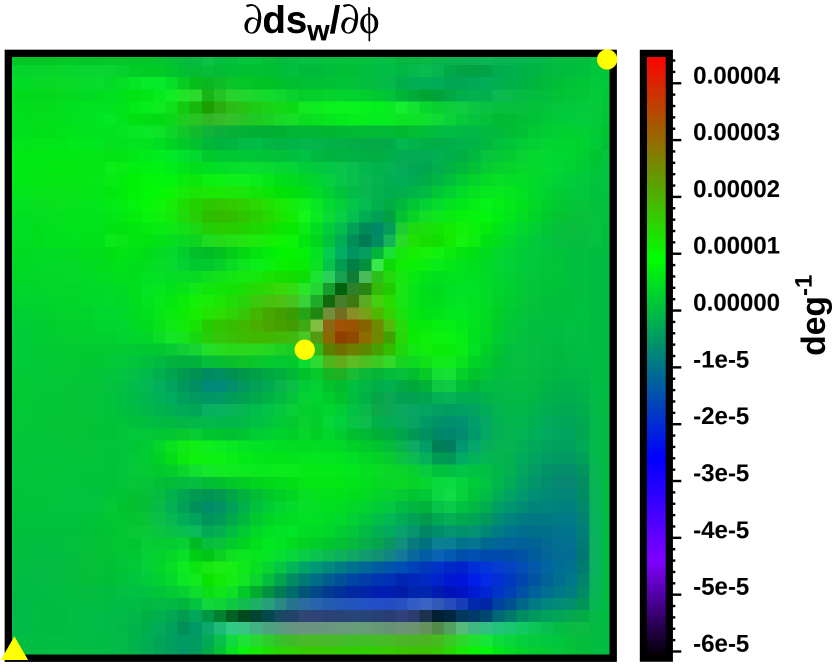

Figure 5.84: Sensitivity of the average change in water saturation between 100 and 800 days with respect to the channel displacement, as calculated by substitution method.

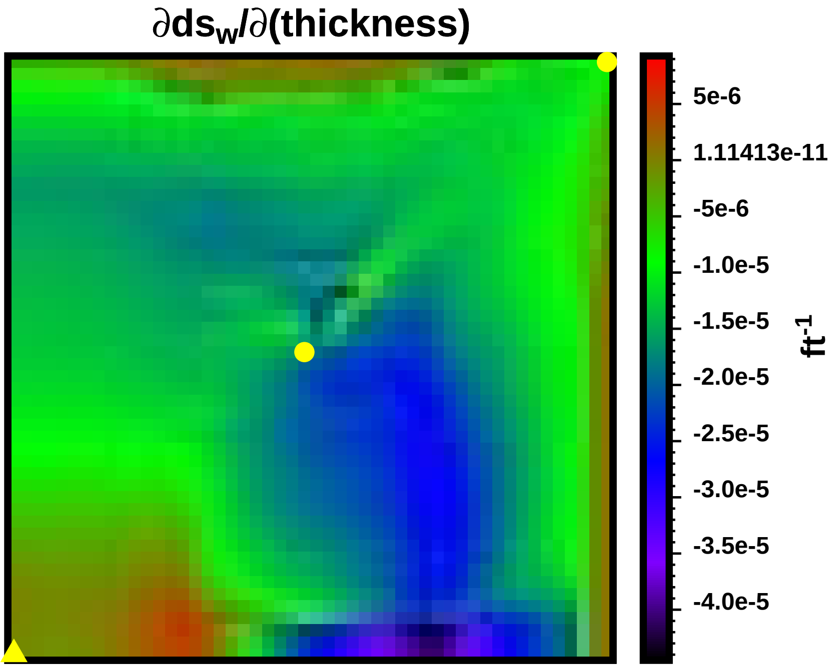

Figure 5.85: Sensitivity of the average change in water saturation between 100 and 800 days with respect to the channel thickness, as calculated by analytical method.

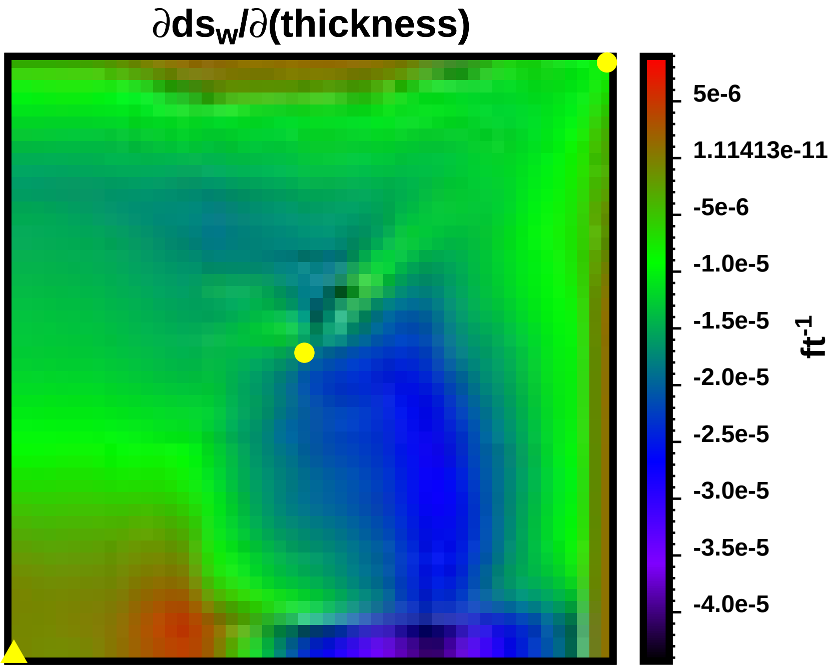

Figure 5.86: Sensitivity of the average change in water saturation between 100 and 800 days with respect to the channel thickness, as calculated by substitution method.

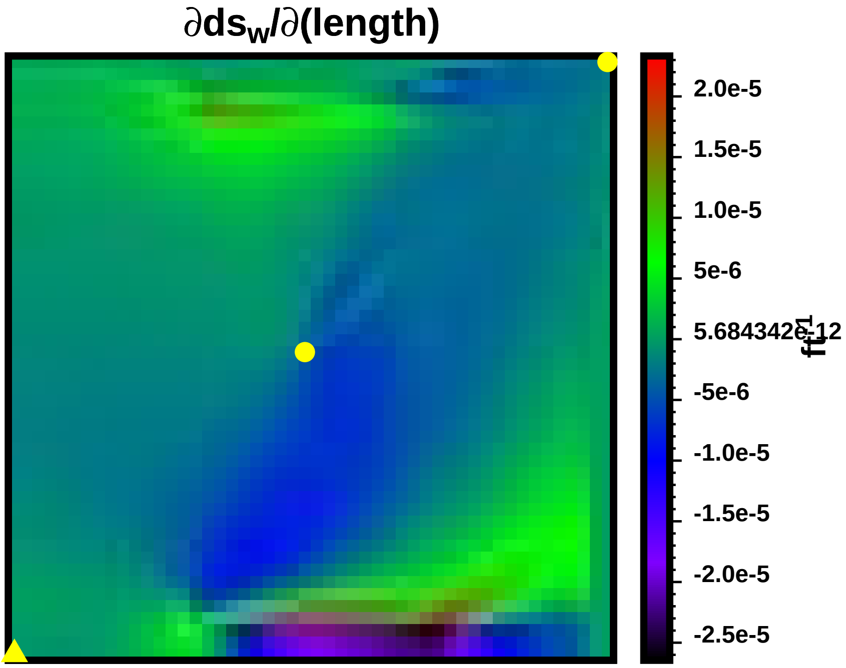

Figure 5.87: Sensitivity of the average change in water saturation between 100 and 800 days with respect to the channel length, as calculated by analytical method.

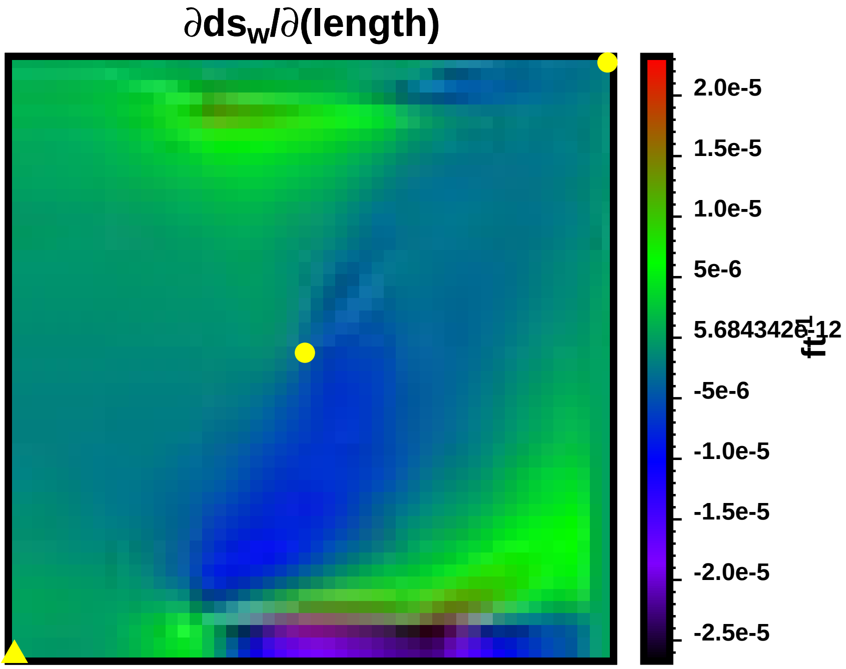

Figure 5.88: Sensitivity of the average change in water saturation between 100 and 800 days with respect to the channel length, as calculated by substitution method.

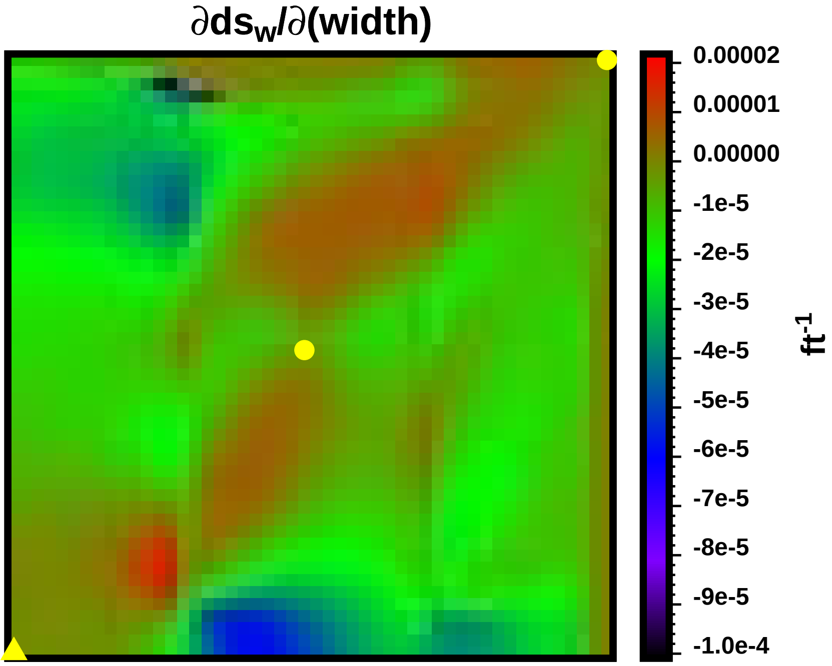

Figure 5.89: Sensitivity of the average change in water saturation between 100 and 800 days with respect to the channel width, as calculated by analytical method.

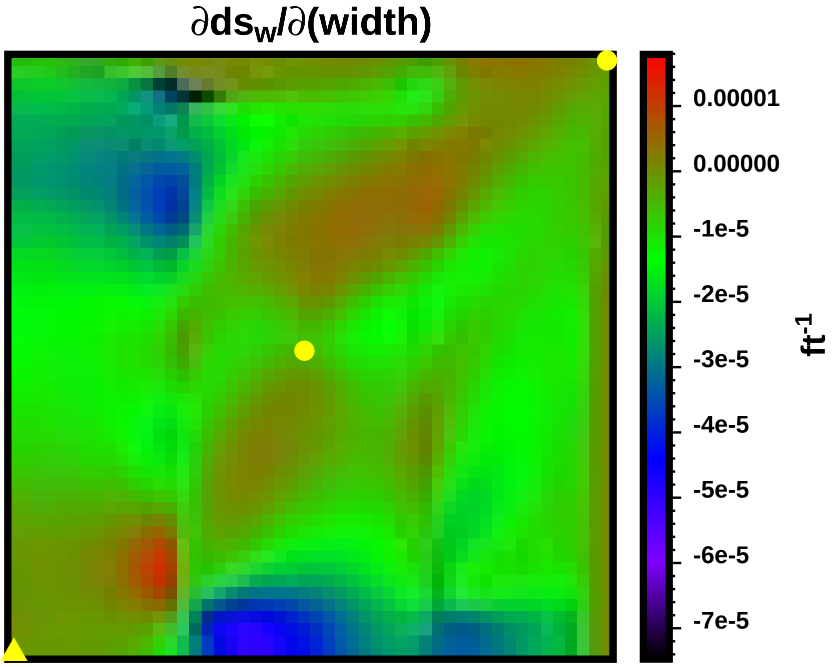

Figure 5.90: Sensitivity of the average change in water saturation between 100 and 800 days with respect to the channel width, as calculated by substitution method.

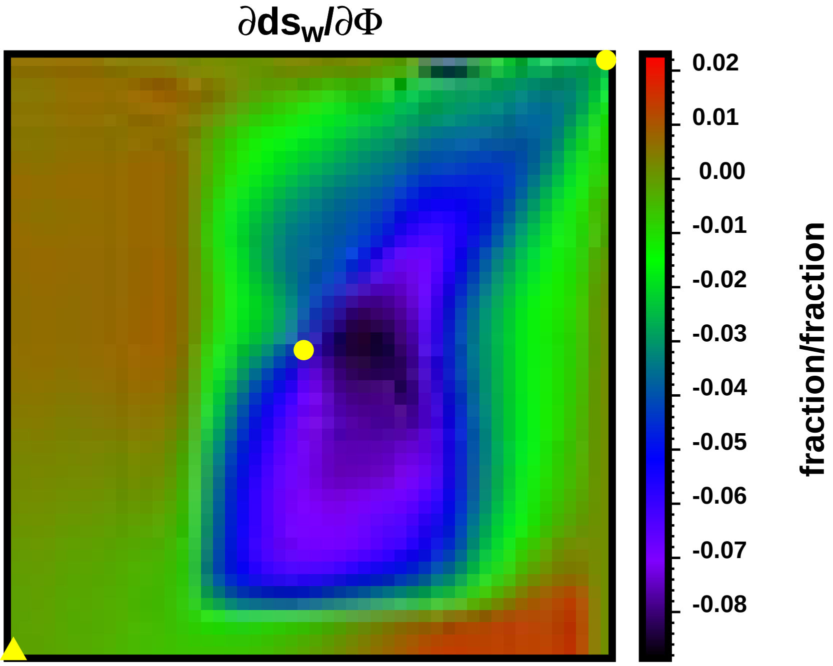

Figure 5.91: Sensitivity of the average change in water saturation between 100 and 800 days with respect to the channel porosity, as calculated by analytical method.

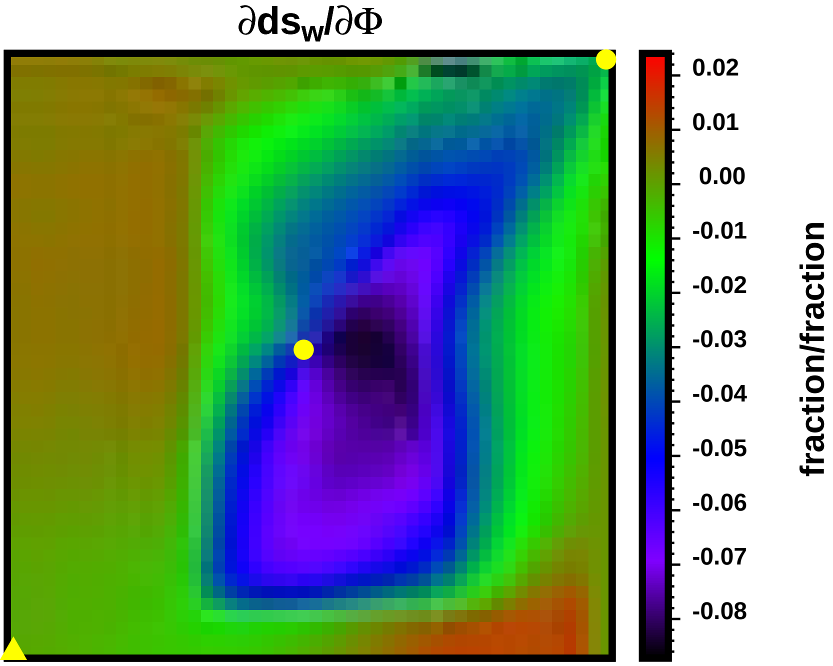

Figure 5.92: Sensitivity of the average change in water saturation between 100 and 800 days with respect to the channel porosity, as calculated by substitution method.

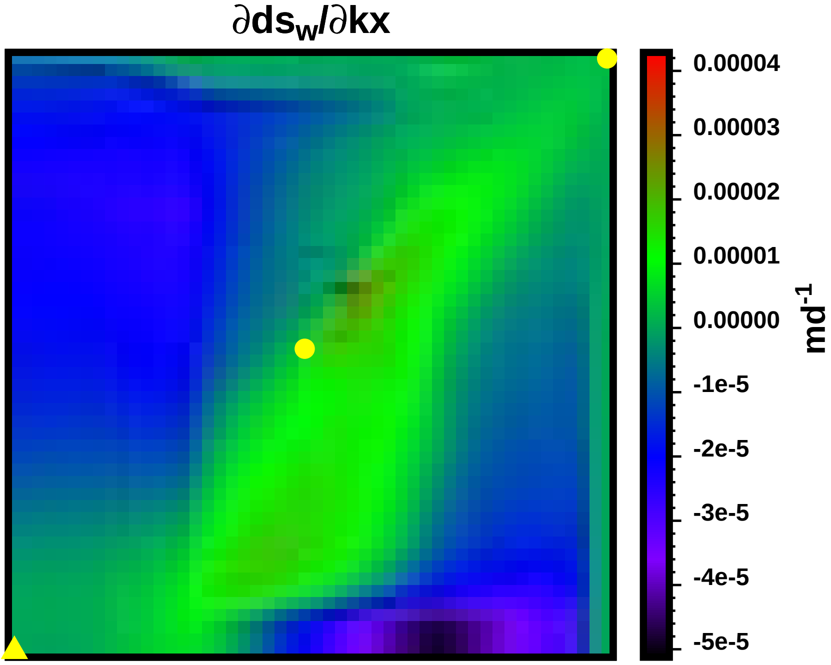

Figure 5.93: Sensitivity of the average change in water saturation between 100 and 800 days with respect to the channel permeability in x-direction, as calculated by analytical method.

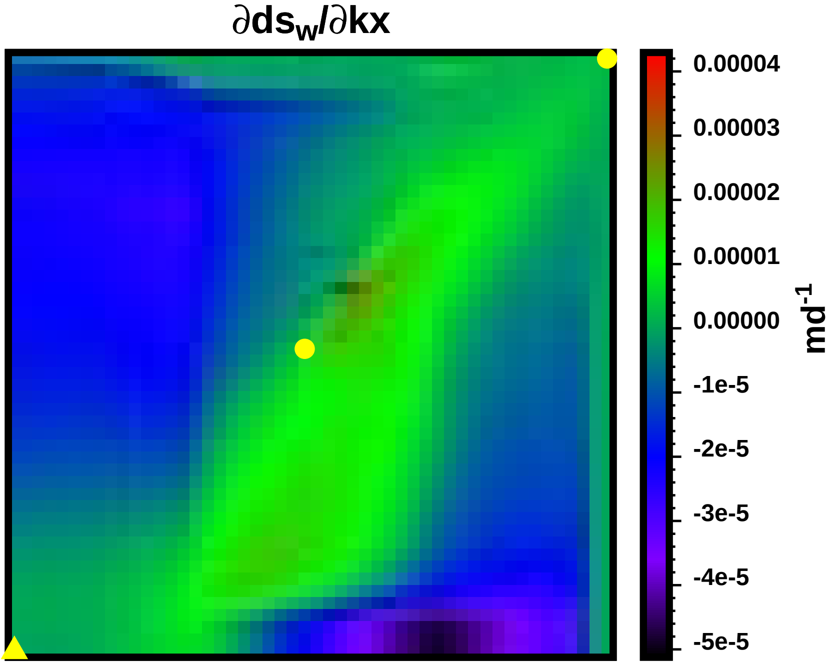

Figure 5.94: Sensitivity of the average change in water saturation between 100 and 800 days with respect to the channel permeability in x-direction, as calculated by substitution method.

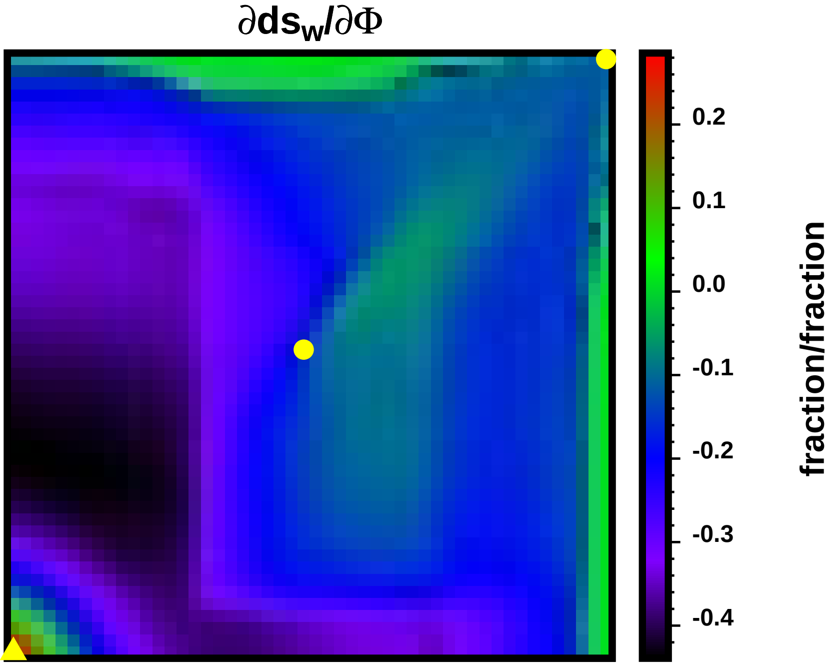

Figure 5.95: Sensitivity of the average change in water saturation between 100 and 800 days with respect to the background porosity, as calculated by analytical method.

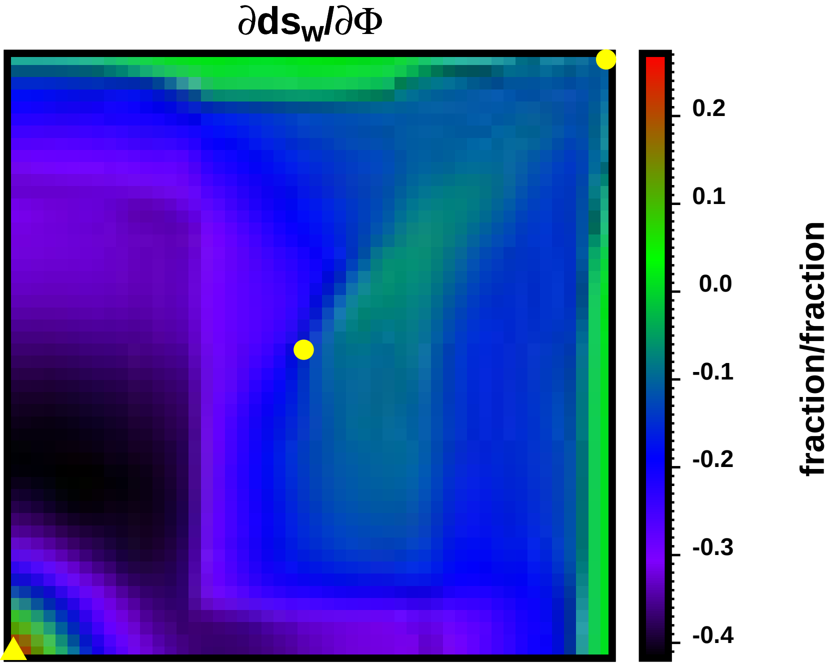

Figure 5.96: Sensitivity of the average change in water saturation between 100 and 800 days with respect to the background porosity, as calculated by substitution method.

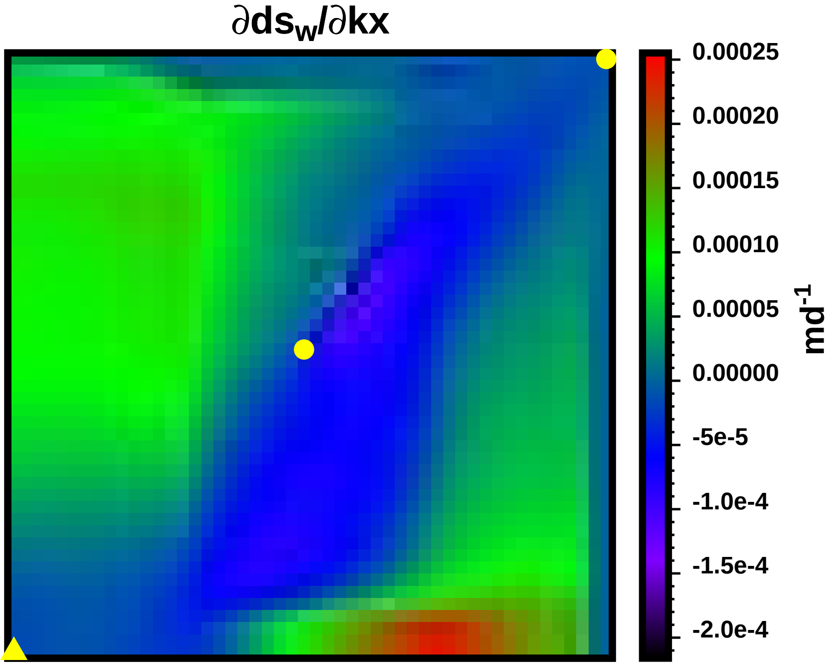

Figure 5.97: Sensitivity of the average change in water saturation between 100 and 800 days with respect to the background permeability in x-direction, as calculated by analytical method.

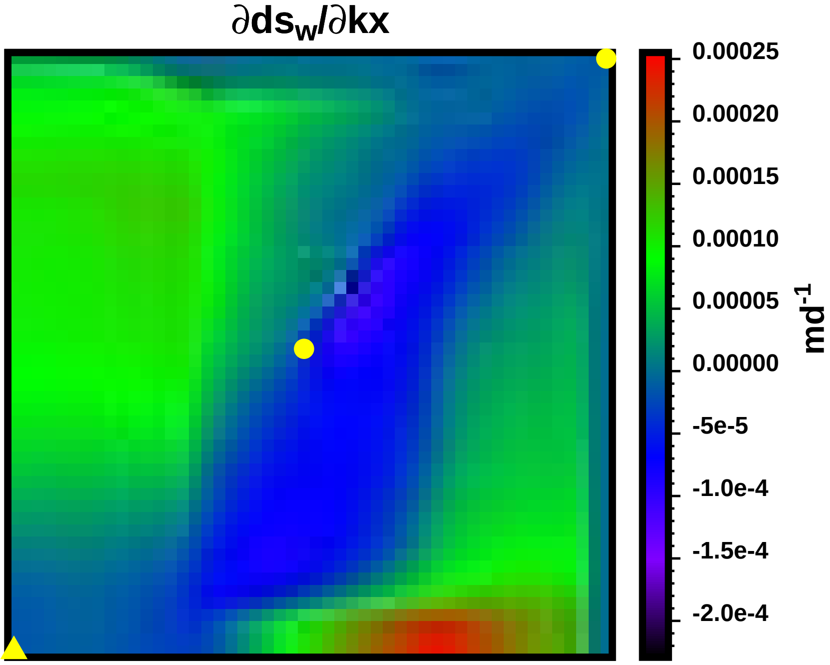

Figure 5.98: Sensitivity of the average change in water saturation between 100 and 800 days with respect to the background permeability in x-direction, as calculated by substitution method.

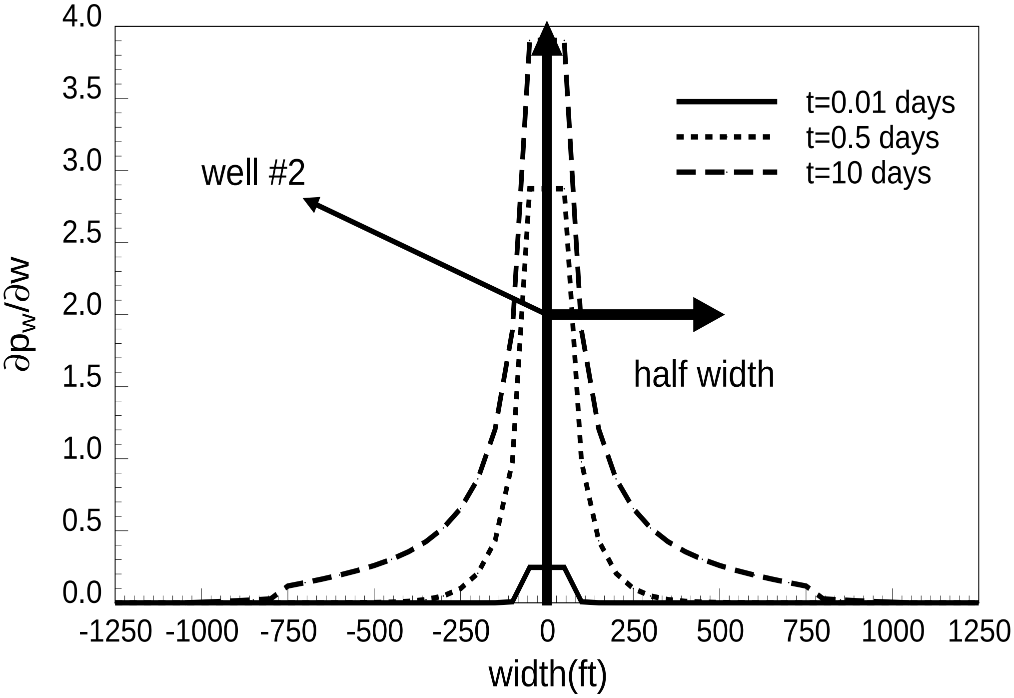

Figure 5.99: Sensitivity of pressure at well #2 with respect to the channel width.

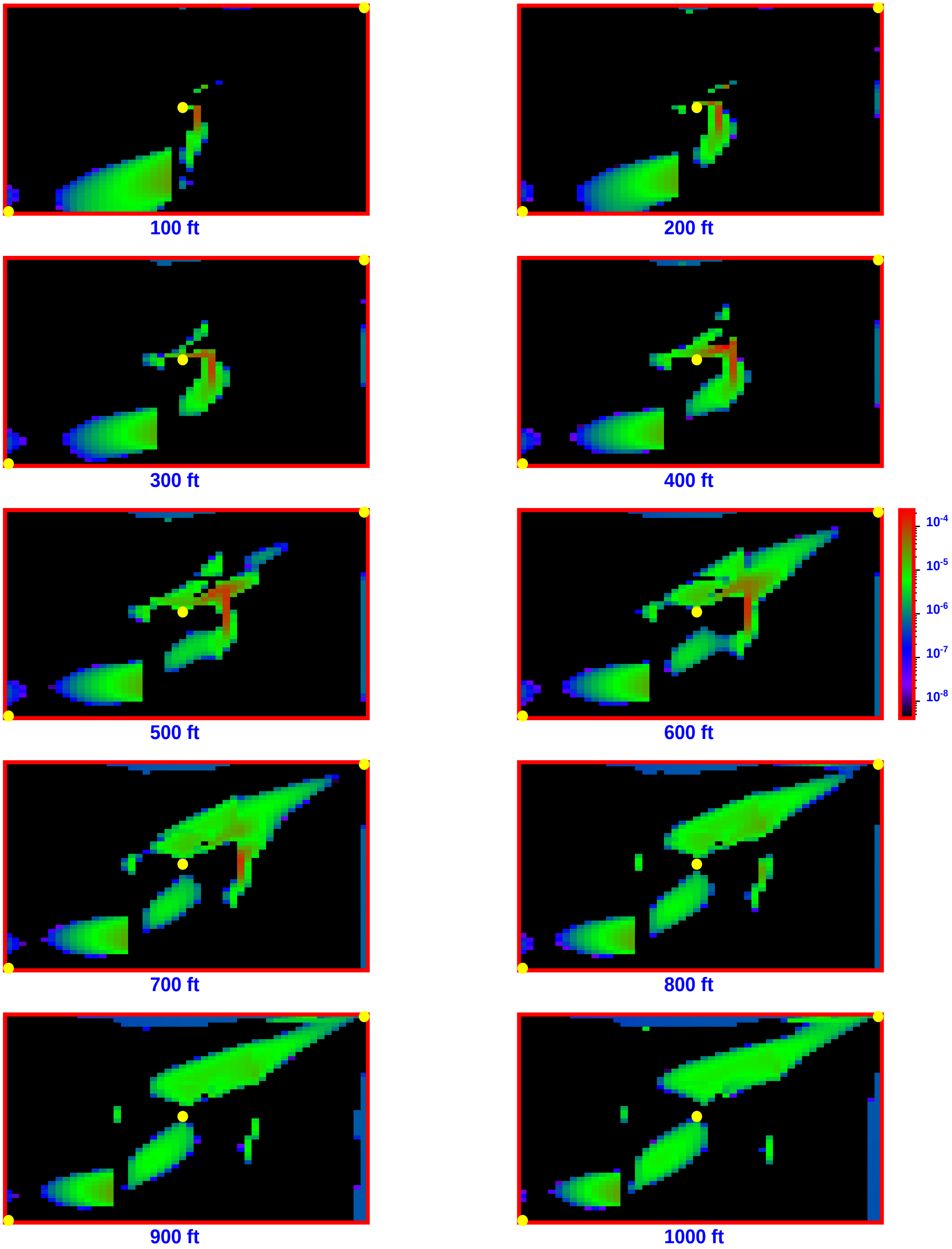

Figure 5.100: Sensitivity of the average change in water saturation between 100 and 800 days with respect to the channel width.

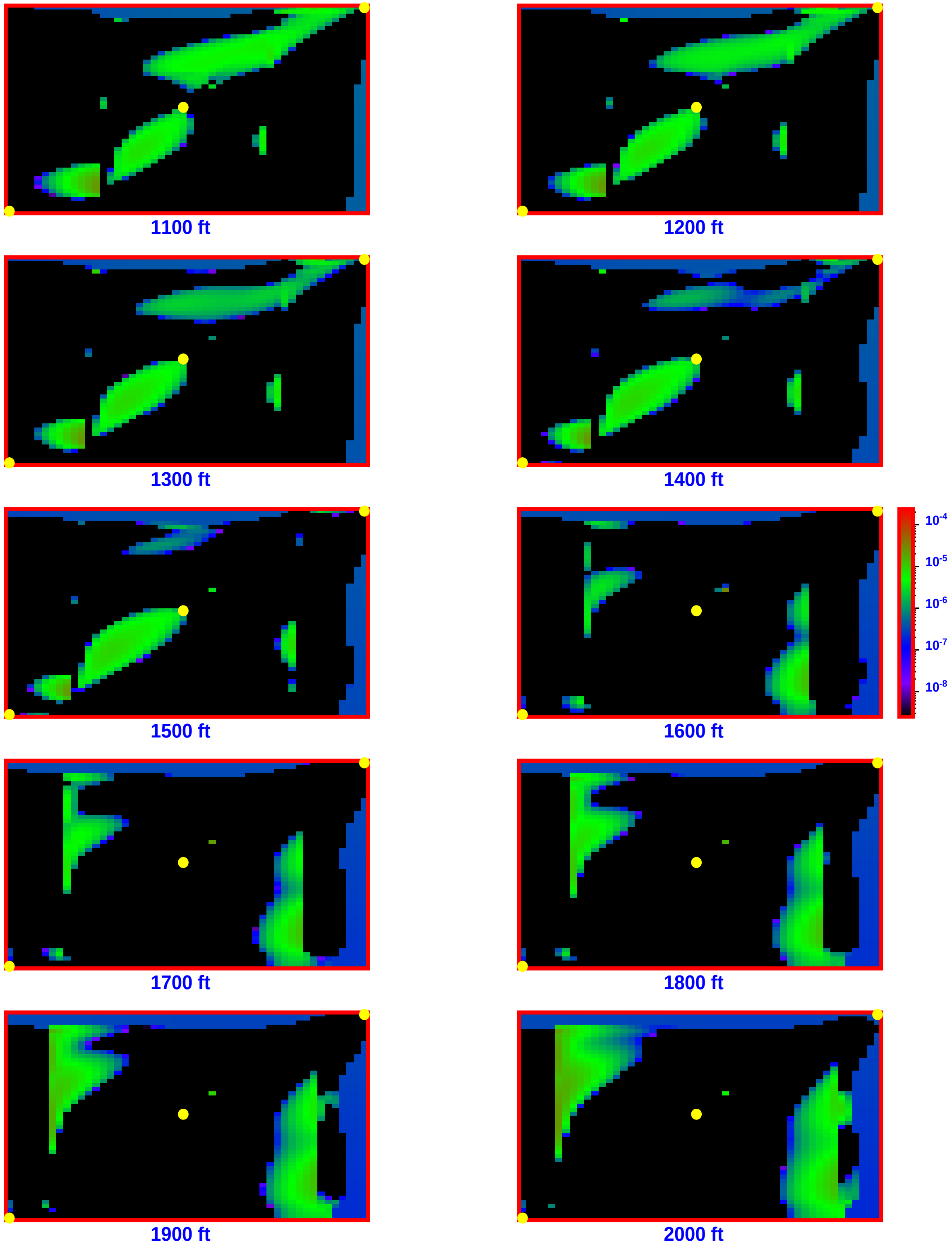
1100 ft
1200 ft
1300 ft
1400 ft
1500 ft
1600 ft
1700 ft
1800 ft
1900 ft
2000 ft

Figure 5.101: Sensitivity of the average change in water saturation between 100 and 800 days with respect to the channel width.

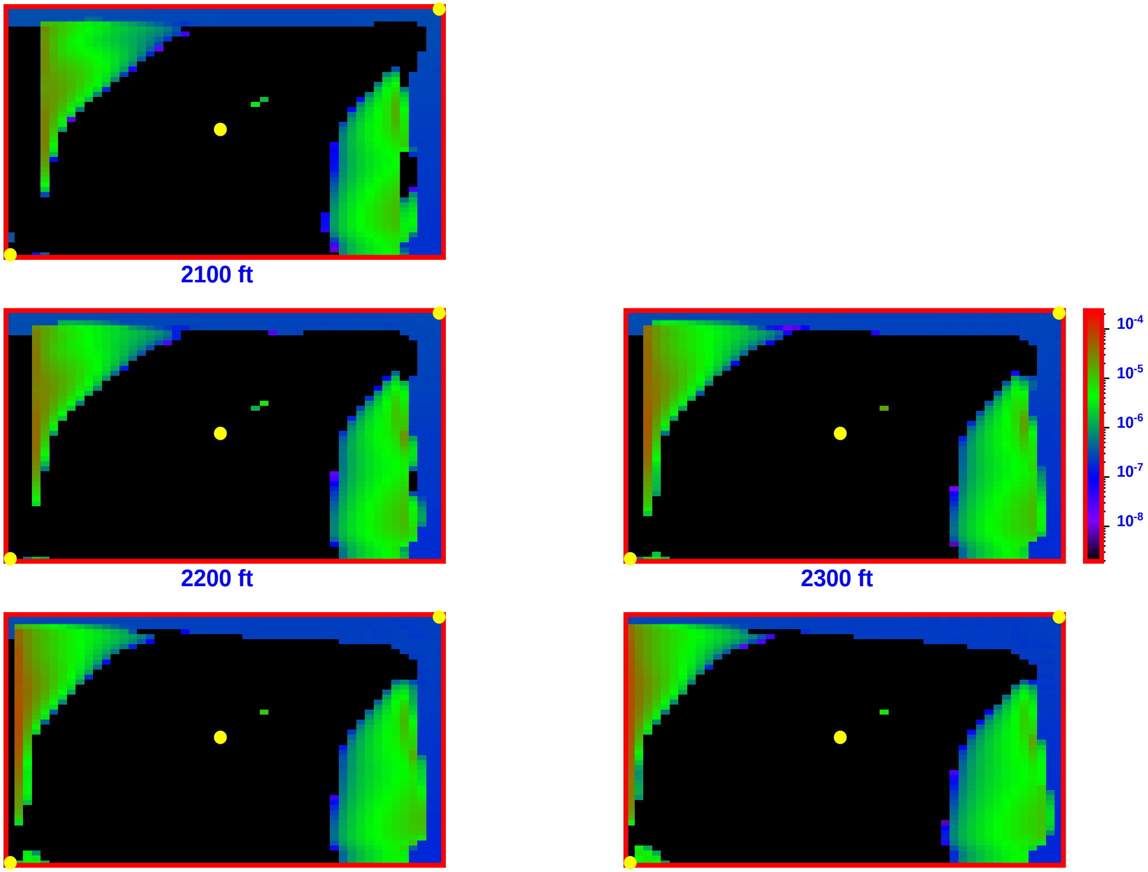

2100 ft

2200 ft

2300 ft

2400 ft

2500 ft

Figure 5.102: Sensitivity of the average change in water saturation between 100 and 800 days with respect to the channel width.

Chapter 6

Mathematical Tests

In this chapter, we evaluate and test the ability of the subcell method to identify the geometry and properties of geological features in a fluvial reservoir from such dynamic data as 4-D seismic and multiple well production histories, using several synthetic examples. The purpose in using synthetic examples was to investigate problems in which the correct solutions were known exactly so that the accuracy of the inversion process could be determined. In each example, a set of reference geological objects were first constructed leading to the generation of reference permeability and porosity fields which were then input into a numerical reservoir simulator to simulate the dynamic response used as data measurements. Based on the synthetic data simulated, the subcell method was used to invert for the geometry of the objects that match the data. The inverted solutions were then compared with the reference objects to evaluate the capability of the subcell method.

For the examples shown in Sections 6.1 and 6.2, the reservoir model is a quarter of a five-spot pattern with an injector at the lower left and a producer at the upper right corner. For the examples shown in Sections 6.3, the reservoir model is a full five-spot pattern. The production and injection rates used in all examples were known and consist of a series of different flow periods. This results in several upward and downward trends in the pressure response data.

6.1 Single Channel

The first attemp to match the data was by considering only one parameter as unknown to be determined and the other parameters were kept fixed. The purpose was to test if it was possible to recover the true value of the unknown parameter. The objective function to minimize had a weighted least square form with the weights chosen such that data sets with different scales contribute to the objective function approximately the same weighted magnitudes. That is, the pressure component of the objective function had approximately the same weighted magnitudes as the components corresponding to the water cut and change of saturation data sets. Figure 6.1(a) shows a two-dimensional view of the true channel whose parameters are given in Table 6.1. This channel is embedded in a background of 50md permeability and 10% porosity material. This synthetic channel was used to generate the downhole pressure data at the two wells (see Figures 6.1(b) and (c)), water cut at the producer (see Figures 6.1(d)), and the simulated change in water saturation between the two instants in time as would be obtained from a 4-D seismic survey given by Figures 6.1(e). Water breaks through at 930 days after the time of injection. Figures 6.2, 6.3, and 6.4 show the three sequences of images obtained during the process of matching production and seismic data corresponding to a single-channel model in which the estimations of channel translation, rotation, and sinuosity are considered separately. In the case of estimating channel translation, the initial guess was a homogeneous reservoir, which means a complete ignorance of the channel. In the case of estimating channel rotation, the initial guess was a channel with East-West orientation. Finally, for the case of estimating channel sinuosity, the initial guess was a vertical bar channel. In these three cases, the first guesses corresponded to arbitrary channels that were substantially different from the references. For single-channel cases, the algorithm converged to the reference after about 5 to 9 iterations.

Table 6.1: Channel parameters - single channel

Channel Orientation	Channel Sinuosity (cycles/ft)	Width (ft)	Length (ft)	ϕ (%)	k (md)
North-South	6/10,000	300	2000	20	800

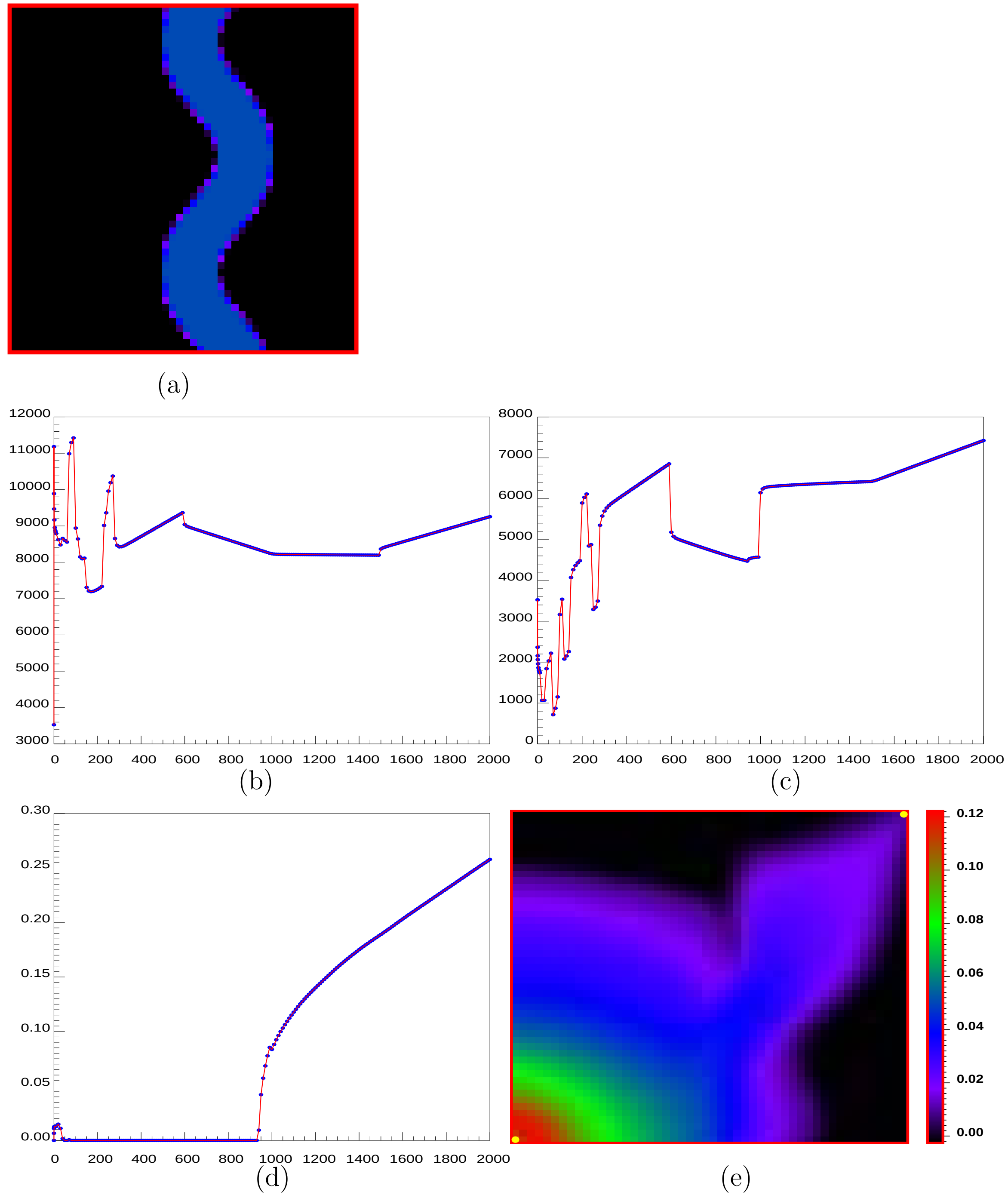

Figure 6.1: (a): Reference channel. (b): Pressure at the injector. (c): Pressure at the producer. (d): Water cut at the producer. (e): Change in water saturation.

iter #1 iter #2 iter #3

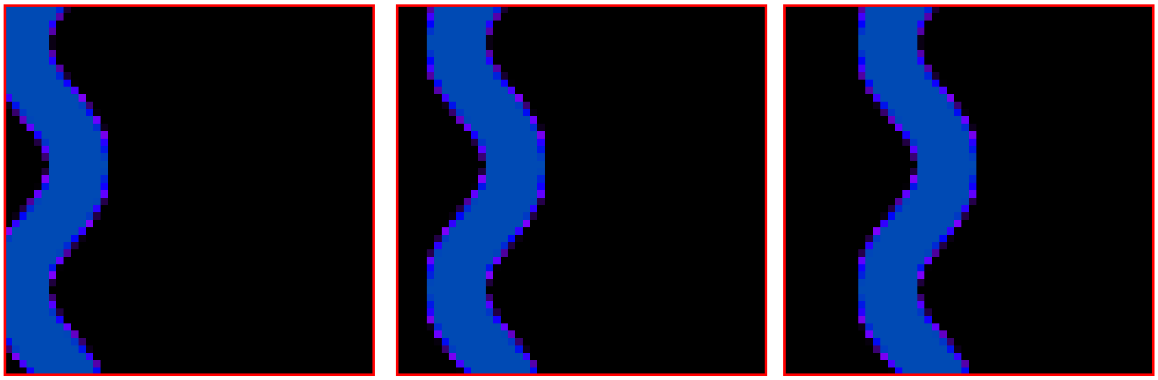

iter #4 iter #5 iter #6

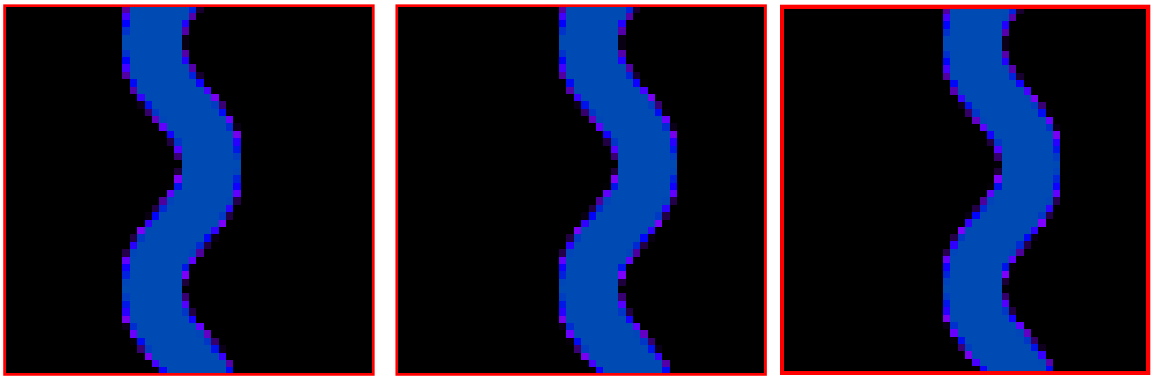

iter #7 iter #8 Reference

Figure 6.2: Matching iterations: Channel translation.

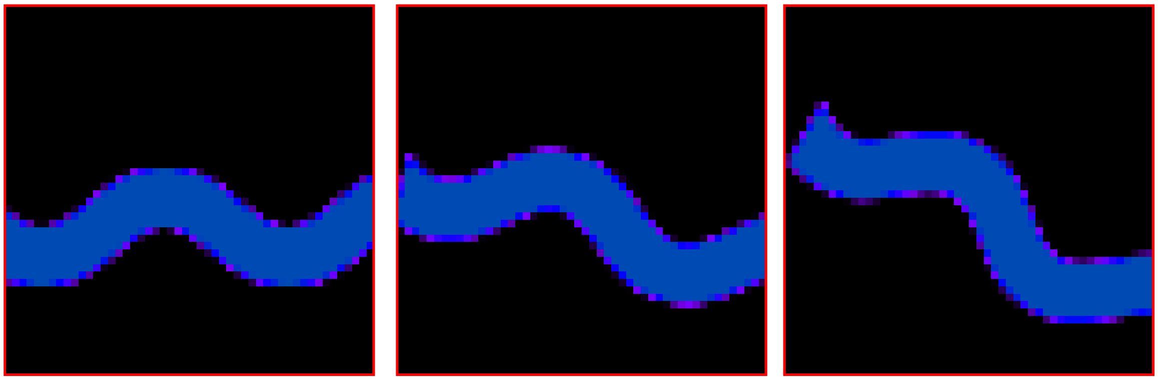

iter #1 iter #2 iter #3

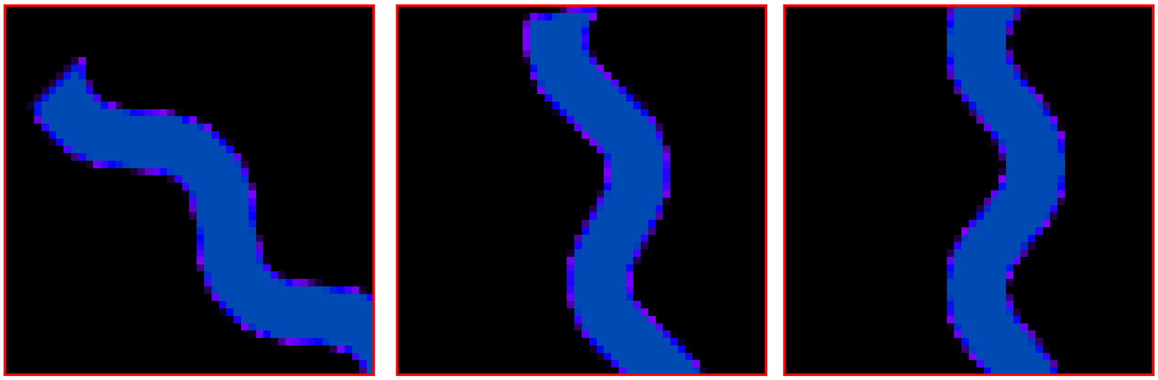

iter #4 iter #5 Reference

Figure 6.3: Matching iterations: Channel rotation.

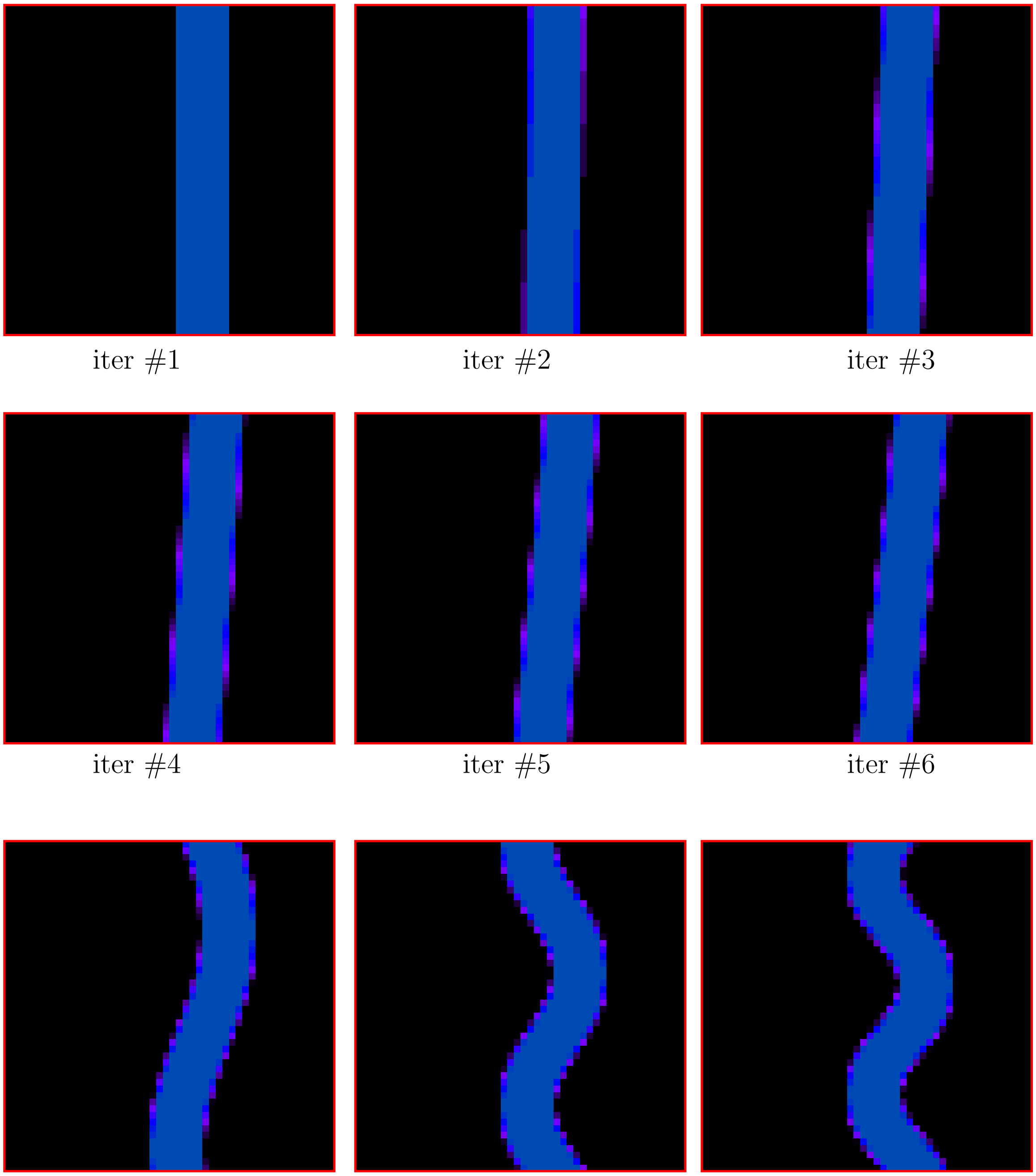

iter #1 iter #2 iter #3

iter #4 iter #5 iter #6

iter #7 iter #8 Reference

Figure 6.4: Matching iterations: Channel sinuosity.

6.2 Multiple Channels

In this case, a total of six channels were considered. The parameters describing these channels are given in Table 6.2 where the channel orientations are measured from the West-East direction. The background permeability and porosity are 150md and 10% respectively. A two-dimensional view of this reservoir is shown in Figure 6.5(a). The lower left injector intersects one of the channels and the upper right producer is located in the background flood/plain field. Figures 6.5(b) and (c) present the pressure data gauged at the injector and producer respectively. Figures 6.5(d) shows a water-cut history collected at the producer indicating a water breakthrough at about 750 days after the time of injection and Figures 6.5(e) gives the simulated change in water saturation between the two instants in time as would be obtained from a 4-D seismic survey. A sequence of two-dimensional views of the reservoir obtained during the process of matching pressure, water cut, and the simulated seismic data is shown in Figure 6.6. The regression parameters considered here are only the translations of the six channels. Another resulting sequence of two-dimensional views of the reservoir is given in Figure 6.7 where both the channel translations and rotations were estimated simultaneously. It is noted here that the initial guess models contain a very small fraction of channels at the West side and both the injector and producer are located in the low permeability/porosity background flood/plain field. All channels are translated and rotated independently of each other. As observed from Figure 6.7, the reservoir corresponding to the first iteration (initial guess) indicated almost no channels but after only the third iteration the algorithm was able to translate most of the channels toward the inside regions of the reservoir. This is a very difficult task since there was no mathematical constraint to keep all the channels inside the reservoir. The constraints arose naturally from the dynamic data. If the channels were located outside the reservoir the production data would be greatly affected, the objective function would increase and such a change would be rejected. For multiple-channel cases, the algorithm converged to the reference model after about 14 iterations if regressing on the channel translations and 31 iterations if regressing on both the channel translations and rotations. In these cases, each iteration requires two simulation runs on average.

So far, the test examples were restricted to only some parameters, next we considered another problem where all channel parameters were treated as unknowns to be determined. The unknown parameters include the x- and y-translations, rotations, departure, sinuosity, displacement, width, length, permeabilities, and porosities of the channels. Figures 6.8(a) and (b) show the permeability and porosity distributions representing a set of six reference channels accounting for a total of 60 parameters (ten parameters for each channel). The long-term pressure histories at the injector, at the producer, and the water cut at the producer are plotted in Figures 6.8(c), (d) and (e) respectively. Interpreted 4-D seismic data are shown in Figures 6.8(f). Figure 6.9 shows selected views of the reservoir permeabilities obtained during the matching process. It is noted here that the permeability and porosity in each channel were treated independently. It was observed that the progress was slow from iteration 10 to 22 and after iteration 34. After 47 iterations, the algorithm was able to converge to a minimum. Figure 6.10 compares maps of reference and calculated permeability and porosity and maps of observed and calculated 4-D seismic data. Figure 6.11 shows the match of long-term pressure and water cut at the wells. The production and seismic data were matched almost perfectly. However, the solutions were significantly different from the references and indicated several interesting observations. The computed permeabilities of channels were observed at high values where values of porosity in the same channels were low and vice versa. This observation is not consistent with the nature of typical reservoir rock where high values of permeability are associated with high values of porosity. This may due to various reasons. First, the amount of data is not sufficient to recognize any correlation between permeability and porosity. Second, the number of unknown parameters to be estimated in this case is 60 which is large as compared to the amount of data. Third, and most importantly, as was shown in Section 5.6, the sensitivity coefficients with respect to permeability and porosity of the same channel sometimes show opposite signs. This means that an increment in permeability has the same effect as a decrement in porosity in the same channel, or in other words, an increase in permeability in a channel can be compensated by a decrease in porosity in the same channel. The algorithm can either increase the permeability of a certain channel or decrease porosity of the same channel to obtain the same gradient of data and this results in some channels with high permeability values and low porosity values and vice versa.

Table 6.2: Channel parameters - six channels.

Channel #	Channel Orientation (^{0}deg)	Channel Sinuosity (cycles/ft)	Width (ft)	Length (ft)	ϕ (%)	k (md)
1	90	6/10,000	400	2000	20	800
2	45	8/10,000	600	3000	30	1200
3	135	4/10,000	300	2000	40	1800
4	-35	3/10,000	300	4000	40	500
5	100	3/10,000	400	1000	40	1000
6	35	3/10,000	500	2000	40	1000

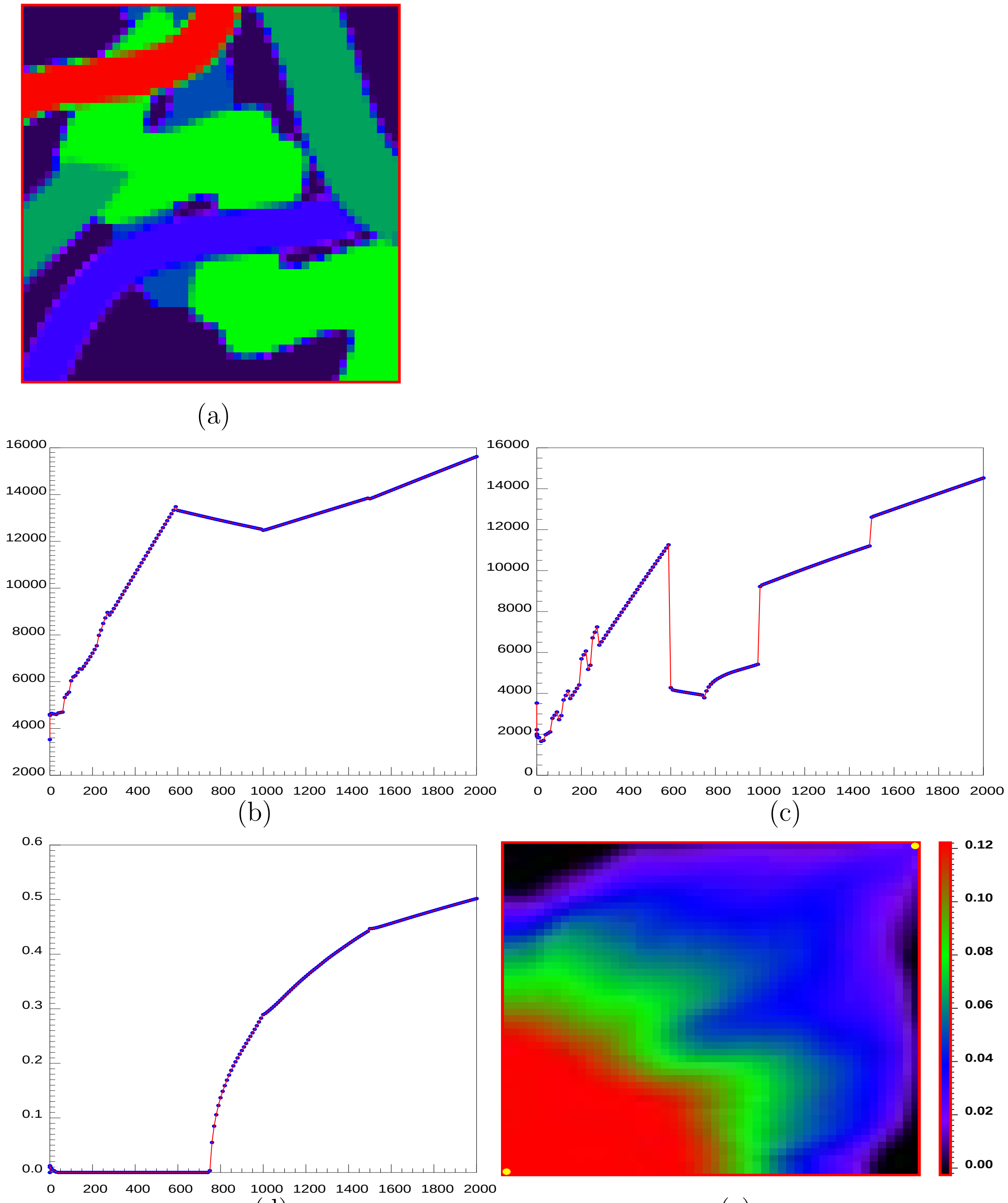

Figure 6.5: (a): Reference channels. (b): Pressure at the injector. (c): Pressure at the producer. (d): Water cut at the producer. (e): Change in water saturation.

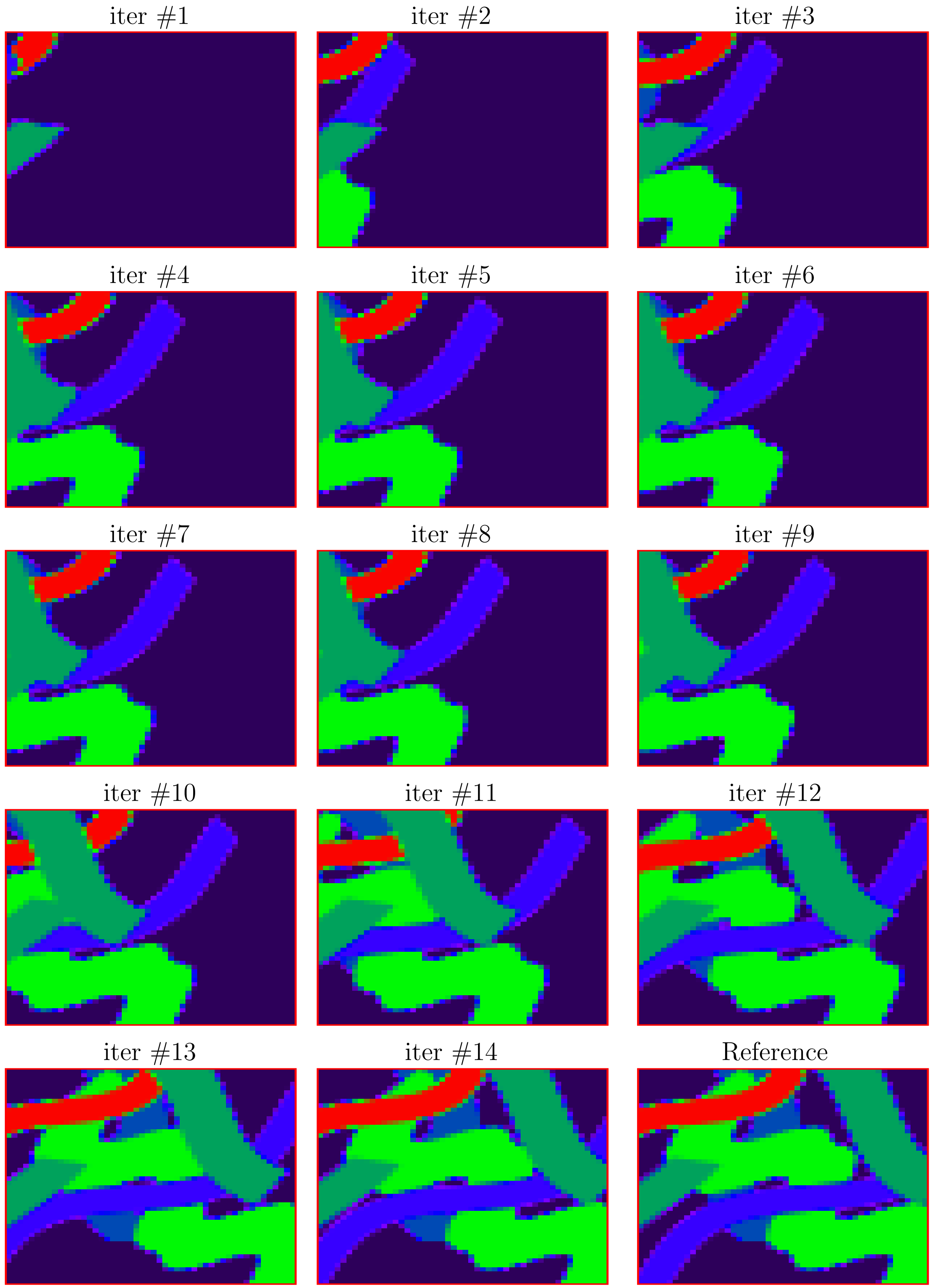

iter #1 iter #2 iter #3

iter #4 iter #5 iter #6

iter #7 iter #8 iter #9

iter #10 iter #11 iter #12

iter #13 iter #14 Reference

Figure 6.6: Matching iterations: Multiple channels - translations.

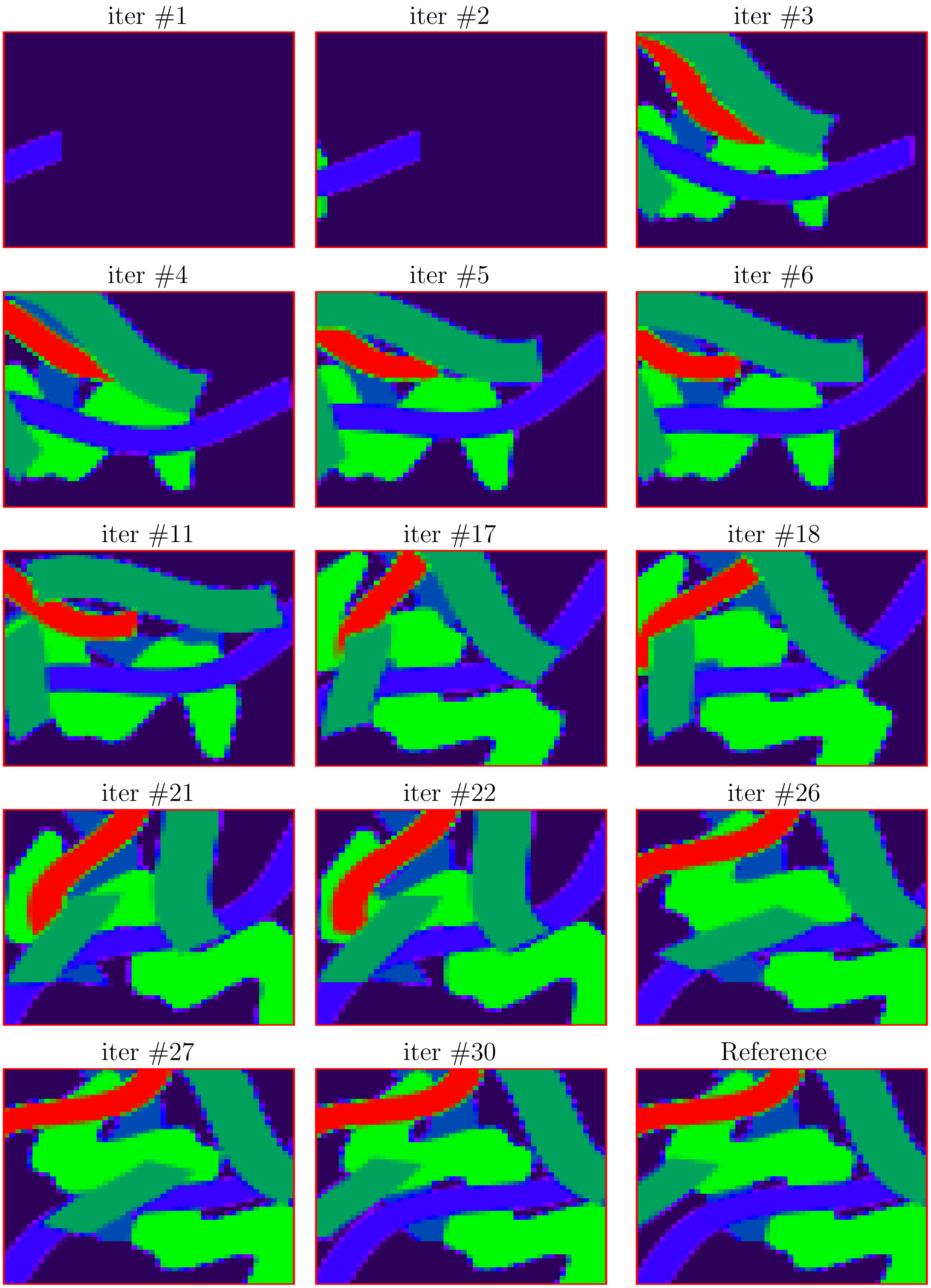

Figure 6.7: Matching iterations: Multiple channels - translations and rotations.

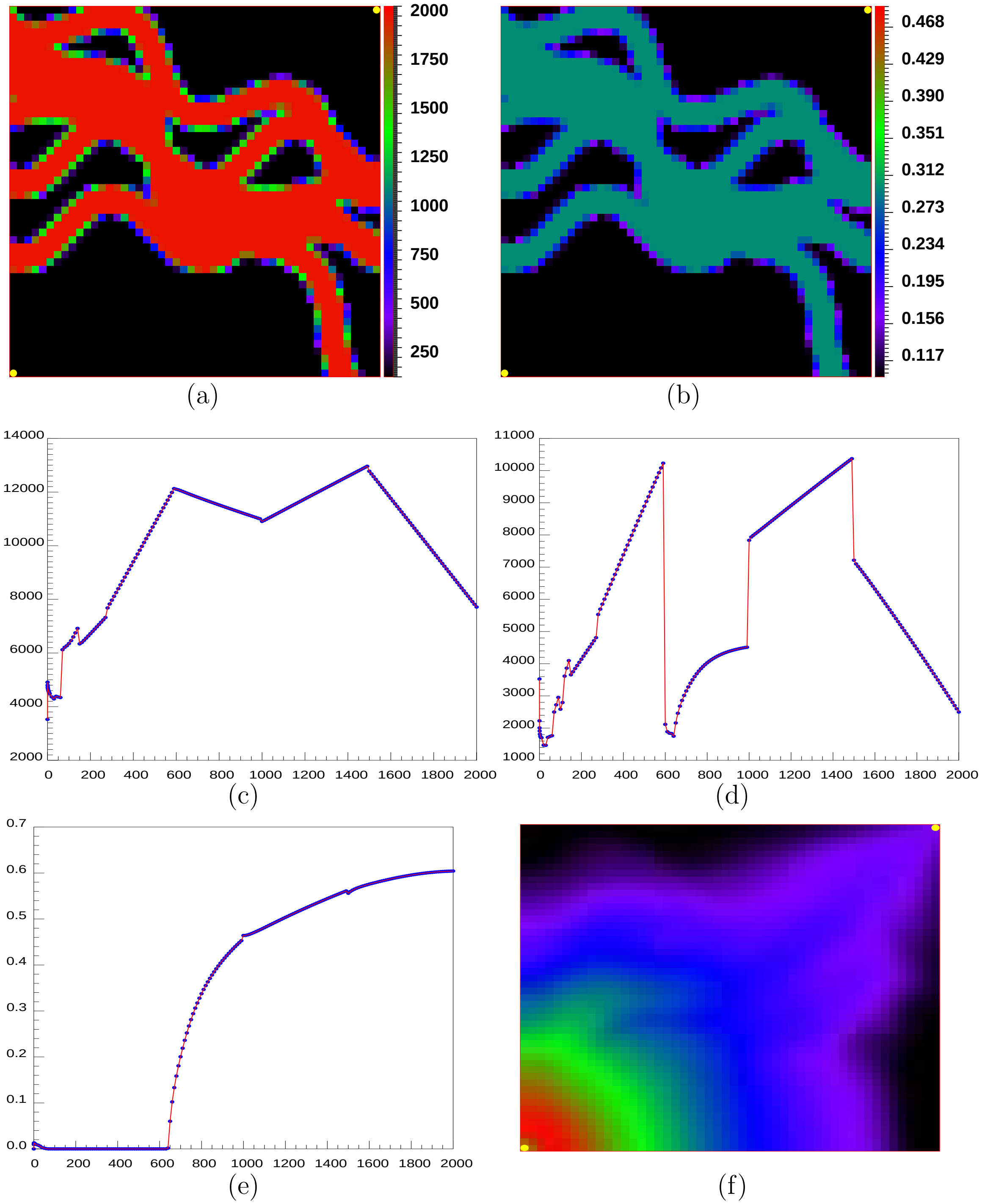

(a) (b) (c) (d) (e) (f)

Figure 6.8: (a): Reference channels - permeability. (b): Reference channels - porosity. (c): Pressure at the injector. (d): Pressure at the producer. (e): Water cut at the producer. (f): Change in water saturation.

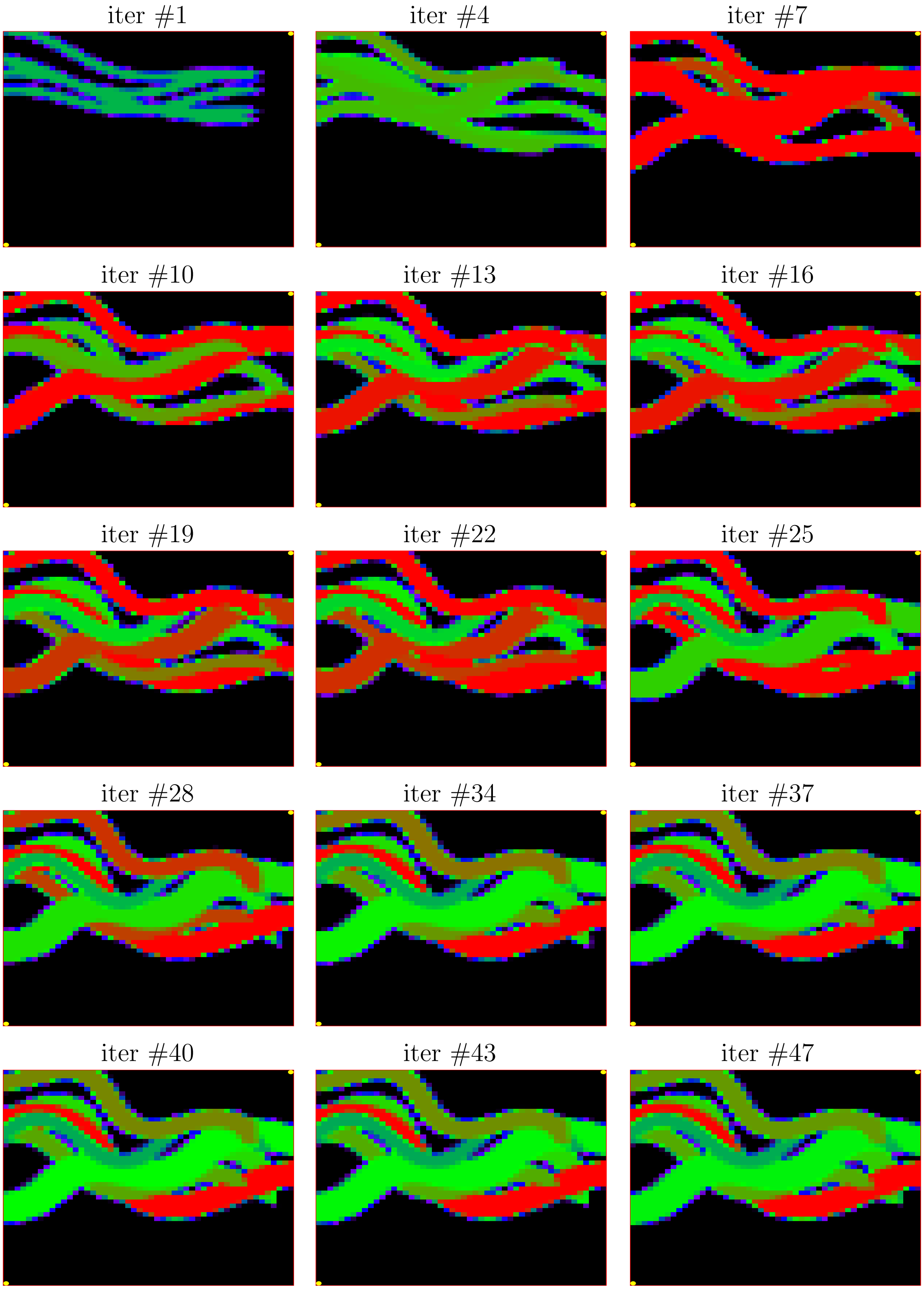

iter #1
iter #4
iter #7
iter #10
iter #13
iter #16
iter #19
iter #22
iter #25
iter #28
iter #34
iter #37
iter #40
iter #43
iter #47

Figure 6.9: Matching iterations: Multiple channels - all parameters are unknown.

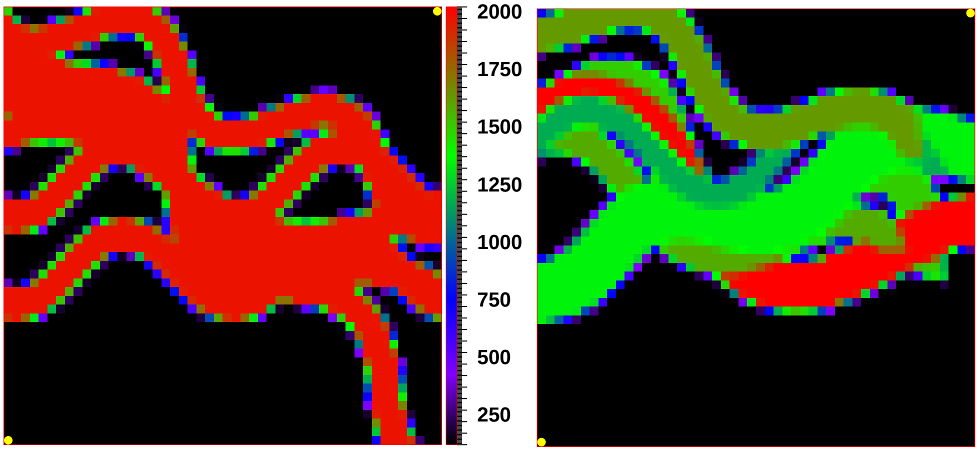

Reference permeability Calculated permeability

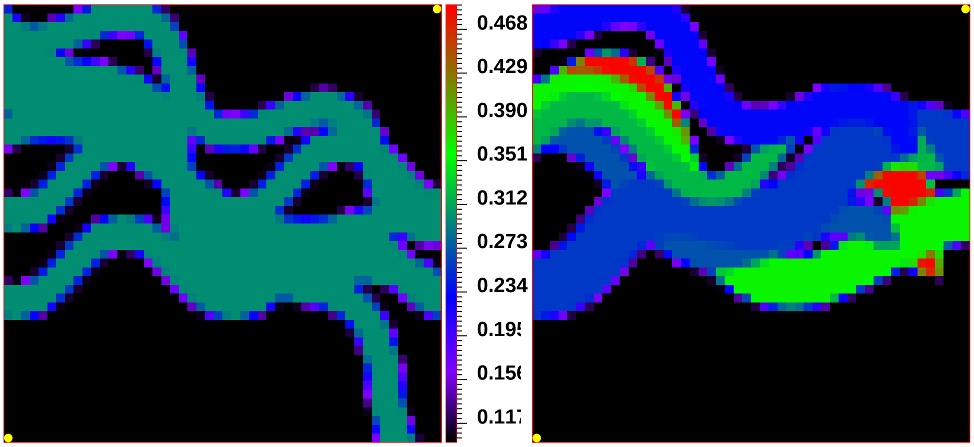

Reference porosity Calculated porosity

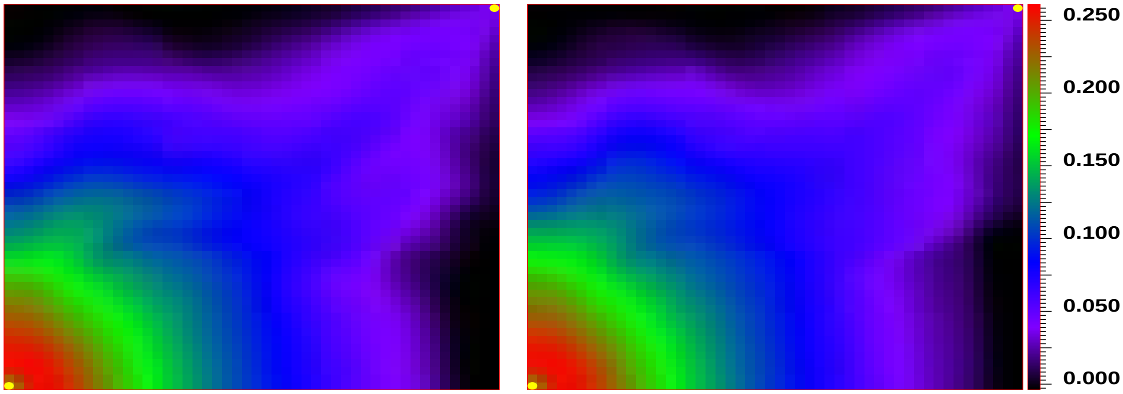

Observed seismic Calculated seismic

Figure 6.10: Matching results : Multiple channels - all parameters are unknown.

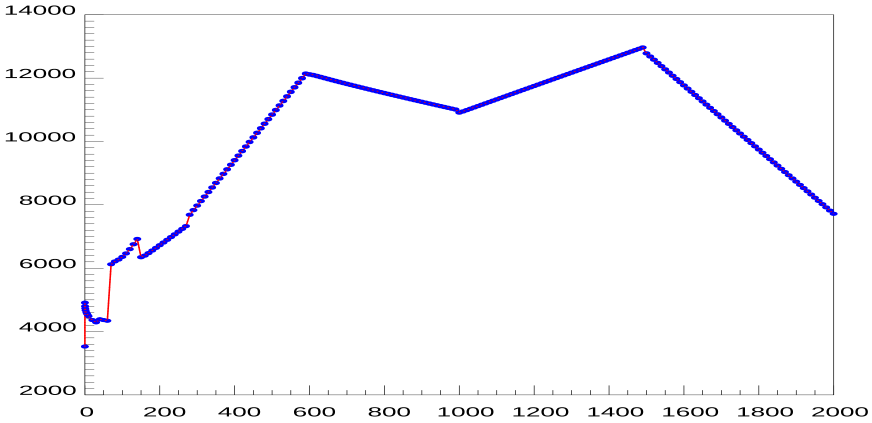

Match of pressure at the injector.

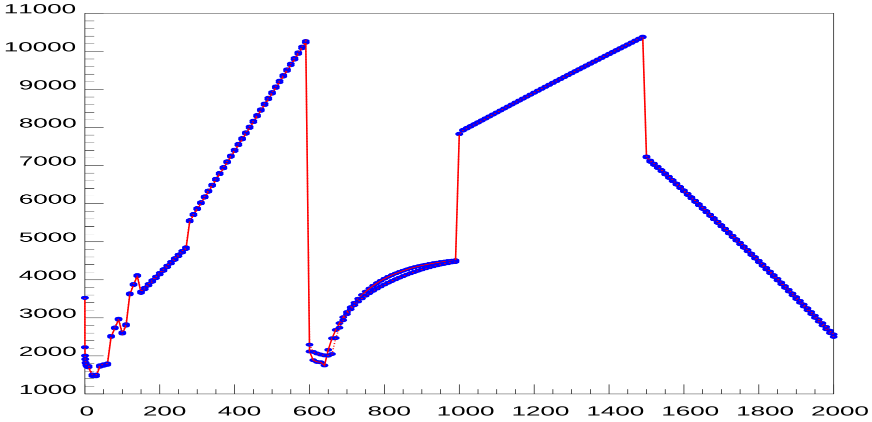

Match of pressure at the producer.

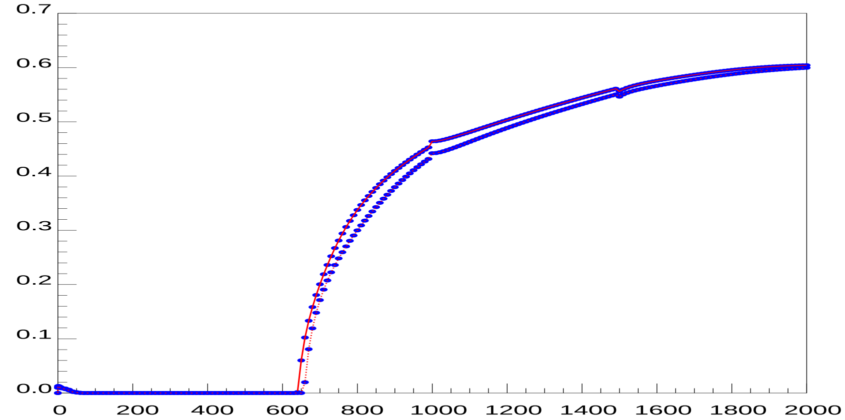

Match of water cut at the producer.

Figure 6.11: Matching results : Multiple channels - all parameters are unknown.

6.3 Contrast in Seismic Amplitude Maps

Whether or not we can determine the position of a channel from seismic data alone depends on the contrast in seismic-related rock properties such as P and S wave impedance, velocity, Poisson's ratio etc. between the rocks in the channel and those outside the channel. If a seismic amplitude map provides high contrast between channel and nonchannel facies (though this rarely happens in practice), the distribution and geometry of channels can then be determined from the seismic amplitude map alone with high certainty. The remaining unknowns are the rock properties inside the channels. In most cases, the amplitude map does not show high contrast between channel and nonchannel facies and thus can not be used to infer the channel position. In this case, the amplitude map is rather used as soft conditioning data to constrain the prediction of facies distribution in a stochastic process and information about spatial distribution and geometric shapes of channels are then associated with high uncertainty. Two situations regarding the contrast in seismic amplitude map were examined. The second situation corresponding to a low contrast in seismic amplitude map will be discussed fully in Chapter 8.

In the first situation, the geometry of channels can be determined from the seismic amplitude map alone and are known to us and the remaining unknowns are the permeabilities and porosities of the channels. To illustrate the application of the subcell method in this situation, 100 synthetic channels were generated stochastically. The geometries of the synthetic channels were generated from triangular distributions given in Table 6.3. The permeability values of the channels were drawn from Gaussian distribution with a mean of 10000 md and a standard deviation of 2000 md. The porosity values of the channels were correlated to the permeabilities by the relation $log(k) = 6\phi + 1.5$. The resulting permeability distribution of the 100 generated channels was shown in Figure 6.12. Figure 6.13 depicts the time-dependent flow rate history of all five wells in a five-spot pattern with the injector located at the center of the reservoir and the four producers located at the four corners. The observed data were generated from this set of 100 synthetic channels by using a numerical simulator and are shown in Figure 6.14. The wiggles observed in the pressure history at all five wells were due to the step changes of the specified flow rates. Figure 6.14(f) shows the change in water saturation between 100 and 1800 days as might be determined from 4-D seismic data. Three scenarios regarding matching different types of data were investigated: one in which both 4-D seismic and production data were used, one in which only pressure history data were used, and one in which only water-oil ratio history data were used. Figure 6.15 shows the evolution of the intermediate permeability maps obtained during the inversion process when matching both production and 4-D seismic data. The initial guess corresponded to identical permeabilities across all channels, which means a complete ignorance of the geological events associated with the channels. The algorithm converged rapidly in six iterations to the true reservoir. It was observed from the sequence of images that the algorithm developed in this work has the capability to constrain a large number of channels to geological events, that is to honor the assumption of geological event which states that the immature channels replace the mature ones. Two other resulting sequences of iterative images obtained by matching only the pressure and water cut history separately are shown in Figures 6.16 and 6.17. The algorithm converged after 16 iterations when matching pressure and 12 iterations when matching water cut. It can be observed from these figures that the solution obtained by matching pressure history is closer to the reference than that obtained by matching water cut. This result can be summarized by computing the resolution matrices corresponding to matching different data types as are shown in Figure 6.18. The resolution matrix presents the relationship between the estimated parameters and the true parameters. The closer this matrix to identity or the more dominant the diagonal over the off-diagonal elements then the closer the estimated values lie to the true values. As indicated in Figure 6.18, the resolution matrix from matching both production and seismic data contains mainly the diagonal while the resolution matrix from matching pressure history does contain significant off-diagonal elements and finally the diagonal elements are barely recognized in the matrix from matching only the water cut.

Table 6.3: Triangular distributions for channel parameters

Channel Parameters	Low	Mode	High
x-translation (ft)	0	2500	8000
y-translation (ft)	0	2500	8000
channel rotation ($^o deg$)	0	60	120
channel departure (ft)	50	100	200
channel sinuosity (cycles/10,000ft)	1	5	10
channel displacement (ft)	0	0	0
channel width (ft)	200	250	300
channel length (ft)	500	3000	10000

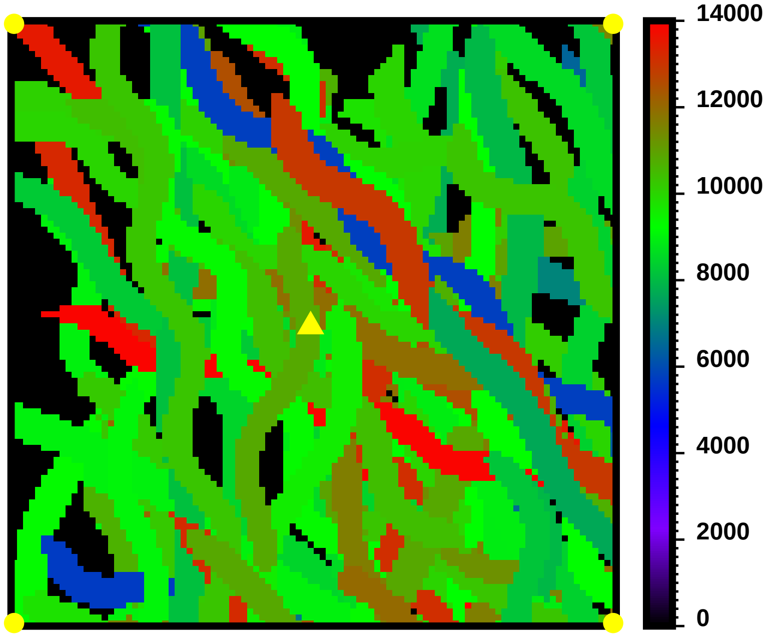

Figure 6.12: Permeability distribution of 100 channels.

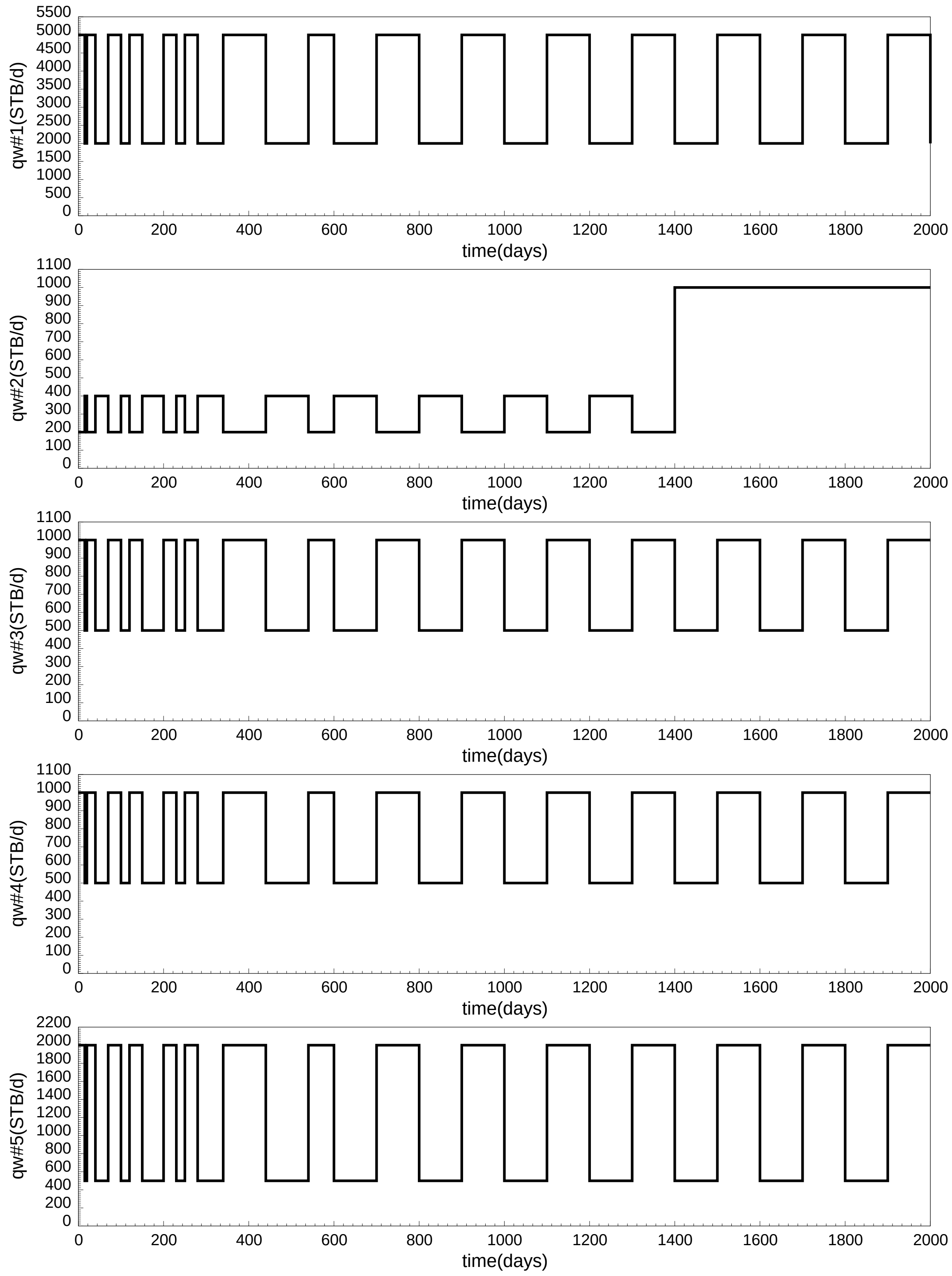

Figure 6.13: Time-dependent rate history of five wells.

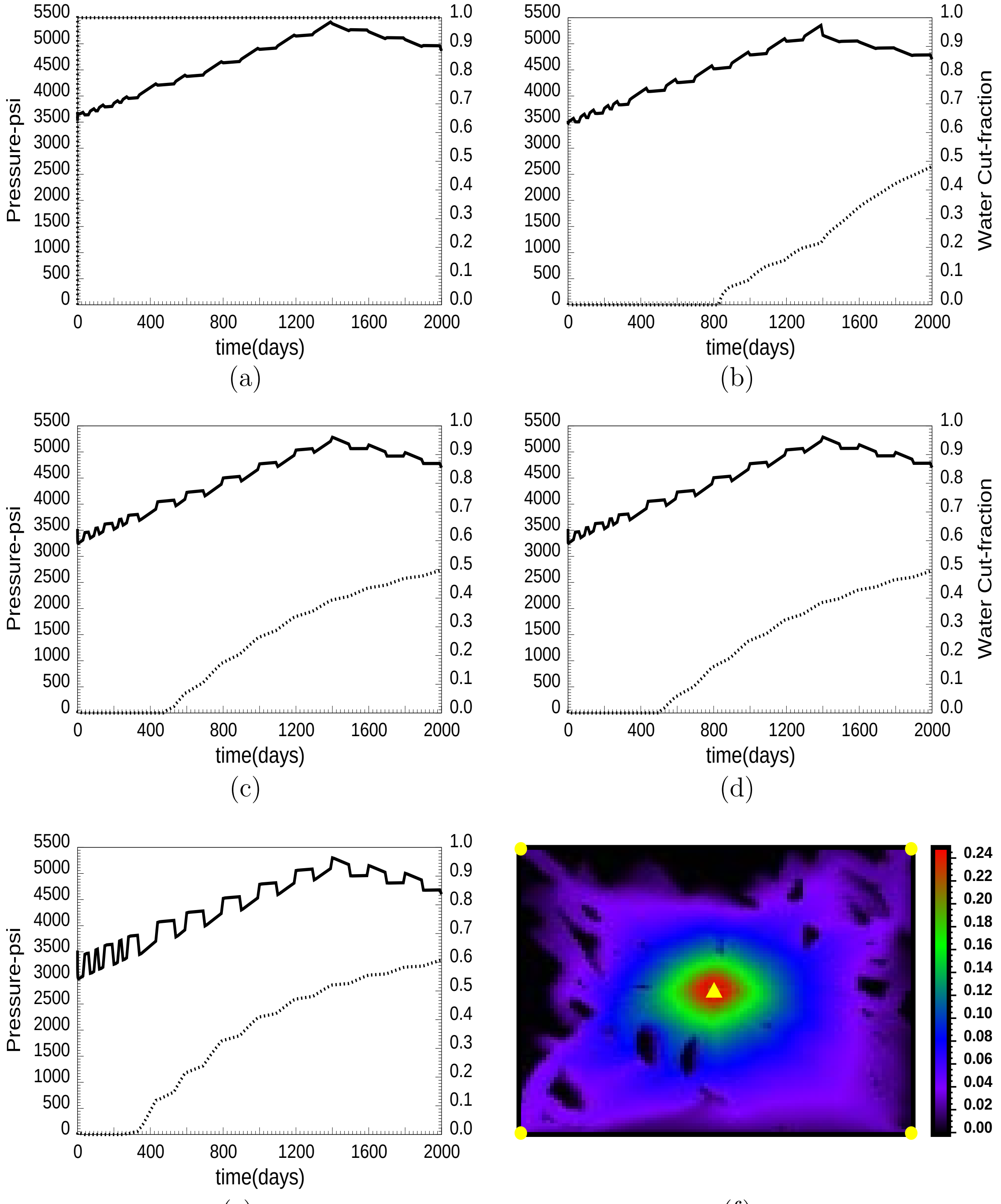

(a) (b) (c) (d) (e) (f)

Figure 6.14: (a): Pressure and water cut at well #1. (b): Pressure and water cut at well #2. (c): Pressure and water cut at well #3. (d): Pressure and water cut at well #4. (e): Pressure and water cut at well #5. (f): Change in water saturation between 100 and 1800 days.

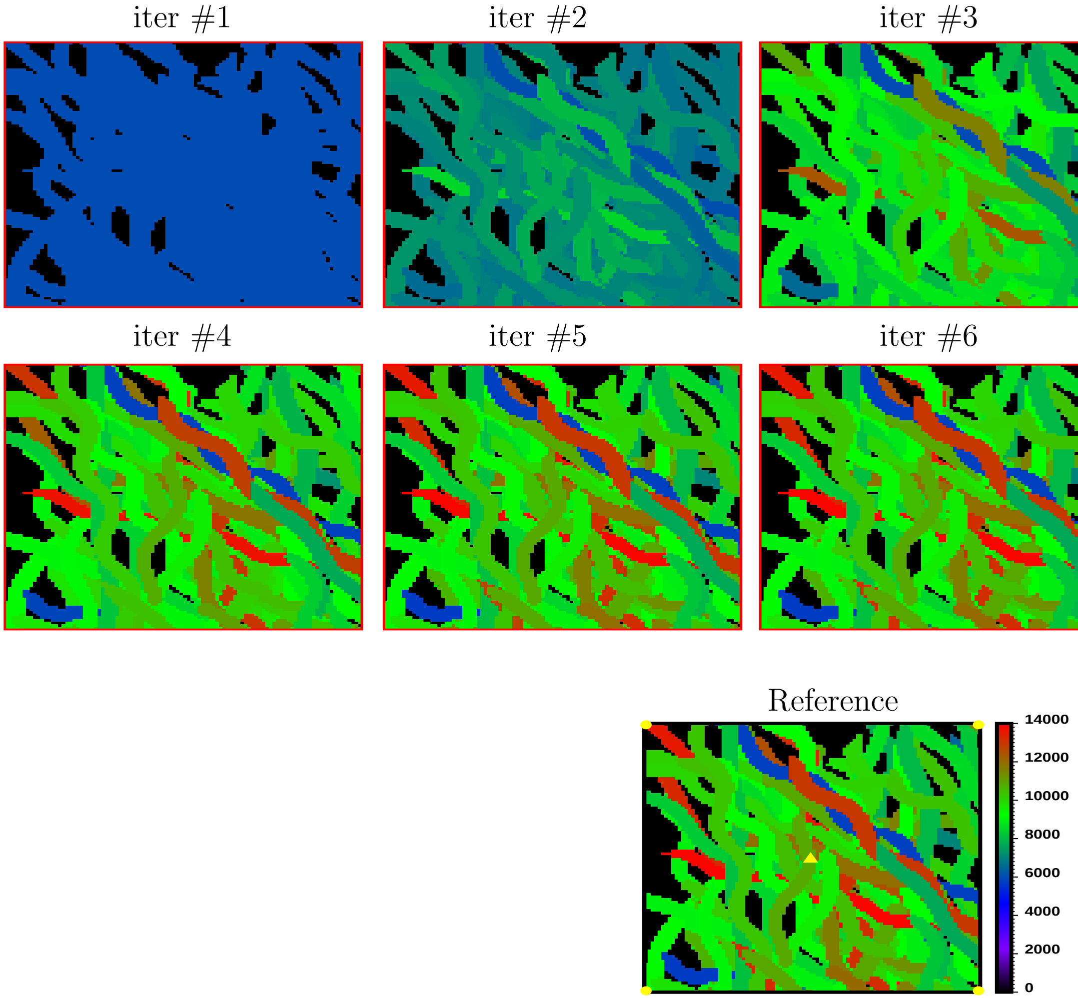

Figure 6.15: Matching iterations of production and seismic data: Regressing on permeabilities of 100 channels.

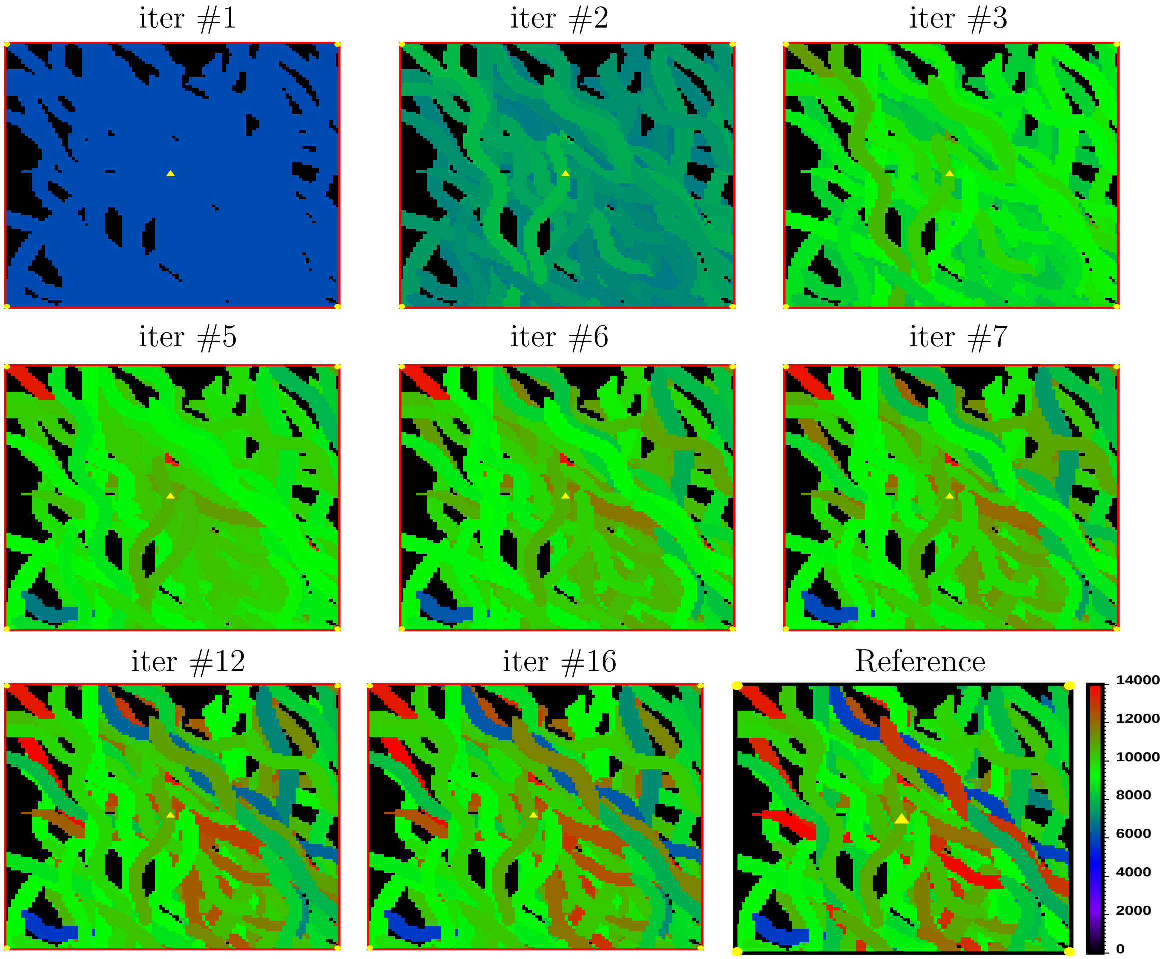

Figure 6.16: Matching iterations of pressure history: Regressing on permeabilities of 100 channels.

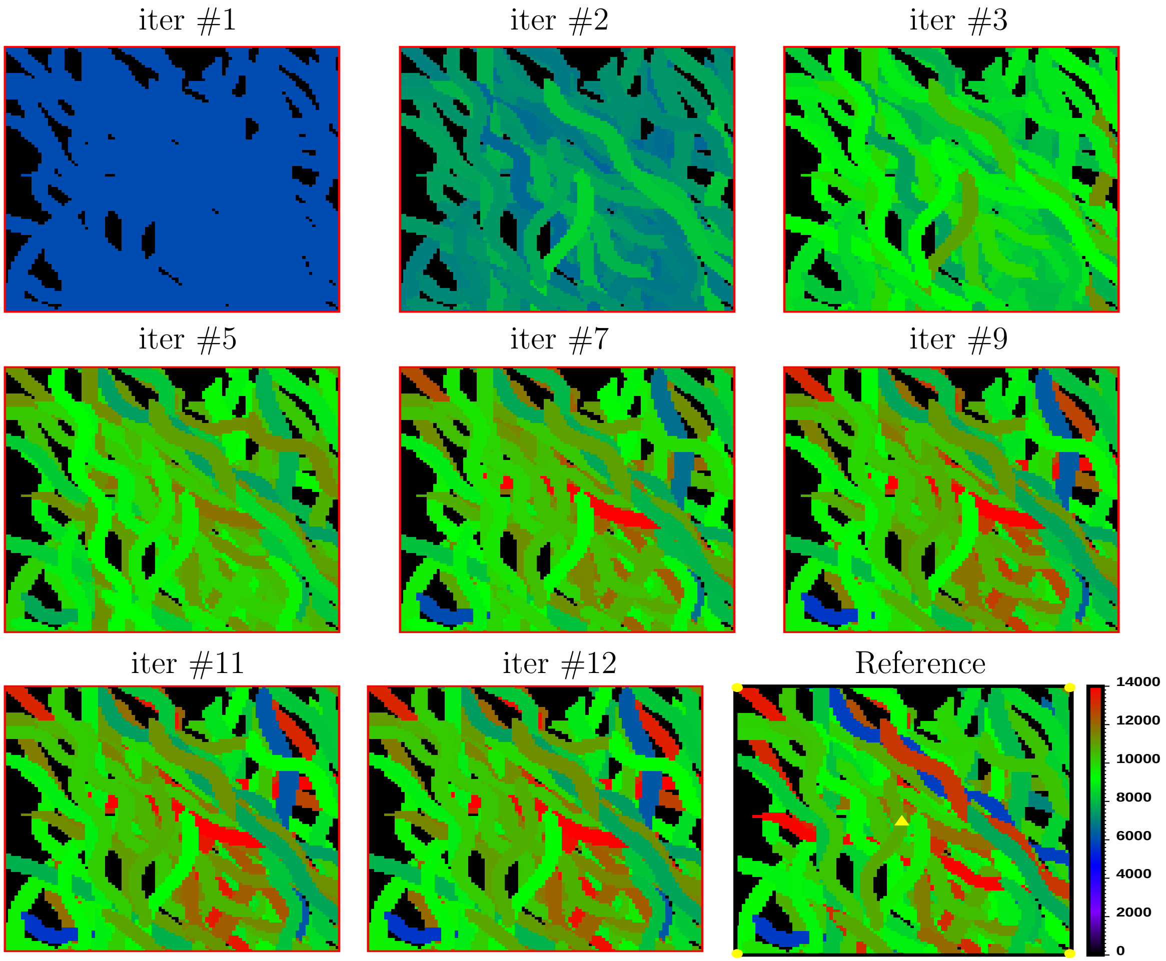

Figure 6.17: Matching iterations of water cut history: Regressing on permeabilities of 100 channels.

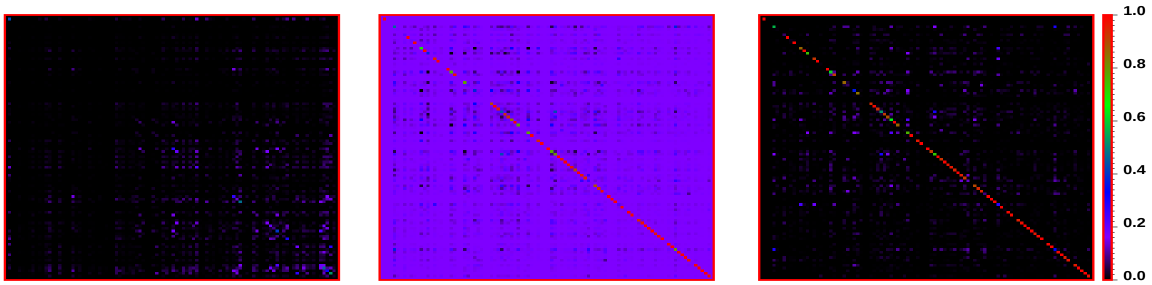

Data: Water cut history

Data: Pressure history

Data: Pressure, water cut, and 4-D seismic

Figure 6.18: Resolution matrices corresponding to matching various data types.

6.4 Well Log Constraints

So far, we have used production and 4-D seismic data as sources of information about the geometry and property of geological features. Production data are available only at the well locations and rich in information after the arrival of water front. 4-D seismic data provide areally-distributed information and therefore have a higher areal resolution than the production data, however 4-D seismic data have a poor resolution image of depth-dependent properties. On the other hand, well logs provide direct, high resolution (but laterally sparse) sampling of information about various reservoir rock parameters. Lithofacies data extracted from well logs provides information regarding the positions where the channels are present. In this section, we shall discuss how to use this type of data to constrain the inversion of dynamic data and to reduce the uncertainties of the parameter estimates.

Suppose well log data indicate the presence of a channel at point M with global coordinates (X, Y, Z). The goal is to establish mathematical constraints on the parameters so as to guarantee point M is always located inside the channel. Figure 6.19 shows a two-dimensional view of the channel in the $x - y$ plane where (x, y, z) is the local coordinate system defining the channel.

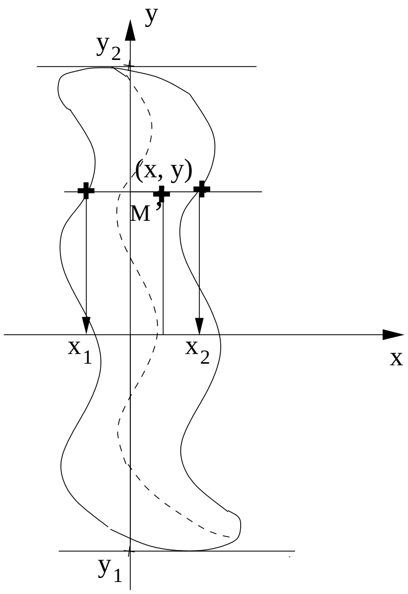

Figure 6.19: Lithofacies constraint.

M' is the projection of point M on the $x-y$ plane. Since the channel is delimited in the x-direction by x_1 and x_2, in the y-direction by y_1 and y_2, and in the z-direction by z_1 and z_2, the necessary and sufficient conditions for point M to be inside the channel are given by

$$\begin{cases} x_1 & \leq x & \leq x_2 \\ y_1 & \leq y & \leq y_2 \\ z_1 & \leq z & \leq z_2 \end{cases} \tag{6.1}$$

The channel boundaries x_1 and x_2 can be obtained from the channel center line as (see Equations 2.19, 2.20, 2.21, and 2.22)

$$x_1 = A\sin(2\pi fs+\theta) - \frac{w}{2\cos(\arctan\left(2\pi fA\cos(2\pi fs+\theta)\right))} \tag{6.2}$$

$$x_2 = A\sin(2\pi fs+\theta) + \frac{w}{2\cos(\arctan\left(2\pi fA\cos(2\pi fs+\theta)\right))} \tag{6.3}$$

and the local coordinates (x, y, z) can be expressed in terms of the global (X, Y, Z) through a linear transformation given in Equation 2.28

$$\begin{bmatrix} x \\ y \\ z \end{bmatrix} = \mathbf{R}_y^{-1}\mathbf{R}_x^{-1}\mathbf{R}_z^{-1} \begin{bmatrix} X - X_0 \\ Y - Y_0 \\ Z - Z_0 \end{bmatrix} \tag{6.4}$$

In the local coordinate system, the channel is delimited in the y-direction by half of the specified length

$$\begin{cases} y_1 = -\frac{l}{2} \\ y_2 = \frac{l}{2} \end{cases} \tag{6.5}$$

and delimited in the z-direction by half of the specified thickness

$$\begin{cases} z_1 = -\frac{t}{2} \\ z_2 = \frac{t}{2} \end{cases} \tag{6.6}$$

By combining Equations 6.1 through 6.6, the lithofacies constraints on the parameters can be expressed by the following matrix inequality

$$\begin{bmatrix} A\sin(2\pi fs+\theta) - \frac{w}{2\cos(\arctan(2\pi fA\cos(2\pi fs+\theta)))} \\ -\frac{l}{2} \\ -\frac{t}{2} \end{bmatrix} \leq \mathbf{R}_y^{-1}\mathbf{R}_x^{-1}\mathbf{R}_z^{-1} \begin{bmatrix} X - X_0 \\ Y - Y_0 \\ Z - Z_0 \end{bmatrix} \leq \begin{bmatrix} A\sin(2\pi fs+\theta) + \frac{w}{2\cos(\arctan(2\pi fA\cos(2\pi fs+\theta)))} \\ \frac{l}{2} \\ \frac{t}{2} \end{bmatrix} \tag{6.7}$$

where the rotation matrices about the z axis ($\mathbf{R}_z$), about the x axis ($\mathbf{R}_x$), and about the y axis ($\mathbf{R}_y$) are given in terms of the three angles of azimuth, dipping, and plunging by Equations 2.25, 2.26, and 2.27. As indicated in Equation 6.7, lithofacies constraints are nonlinear inequalities and were implemented in the optimization problem in this work, like other constraints, by means of the penalty functions and step-length controller. A detailed discussion of these methods can be found in Phan (1998). It is important to note here that the maximum feasible step size was computed using a two-step approach. The step size was first computed analytically based on linear constraints and then reduced gradually until all nonlinear constraints were satisfied. Such feasible step sizes always exist provided that the initial guess is an interior point.

The approach developed here was examined with a synthetic example. Figure 6.20 shows the data for the inversion problem. A quarter of a five-spot pattern was used with an injector at the lower left and a producer at the upper right corner. The reference channel has a permeability of 2000md and a porosity of 30% embedded in a background of 50md permeability and 10% porosity material. Lithofacies data acquired at the two wells marked by symbols + indicated a presence of channels. It should be noted here that the production data were only available at the two wells located at the lower left and upper right corners and shown in Figures 6.20(c), (d), and (e). The 4-D seismic data are shown in Figure 6.20(f). Three different initial guesses with channels passing through the two wells marked with symbols + to honor the lithofacies data were used. For the case in which the initial guess consisted of one channel as depicted in Figure 6.21(a), the algorithm converged to the reference channel as shown in Figure 6.21(d). For the case in which the initial guess consisted of two channels of similar sizes as depicted in Figure 6.21(b), the algorithm converged to two channels as shown in Figure 6.21(e). It noticed that the resulting union of these two calculated channels is close to the reference channel. For the case in which the initial guess consisting of two channels of different sizes as depicted in Figure 6.21(c), the algorithm converged to two channels as shown in Figure 6.21(f). However, the smaller channel had almost vanished and the larger channel converged to the reference channel. The production and seismic data in all cases were matched almost perfectly. Figure 6.21(h) shows a match of water cut data corresponding to the calculated reservoir shown in Figure 6.21(e). It is worth noticing here that the data in this test problem was designed to overdetermine the channel parameters so that the problem of nonuniqueness was avoided. This implied that there is only one unique solution which is the reference channel and the algorithm should converge to this reference channel regardless of different initial guesses. Figure 6.21 shows one interesting aspect of this case. If using initial guesses consisting of two channels, the algorithm attempts to convert two channels into one by either joining the two channels as in the case of Figure 6.21(e) or making one vanish as in the case of Figure 6.21(f).

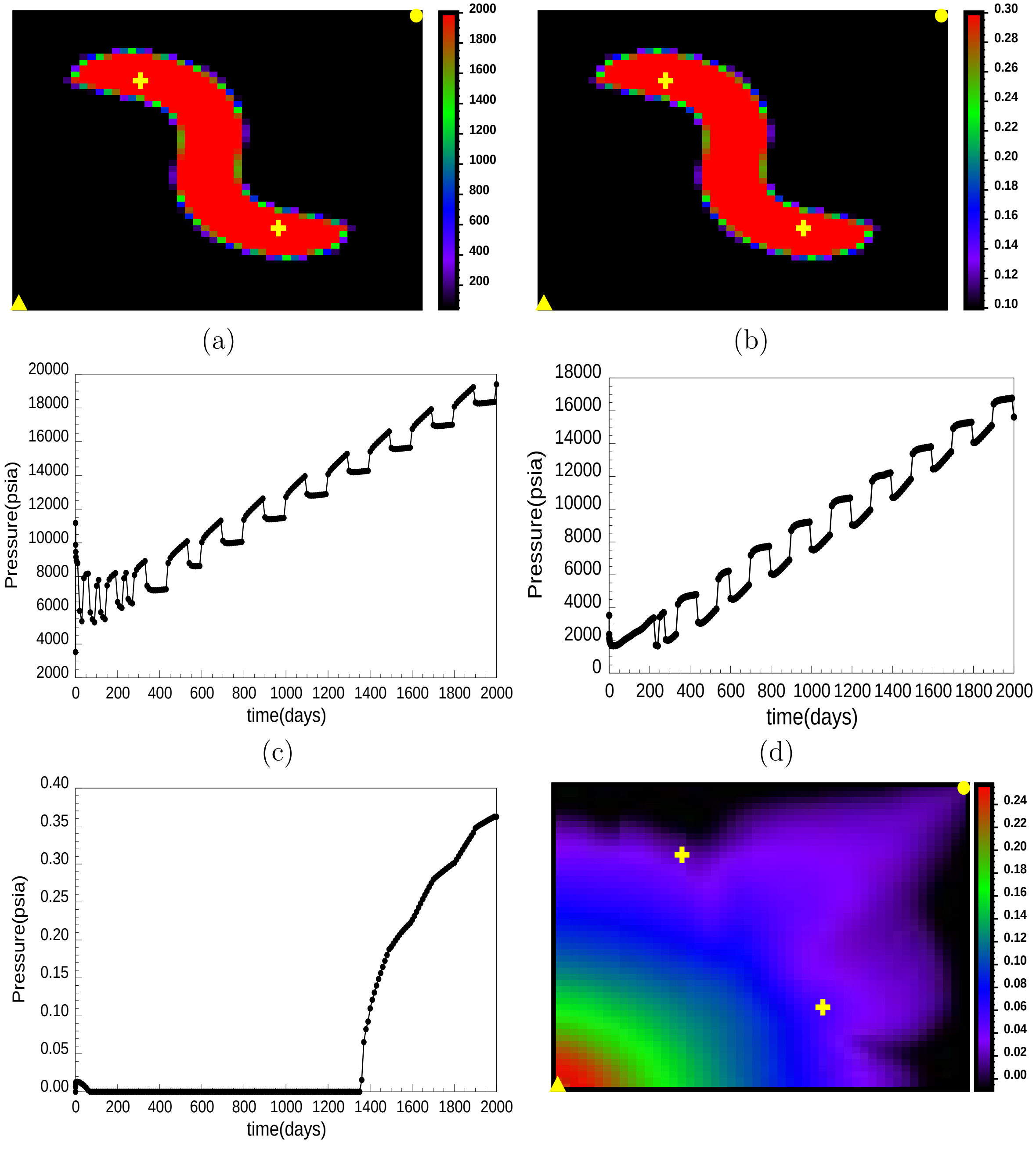

(a) (b) (c) (d) (e) (f)

Figure 6.20: (a): Reference channels - permeability. (b): Reference channels - porosity. (c): Pressure at the injector. (d): Pressure at the producer. (e): Water cut at the producer. (f): Change in water saturation.

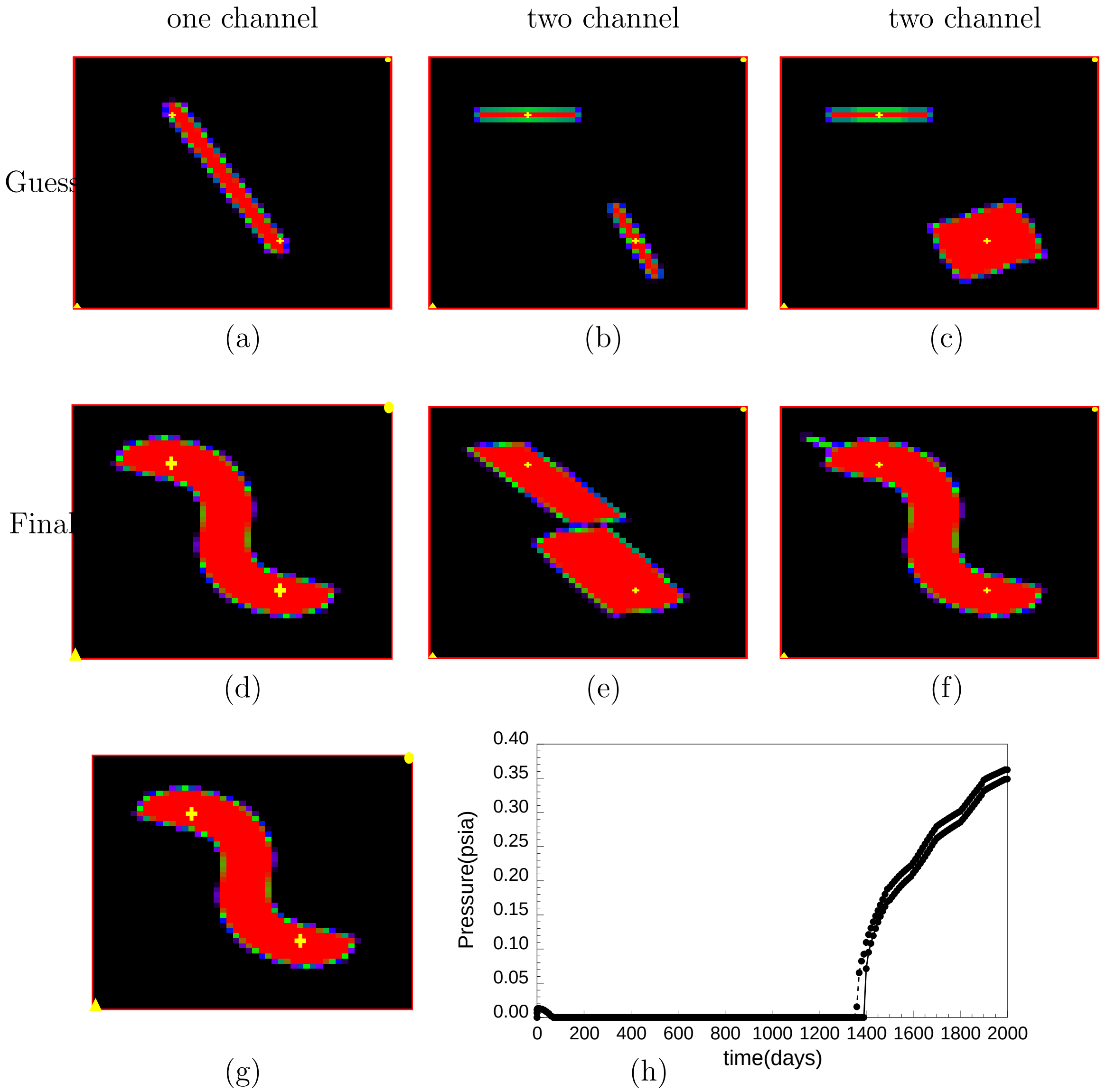

(a) (b) (c)

(d) (e) (f)

(g) (h)

Figure 6.21: (a): Guessed by one channel. (b): Guessed by two channels with similar sizes. (c): Guessed by two channels with different sizes. (d)-(f): Calculated channels. (g): Reference channel. (h): Comparison of observed and calculated water cut corresponding to (e).

6.5 Effect of Noisy Data

So far, we have assumed that the data are clean, that is the data are inaccurate due only to errors in measurement. However, in reality, the data are usually corrupted by noise that comes from a wide variety of sources. The errors in measurement and the noise contribute to differences between the true and the observed data. In this section, we shall explore effects of noise on the inversion results, particularly by addressing the following issues:

1. What type of noise has largest impact on the inversion results?
2. What levels of noise cause the inversion to no longer recover a sensible result?
3. What parameters are most and least influenced by noise?
4. How can different data types be used simultaneously to reduce the effects of noise and thus the bias of the parameter estimates?

A common approach in answering these questions is to compare the inversion results by matching noisy data to those by matching clean data without noise. For this purpose, two types of noise were introduced additively to the synthetic data sets as random offsets independent of the datum values. The noise-free synthetic 4-D seismic data are depicted in Figure 6.22(a). A uniform and a Gaussian random noise with identical means of zero and identical standard deviationrs of 0.05 were added to this clean data set resulting in the two noisy 4-D seismic data sets shown in Figures 6.22(b) and (c) respectively. The next row of this figure shows the results of inversion of the data shown in the first row. The calculated channels by matching the noise-free 4-D seismic data set, the 4-D seismic data set corrupted by uniform random distribution, and the 4-D seismic data set corrupted by Gaussian random distribution are shown in Figures 6.22(d), (e), and (f) respectively. It can be seen that the noise-free and the data set corrupted by uniform noise yield the reference channels while the data set corrupted by Gaussian noise does not. The two types of noise added have the same mean and standard deviation, however the Gaussian noise has two long tails and this distorted the original data significantly as indicated in Figure 6.22(c). The rich information along the water front has almost vanished as the calculated water front is distorted by data from the two long tails. One can see that the water front is completely blurred out and can not be recognized as it can easily in Figure 6.22(b). However, the Gaussian noise does not influence the channel orientation which, as shown in Figure 6.22(f), was recovered well. One concluding remark drawn from these figures is that the result of the inversion is more sensitive to the noise level than it is to the noise frequency and as the noise gets stronger, the inversion becomes more unreliable.

Figure 6.22(g) is similar to Figure 6.22(c), except that it was used, in this scenario, together with pressure and water cut history collected at the two wells as additional matching data sets. Figure 6.22(h) shows the result of inversion of these data sets simultaneously. It can also be seen that the errors in the inversion are significantly improved in this case. Not only the channel orientation but the channel sinuosity were also recovered well and this is consistent with the results from the sensitivity analysis performed in Section 5.6 which indicated that the data are most sensitive to these two channel parameters.

The comparision of various plots in this section indicates that it is the noise levels that are more important than the noise frequency in influencing the bias of the inversion results. Good solutions can frequently be obtained even in the presence of dense noise in the field measurements. Though pressure and water cut history are collected only at the wells, these types of data help in reducing the bias of the inversion results caused by the spatially distributed noise from 3-D seismic serveys.

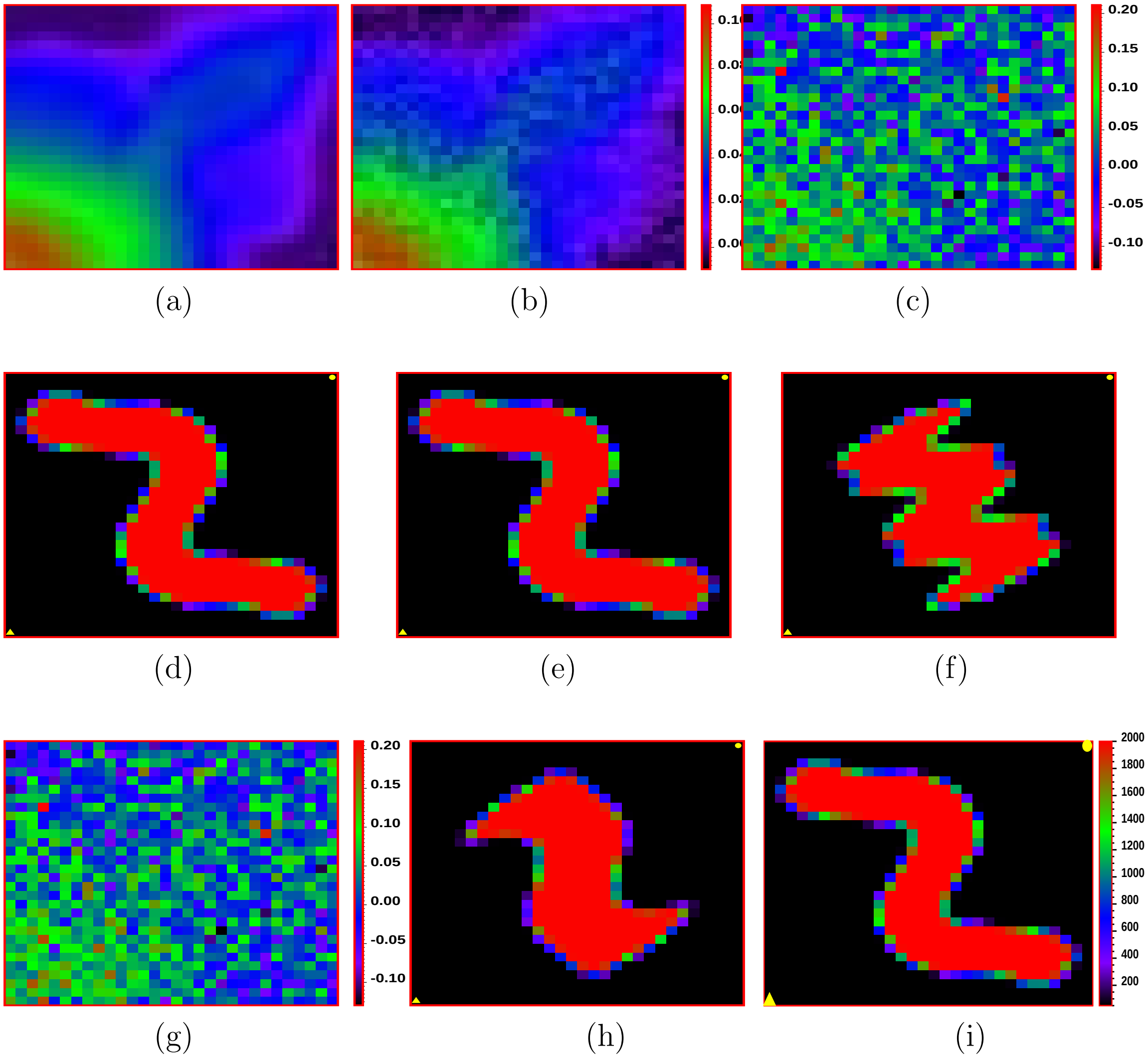

(a) (b) (c)

(d) (e) (f)

(g) (h) (i)

Figure 6.22: (a): Noise-free seismic data. (b): Seismic data with uniform noise ($\mu = 0; \sigma = 0.05$). (c): Seismic data with Gaussian noise ($\mu = 0; \sigma = 0.05$). (d): Calculated channel by inverting (a). (e): Calculated channel by inverting (b). (f): Calculated channel by inverting (c). (g): Same as (c). (h): Calculated channel by inverting (g)+$p_{wf} + w_{ct}$. (i): Reference channel.

Chapter 7

Uncertainty Assessment

In the previous chapter we have evaluated and tested the successful implementation of the subcell method in identifying the geometry and estimating the properties (permeability and porosity) of channels in a fluvial reservoir from various dynamic and static data types such as production, 4-D seismic and well logs using several synthetic examples. In this chapter we shall discuss the meaning of the parameters estimated in the context of a reservoir inversion problem and show the effects each type of data can have upon the uncertainty in estimating channel parameters and thus the uncertainty in predicting future performance of a typical fluvial reservoir. Perhaps, the ultimate purpose of investigating mathematical techniques for the modeling of fluvial reservoirs conditioned to various sources of data is not to describe geological objects but to predict the future reservoir performance under given conditions. The estimation procedures provide values for the reservoir parameters to be inserted into the prediction equations. The uncertainty in reservoir forecasting using the prediction equations is associated with the uncertainty in estimating such reservoir parameters which in turn depends on not only the amount and the type of historical data but various sources of errors such as errors in data measurements, errors in setting surface conditions, and errors in the modeling equations. Due to the imprecise nature of measurements we can never hope to have a completely accurate data set. Instead, the data set is always associated with some errors. Yet, due to the nature of the nonuniqueness of the solution of the inverse problem, we may have other solutions of geological objects that also match the given data sets. All of these sources result in the overall uncertainty in our estimates which consequently can not be considered as true parameters. Therefore, it would not be sufficient to compute the solution and simply to state that these are the estimated values of the unknown parameters. It is also important to investigate the reliability and precision of the estimates. In particular, the goal is to address the following issues:

1. What is the uncertainty associated with the estimation of each parameter?
2. How well can each parameter be determined with a given data set?
3. What data are necessary to resolve channel parameters?
4. Which channel parameters are important for reservoir forecasting and need to receive most modeling effort?
5. What is the uncertainty associated with reservoir forecasting?
6. Can detailed geologic information lost during upscaling process be recovered from production data?

These issues can be answered quantitatively using the mathematical approach presented in this chapter.

7.1 Variance and Resolution Analysis

For highly nonlinear problem, answering these questions quantitatively is still left unresolved. However, the resolution of parameters can be well understood for linear or weakly nonlinear cases, in which the response of the model is linear or close to linear with respect to parameters. The mathematical approach is described in the literature by Jackson (1972) and Menke (1989). In this work, this theory was used for the nonlinear case in a manner similar to that of Landa (1997), Phan (1998), and Datta-Gupta, Vasco, and Long (1995).

The dynamic response, denoted by $\vec{d}$, of the model correspondent to a given dynamic data set such as production and interpreted 4-D seismic is a function of the matching parameters $\vec{\alpha}$.

$$\vec{d} = \vec{d}(\vec{\alpha}) \tag{7.1}$$

A Taylor series expansion in the neighborhood of $\vec{\alpha}_0$ yields

$$\begin{aligned}\vec{d}(\vec{\alpha}) &= \vec{d}(\vec{\alpha}_0) + \frac{\partial \vec{d}}{\partial \vec{\alpha}}\delta\vec{\alpha} + \frac{1}{2}\begin{bmatrix} \delta\vec{\alpha}^T\mathbf{H^1}\delta\vec{\alpha} \\ \delta\vec{\alpha}^T\mathbf{H^2}\delta\vec{\alpha} \\ . \\ . \\ . \\ \delta\vec{\alpha}^T\mathbf{H^{nobs}}\delta\vec{\alpha} \end{bmatrix} + O(|\delta\vec{\alpha}|^3) \\ &= \vec{d}(\vec{\alpha}_0) + \mathbf{G}\delta\vec{\alpha} + \frac{1}{2}\begin{bmatrix} \delta\vec{\alpha}^T\mathbf{H^1}\delta\vec{\alpha} \\ \delta\vec{\alpha}^T\mathbf{H^2}\delta\vec{\alpha} \\ . \\ . \\ . \\ \delta\vec{\alpha}^T\mathbf{H^{nobs}}\delta\vec{\alpha} \end{bmatrix} + O(|\delta\vec{\alpha}|^3)\end{aligned} \tag{7.2}$$

where $\mathbf{G} = \frac{\partial \vec{d}}{\partial \vec{\alpha}}$ is the sensitivity matrix and $\mathbf{H^k}$, $k = 1 \rightarrow nobs$ are the Hessian matrices and given by

$$H^k_{(i,j)} = \frac{\partial^2 d_k}{\partial \alpha_i \partial \alpha_j}; \qquad \forall i, j = 1 \rightarrow npar \tag{7.3}$$

Since the Hessian matrices vanish for linear models and nearly zeros for weakly nonlinear models, the second-order and higher terms in Equation 7.2 are neglected relative to the first-order term resulting in a linear approximation of the form

$$\vec{d}(\vec{\alpha}) = \vec{d}(\vec{\alpha}_0) + \mathbf{G}\delta\vec{\alpha} \tag{7.4}$$

or by rearranging

$$\begin{aligned}\vec{d}(\vec{\alpha}) &= \vec{d}(\vec{\alpha}_0) - \mathbf{G}\vec{\alpha}_0 + \mathbf{G}\vec{\alpha} \\ &= \mathbf{G}\vec{\alpha} + Const\end{aligned} \tag{7.5}$$

Without affecting the results of the analysis, the constant term is dropped out and the linearized model becomes

$$\vec{d} = \mathbf{G}\vec{\alpha} \tag{7.6}$$

This linear model enables the estimate of the three matrices that are important for the uncertainty analysis. These three matrices are:

1. The *resolution* matrix, **R**, determines the relationship between the estimated parameters and the true parameters. If **R** is close to identity, the estimated parameters have good resolution and are close to the true values.

2. The *information density* matrix, $\mathbf{S}_{inf}$, determines the relationship between the calculated response and the true response. If $\mathbf{S}_{inf}$ is close to identity, the estimated parameters yields a good match of the data.

3. The *covariance* matrix, **C**, measures the uncertainty of the parameter estimates. If **C** is close to diagonal, the estimated parameters are near linearly independent.

The inversion problem is reduced to the problem of finding the solution of a linear system

$$\vec{d}_{obs} = \mathbf{G}\vec{\alpha} \tag{7.7}$$

In general, the sensitivity matrix **G** is not square. The best least square solution, $\vec{\alpha}^*$, of Equation 7.7 can be found by minimizing the two-norm

$$\vec{\alpha}^* = arg \min_{\vec{\alpha}} \parallel \vec{d}_{obs} - \mathbf{G}\vec{\alpha} \parallel_2 \tag{7.8}$$

and the resulting normal equation is given by

$$\mathbf{G}^T\mathbf{G}\vec{\alpha} = \mathbf{G}^T\vec{d}_{obs} \tag{7.9}$$

or,

$$\vec{\alpha}^* = (\mathbf{G}^T\mathbf{G})^{-1}\mathbf{G}^T\vec{d}_{obs} = \mathbf{G}^{-g}\vec{d}_{obs} \tag{7.10}$$

where $\mathbf{G}^{-g} = (\mathbf{G}^T\mathbf{G})^{-1}\mathbf{G}^T$ is the pseudoinverse of matrix **G**. The true parameters, $\vec{\alpha}_t$, are used to generate the observed data $\vec{d}_{obs}$ using Equation 7.6

$$\vec{d}_{obs} = \mathbf{G}\vec{\alpha}_t \tag{7.11}$$

Combining Equation 7.10 and Equation 7.11 we have,

$$\vec{\alpha}^* = \mathbf{G}^{-g}\mathbf{G}\vec{\alpha}_t = \mathbf{R}\vec{\alpha}_t \tag{7.12}$$

and the calculated response $\vec{d}_{cal}$ is computed from the solution $\vec{\alpha}^*$ using Equation 7.6 and 7.10

$$\vec{d}_{cal} = \mathbf{G}\vec{\alpha}^* = \mathbf{G}\mathbf{G}^{-g}\vec{d}_{obs} = \mathbf{S}_{inf}\vec{d}_{obs} \tag{7.13}$$

where $\mathbf{R} = \mathbf{G}^{-g}\mathbf{G}$ is the resolution matrix and $\mathbf{S}_{inf} = \mathbf{G}\mathbf{G}^{-g}$ is the information density matrix. The covariance matrix of the parameter estimates can be calculated as:

$$\begin{aligned}\mathbf{C}\{\vec{\alpha}^*\} = \mathbf{C}(\vec{\alpha}^*, \vec{\alpha}^*) = \mathbf{C}(\mathbf{G}^{-g}\vec{d}_{obs}, \mathbf{G}^{-g}\vec{d}_{obs}) &= \mathbf{G}^{-g}\mathbf{C}(\vec{d}_{obs}, \vec{d}_{obs})\mathbf{G}^{-g^T} \\ &= \mathbf{G}^{-g}\mathbf{C}\{\vec{d}_{obs}\}\mathbf{G}^{-g^T}\end{aligned} \tag{7.14}$$

where $\mathbf{C}\{\vec{d}_{obs}\}$ is the covariance of the observed data. If the measurement errors are independent, $\mathbf{C}\{\vec{d}_{obs}\}$ is a diagonal matrix. As was seen the three matrices $\mathbf{R}$, $\mathbf{S}_{inf}$, and $\mathbf{C}$ depend on the sensitivity matrix $\mathbf{G}$, the pseudoinverse of the sensitivity matrix $\mathbf{G}^{-g}$, and the covariance matrix of the measurement errors $\mathbf{C}\{\vec{d}_{obs}\}$. The data covariance matrix $\mathbf{C}\{\vec{d}_{obs}\}$ is dependent on the measurement techniques and is given. The sensitivity matrix $\mathbf{G}$ can be computed from the full sensitivity matrix as was shown in Section 5.3.2. Finally, the pseudoinverse $\mathbf{G}^{-g}$ of the sensitivity matrix can be computed based on the *Singular Value Decomposition* theory as described next.

For any nonsquare matrix $\mathbf{G}$ of size *nobs* x *npar*, the singular value decomposition (SVD) of $\mathbf{G}$ is the factorization of the form

$$\mathbf{G} = \mathbf{U}\mathbf{\Lambda}\mathbf{V}^T \tag{7.15}$$

where $\mathbf{U}$ and $\mathbf{V}$ are orthogonal matrices. $\mathbf{U}$ is *nobs* x *nobs* and $\mathbf{V}$ is *npar* x *npar*. $\mathbf{\Lambda}$ is a diagonal *nobs* x *npar* matrix with positive or zero elements (the singular values).

$$\mathbf{U}^T\mathbf{U} = \mathbf{U}\mathbf{U}^T = \mathbf{I}_{nobs} \tag{7.16}$$

$$\mathbf{V}^T\mathbf{V} = \mathbf{V}\mathbf{V}^T = \mathbf{I}_{npar} \tag{7.17}$$

$$\mathbf{\Lambda} = \begin{bmatrix} \mathbf{\Lambda}_p & 0 \\ 0 & 0 \end{bmatrix} \tag{7.18}$$

where **I** is the identity matrix, $\mathbf{\Lambda}_p$ is a square diagonal p x p matrix with positive elements, and p is the number of nonzero elements on the diagonal of $\mathbf{\Lambda}$.

Matrices **U** and **V** can be expressed as:

$$\mathbf{U} = \begin{bmatrix} \mathbf{U}_p & \mathbf{U}_0 \end{bmatrix} \tag{7.19}$$

$$\mathbf{V} = \begin{bmatrix} \mathbf{V}_p & \mathbf{V}_0 \end{bmatrix} \tag{7.20}$$

where $\mathbf{U}_p$ is called the left singular vectors composed of columns of **U** corresponding to the nonzero elements in $\mathbf{\Lambda}$. $\mathbf{V}_p$ is called the right singular vectors composed of columns of **V** corresponding to the nonzero elements in $\mathbf{\Lambda}$. $\mathbf{U}_0$ and $\mathbf{V}_0$ are the columns of **U** and **V** respectively corresponding to the zero elements in $\mathbf{\Lambda}$. Since **U** and **V** are orthogonal matrices, Equations 7.19 and 7.20 result in

$$\mathbf{U}_p^T\mathbf{U}_p = \mathbf{I}_p \tag{7.21}$$

$$\mathbf{V}_p^T\mathbf{V}_p = \mathbf{I}_p \tag{7.22}$$

Combining Equation 7.15 and Equations 7.18 through 7.20, matrix **G** can be expressed in terms of the left and right singular vectors as follows:

$$\mathbf{G} = \mathbf{U\Lambda V}^T = \begin{bmatrix} \mathbf{U}_p & \mathbf{U}_0 \end{bmatrix} \begin{bmatrix} \mathbf{\Lambda}_p & 0 \\ 0 & 0 \end{bmatrix} \begin{bmatrix} \mathbf{V}_p^T \\ \mathbf{V}_0^T \end{bmatrix} = \mathbf{U}_p\mathbf{\Lambda}_p\mathbf{V}_p^T \tag{7.23}$$

Combining Equations 7.21 through 7.23 to the definition of the pseudoinverse of matrix **G** in Equation 7.10 gives:

$$\mathbf{G}^{-g} = (\mathbf{G}^T\mathbf{G})^{-1}\mathbf{G}^T = \left((\mathbf{U}_p\mathbf{\Lambda}_p\mathbf{V}_p^T)^T(\mathbf{U}_p\mathbf{\Lambda}_p\mathbf{V}_p^T)\right)^{-1}(\mathbf{U}_p\mathbf{\Lambda}_p\mathbf{V}_p^T)^T = \mathbf{V}_p\mathbf{\Lambda}_p^{-1}\mathbf{U}_p^T \tag{7.24}$$

Combining Equations 7.21, 7.23, and 7.24, the resolution matrix can be expressed as

$$\mathbf{R} = \mathbf{G}^{-g}\mathbf{G} = \mathbf{V}_p\mathbf{\Lambda}_p^{-1}\mathbf{U}_p^T\mathbf{U}_p\mathbf{\Lambda}_p\mathbf{V}_p^T = \mathbf{V}_p\mathbf{V}_p^T \tag{7.25}$$

Similarly, by combining Equations 7.22 through 7.24, the information density matrix can be expressed as

$$\mathbf{S}_{inf} = \mathbf{G}\mathbf{G}^{-g} = \mathbf{U}_p\mathbf{\Lambda}_p\mathbf{V}_p^T\mathbf{V}_p\mathbf{\Lambda}_p^{-1}\mathbf{U}_p^T = \mathbf{U}_p\mathbf{U}_p^T \tag{7.26}$$

An alternative method, which was used in this work to compute the component matrices in Equation 7.23, makes use of the eigenvalue decomposition. From Equation 7.23 $\mathbf{G}$ is given by:

$$\mathbf{G} = \mathbf{U}_p \mathbf{\Lambda}_p \mathbf{V}_p^T \tag{7.27}$$

Then we can construct matrix $\mathbf{M}$ defined as:

$$\mathbf{M} = \mathbf{G}^T \mathbf{G} = (\mathbf{U}_p \mathbf{\Lambda}_p \mathbf{V}_p^T)^T \mathbf{U}_p \mathbf{\Lambda}_p \mathbf{V}_p^T = \mathbf{V}_p \mathbf{\Lambda}_p^T \mathbf{U}_p^T \mathbf{U}_p \mathbf{\Lambda}_p \mathbf{V}_p^T = \mathbf{V}_p \mathbf{\Lambda}_p^2 \mathbf{V}_p^T \tag{7.28}$$

The matrix $\mathbf{M}$ is symmetric and thus can be decomposed by *eigenvalue* decomposition to find $\mathbf{V}_p$ and $\mathbf{\Lambda}_p^2$. From Equation 7.27, $\mathbf{U}_p$ is then determined by:

$$\mathbf{U}_p = \mathbf{G} \mathbf{V}_p \mathbf{\Lambda}_p^{-1} \tag{7.29}$$

using Equation 7.24, the covariance matrix of the parameter estimates from Equation 7.14 can be calculated as

$$\mathbf{C}\{\vec{\alpha}^*\} = \mathbf{G}^{-g} \mathbf{C}\{\vec{d}_{obs}\} \mathbf{G}^{-g^T} = \mathbf{V}_p \mathbf{\Lambda}_p^{-1} \mathbf{U}_p^T \mathbf{C}\{\vec{d}_{obs}\} \mathbf{U}_p \mathbf{\Lambda}_p^{-1} \mathbf{V}_p^T \tag{7.30}$$

Combining Equations 7.28 through 7.30 gives

$$\begin{aligned} \mathbf{C}\{\vec{\alpha}^*\} &= \mathbf{V}_p \mathbf{\Lambda}_p^{-1} \mathbf{\Lambda}_p^{-1} \mathbf{V}_p^T \mathbf{G}^T \mathbf{C}\{\vec{d}_{obs}\} \mathbf{G} \mathbf{V}_p \mathbf{\Lambda}_p^{-1} \mathbf{\Lambda}_p^{-1} \mathbf{V}_p^T \\ &= \mathbf{V}_p \mathbf{\Lambda}_p^{-2} \mathbf{V}_p^T \mathbf{G}^T \mathbf{C}\{\vec{d}_{obs}\} \mathbf{G} \mathbf{V}_p \mathbf{\Lambda}_p^{-2} \mathbf{V}_p^T \\ &= \mathbf{M}^{-1} \bar{\mathbf{C}} \mathbf{M}^{-1} \end{aligned} \tag{7.31}$$

where the matrices $\mathbf{M}^{-1}$ and $\bar{\mathbf{C}}$ are (*npar* x *npar*) and are given as follows:

$$\mathbf{M}^{-1} = \mathbf{V}_p \mathbf{\Lambda}_p^{-2} \mathbf{V}_p^T \tag{7.32}$$

$$\bar{\mathbf{C}} = \mathbf{G}^T \mathbf{C}\{\vec{d}_{obs}\} \mathbf{G} \tag{7.33}$$

The uncertainties associated with the estimation of parameters are measured by the standard deviations ($\sigma_{\alpha_i}; i = 1 \rightarrow npar$) which can be obtained directly from the diagonal of the covariance matrix of parameters $\mathbf{C}\{\vec{\alpha}^*\}$ as:

$$\sigma_{\alpha_i} = \sqrt{\mathbf{C}\{\vec{\alpha}^*\}_{(i,i)}} = \sqrt{\sum_{k=1}^{npar} \sum_{j=1}^{npar} M_{i,j}^{-1} \bar{C}_{j,k} M_{k,i}^{-1}} \tag{7.34}$$

7.2 Numerical Experiments

This section describes a set of numerical experiments that were designed to serve the purpose of understanding various aspects associated with the goodness of fit and the variance/resolution of the estimated parameters. The analysis was also to answer various uncertainty issues posed at the beginning of this chapter mainly by investigating the crucial question of how the data is related to the resolution of parameters and their corresponding variances. The analysis was performed based on the mathematical approach presented in the previous section. Figures 7.1(a) and (b) show maps of permeability and porosity of an example reservoir model consisting of a single synthetic channel that was used for the analysis. Wells were in a quarter five-spot pattern with one injector at the lower left and one producer at the upper right corner. Figures 7.1(c) and (d) present the long term pressure history collected at the two wells. The reservoir size and the flow rates were set in such a way to result in a water breakthrough in a short period of time of roughly 140 days as indicated in Figure 7.1(e). Figure 7.1(f) shows the 4-D seismic data that would be interpreted from two 3-D seismic surveys at 100 and 380 days. Based on Equation 7.33, calculating the variance of the estimates requires the covariance matrix of the errors in data measurements. Since in general (see Landa, 1997), there always exists a linear transformation to transform a dependent data set to an independent set, therefore, with out loss of generality, we can assume that these errors are statistically independent and thus result in a diagonal covariance matrix. The covariance matrix of data used in this analysis has the diagonal form

$$\mathbf{C}\{\vec{d}_{obs}\} = \begin{bmatrix} \sigma_p^2\mathbf{I}_p & 0 & 0 \\ 0 & \sigma_w^2\mathbf{I}_w & 0 \\ 0 & 0 & \sigma_{\Delta s_w}^2\mathbf{I}_{\Delta s_w} \end{bmatrix} \tag{7.35}$$

where the $\mathbf{I}_p$, $\mathbf{I}_w$, and $\mathbf{I}_{\Delta s_w}$ are identity matrices with appropriate sizes and σ_p, σ_w, and $\sigma_{\Delta s_w}$ are respectively the standard deviations of pressure, water cut, and 4-D seismic data. For this numerical experiment, these standard deviations were assumed to have the following values

$$\begin{aligned}\sigma_p &= 0.1 \quad \text{psia}\\ \sigma_w &= 0.01\\ \sigma_{\Delta s_w} &= 0.05\end{aligned}$$

The pressure data set was composed of 174 data points, the water cut data set was composed of 87 data points, and the 4-D seismic data set was composed of 900 data points. This resulted in a total of 1161 observation points. The analysis was performed on a total of seven channel parameters as follows:

- x: the translation in x-direction,
- y: the translation in y-direction,
- α: the channel orientation,
- δ: the channel departure,
- F: the channel sinuosity,
- W: the channel width, and
- L: the channel length.

Several scenarios matching different data sets were implemented and the results are shown in Figure 7.2. The first row is the starting point used in all scenarios. The second through the fifth rows show the calculated reservoir and the corresponding matches by matching different data sets separately. The second row corresponds to matching water cut history, the third row corresponds to matching 4-D seismic data, the fourth row corresponds to matching pressure history, and the fifth row corresponds to matching jointly both pressure and water cut history. For the case of matching 4-D seismic data, the reference channel is recovered correctly. For all other cases, the estimated channel differed significantly from the reference. The uncertainties of the estimates of the seven channel parameters corresponding to matching various data types were calculated using Equation 7.34 and the results are depicted in Figure 7.3. In particular, the following five sets of combined data were analyzed:

1. Water cut history only.
2. Pressure history only.
3. Pressure and water cut history.
4. 4-D seismic data only.
5. Pressure, water cut, and 4-D seismic data.

Figure 7.4 summarized the results of how different data sets can be related to the overall uncertainty. The resolution matrices corresponding to matching the five combined data sets were calculated using Equation 7.25 and the results are shown in Figure 7.5. The resolution matrix presents the relationship between the estimated parameters and the true parameters. The closer this matrix to identity or the more dominant the diagonal over the off-diagonal elements then the closer the estimated values lie to the true values. As indicated in Figure 7.5, the diagonal elements are barely recognized in the matrix by matching only the water cut, become dominant by matching only pressure history and become even more dominant over the off-diagonal elements by matching both pressure and water cut history. The resolution matrix by matching 4-D seismic data contains mainly the diagonal. The resolution matrix by matching all the data, namely pressure, water cut, and 4-D seismic data contains only the diagonal.

The following remarks and observations can be drawn from the results:

1. The overall uncertainty can always be reduced by adding more data.
2. Water cut data provide least information on the channel parameters. One reason could be that water cut is available only at the producer and carries information only after the arrival of water front.
3. Pressure data, on the other hand, are available at the two wells and carry richer information than water cut.
4. 4-D seismic data provides richest information on the channel parameters and reduces the overall uncertainty remarkably. This is because the 4-D seismic data provides information that is spatially distributed.

5. The channel orientation and sinuosity are best resolved. This is because the data are most sensitive to these two parameters.

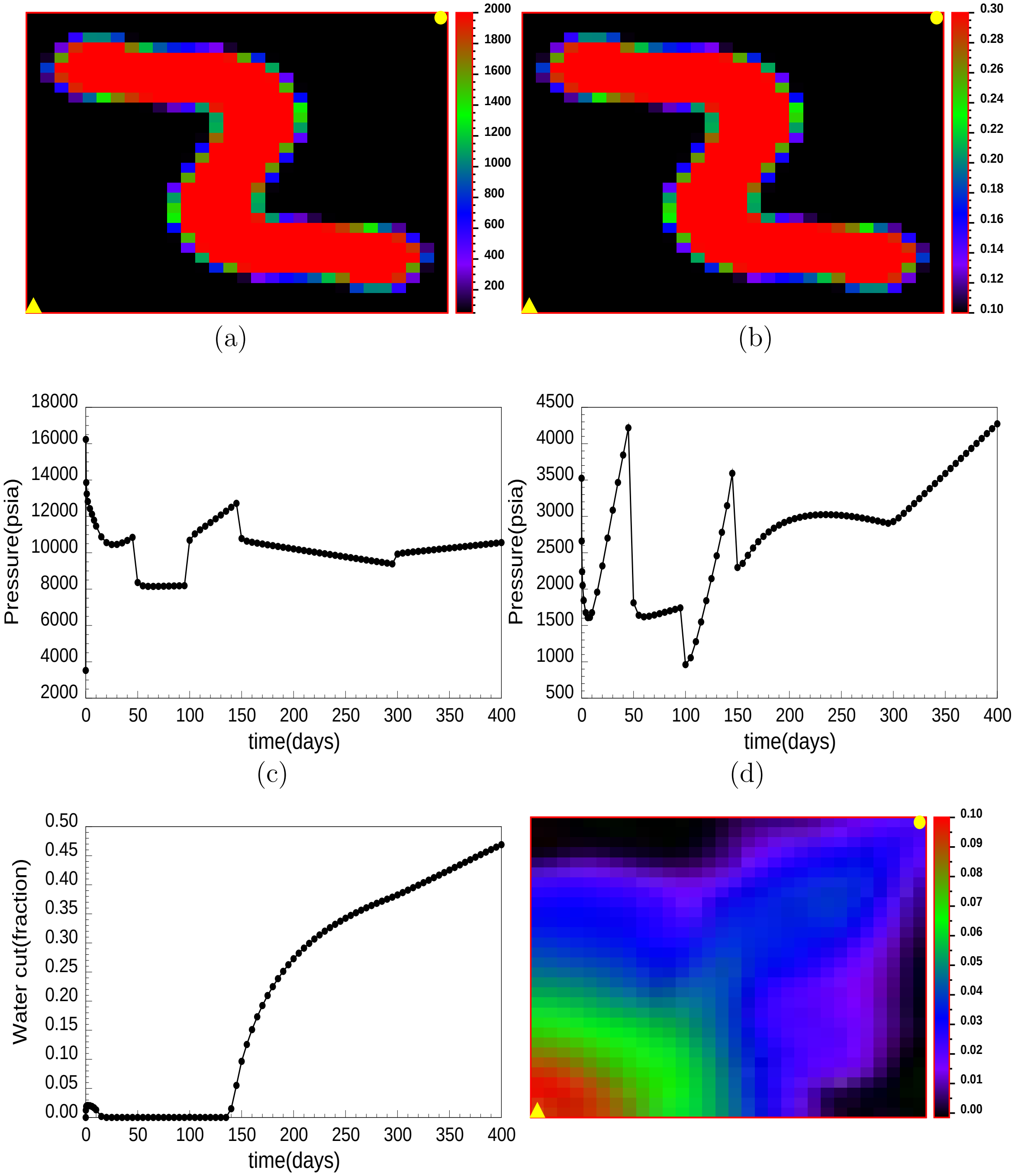

(a) (b) (c) (d) (e) (f)

Figure 7.1: (a): Reference channels - permeability. (b): Reference channels - porosity. (c): Pressure at the injector. (d): Pressure at the producer. (e): Water cut at the producer. (f): Change in water saturation between 100 and 380 days.

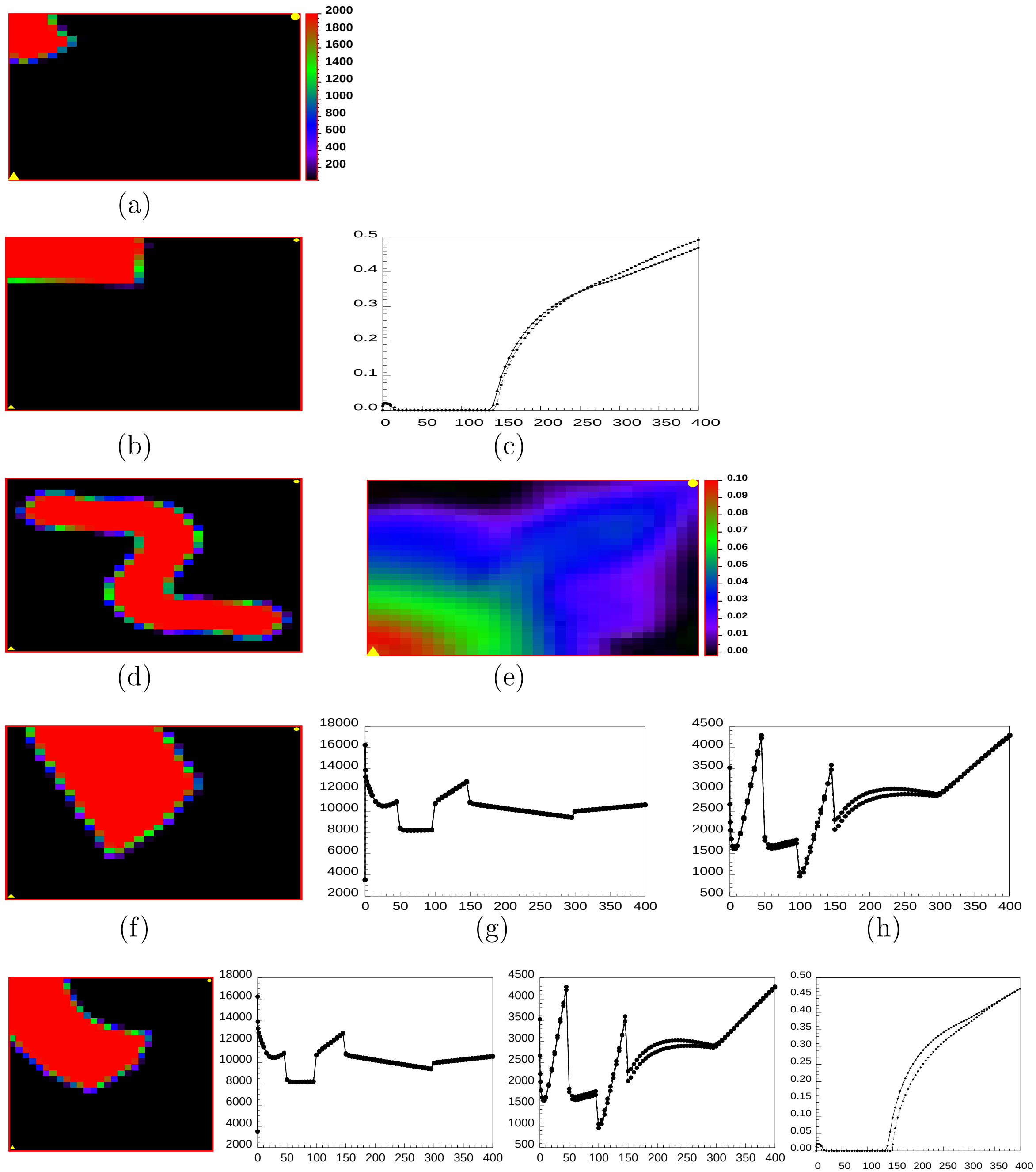

(a)

(b) (c)

(d) (e)

(f) (g) (h)

(i) (j) (k) (l)

Figure 7.2: (a): Starting point. (b)-(c): Calculated from matching water cut. (d)-(e): Calculated from matching change in water saturation. (f)-(h): Calculated from matching pressure history. (i)-(l): Calculated from matching pressure and water cut history.

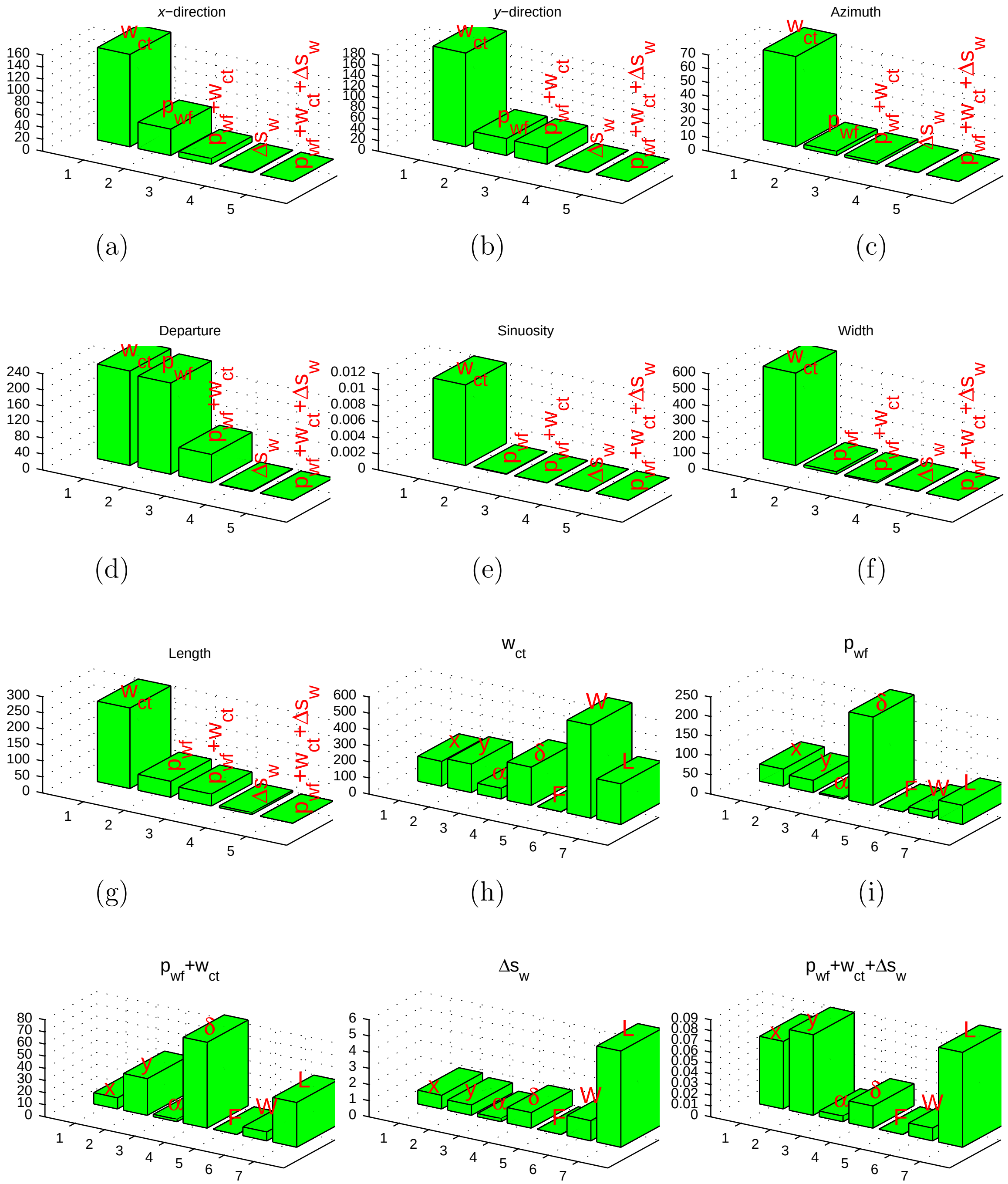

(a) (b) (c)

(d) (e) (f)

(g) (h) (i)

(j) (k) (l)

Figure 7.3: (a)-(g): Uncertainties corresponding to matching various data types. (h)-(l): Uncertainties with respect to parameters. - x: x-direction. y: y-direction. α: Orientation. δ: Departure. F: Sinuosity. W: Width. L: Length.

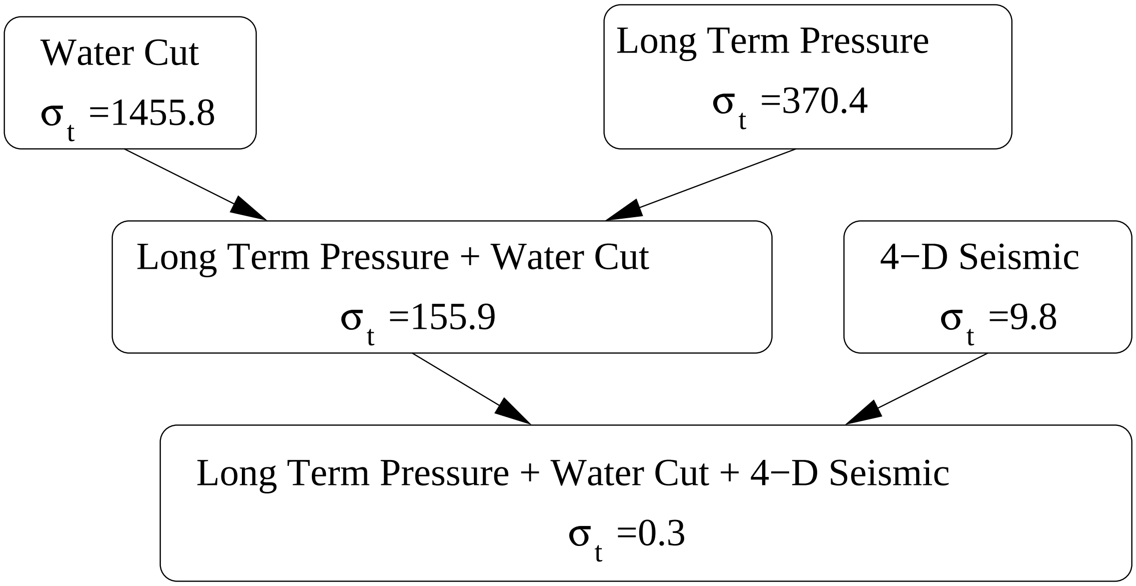

Figure 7.4: Total relative uncertainties over all channel parameters corresponding to matching various data types.

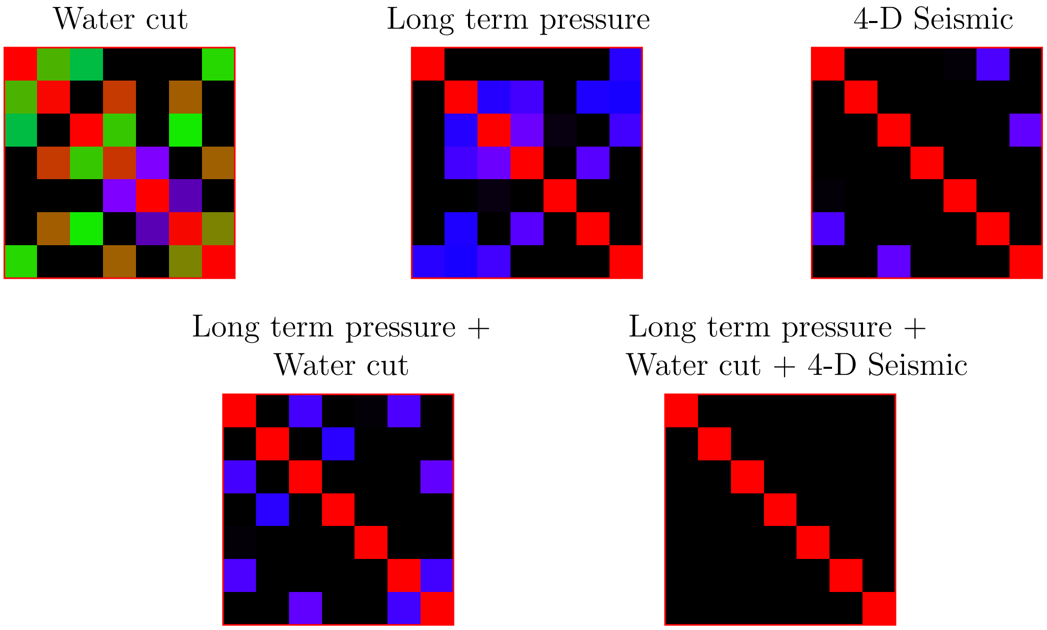

Figure 7.5: Resolution matrices corresponding to matching various data types.

7.3 Uncertainty in Reservoir Forecasting

Uncertainty in reservoir forecasting is unavoidable and one major challenge facing reservoir engineers and geoscientists is to quantify and minimize such uncertainty. In this section, we shall develop a mathematical formula to estimate the errors and uncertainty in the prediction of reservoir performance. Let us say that we wish to predict the value of some vector $\vec{f}$ representing the future performance of a reservoir under study, based on the value of a vector of independent variables $\vec{s}$ representing various surface condition settings and a vector of parameters $\vec{\alpha}^*$. The prediction is to be made on the basis of the model

$$\vec{f}_p = \vec{f}(\vec{s}, \vec{\alpha}^*) \tag{7.36}$$

where the subscript p stands for the predicted value. As was also mentioned at the begining of this chapter, there are three possible sources of inaccuracy in the predictions: errors in the estimated $\vec{\alpha}^*$, errors in the setting of surface conditions of $\vec{s}$, and errors in the measurement of the reservoir future performance $\vec{f}$. By assuming the model equation itself is correct, these are the only three sources of errors contributing to the difference between the predicted value $\vec{f}_p$ and the eventual observations $\vec{f}_o$. Suppose the three errors are denoted by $\delta\vec{\alpha}$, $\delta\vec{s}$, and $\delta\vec{f}$ respectively. The true value of surface condition settings is $\vec{s}+\delta\vec{s}$, the true value of parameters is $\vec{\alpha}^*+\delta\vec{\alpha}$, and the true value of the reservoir performance is $\vec{f}(\vec{s}+\delta\vec{s}, \vec{\alpha}^*+\delta\vec{\alpha})$. The eventually observed of future reservoir performance, $\vec{f}_o$, can be given by

$$\vec{f}_o = \vec{f}(\vec{s}+\delta\vec{s}, \vec{\alpha}^*+\delta\vec{\alpha}) + \delta\vec{f} \tag{7.37}$$

A Taylor series expansion up to linear terms yields

$$\vec{f}(\vec{s}+\delta\vec{s}, \vec{\alpha}^*+\delta\vec{\alpha}) = \vec{f}(\vec{s}, \vec{\alpha}^*) + \frac{\partial\vec{f}}{\partial\vec{s}}\delta\vec{s} + \frac{\partial\vec{f}}{\partial\vec{\alpha}}\delta\vec{\alpha} \tag{7.38}$$

Combining Equations 7.36 through 7.38 gives the error between the eventually observed and the prediction of future reservoir performance

$$\vec{f}_o - \vec{f}_p = \frac{\partial\vec{f}}{\partial\vec{s}}\delta\vec{s} + \frac{\partial\vec{f}}{\partial\vec{\alpha}}\delta\vec{\alpha} + \delta\vec{f} \tag{7.39}$$

By assumimg the errors from the three sources are statistically independent, then the covariance matrix of the prediction errors can be approximated as

$$\begin{aligned} \mathbf{C}\{\vec{f}_o - \vec{f}_p\} &\equiv E(\vec{f}_o - \vec{f}_p)(\vec{f}_o - \vec{f}_p)^T \qquad (7.40) \\ = \left(\frac{\partial \vec{f}}{\partial \vec{s}}\right) \mathbf{C}\{\delta\vec{s}\} \left(\frac{\partial \vec{f}}{\partial \vec{s}}\right)^T &+ \left(\frac{\partial \vec{f}}{\partial \vec{\alpha}}\right) \mathbf{C}\{\delta\vec{\alpha}\} \left(\frac{\partial \vec{f}}{\partial \vec{\alpha}}\right)^T + \mathbf{C}\{\delta\vec{f}\} \end{aligned}$$

where $\mathbf{C}\{\delta\vec{s}\}$, $\mathbf{C}\{\delta\vec{\alpha}\}$, and $\mathbf{C}\{\delta\vec{f}\}$ are, respectively, the covariance matrices of the three errors $\delta\vec{\alpha}$, $\delta\vec{s}$, and $\delta\vec{f}$. Normally, the first term on the right hand side of Equation 7.40 may be omitted if the surface condition settings $\vec{s}$ can be set or is known precisely. The matrix $\mathbf{C}\{\delta\vec{\alpha}\}$ can be calculated as shown in the previous section using Equation 7.31. The matrix $\mathbf{C}\{\delta\vec{f}\}$ depends on the measurement technology and is usually given. It is noted here that if the vector $\vec{f}$ corresponds to the observed data in the history matching process then $\mathbf{C}\{\delta\vec{f}\}$ coincides with the matrix $\mathbf{C}\{\vec{d}_{obs}\}$. Finally, the matrix $\frac{\partial \vec{f}}{\partial \vec{\alpha}}$ can be obtained from the sensitivity matrix $\mathbf{G}$ evaluated at the times of prediction.

Chapter 8

Applications of the Method

In previous chapters, we discussed the development of modeling techniques involving two- and three-dimensional geological objects. In Chapter 6, we have evaluated and tested the ability of these techniques through a variety of synthetic examples. In this chapter, we shall present the application of the proposed procedure for reservoir parameter inversion in a more general and realistic environment. The purpose is to demonstrate the capability of the approach developed in this work in solving practical problems and to explore the difficulties and areas that require further research.

In particular, the application of the proposed method is described in the following cases:

1. The number of channels is not *a priori* knowledge but rather an unknown parameter to be estimated.

2. The properties (permeability and porosity) of the rock inside the channels and background are distributed rather nonuniformly but with fixed patterns.

3. The nonuniqueness of the inverse problems is unavoidable and the true solution must be selected without bias from a large set of possible solutions. One approach to generate equiprobable solutions without bias is to model the geometry and properties of channels stochastically.

8.1 Unknown Number of Channels

Let n denote the number of channels and $\vec{\alpha}$ denote a set of matching parameters, the objective is to find a minimal number of channels n^* and an optimal set of parameters $\vec{\alpha}^*$ such that

$$\{n^*, \vec{\alpha}^*\} = arg \min_{n \in \mathbf{N}, \vec{\alpha} \in D} E(n, \vec{\alpha}) \tag{8.1}$$

where D is the feasible domain determined by a set of constraints on parameters and $\mathbf{N}$ is a set of nonnegative integers. The optimal solution $(n^*, \vec{\alpha}^*)$ in Equation 8.1 can be found by a two-step optimization procedure. The first step is to minimize the objective function with respect to parameters $\vec{\alpha}$ for each fixed value of integer n

$$E(n, \vec{\alpha}^*(n)) = \min_{\vec{\alpha} \in D} E(n, \vec{\alpha}) \tag{8.2}$$

The second step is to find an optimal value of n such that

$$\{n^*, \vec{\alpha}^*\} = arg \min_{n \in \mathbf{N}} E(n, \vec{\alpha}^*(n)) \tag{8.3}$$

Since we can add one more channel into the set of n existing channels without changing the objective function by overlapping one of the existing channels with the new channel, it is easy to verify that the following property holds

$$\min_{\vec{\alpha} \in D} E(1, \vec{\alpha}) \geq \min_{\vec{\alpha} \in D} E(2, \vec{\alpha}) \geq ... \min_{\vec{\alpha} \in D} E(n^*, \vec{\alpha}) \geq \min_{\vec{\alpha} \in D} E(n^* + 1, \vec{\alpha})... \tag{8.4}$$

Moreover, since $(n^*, \vec{\alpha}^*)$ is a global minimum, we also have

$$\min_{\vec{\alpha} \in D} E(n^*, \vec{\alpha}) = E(n^*, \vec{\alpha}^*) \leq E(n^* + k, \vec{\alpha}) \quad \forall \vec{\alpha} \in D \tag{8.5}$$

where k is a fixed integer. Equivalently, Equation 8.5 can be written as

$$\min_{\vec{\alpha} \in D} E(n^*, \vec{\alpha}) = E(n^*, \vec{\alpha}^*) \leq \min_{\vec{\alpha} \in D} E(n^* + k, \vec{\alpha}) \tag{8.6}$$

Combining Equations 8.4 and 8.6 yields

$$\begin{aligned} \min_{\vec{\alpha} \in D} E(1, \vec{\alpha}) \geq \min_{\vec{\alpha} \in D} E(2, \vec{\alpha}) \geq ... \min_{\vec{\alpha} \in D} E(n^* - 1, \vec{\alpha}) \geq \min_{\vec{\alpha} \in D} E(n^*, \vec{\alpha}) = \\ \min_{\vec{\alpha} \in D} E(n^* + 1, \vec{\alpha}) = \min_{\vec{\alpha} \in D} E(n^* + 2, \vec{\alpha})... \end{aligned} \tag{8.7}$$

Equation 8.7 implies that $\min_{\vec{\alpha}\in D} E(n, \vec{\alpha})$ is a nonincreasing function of n for $n \leq n^*$ and becomes constant for $n \geq n^*$. A *brute force* algorithm would be to increase the number of channels until the optimal objective function is no longer significantly reduced. One obvious drawback of this algorithm is that it is very expensive from the computational point of view when the solution is correspondent to a large number of channels. A more efficient method considered in this work made use of the *bisection* technique in which the root-containing interval is divided in half until the optimal objective function at the midpoint of the interval is the same order of magnitude as that of a given threshold. To demonstrate the ability of the two-step optimization procedure described above making use of the bisection technique, a synthetic two-dimensional reservoir model was generated by upscaling the Stanford V data set depicted in Figure 8.1. Stanford V data set is a three-dimensional fluvial channel reservoir generated on a mesh grid of 100x130x10 for the general purpose of testing and evaluating stochastic algorithms (Stanford V reservoir - Mao, 1998). A number of data such as vertical, horizontal, and deviated wells are also available from this reference data set to mimic actual well log data. The grid dimensions for the upscaled model, used as a synthetic two-dimensional reservoir in this example, is 50x65x1. There is a total of eight wells consisting of three injectors and five producers. Producers #1, #2, #3, and #4 have time-dependent oil rate history depicted in Figure 8.2. The remaining four wells including the three injectors and one producer #5 have constant flow rate history. The water injection rates of the three injectors (#1, #2, and #3) were set to 7,000 STB/day, 3,000 STB/day, and 7,000 STB/day respectively and the producer #5 produced at a constant oil rate of 2,000 STB/day. A map of reference permeability is shown in Figure 8.3(a). The reference porosity is assumed to be a function of permeability by the relation $log(k) = 9\phi - 0.3$. This correlation could be obtained from the data analysis of cores taken from well logs. Figure 8.3(b) shows a map of reference porosity calculated from the permeability-porosity correlation. The three injectors are marked by triangular symbols with the well numbers in red color shown nearby and the five producers are marked by circular symbols with the well numbers in white color shown nearby. All wells are located inside channels and are relatively well connected. The synthetic pressure data as would be obtained from permanent gauges installed at all wells were simulated from the upscaled model and are plotted in Figure 8.3(c) for the three injectors and in Figure 8.3(d) for the five producers. The upward and downward trends in pressure at the producer wells at 100 and 200 days are due to the abrupt changes in flow rates as indicated in Figure 8.2. Figure 8.3(e) shows the history of the water cut measured at each producer well. Except for producer #3, the other producers were observed to have water breakthrough early before 300 days. This is because they are located in regions that are near and well connected to the injectors. Injection water does not reach producer #3 because of the surrounding poor permeability regions isolating this well from the injectors. Figure 8.3(f) shows a map of the change in water saturation between 100 and 580 days. This map is assumed to have been interpreted from two 3-D seismic surveys. Geophysical interpretation can not provide the saturation values from each seismic survey. However, it can provide the change of saturations between two surveys. The skin factors of all wells and the permeability-porosity correlation were considered to be known. The unknown parameters for the inversion in this example consist of the number of channels and all geometric and property parameters defining the position, size, shape, permeability, and porosity of channels. The two-step optimization procedure described above was used to invert for all unknown parameters. The resulting bisection tree corresponding with a threshold of 10^9 is illustrated in Figure 8.4. It should be noted here that each node of the tree represents the first step of the two-step optimization procedure which corresponds to solving the optimization problem given in Equation 8.2 for each fixed value of n (the number of channels) given on the node. Techniques for solving this equation were discussed in Chapter 3. The resulting values of the objective function are listed nearby the nodes in Figure 8.4. The threshold value must not be less than the global minimum to ensure the existence of the solution and was chosen based on the initial run with 41 channels as indicated at the first node of the tree. The algorithm started out with an initial guess of 21 identically overlapping channels as shown in Figure 8.5(a) resulting in an optimal objective function value of 10^7 (see Figure 8.4). This value is less than the threshold and therefore the number of channels was reduced to 11 which is the next midpoint between 1 and 21. The new second midpoint resulted in an optimal value of $E \approx 10^{11}$ which is greater than the threshold and the algorithm increased the number for channels to the third midpoint of 16 channels between 11 and 21. The third midpoint with 16 channels yielded an optimal value of $E \approx 10^8$. This value is less than the threshold and the algorithm reduced the number of channels to a fourth midpoint between 11 and 16. The fourth midpoint resulted in an optimal value of $E \approx 10^9$ which is the same magnitude as that of the threshold and the bisection algorithm terminated with 14 channels. A total of 100 flow simulation runs were made to build the entire resulting bisection tree. Each node in the tree took roughly 25 runs and the CPU time required for each flow simulation run was about 6 minutes on a UNIX workstation running at 400 MHz. The final calculated 14 channels and the match of pressure, water cut, and 4-D seismic data are shown in Figure 8.5. The pressure and water cut data are plotted in triangular symbols and the calculated values are plotted with solid lines. The water cut at the producers (except for well #4) and the 4-D seismic data were matched reasonably well. The pressure matches of all wells (except for well #4) are considered to be acceptable. Well #4 is poorly matched and this is consistent with the results from the calculated reservoir with 14 channels where this well is located inside one of the channels that is isolated from others and is observed to have different permeability from the true value. The most important reason was due to a high threshold of the objective function. the matches would be improved by reducing the threshold value. The calculated reservoir differs from but looks similar to the reference reservoir in terms of channel distribution, orientations, and sinuosity. The reservoir was compartmentalized into three regions mainly containing channels. The bottom region connects the injector #1 and the two producer wells #2 and #5. The middle region connects the injector #3 and the two producer wells #3 and #4. The top region connects the injector #2 and the producer #1. The same compartmentalization was also observed in the calculated reservoir. Another interesting result observed from Figures 8.5(b) and (c) is that each channel connecting two wells in the reference map was replaced, in the calculated map, by two channels almost joined at the point where the permeability was lowest in the reference map. This result illustrates what probably would happen in field cases where the information is more detailed than the resolution of parameters.

The channels were assumed to possess uniform properties and this assumption was evidently not consistent with the Stanford V fluvial data set where the permeability and porosity within each channel were distributed nonuniformly. The following sections will consider examples in which the distributions of permeability and porosity inside channels are not restricted to uniformity.

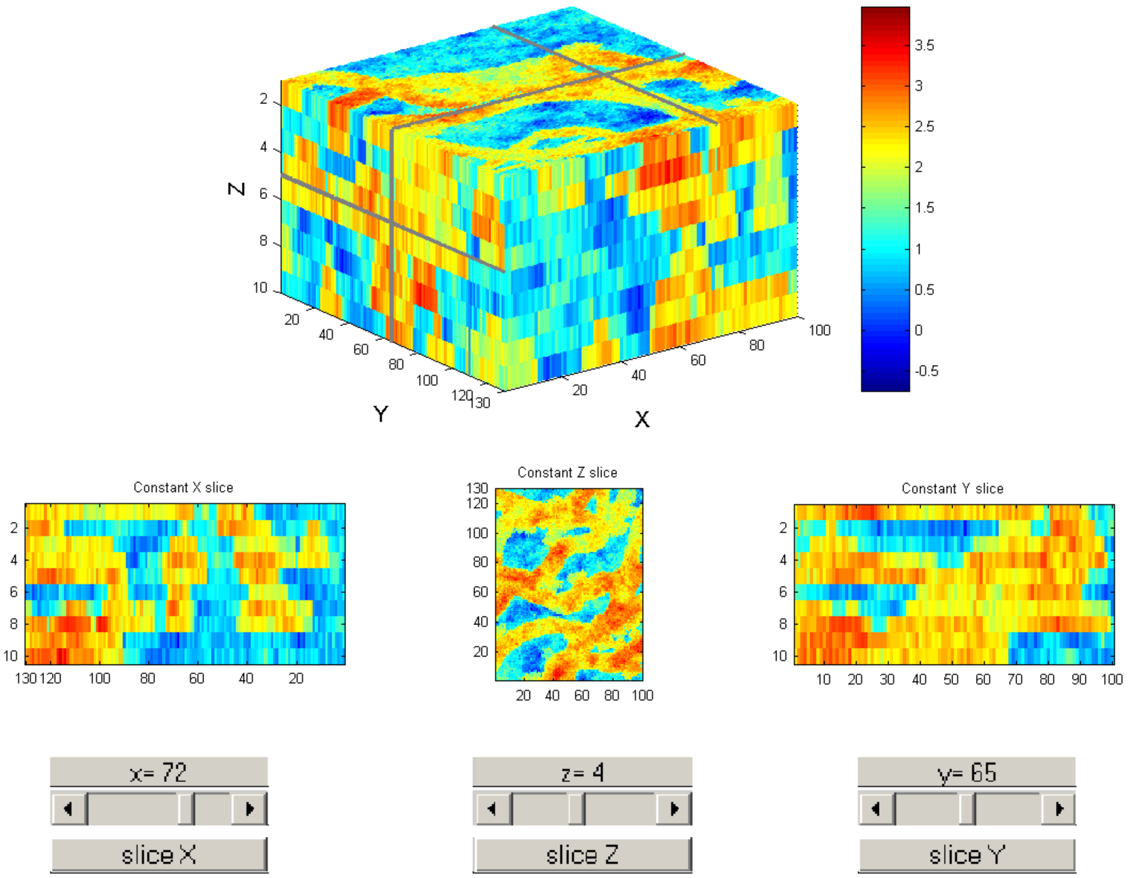

Figure 8.1: Log-permeability distribution.

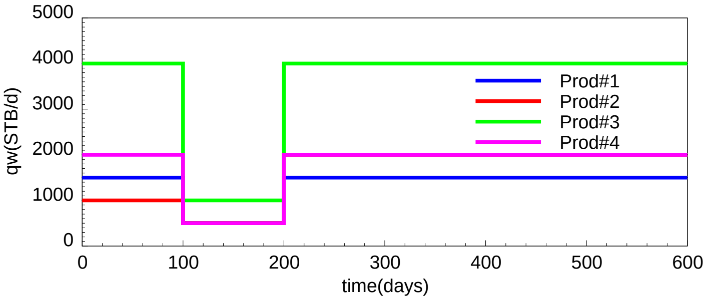

Figure 8.2: Flow rate history.

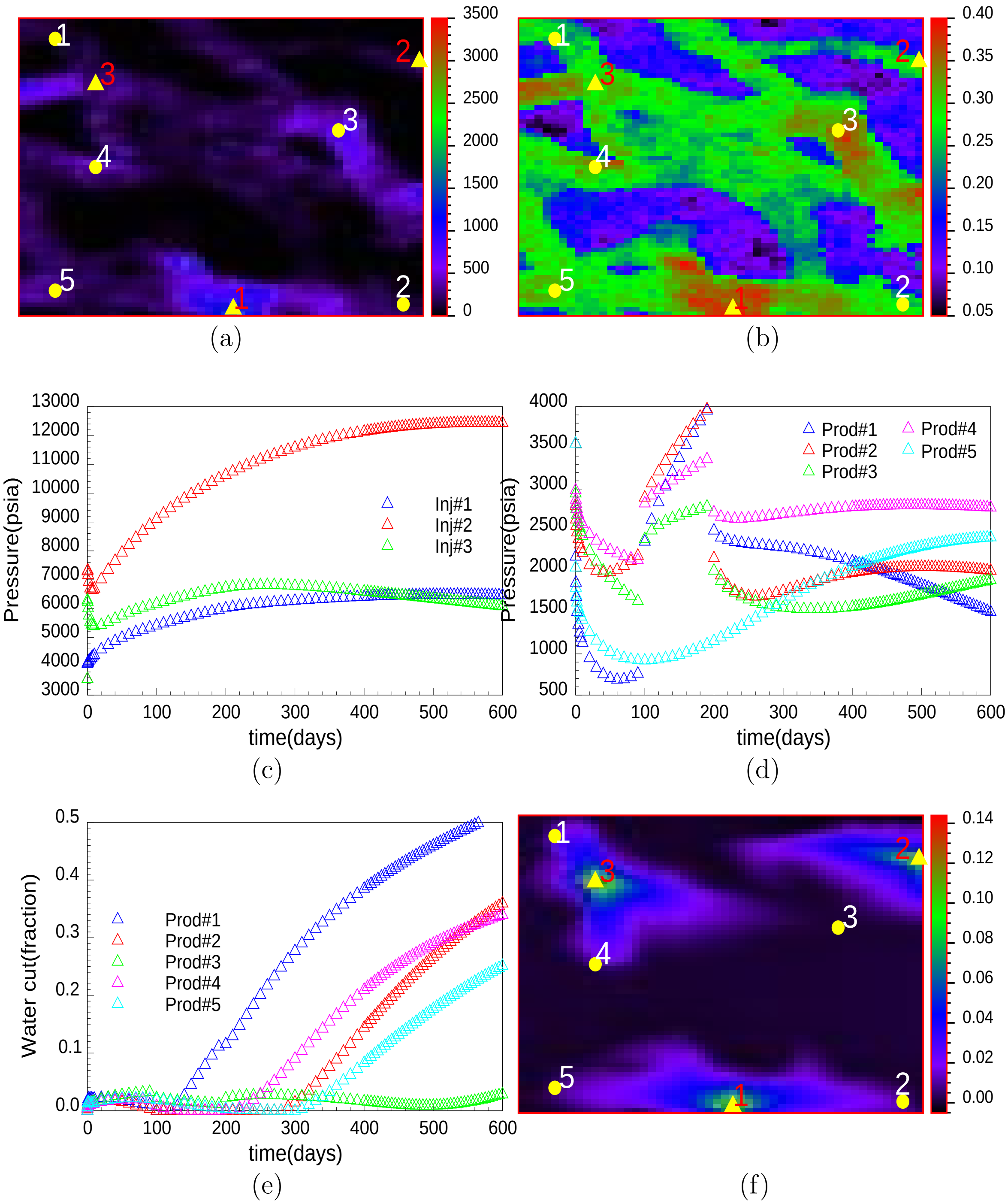

(a) (b)

(c) (d)

(e) (f)

Figure 8.3: (a): Reference channels - permeability. (b): Reference channels - porosity. (c): Pressure at the injectors #1, #2, and #3. (d): Pressure at the producers #1, #2, #3, #4, and #5. (e): Water cut at the producers #1, #2, #3, #4, and #5. (f): Change in water saturation between 100 and 580 days.

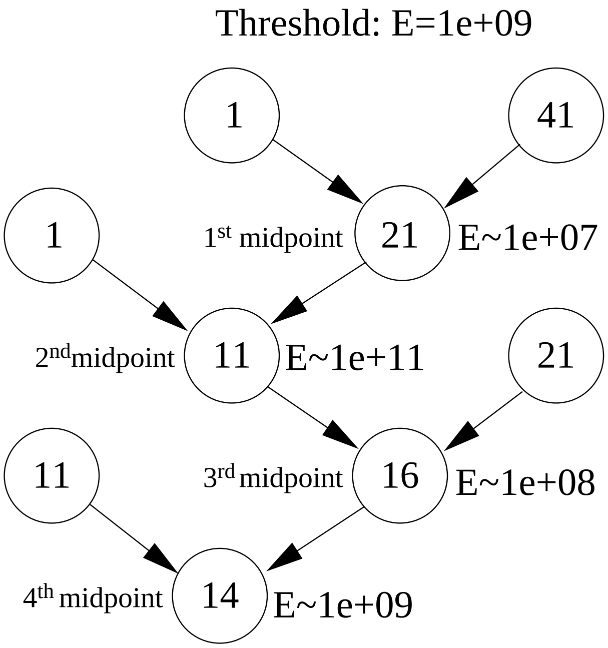

Figure 8.4: Resulting bisection tree: the numbers inside each circle are the intermediate calculated number of channels.

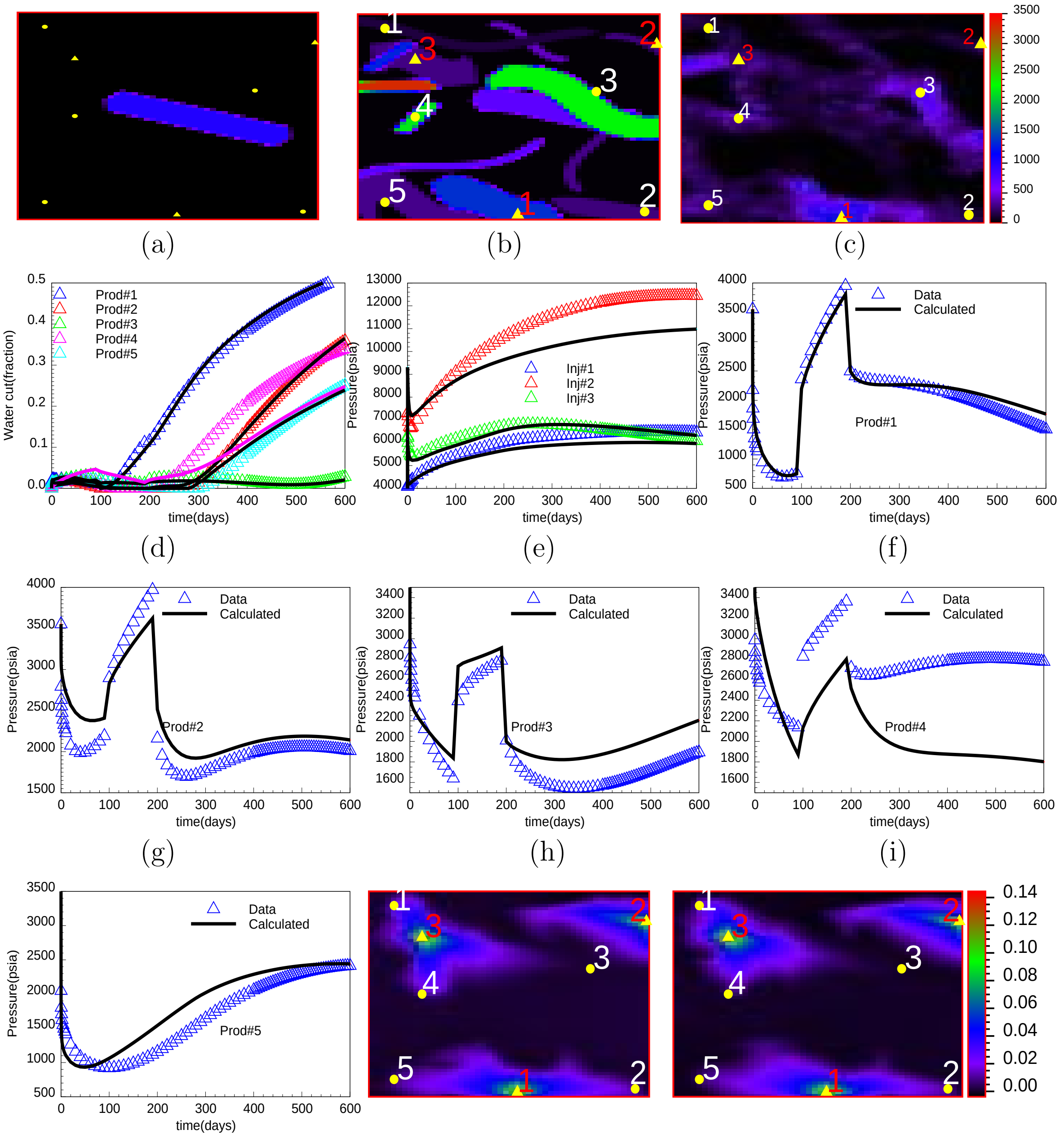

(a) (b) (c)

(d) (e) (f)

(g) (h) (i)

(j) (k) (l)

Figure 8.5: (a): Starting point with 21 channels. (b): Calculated permeability with 14 channels. (c): Reference permeability. (d): Comparison of water cut at the five producers. (e): Comparison of pressure at the three injectors. (f): Comparison of pressure at producer#1. (g): Comparison of pressure at producer#2. (h): Comparison of pressure at producer#3. (i): Comparison of pressure at producer#4. (j): Comparison of pressure at producer#5. (k): Reference 4-D seismic data. (l): Calculated 4-D seismic.

8.2 Deterministic Integration of 3-D Seismic Data

Geometries of channels can be known with relatively high certainty from the seismic amplitude maps that show high contrast between the channel and nonchannel facies but the distributions of permeability and porosity inside channels and background remain unknown. This situation was previously examined in Section 6.3. However, the discussion has been restricted to conditions where permeability and porosity within each channel were assumed to be uniformly distributed (though they differ across channels). This was because the discussion was intended to illustrate the ability of the proposed method in handling a large number of objects and also to investigate how different data sets would be related to the resolution of parameters and their corresponding variances. In this section, we shall revisit this situation from a different point of view where the distributions of permeability and porosity inside channels and background are not constrained to uniformity. A reservoir model for this test was constructed consisting of a set of ten channels drawn from triangular distributions given in Table 8.1. The grid dimensions were 100x100x50 in the x, y, and z directions, respectively. The mesh grid was uniform and each grid cell was 25 ft. x 25

Table 8.1: Triangular distributions for channel parameters.

Channel Parameters	Low	Mode	High
x-translation (ft)	0	1250	2500
y-translation (ft)	0	1250	2500
z-translation (ft)	0	250	500
channel *Azimuth* ($^o deg$)	0	60	120
channel dipping ($^o deg$)	-15	0	15
channel plunging ($^o deg$)	90	90	90
channel departure (ft)	50	100	200
channel sinuosity (cycles/10,000ft)	5	10	15
channel displacement (ft)	0	0	0
channel width (ft)	50	100	150
channel length (ft)	500	2000	2500
channel thickness (ft)	100	200	300

ft. x 10 ft. Figure 8.7 presents a three-dimensional view of the constructed channels together with three cross sections at x=50, y=50, and z=25. One injection well (well #1 in red color) and three production wells (well #2, #3, and #4 in green color) were positioned in the test model as shown in Figure 8.7. Wells #1, #2, and #3 intersected large portions of channels while well #4 was located inside background. The water injection rate of the injector and the total liquid (water and oil) rates of the producers were time-dependent and are plotted in Figure 8.8. The synthetic 3-D seismic impedance was generated by a two-step procedure. The first step was to calculate the distribution of facies for the reservoir model consisting of ten channels constructed by assigning a value of one at cells inside the channels and a value of zero at cells outside the channels. The second step was to generate the synthetic 3-D seismic impedance values within each facies making use of a Sequential Gaussian Simulation (sgsim) geostatistical algorithm (geostatistical software package Deutsch and Journel, 1998). The resulting two simulated impedance fields were constrained to the two desired histograms (one for each facies, see Figure 8.9) and the two spherical variograms. The variogram of background facies has an azimuth of 60 degrees and ranges of 50 ft, 5 ft, and 2 ft in horizontal maximum, horizontal minimum, and vertical dimensions while the variogram of channel facies has the same azimuth of 60 degrees but with larger ranges of 500 ft, 30 ft, and 4 ft in horizontal maximum, horizontal minimum, and vertical dimensions. Both variograms of the two facies have the same constant nugget effect of 0.1 and sills of 0.9. Finally, the synthetic seismic impedance was generated by a merger of the two seismic fields using the facies distribution calculated from the first step. The information that is known to us and thus that can be used to find the distributions of permeability and porosity inside channels and background can be summarized as follows:

1. Long term pressure and water cut history. Figure 8.10(a) shows the long-term pressure history from permanent down-hole gauges installed at the four wells and water cut history from production data collected at the producers. The upward and downward trends in pressure were due to the changes in the specified flow rates.

2. Depth-average 4-D seismic data (for thin reservoir, only the average change of water saturation in depth dimension is available). Figure 8.10(b) shows the average change of water saturation distribution in the depth dimension between 100 and 800 days. We assumed that this information would be available from the interpretation of two 3-D seismic surveys.

3. An unknown relationship between permeability and porosity in each of the facies. Figure 8.10(c) shows such relationships where the logarithm of permeability is correlated linearly to porosity. However, the slopes and intercepts of the lines are unknown. We assumed that the existence of the linear relationship can be verified either from outcrop observations or from core data analysis. Phan (1998) has shown that using a relationship whose linearity was not validated could result in the distortion of the estimates.

One simple way to maintain the geological features observed in the 3-D seismic data distribution is to seek the following distribution of permeability:

$$\vec{k} = m\vec{s} + t \tag{8.8}$$

where $\vec{k}$ denotes the permeability field, $\vec{s}$ denotes the seismic-related rock property field such as P and S wave impedance, and m and t are the two scalars representing the multiplier and the translation of the original distribution. The two parameters m and t are constant for each facies but they may differ between facies.

8.2.1 Constraints on the multipliers and translations

There are no physical constraints imposed on this type of parameter rather they are constrained through the physical limits imposed on the permeability for each facies.

$$k_1 \leq ms + t \leq k_2 \tag{8.9}$$

This is equivalent to

$$\left\{ \begin{array}{ccc} m & \geq & 0 \\ ms_{max} + t & \leq & k_2 \\ ms_{min} + t & \geq & k_1 \end{array} \right. \tag{8.10}$$

and

$$\begin{cases} m & \leq & 0 \\ ms_{max} + t & \geq & k_1 \\ ms_{min} + t & \leq & k_2 \end{cases} \tag{8.11}$$

where s_{min} and s_{max} are the minimum and maximum values of the 3-D seismic data in each facies. It is easy to see that the inequalities 8.10 and 8.11 are satisfied for all points inside the shaded region depicted in Figure 8.6 and in the iterative search optimization, the parameters (m, t) for each facies must be confined inside such shaded regions. In this work, the permeability in the x-direction was calculated using Equation 8.8, the permeability in the y-direction was assigned to be equal to the permeability in the x-direction, and the permeability in the z-direction was assigned to be equal to one-tenth of the permeability in the x-direction. The main steps in constructing the reference reservoir model for this example can be summarized as follows:

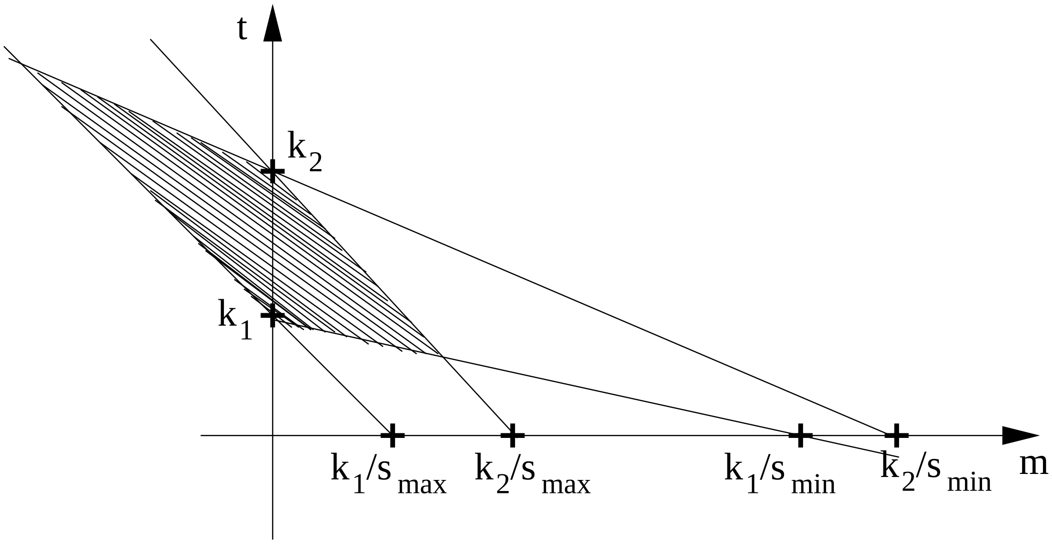

Figure 8.6: Feasible regions of parameters (m, t).

- Generating a set of ten 3-D channels with geometry drawn from triangle distributions. It should be noted here that the channel geometry were frozen during the inversion process.

- Calculating facies distribution based on the set of generated channels.
- Populating synthetic 3-D seismic data within each facies honoring variogram models and external histograms.
- Calculating the x-permeability using the seismic multiplier and translation constants.
- Calculating the y-permeability and z-permeability using the relations; $k_x = k_y$ and $k_z = 0.1k_x$.
- Calculating porosity using the linear correlations between the logarithm of the x-permeability and porosity: $log(k_x) = a\phi + b$.
- Upscaling the permeability and porosity fields using Unweighted area sampling technique. The mesh grid of the upscaled model were 50 x 50 x 5.

The set of parameters used in the previous steps to generate the synthetic data were referred to as the true parameters. For this example, the following eight parameters were chosen to be the parameters of inversion:

- *Parameter # 1* (m_0): the seismic multiplier used for the background facies.
- *Parameter # 2* (t_0): the seismic translation used for the background facies.
- *Parameter # 3* (m_1): the seismic multiplier used for the channel facies.
- *Parameter # 4* (t_1): the seismic translation used for the channel facies.
- *Parameter # 5* (a_0): the slope in the log $k - \phi$ correlation used for the background facies.
- *Parameter # 6* (b_0): the intercept in the log $k - \phi$ correlation used for the background facies.
- *Parameter # 7* (a_1): the slope in the log $k - \phi$ correlation used for the channel facies.

- *Parameter # 8* (b_1): the intercept in the log $k - \phi$ correlation used for the channel facies.

Table 8.2 shows the evolution of each parameter during the inversion process. The algorithm was able to converge to the true parameters after 16 iterations. In the first four iterations, the seismic multipliers were changed significantly toward the true values resulting in a major reduction of the objective function. After the fourth iteration, the algorithm focused mainly on changing the other parameters to achieve further reduction of the mismatch of the data. The last two rows show the true parameters and the uncertainties in estimating each parameter. The uncertainties of the estimates of seismic multipliers were at least two order of magnitudes better than those of the translations. Overall, parameters associated with the channel facies were resolved better with lower uncertainties than those associated with the background facies. This was because most wells were located inside the channels. The resulting resolution matrix of parameters was approximately identical to identity and is shown in Figure 8.11. Figure 8.12 shows a three-dimensional view of the calculated permeability in the x-direction together with the three cross-sections indicating the heterogeneity and the constrast between the channel and the background facies. It was noticed that the steepest-descent method in this case was shown to have a better performance than the Gauss-Newton method.

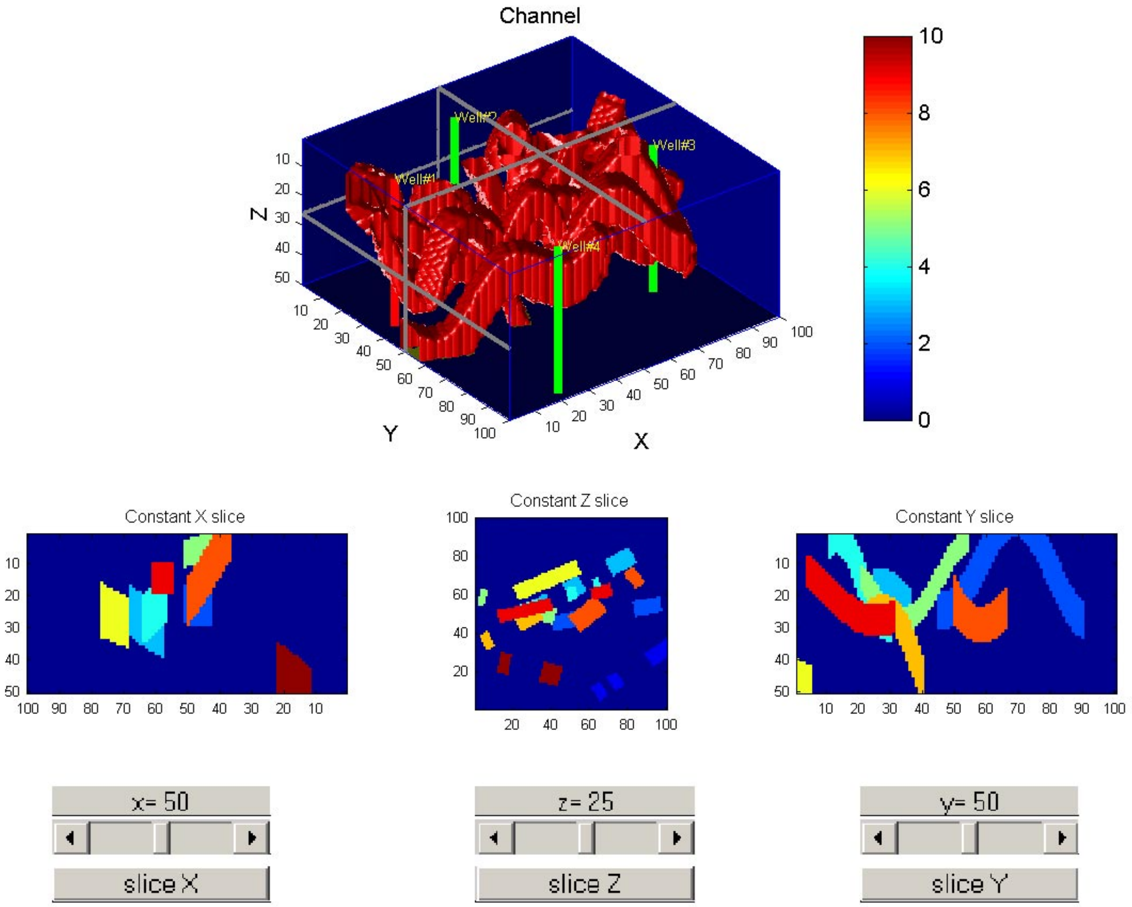

Figure 8.7: Channel reservoir - Geometry frozen for history matching.

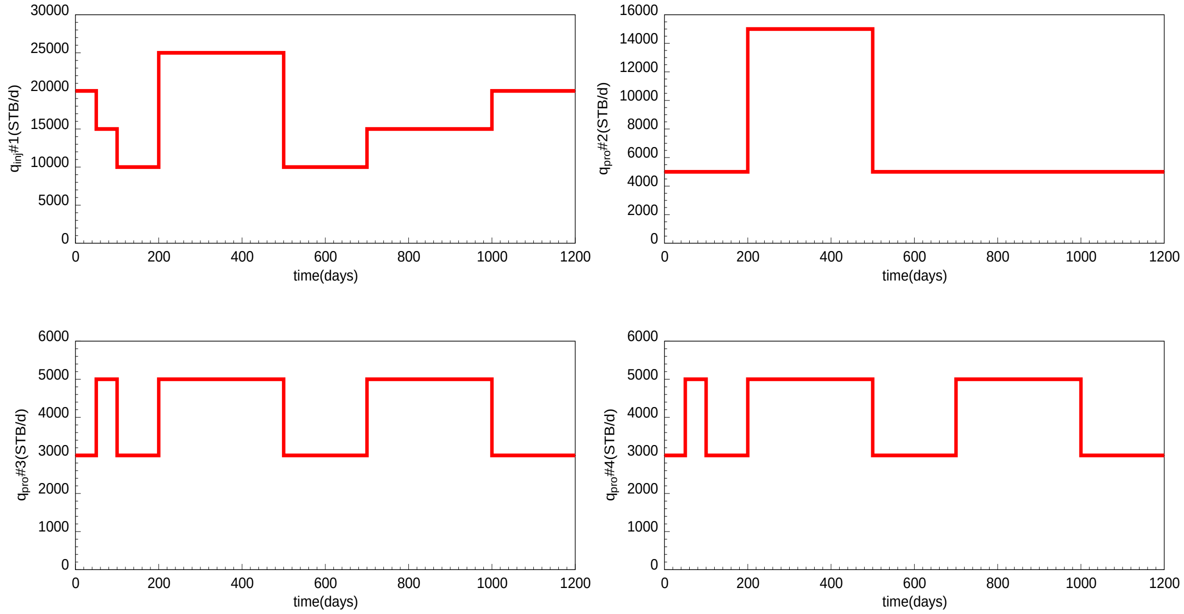

Figure 8.8: Time-dependent rate history.

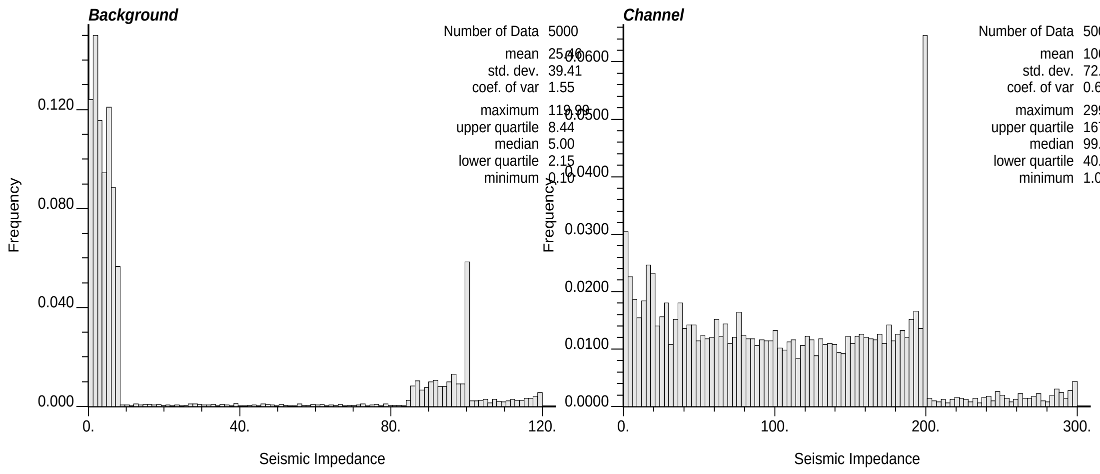

(a) (b)

Figure 8.9: (a): Histogram of seismic impedance in background facies. (b):Histogram of seismic impedance in channel facies.

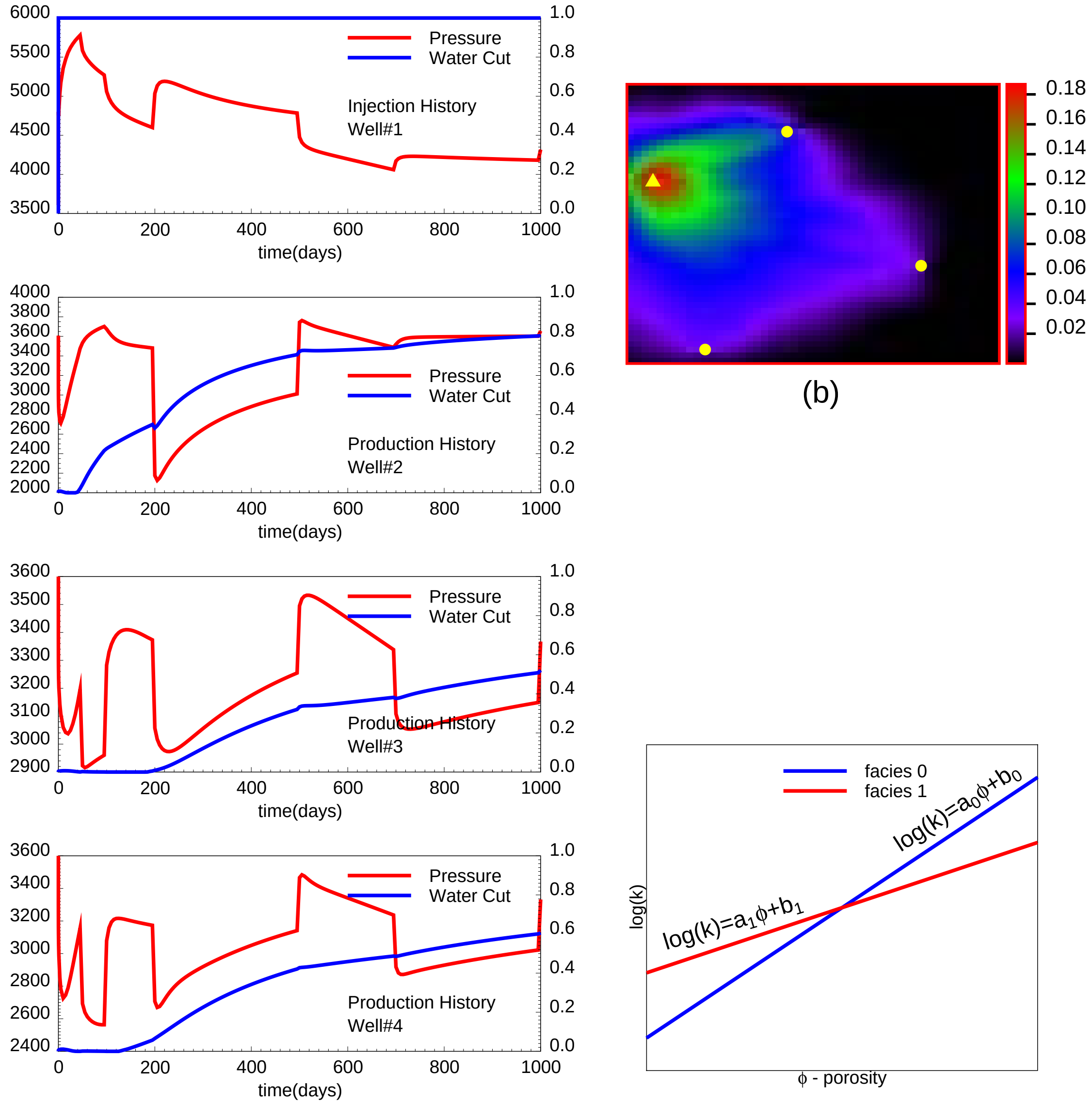

(a) (c)

Figure 8.10: (a): Long-term pressure and water cut history collected at four wells. (b): Average 4-D seismic data between 100 and 800 days. (c): Unknown permeability-porosity correlations of the two facies.

Table 8.2: Evolution of parameters during the inversion process - integrating all data types.

Iterations	#1	#2	#3	#4	#5	#6	#7	#8
	(m_0)	(t_0)	(m_1)	(t_1)	(a_0)	(b_0)	(a_1)	(b_1)
Initial Guess	1.0	0.0	1.0	0.0	25.0	-10.0	25.0	-10.0
2	2.583	0.019	2.568	0.012	25.073	-9.834	25.027	-9.943
4	3.023	-0.127	5.208	0.034	26.390	-6.772	25.514	-8.940
6	2.839	-0.157	5.430	0.036	26.420	-6.660	25.566	-8.824
13	3.099	0.525	5.505	20.069	15.426	-3.349	16.903	-4.588
15	3.121	1.157	5.475	22.011	11.602	-2.101	11.704	-2.139
16	3.120	1.230	5.480	21.380	11.651	-2.116	11.651	-2.116
True value	3.120	1.230	5.480	21.380	11.651	-2.116	11.651	-2.116
Uncertainty(10^{-3})	1.464	207.7	0.510	27.63	141.0	58.19	17.70	6.20

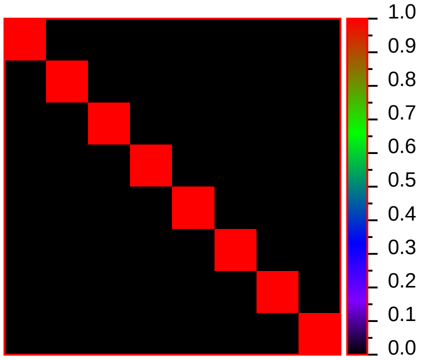

Figure 8.11: Resolution matrix.

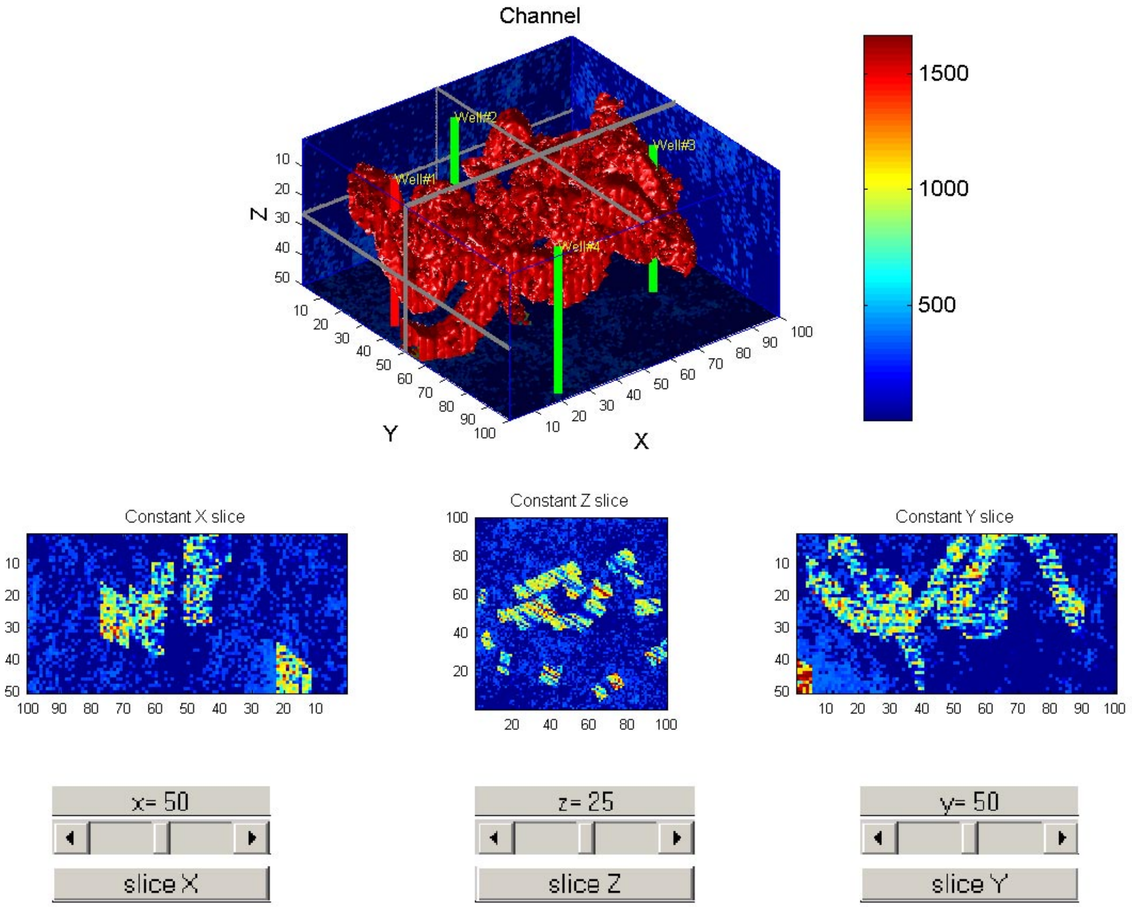

Figure 8.12: Calculated x-permeability distribution.

8.3 Probabilistic Integration of 3-D Seismic Data

In the previous section, the permeability in the x-direction was calculated based on the seismic multipliers and translations and this provided a deterministic approach in transferring the geological features observed in the 3-D seismic data to the permeability distribution. As was mentioned in Section 2.3, an alternative method for maintaining the geological features observed in the seismic data volume is to make use of a pixel-based geostatistical algorithm where the 3-D seismic data is used as soft conditioning data to constrain the generation of permeability. The reservoir model in the previous example was used, the only difference was that the x-permeability was simulated using the collocated geostatistical algorithm. The x-permeability honored the hard data at 100 points that would be obtained from core data analysis. The synthetic 3-D seismic impedance calculated from the previous example were used as soft data for the collocated simulation. The correlation coefficient between the x-permeability and the collocated seismic impedance was set to be equal to 0.85. The variogram models for each facies were the same ones described in the previous section. The resulting static model constructed by this algorithm was guaranteed to honor all available sources of static data. The knowledge about the 100 hard data and the correlation coefficient can be known with relatively high certainty. What were most uncertain were the parameters defining the variogram models and these were considered as the parameters of inversion. A list of parameters chosen for the inversion in this example were as follows:

- *Parameter # 1* (c^1): the *sill* of the variogram model used for channel facies representing a contribution of the spherical structure.
- *Parameter # 2* (α^1_{max}): the *azimuth* defining the geometric anisotropy of the variogram used for channel facies.
- *Parameter # 3* (a^1_{max}): the range along the direction of maximum continuity in the channel facies.
- *Parameter # 4* (c^0): the *sill* of the variogram model used for background facies representing a contribution of the spherical structure.

- *Parameter # 5* (α^0_{max}): the *azimuth* defining the geometric anisotropy of the variogram used for background facies.
- *Parameter # 6* (a^0_{max}): the range along the direction of maximum continuity in the background facies.
- *Parameter # 7* (a_0): the slope in the log $k - \phi$ correlation used for the background facies.
- *Parameter # 8* (b_0): the intercept in the log $k - \phi$ correlation used for the background facies.
- *Parameter # 9* (a_1): the slope in the log $k - \phi$ correlation used for the channel facies.
- *Parameter # 10*(b_1): the intercept in the log $k - \phi$ correlation used for the channel facies.

The first attempt to match the data was to choose the parameters of inversion to be those defining the variogram models of the two facies while keeping the coefficients of the permeability-porosity correlation constant. Table 8.3 shows the evolution of each parameter during the inversion process. The last two rows show the true value and the relative uncertainty in estimating each parameter. The algorithm was able to converge after 20 steepest-descent iterations and all the data were matched perfectly. It should be noted here that the Gauss-Newton method was observed to experience a very slow progress. The two directions of maximum continuity in the two facies were recovered almost perfectly. The range along the direction of maximum continuity in the channel facies was resolved better than that in the background facies. During the first ten iterations the direction of continuity inside the channel were changed but the correlation ranges were not. At iteration number 13 where the continuity reaches an angle of 56 degrees, the range was changed abruptly. This was because before this critical angle, the water has not broken through and no reservoir information can be collected at the producers. After this angle of continuity, water has broken through suffciently, pressure and water cut at the wells became most informative and the algorithm reduced the range significantly in response to the pressure and water cut data.

The second parameterization scheme was to include the coefficients in the permeability-porosity correlations in both channel and background facies. A total of eight parameters were considered. Table 8.4 shows the evolution of each parameter during the inversion process and the last two rows show the true value and the relative uncertainty in estimating each parameter. In this case, only the correlation range and coefficients of channel facies were relatively recovered. The other parameters were far from the true values. A three-dimensional view of the calculated x-permeability was also shown in Figure 8.13.

Table 8.3: Evolution of parameters during the inversion process - parameters of variograms.

Iterations	#1	#2	#3	#4
	(α^1_{max})	(a^1_{max})	(α^0_{max})	(a^0_{max})
Initial Guess	35.0	700.0	40.0	120.0
2	36.51	699.67	35.00	117.5
3	47.27	698.57	58.97	110.7
4	51.79	698.47	60.21	110.3
7	53.49	698.17	59.75	108.1
10	54.34	698.07	59.98	107.8
13	56.58	588.60	59.28	139.1
17	58.61	563.80	59.23	144.40
20	59.61	562.00	59.23	144.8
True value	60.0	500.0	60.00	50.0
σ_α/α	0.0	0.54	0.0	0.61

Table 8.4: Evolution of parameters during the inversion process - parameters of variogram and permeability-porosity coefficients.

Iterations	#1	#2	#3	#4	#5	#6	#7	#8
	(α^1_{max})	(a^1_{max})	(α^0_{max})	(a^0_{max})	(a_0)	(b_0)	(a_1)	(b_1)
Initial Guess	35.0	700.0	40.0	120.0	15.0	-5.0	15.0	-5.0
2	31.56	488.9	38.91	192.0	14.29	-4.11	8.86	-1.40
3	32.36	334.37	38.44	81.24	21.55	-6.80	10.42	-1.69
4	32.92	303.47	38.18	90.06	22.09	-7.02	10.48	-1.71
5	32.37	569.25	38.66	18.06	24.40	-7.99	10.74	-1.80
6	32.44	526.87	30.87	20.31	24.50	-8.03	10.75	-1.80
7	32.41	526.80	30.83	20.30	24.60	-7.83	10.76	-1.78
8	32.42	526.80	30.85	20.30	24.61	-7.79	10.76	-1.79
9	33.17	527.50	31.79	21.30	24.60	-7.79	10.85	-1.82
10	33.16	527.50	31.80	21.30	24.60	-7.79	10.85	-1.82
True value	60.0	500.0	60.00	50.0	11.65	-2.11	11.65	-2.11
σ_α/α	2.4	0.04	12.4	27.6	113.7	155.7	4.0	8.7

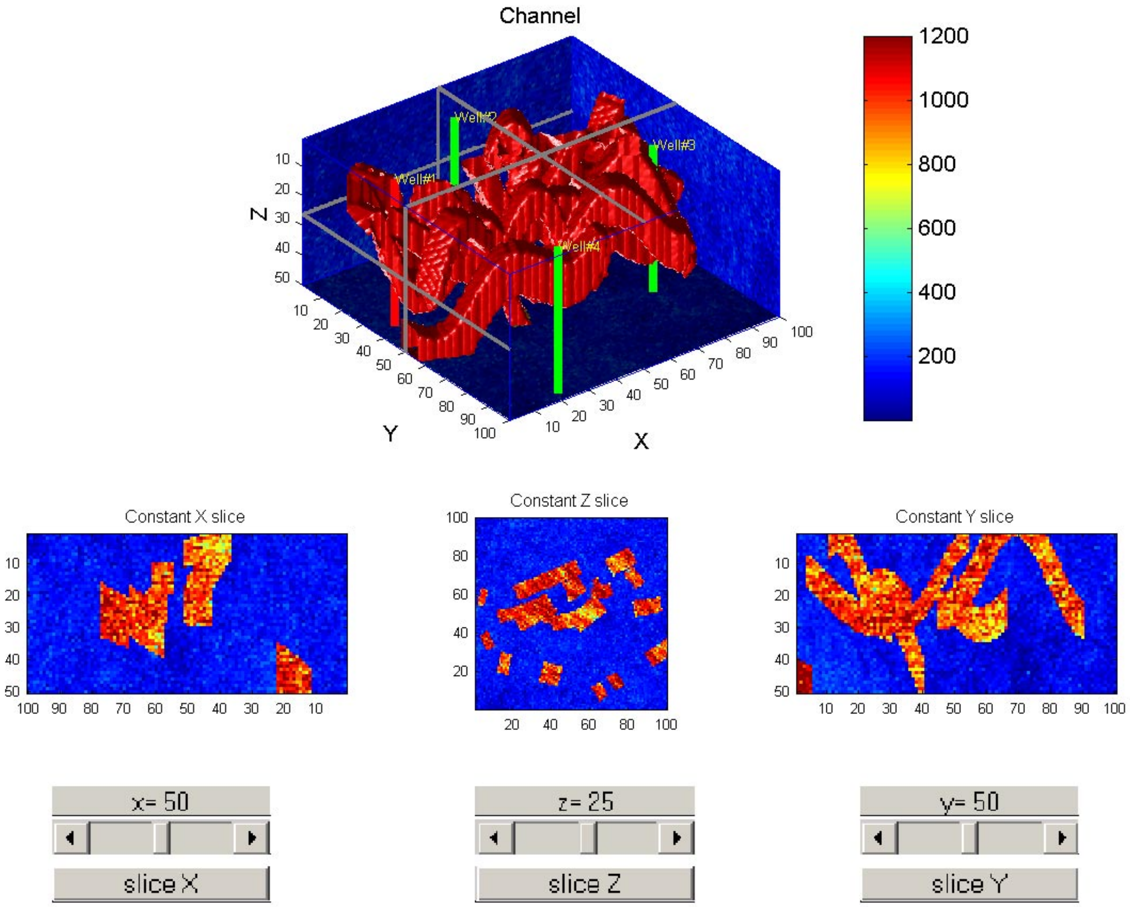

Figure 8.13: Calculated x-permeability distribution.

8.4 Random Seed as Parameter of Inversion

Besides the variogram, the random seed is another input parameter used in pixel-based geostatistical algorithms. By choosing different random seeds, the algorithms can generate equiprobable solutions constrained to all static data and geological information. However, the solutions generated may not honor the dynamic data. The goal is to seek values of the random seed so that the generated realizations also honor dynamic data. In this example, we shall demonstrate another useful application of the subcell technique to the calculation of sensitivity coefficients where the parameter of inversion is the random seed number. The random number generator is an algorithm that can take as input a real random seed and the sequence of uniformly distributed random numbers can be precalculated by subsequent calls to the algorithm. This sequence is then used in the pixel-based geostatistical algorithms for making random choices. Given knowledge of the random seed used, the random number generator results in a completely predictable sequence of random numbers and thus, the realizations generated by pixel-based geostatistical algorithms can be calculated as a function of the random seed. Mathematically, this enables the deterministic calculation of static gradients (the gradients of discrete permeability field) with respect to the random seed. In this work, the static gradients with respect to the random seed were calculated numerically by perturbing the random seed by an amount of 10^{-4}. The reference distribution of facies was generated on a mesh grid of $100 \times 130 \times 10$ making use of a hierarchical object-based geostatistical algorithm (fluvsim) developed by Deutsch and Wang (1996). The x-permeability was populated within each facies by means of a Sequential Gaussian Simulation (sgsim) geostatistical algorithm (geostatistical software package Deutsch and Journel, 1998). The y-permeability was taken to be equal to the x-permeability and z-permeability was assigned to be equal to one-tenth of the x-permeability. The random seed used as an input parameter into the sgsim algorithm was the only parameter of inversion considered in this example. A reference random seed of 9936748 was used and the resulting three-dimensional channel reservoir is depicted in Figure 8.14(a). The mesh grid of the upscaled model were $50 \times 65 \times 5$. Figure 8.14(b) shows the depth-averaged 4-D seismic data between

100 and 800 days. The well locations are also shown in red color for the three injectors and in white color for the six producers. Figure 8.15 illustrates the mismatches of pressure, water cut, and 4-D seismic data corresponding to the initial random seed of 84763998. The algorithm was able to converge to the calculated random seed of 3.96^7 after eight Gauss-Newton iterations. The matches of the data were almost perfect and are shown in Figure 8.16. A three-dimensional view of the calculated x-permeability is also depicted in Figure 8.17.

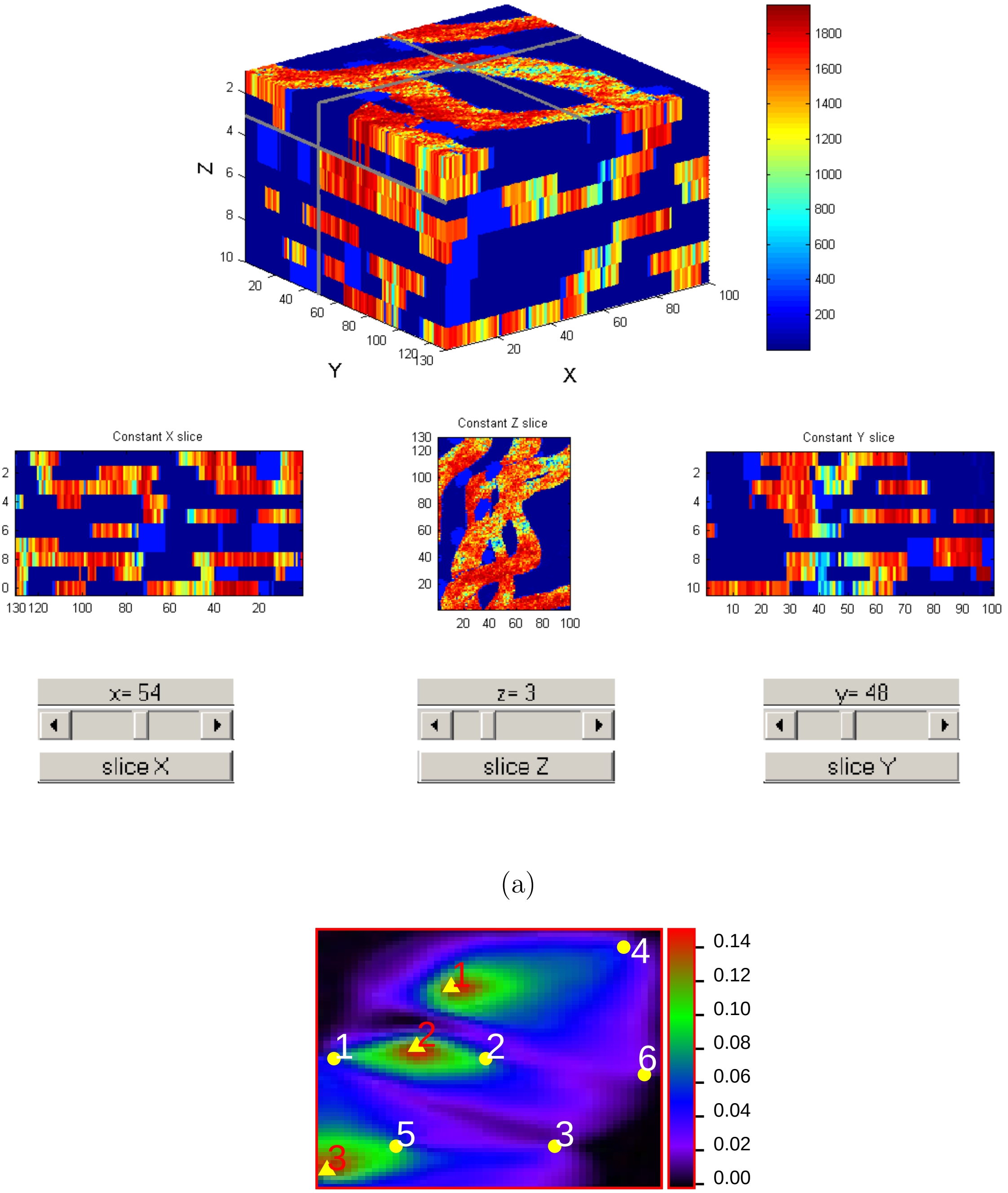

(a)

(b)

Figure 8.14: (a): Reference three-dimensional channel reservoir corresponding to the reference random seed of 9936748. (b): Depth-average 4-D seismic data between 100 and 800 days.

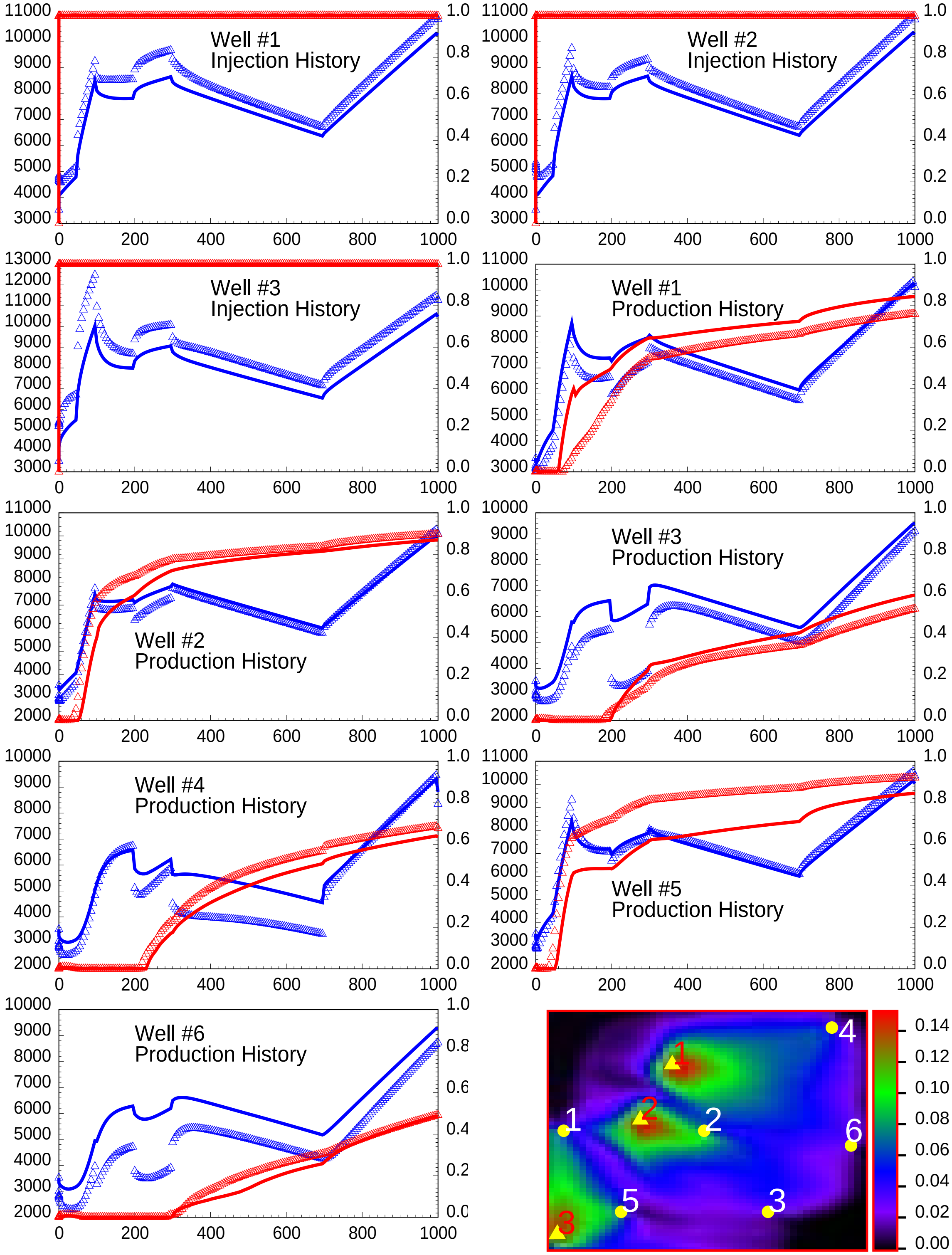

Figure 8.15: Nonmatches of pressure, water cut, and 4-D seismic data at initial random seed of 84763998.

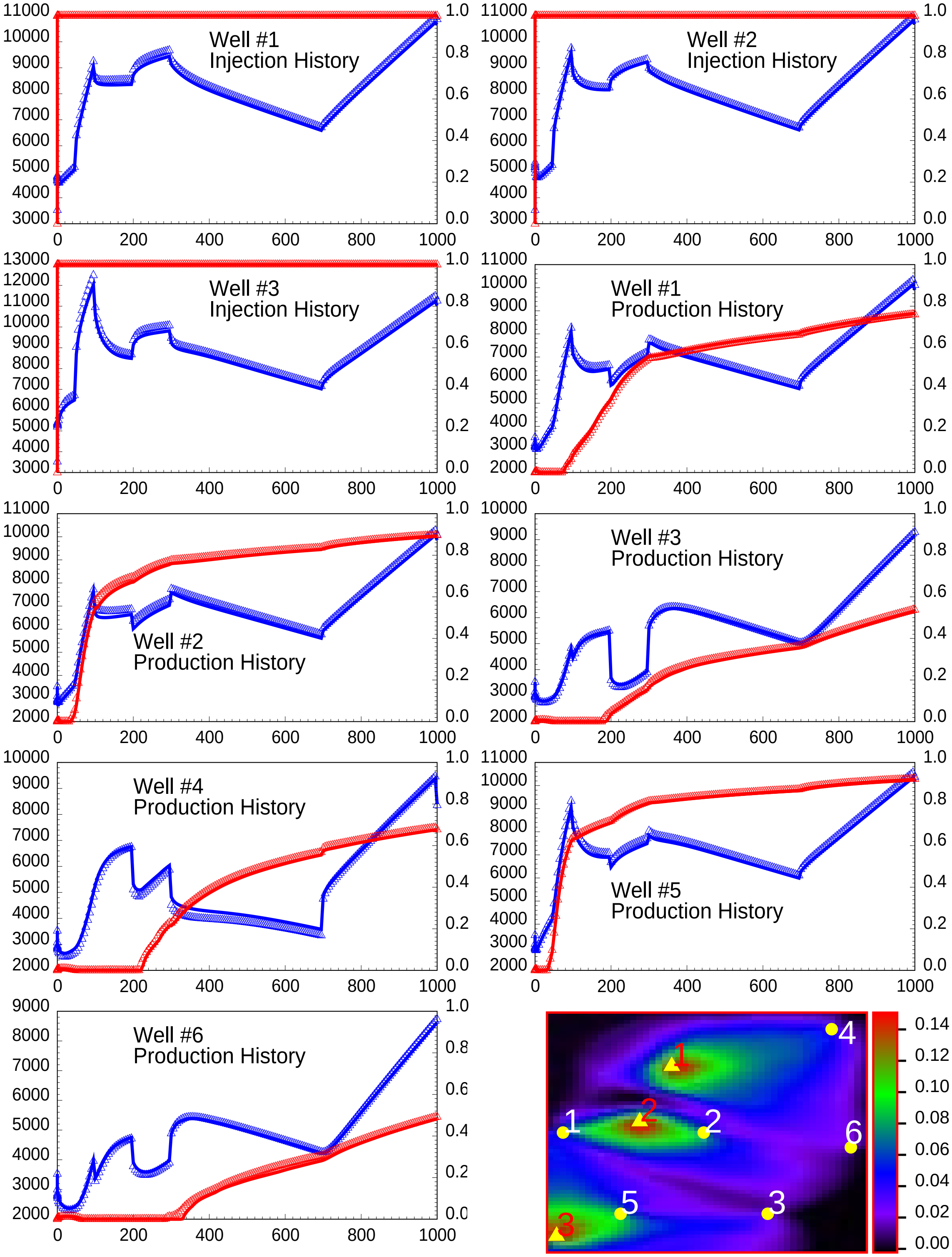

Figure 8.16: Matches of pressure, water cut, and 4-D seismic data corresponding to the calculated random seed of 3.96^7.

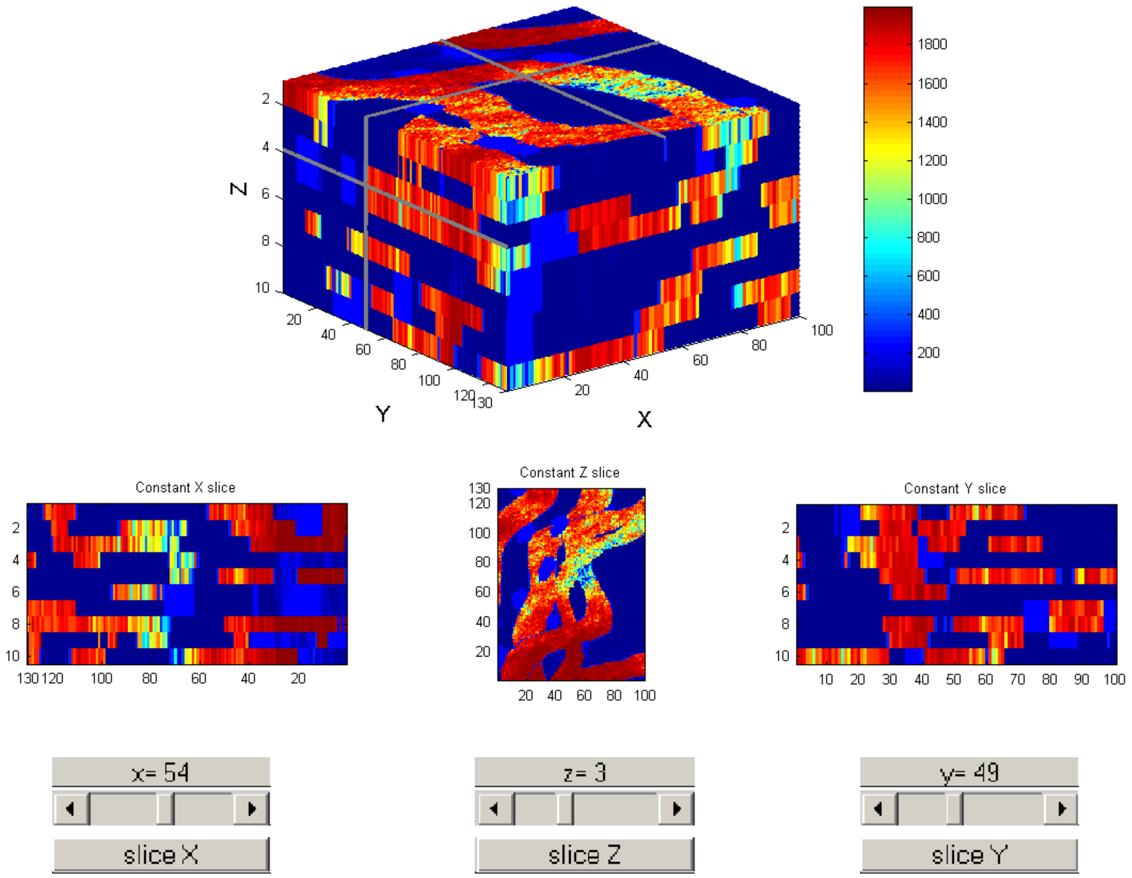

x= 54

z= 3

y= 49

Figure 8.17: Calculated three-dimensional channel reservoir corresponding to the calculated random seed of 3.96^7.

Chapter 9

Conclusions

In this work, we discussed the development of modeling techniques involving two- and three-dimensional geological objects. The objects were constructed based on the mathematical approach presented in Chapter 4 making use of various concepts such as geometric function, indicator function, and parity rule. We also introduced a useful set of Boolean algebra operations, such as union, difference, and intersection together with the *CSG* technique in which the application of these operations on a set of indicator functions enables the construction of more complex bodies from simple objects and makes possible the calculations of intersection volumes. Various optimization algorithms using gradient-based techniques were discussed and utilized to ensure that the geological model constructed reflects the observed data as closely as possible. In Chapter 5, we presented a hybrid method making use of the recursive adjoint-state equation to generate the sensitivity coefficients needed for the optimization algorithms. A substitution method was also implemented to validate the correctness of the sensitivity coefficients generated. In Chapter 6, we have evaluated and tested the ability of the proposed modeling techniques to identify geological features in a fluvial reservoir through a variety of synthetic examples. An assessment of the uncertainty associated with the model constructed and the prediction of future reservoir performance were investigated in Chapter 7. In Chapter 8, we demonstrated the successful implementation of the algorithms developed in this work in a number of realistic scenarios. The purpose was to illustrate the capability of the approach to solve practical problems and to also explore the difficulties and areas that require further research. These areas will be presented in this chapter together with concluding remarks.

This research was geared mainly toward the development of modeling techniques for generating descriptions of geometry and petrophysical properies (permeability and porosity) of a fluvial reservoir constrained to various sources of static and dynamic data. One aspect of this research was to develop mathematical foundations for describing multiple geological objects dynamically and realistically. Another aspect was to develop methods to assess the uncertainty associated with the calculated models and with the prediction of future reservoir performance, and finally to determine the value of each type of data in regard to the information richness.

The procedure developed as a result of this research allowed us to integrate data from several sources. The information that was integrated in this research included:

- Long-term pressure (from permanent down hole gauges)
- Production history (water cut, injection and production rates)
- Interpreted 4-D seismic data (change in water saturation)
- Permeability-porosity correlations
- Lithofacies information (from well log data)
- Hard data (from core analysis)
- Variogram models
- 3-D seismic data volume (results of seismic inversion)
- Geological events

3-D seismic data, in this work, was considered as two different sources of information. One source was used as a soft conditioning data to constrain the generation of the permeability and another was used as a source of raw distribution which simply differs from the permeability field by only a multiplier and a translation factor. The procedure can be adapted easily to the case where the seismic data are related to the permeability field in a more complex fashion. For example, the logarithm of the permeability field could be a quadratic or a function of the seismic-related properties where the quadratic coefficients and the weights defining the function are unknown parameters of inversion.

Similarly, 4-D seismic data were used as a change of saturation and this is not always a good approximation. This is because in many cases it is impossible to decouple geology effects from fluid-flow effects and consequently, the 4-D seismic data may not just be simply a function of the change of saturation but rather be a complex function of saturation, pressure, fluid density, permeability, porosity, etc. The method can also be adapted to integrate this type of 4-D seismic data provided that such a function is known either analyticaly or numerically even if with unknown coefficients.

From the results presented in this work, it has become apparent that by choosing the geometric and geostatistical quantities involved in the workflow for constructing the static model and associated with uncertainty to be parameters of inversion, the algorithms developed in this work can produce models that honor both static and dynamic data simultaneously. The method made possible the adjustment of the fine-scale model in a geologically sound fashion while performing the simulation history matching process at the upscaled level in a systematic procedure. In addition to the complex level of parameterization for the inversion, what distinguishes the method proposed in this work from the others described in literature was the use of geological events, the computational efficiency of the proposed algorithms, and the capability of solving practical problems.

The principle components developed in this research were as follows:

- A mathematical approach to construct two- and three-dimensional geological objects dynamically and realistically making use of various tools such as geometric function, indicator function, and parity rules.

- A method to calculate petrophysical properties (permeability and porosity) at geological scale making use of Boolean algebra operations such as union, difference, and intersection together with geological events.

- A method to compute the discrete permeability/porosity fields using appropriate area sampling techniques to ensure the continuity of the calculated fields with respect to geometric parameters.
- A subcell method to calculate the static gradients of the discrete permeability/porosity fields with respect to geometric parameters.
- A Boolean method making use of the *CSG* technique to construct more complex geological bodies from simple objects and to calculate the intersection volumes.
- A numerical three-dimensional two-phase flow simulator with the capability of computing sensitivity coefficients as part of the solution process.
- A hybrid method making use of the adjoint-state equation to generate the sensitivity coefficients.
- A constrained optimization algorithm using gradient-based techniques including steepest-descent, Gauss-Newton, and Levenberg-Marquardt combined with penalty function and step-length controller for constraints, Marquardt modification for stabilization, Cholesky factorization for the solution to a symmetric semipositive definite system, and line search together with quadratic proxy.
- A mathematical approach for performing variance/resolution analysis and an assessment of uncertainty associated with the prediction of future reservoir performance.

The subcell method is a key for achieving efficiency and accuracy in calculating the static gradients and thus, the sensitivity coefficients. This approach enables the recursive adjoint-state equation to generate sensitivity coefficients for complex geological models consisting of any number of geological objects with arbitrary geometric shapes. The accuracy of the sensitivity coefficients is not only a key for fast and feasible inversion but also critical in performing variance/resolution analysis and in assessing the uncertainty associated with reservoir forecasting. From the results of the numerical experiments performed in this research, it would be possible to conclude that the proposed procedure can be considered as an advanced reservoir simulation history matching process and can be utilized as a tool for reservoir characterization with a complex level of parameterization. The level of complexity depends on the set of parameters chosen for the inversion. Such a set could include conventional parameters that appear explicitly in the discrete equations of state such as the discrete permeability and porosity at every cell of the simulation mesh grid, or the parameters that are not found in the model equations such as geometric and geostatistical parameters.

The more interesting conclusions obtained from the results of this work are regarding the kinds of information each type of data carries. Long-term pressure are richest in information about the channel permeability and porosity but 4-D seismic data are most informative about the channel geometry. Water cut data always provide least information on the channel parameters. This is due to the fact that 4-D seismic data provides information that is spatially distributed in the reservoir in contrast to the other data that are localized at the wells. Stand-alone water cut data do not seem to carry much information on the channel geometry but result in a large increase in the resolution of pressure data when the two data are combined. By adding the 4-D seismic data, the integration of the three data types increases the resolution of the stand-alone 4-D seismic data by several orders of magnitudes. It was also found that it is mainly the noise level that causes the distortion of the channel geometry while the noise frequency does not. Good solutions can frequently be obtained even in the presence of dense noise in the field measurements but not in the presence of sparse (but high level) noise. Though pressure and water cut history are collected only at the wells, these types of data help significantly in reducing the bias of the inversion results caused by the spatially distributed noise from 3-D seismic surveys. Finally, the channel orientation and sinuosity are the two parameters that were found to be best resolved.

9.1 Areas that Need Futher Research

The results of this study give rise to a number of areas that need further research. Those areas are summarized here.

The error in the forward modeling equations contributes a source of uncertainty associated with the solution of the inversion problem. The theory of the inversion problem in this work assumed implicitly that the forward mathematical models are complete and exact. This assumption is normally not true in cases where a complex physical situation needs to be described and various effects have been neglected in its formulation or in cases where the forward solution technique is subject to significant errors. This is critical in finding the solution of the inversion problem because we would match the data to the inaccurate model response and this may result in a distortion of the estimates of the parameters. Therefore, it is important to conduct more research in the forward flow modeling, specially in the areas of well modeling in multiphase regimes, well modeling near boundaries, and in the areas of controlling numerical dispersion in finite difference methods.

Another research area in the context of this work concerns the problem of upscaling. All parameters of inversion considered in this work are related directly to the construction of the fine-scale model which is connected to the simulation model through an upscaling algorithm. Therefore, the upscaling algorithm also plays an important component in the entire workflow and utilizing a good algorithm is crucial in this type of inversion problem.

In this work, the uncertainty of the parameter estimates was calculated based on a purely linear model and this assumption is obviously not consistent with the complex relationship between the reservoir response and the underlying rock and fluid properties. As a result, there will be some bias in the uncertainty estimates and if this bias is small compared to the other errors involved, then the linear model would yield a good approximation to the covariance matrix of the estimated parameters. Otherwise, further research has to be conducted to investigate an alternative method for calculating the uncertainty.

Nomenclature

p	Pressure
s	Saturation - *fraction*
D	Depth
g	Gravitational acceleration or geometric function
u	Positions
y	Solution of the forward problem
p_{ref}	Pressure at reference depth
U	Darcy velocity
k_r	Relative permeability
k	Absolute permeability
A	Departure
f	Sinuosity
B	Formation volume factor
q	Volume metric flow rate at standard condition
s_k	Well skin factor
$npar$	Number of parameters
$nobs$	Number of observations
$ncons$	Number of constraints
d	Data
p_{wf}	Pressure data
w_{ct}	Water cut data

E	Objective function
R	Residual in material balance
I	Indicator function
$\mathbf{J}$	Jacobian matrix
$\mathbf{R}$	Resolution matrix
$\mathbf{S}_{inf}$	Information matrix
$\mathbf{C}$	Covariance matrix
$\mathbf{G}$	Sensitivity matrix
$\mathbf{S}$	Full sensitivity matrix
$\mathbf{H}$	Hessian matrix
$\mathbf{U}$	SVD factor matrix
$\mathbf{V}$	SVD factor matrix
$\mathbf{W}$	Weight matrix
q	Production (Injection) rate

Symbols

α	Parameter
φ	Porosity
θ	Displacement
Θ	Model parameters
ω	Weighting function in *weighted area sampling* technique
μ	Viscosity or *Levenberg-Marquardt* coefficient
Φ	Flow potential
ρ	Density or step size in linear search
γ	Specific weight
Λ	Diagonal matrix of singular values
Δ	Difference
∇	Gradient operator
σ	Standard deviation

Subscripts

w	Water phase
o	Oil phase
p	Nonzero singular values
cal	Calculated data
obs	True or observed data

Superscripts

$\vec{\ }$	Vector

References

[1] Allen, L. J.: "Studies in Fluviatile Sedimentation: An Exploratory Quantitative Model for the Architecture of Avulsion-Controlled Alluvial Suites," *Sedimentary Geology* (1978) **21**, 129–147.

[2] Alexander, J.: "Idealized Flow Models to Predict Alluvial Sandstone Body Distribution in the Middle Jurassic Yorkshire Basin," *Marine and Petroleum Geology* (1986) **3**, 298–305.

[3] Augedal, H. O., Stanley, K. O., and More, H.: "A Program for Stochastic Modeling and Evaluation of Reservoir Geology," presented at the 1986 IFE/SSI Conference on Reservoir Description and Simulation With Emphasis on EOR, Oslo, September 3-5.

[4] Bard, Y.: *Nonlinear Parameter Estimation*, Academic Press, New York, NY (1970).

[5] Begg, S. H., Gustason, E. R., and Deacon, M. W.: "Characterization of a Fluvial-Dominated Delta: Zone 1 of the Prudhoe Bay Field," paper SPE 24698 presented at the 1992 67th Annual Technical Conference and Exhibition, Washington, DC, October 4-7.

[6] Begg, S. H., Kay, A., Gustason, E. R., and Angert, P. F.: "Characterization of a Complex Fluvial-Deltaic Reservoir for Simulation," *SPEFE* (September 1996) 147–153.

[7] Bi, Z., Olivier, D. S., and Reynolds, A. C.: "Conditioning 3D Stochastic Channels to Pressure Data," paper SPE 56682 presented at the 1999 SPE Annual Technical Conference and Exhibition, Houston, Texas, October 3-6.

[8] Branagan, P. T., Lee, S. J., Cipolla, C. L., and Wilmer, R. H.: "Pre-Frac Interference Testing of a Naturally Fractured, Tight Fluvial Reservoir," paper SPE 17724 presented at the 1988 SPE Gas Technology Symposium, Dallas, Texas, June 13-15.

[9] Bridge, J. S. and Leeder, M. R.: "A Simulation Model of Alluvial Stratigraphy.," *Sedimentology* (1997) **26**, 617–44.

[10] Broyden, C. G.: "The Convergence of a Class of Double-Rank Minimization Algorithm," *J. Inst. Maths Applics* (1970) **6**, 76–90.

[11] Clementsen, R.: "A Computer Program for Evaluation of Fluvial Reservoirs.," presented at the International Conference on North Sea Oil and Gas Reservoirs, Trondheim, June 8-11, 1989.

[12] Datta-Gupta, A., Vasco, D. W., and Long, J. C. S.: "Sensitivity and Spatial Resolution of Transient Pressure and Tracer Data For Heterogeneity Characterization," paper SPE 30589 presented at the 1995 SPE Annual Technical Conference and Convention, Dallas, TX, October, 22-25.

[13] Deutsch, C. V. and Wang, L.: "Hierarchical Object-Based Geostatistical Modeling of Fluvial Reservoirs," paper SPE 36514 presented at the 1996 SPE Annual Technical Conference and Exhibition, Denver, October, 6-9.

[14] Deutsch, C. V. and Journel, A. G.: *Geostatistical Software Library and User's Guide Second Edition*, Oxford University Press, New York, NY (1998).

[15] Dixon, T. N., Seinfeld, J. H., Starzman, R. A., and Chen, W. H.: "Reliability of Reservoir Parameters from History Matched Drillstem Tests," paper SPE 4282 presented at the Third Numerical Simulation Symposium, Houston, Texas, January 10-12, 1973.

[16] Eisenstat, S. C., Schultz, M. H., and Sherman, A. H.: "Yale Sparse Matrix Package, Technical Reports 112 and 114," Yale University Departament of Computer Science (1977).

[17] Fletcher, R.: "A New Approach to Variable Metric Algorithms," *Computer Journal* (1970) **13**, 317–322.

[18] Foley, D. J., Dam, V. A., Feiner, K. S., and Hughes, F. J.: *Computer Graphics, Principles and Practice*, Addison-Wesley (1997).

[19] Gill, P. E., Murray, W., and Wright, M. H.: *Practical Optimization*, Academic Press, San Diego, CA (1981).

[20] Goldfarb, D.: "A Family of Variable Metric Methods Derived by Variational Means," *Mathematics of Computation* (1970) **24**, 23–26.

[21] Haldorsen, H. H. and Lake, L. W.: "A New Approach to Shale Management in Field-Scale Simulation Models," *JPT* (August 1984) 447–457.

[22] He, N., Reynolds, A. C., and Oliver, D. S.: "Three Dimensional Reservoir Description From Multiwell Pressure Data and Prior Information," *JPT* (September 1997) 312.

[23] Henriquez, A., Tyler, K. J., and Hurst, A.: "Characterization of Fluvial Sedimentology for Reservoir Simulation Modeling," *SPEFE* (September 1990) 211–216.

[24] Hower, T. L. and Colins, R. E.: "Detecting Compartmentalization in Gas Reservoirs Through Production Performance," paper SPE 19790 presented at the Annual Technical Conference and Exhibition, San Antonio, Texas, October 8-11, 1989.

[25] Jackson, D.: "Interpretation of Inaccurate, Insufficient and Inconsistent Data," *Geophysical Journal of the Royal Astronomical Society* (1972) **28**, 97–109.

[26] Johnson, H. D. and Krol, D. E.: "Detailed Geological Modeling of a Heterogeneous Sandstone Reservoir: Lower Jurassic Statfjord Formation, Brent Field," paper SPE 13050 presented at the 1984 SPE Annual Technical Conference and Exhibition, Houston, Texas, September 16-19.

[27] Landa, J. L.: *Reservoir Parameter Estimation Constrained to Pressure Transients, Performance History and Distributed Saturation Data*, PhD dissertation, Stanford University (June 1997).

[28] Landa, J. L. and Horne, R. N.: "A Procedure to Integrate Well Test Data, Reservoir Performance History and 4-D Seismic Information into a Reservoir Description," paper SPE 38653 presented at the 1997 SPE Annual Technical Conference and Exhibition, San Antonio, Texas, October 5-8.

[29] Landa, J. L., Kamal, M. M., Jenkins, C. D., and Horne, R. N.: "Reservoir Characterization Constrained to Well Test Data: A Field Example," paper SPE 36511 presented at the 1996 SPE Annual Technical Conference and Exhibition, Denver, Colorado, October 6-9.

[30] Lord, M. E. and Collins, R. E.: "Detecting Compartmented Gas Reservoirs Through Production Performance," paper SPE 22941 presented at the 1991 SPE Annual Technical Conference and Exhibition, Dallas, Texas, October 6-9.

[31] Lord, M. E., Collins, R. E., and Kocberber, S.: "A Compartmented Simulation System for Gas Reservoir Evaluation With Application to Fluvial Deposits in the Frio Formation, South Texas," paper SPE 24308 presented at the 1992 SPE Mid-Continent Gas Symposium, Amarillo, Texas, April 13-14.

[32] Mao, S.: *Multiple Layer Surface Mapping With Seismic Data and Well Data*, PhD dissertation, Stanford University (June 1999).

[33] Massonnat, G. J. and Bandiziol, D.: "Interdependence between Geology and Well Test Interpretation," paper SPE 22740 presented at the 1991 SPE Annual Technical Conference and Exhibition, Dallas, Texas, October 6-9.

[34] Menke, W.: *Geophysical Data Analysis: Discrete Inverse Theory,* Academic Press, Inc., San Diego, CA (1989).

[35] Oliver, D. S., Reynolds, A. C., Bi, Z., and Abacioglu, Y.: "Integration of production data into reservoir models," *Petroleum Geoscience* (2001) **7**, 65–73.

[36] Phan, V. Q.: "Inferring Depth-dependent Reservoir Properties From Integrated Analysis Using Dynamic Data," Master's thesis, Stanford University (June 1998).

[37] Phan, V. Q. and Horne, R. N.: "Determining Depth-Dependent Reservoir Properties Using Integrated Data Analysis," paper SPE 56423 presented at the 1999 SPE Annual Technical Conference and Exhibition, Houston, Texas, October 3-6.

[38] Press, W. H., Teukolsky, S. A., Vetterling, W. T., and Flannery, B. P.: *Numerical Recipes in C –The Art of Scientific Computing– Second Edition*, Cambridge University Press, New York, NY (1996).

[39] Raghavan, R., Dixon, T. N., Robinson, S. W., and Phan, V. Q.: "Integration of Geology, Geophysics, and Numerical Simulation in the Interpretation of a Well Test in a Fluvial Reservoir," paper SPE 62983 presented at the 2000 SPE Annual Technical Conference and Exhibition, Dallas, Texas, October 1-4.

[40] Shanno, D. F.: "Conditioning of Quasi-Newton Methods for Function Minimization," *Mathematics of Computation* (1970) **24**, 647–657.

[41] Smith, P. J. and Morgan, D. T. K.: "Modeling Faulted and Fluvial Reservoirs," paper SPE 15853 presented at the 1986 SPE European Petroleum Conference, London, October 20-22.

[42] Stewart, G. and Whaballa, A. E.: "Pressure Behavior of Compartmentalized Reservoirs," paper SPE 19779 presented at the 1989 SPE Annual Technical Conference and Exhibition, San Antonio, Texas, October 8-11.

[43] Strebelle, S.: "Conditional Simulation of Complex Geological Structures Using Multiple Point Geostatistics," *Mathematical Geology* (2002) **34**, 1–25.

[44] Zheng, S. and Corbett, P.: "The Impact of Variable Formation Thickness on Pressure Transient Behavior and Well Test Permeability in Fluvial Meander Loop Reservoir," paper SPE 36552 presented at the 1996 SPE Annual Technical Conference and Exhibition, Denver, October 6-9.

Appendix A

Computer Programs

A.1 General Overview

A set of computer programs has been developed to implement the algorithms and methods described in this work. Most of these routines were written by the author of this dissertation and the rest were modified from *Numerical Recipes* (see Press, Teukolsky, Vetterling, and Flannery, 1996) and geostatistical software package *GSLIB*. All routines were written in **C++** and consist of the following types:

- Source code files have extensions **.C**.
- Header files have extensions **.h**.
- Input parameter files have extensions **.par**.
- Library files have extensions **.a** (all library routines were from *Numerical Recipes* (1996), *Yale Sparse Matrix Solver* (1977), and geostatistical software package *GSLIB*).
- Output files have extension **.out** (storing computational results from the run).
- Input data files have extensions **.dat** (providing data for the runs such as time-dependent rate and bottom hole pressure, seismic amplitude map etc...).

The files with extensions **.C**, **.h**, and **.a** are for compiling and linking. This job is accomplished by using **make** utility with a provided *makefile*. The procedures to compile and run the programs are as follows:

To compile and link: in `duri` unix workstation, set the variables **LIB** to **LIBDURI** and **EXEC** to **EXECDURI**. In `prudhoe` unix workstation, set the variables **LIB** to **LIBPRUD** and **EXEC** to **EXECPRUD**. Then, key in the `make` command for compiling and linking. The executable code created is named **solvep** on the `prudhoe` machine and **solved** on the `duri` machine.

To run: prepare the relevant `input` data (**.dat**) and parameter files (**.par**) based on the template files and key in **solvep** on `prudhoe` or **solved** on `duri`. The program will generate a series of output data files and postscript files. (noted that the generation of postscript files is only available on `prudhoe` machine).

A.2 Files in `makefile`

In order to make an executable version of the program, the following list of files must be present in the current directory at the time of invoking the `make` command. The task performed by each code was also briefly described.

`makefile`	compiling and linking instructions to create executable code.
`main.C`	main program, driver for parameter estimation algorithm, handle various modeling types including pixel-based, static, and dynamic object-based, read input data files and write output files, compute reservoir response, sensitivity coefficient, resolution, variance, information regarding the estimates, predict and estimate uncertainty in future reservoir performance.
`input.C`	input and perform data checking.
`AlloArrays.C`	allocate storage for working arrays.

`Simulator.C`	compute model response and sensitivity coefficients.
`matrixstruct.C`	compute the structure of the Jacobian matrix.
`NonZero.C`	compute the number of nonzero elements in the Jacobian matrix.
`NUMBER.C`	numbering blocks and wells
`IniPreProData.C`	compute pressure and production data at initial condition.
`Depth.C`	compute depth at all cells.
`Initial.C`	initiliazing reservoir from equilibrium.
`GetQBHP_t.C`	lookup for the specified flow rate and pressure at a given instant in time.
`Mass.C`	compute masses of fluid stored at all cells.
`Flow_dFlow.C`	compute the flow terms and its derivatives with respect to the forward solution.
`Well_dWell.C`	compute the well terms and its derivatives with respect to the forward solution.
`D_Mass.C`	compute the accumulation terms and its derivatives with respect to the forward solution.
`KrSw.C`	compute the phase relative permeability and its derivatives with respect to the forward solution.
`GetResidual.C`	compute the residual vector of material balance equations.
`GetJacobian.C`	compute the Jacobian matrix.
`Solver.C`	solve the system of linear equations.
`Error.C`	compute the error in the Newton-Raphson algorithm.
`GetProData.C`	compute cumulative production data.
`output.C`	output computational results.
`NextTimeStep.C`	compute automatic time step control.
`PressAvg.C`	compute the average reservoir pressure.
`GetIniGuePara.C`	initializing parameters by user's guesses.
`SwapLamda.C`	swap arrays.
`GetRockPro_0.C`	compute initial rock properties.
`Property.C`	compute rock properties at a given cell.

`GetRockPro.C`	compute rock properties at all cells.
`Correlation.C`	compute the permeability-porosity correlation and its derivatives.
`GetUnkSkinCoef.C`	compute the unknown well skin factors and coefficients from parameters.
`Object.C`	compute object geometry and properties from parameters.
`dpars_Zobjs.C`	compute the gradients of the object properties with respect to parameters.
`dpars_Zs.C`	compute the gradients of cell properties with respect to parameters (static modeling).
`dpars_Zcells.C`	compute the gradients of cell properties with respect to parameters (dynamic modeling).
`dpar_WCT.C`	compute the gradients of water cut with respect to parameters.
`dpar_R.C`	compute the gradients of the residual vector with respect to parameters (static modeling).
`dpar_R_obj.C`	compute the gradients of the residual vector with respect to parameters (dynamic modeling).
`Paraestimator.C`	optimization algorithm.
`ParaestimatorObj.C`	optimization algorithm.
`ReadFluvsimSgsim.C`	input parameters for object- and pixel-based geostatistical algorithms.
`Fluvsim.C`	object-based geostatistical algorithms.
`Sgsim.C`	pixel-based geostatistical algorithms.
`ComputeResInfCov.C`	perform resolution and variance analysis.

A.3 Input Parameter File Structure

There are three input parameter files, two of which are used as input parameter files for the object- and pixel-based geostatistical alogorithms and have the **GSLIB** format. The third one, with a fixed name of `solve.par` is used as input parameter file for nonlinear parameter estimation algorithm with data being split into sections.

Each section begins with a semantic key word followed by a brief instruction and then associated data which can be either explicit data or *INCLUDE* file name. The order in which the sections are specified is not important. The data record, within each section, must be terminated with a slash(/). Any lines beginning with two characters '- -' are treated as comments. A data quantity or record can be repeated a required number of times by preceding it with the required number and an asterisk. It noted that for a single data quantity the required number and an asterisk are placed next to the quantity as in 3*55 and this is equivalent to three identical numbers 55 55 55. For a record of data, the required number and an asterisk are placed at least one white space from the data record as in 3* 10 20 30 and this is equivalent to three identical records as

10 20 30
10 20 30
10 20 30

After each section is read a *CHECKING DATA* routine is invoked to ensure the correctness of data input. If data are input improperly a message will be displayed. The displayed message is a warning if the error is minor and the program continues. If the error is fatal the program is terminated. The displayed message contains information about all possibilities that may cause the error. The computer memory is allocated dynamically and can shrink and grow during run time to optimize memory management. Some messages associated with the memory management are also displayed during run time to report the point at which the original allocated memory was insufficient.

A.4 Ancillary Programs

There are some ancillary programs written to facilitate the tasks and to perform data processing that are necessary before or after the job. These programs are described as follows:

`gps`	generate color maps and plots in Postscript format, this program was written by R.C. Wattenbarger at Stanford University in 1992.
`vpwf`	view the comparison between the calculated and the observed pressure.
`vwct`	view the comparison between the calculated and the observed water cut.
`vdsw`	view the comparison between the calculated and the observed 4-D seismic.
`vpermx`	view the comparison between the calculated and the true x-permeability.
`vpermy`	view the comparison between the calculated and the true y-permeability.
`vpermz`	view the comparison between the calculated and the true z-permeability.
`vporo`	view the comparison between the calculated and the true porosity.
`vspwf`	view the comparison between the numerical and analytical gradients of pressures.
`vswct`	view the comparison between the numerical and analytical gradients of water cut.
`vsdsw`	view the comparison between the numerical and analytical gradients of 4-D seismic.
`vres`	view the resolution matrix.
`vcov`	view the covariance matrix.
`genc`	draw channel parameters from triangular distributions.
`genw`	extract sample data from reference data set to mimic actual well data.
`time`	UNIX utility to print out the amount of real, system, and user time used.

A.5 Input Data Files

The names of the input data files with extensions `.dat` are arbitrary and are specified in the `solve.par` file. These data files include:

- one file for restart job.
- one file for user initial condition.
- one file for export time step.
- one file for input specified flow rate.
- one file for input specified bottom hole pressure.
- one file for object definition.
- one file for time-dependent images.
- one file for heterogeneous porosity field.
- one file for heterogeneous permeability in x direction field.
- one file for heterogeneous permeability in y direction field.
- one file for heterogeneous permeability in z direction field.
- one file for parameter distribution.
- a number of files for input channel geometry and properties.
- a number of files for input facies and simulated maps.

A.6 Output Data Files

There is a number of output files created during the execution of the job. A list of these output files together with a brief description of what is being stored in each file during the run are as follows.

`objprotrue.out`	storing true parameter values defining objects.
`skinstrue.out`	storing the true values well skin factors.
`coeffstrue.out`	storing the true coefficients in nonlinear correlation.
`poromaptrue.out`	storing true porosity values.
`permxmaptrue.out`	storing true x-permeability.

`permymaptrue.out`	storing true y-permeability.
`permzmaptrue.out`	storing true z-permeability.
`pwfobs.out`	storing down hole pressure from permanent gauges.
`wctobs.out`	storing observed water cut.
`dswmapobs.out`	storing observed 4-D seismic values.
`culobs.out`	storing observed cumulative production (injection) of liquid.
`cuwobs.out`	storing observed cumulative production (injection) of water.
`liqrobs.out`	storing observed production (injection) liquid rate.
`cuoobs.out`	storing observed cumulative production (injection) of oil.
`oilrobs.out`	storing observed production (injection) oil rate.
`watrobs.out`	storing observed production (injection) water rate.
`objpro_.out`	storing calculated parameter values defining objects for all iterations.
`skins_.out`	storing calculated well skin factors for all iterations.
`coeffs_.out`	storing computed coefficients in nonlinear correlation.
`poromap_xxx.out`	storing computed porosity values at the xxx^{th} iteration.
`permxmap_xxx.out`	storing computed x-permeability at the xxx^{th} iteration.
`permymap_xxx.out`	storing computed y-permeability at the xxx^{th} iteration.
`permzmap_xxx.out`	storing computed z-permeability at the xxx^{th} iteration.
`poromap.out`	storing computed porosity values at the current iteration.
`permxmap.out`	storing computed x-permeability at the current iteration.
`permymap.out`	storing computed y-permeability at the current iteration.
`permzmap.out`	storing computed z-permeability at the current iteration.
`pwf.out`	storing calculated well bottom hole pressure at the current iteration.
`wct.out`	storing computed water cut at the current iteration.
`dswmap.out`	storing computed 4-D seismic values at the current iteration.

`pwf_xxx.out`	storing calculated well bottom hole pressure at the xxx^{th} iteration.
`wct_xxx.out`	storing computed water cut at the xxx^{th} iteration.
`dswmap_xxx.out`	storing computed 4-D seismic values at the xxx^{th} iteration.
`cul.out`	storing calculated cumulative production (injection) of liquid at the current iteration.
`cuo.out`	storing calculated cumulative production (injection) of oil at the current iteration.
`cuw.out`	storing calculated cumulative production (injection) of water at the current iteration.
`liqr.out`	storing calculated production (injection) liquid rate at the current iteration.
`oilr.out`	storing calculated production (injection) oil rate at the current iteration.
`watr.out`	storing calculated production (injection) water rate at the current iteration.
`presmap.out`	storing calculated field pressure at the current iteration.
`satmap.out`	storing calculated field water saturation at the current iteration.
`senpwfa.out`	storing sensitivity of down hole pressure computed analytically.
`senpwfn.out`	storing sensitivity of down hole pressure computed numerically.
`senwcta.out`	storing sensitivity of water cut computed analytically.
`senwctn.out`	storing sensitivity of water cut computed numerically.
`sendswmapa.out`	storing sensitivity of 4-D seismic computed analytically.
`sendswmapn.out`	storing sensitivity of 4-D seismic computed numerically.
`senswmapa.out`	storing sensitivity of water saturation computed analytically.
`senswmapn.out`	storing sensitivity of water saturation computed numerically.

A.7 Sample Session

All input data files and input parameter files must be prepared before the job can be lauched. The input data files are prepared in free format. The same rules as used for the `solve.par` file such as repeated data quantity and comments can also be applied for these files. The reading and writing are sequential in order of x (cycling fastest), y, z, and t. The program checks data as it is read. Various tasks can be performed by selecting options in the following sections in the `solve.par` file:

RUNOPTION
– 0 for simulation only.
– 1 for generating historical data.
– 2 for computing sensitivity coefficients only.
– 3 for parameter estimation.
– 4 for future reservoir prediction.
3/
RUNMETHOD
– ***method of modeling***
– 0 for pixel modeling.
– 1 for static object modeling.
– 2 for dynamic object modeling.
2/
SENMETHOD
– ***method of computing sensitivity coefficients***
– 0 analytical method.
– 1 substitution method.
0/
ALGORITHM
– ***method of optimisation***
– 0 Steepest Descent
– 1 Gauss Newton
– 2 Levenberg-Marquardt - Marquardt parameter (=0.01 recommended)

– 3 Powell ”Dog-Leg”

1 0.01/

RESTARTITER

– ***The iteration number at which the inversion starts from***

1/

Steps, in regarding the use of the `solve.par` file, for designing and solving a test problem and forecasting future reservoir performance can be summarized as follows:

- prepare all necessary input data files.
- define method of modeling by choosing appropriate option under section **RUNMETHOD**.
- generate synthetic data by choosing option 1 under section **RUNOPTION**.
- define method of computing sensitivity coefficients by choosing appropriate option under section **SENMETHOD**.
- compute the sensitivity coefficients by chosing option 2 under section **RUNOPTION**. The purpose for this option is to make sure a good agreement between the calculated gradients using analytical method and those using substitution method.
- define method of optimisation by choosing appropriate option under section **ALGORITHM**.
- solve the parameter estimation problem by chosing option 3 under section **RUNOPTION**.
- forecast future reservoir performance by chosing option 4 under section **RUNOPTION**.

At each iteration during the solve of the parameter estimation problem, the objective function values and the 2-norm of its gradients can be viewed numerically by the file named `iter`. Evolution of parameters and comparison between the model response and the reservoir response can also be graphically viewed making use of ancillary tools as described in Section A.4.